CORRELATED PHOTON PAIRS AND MULTIPHOTON STATES FROM A COLD ATOMIC ENSEMBLE

by

LI YIFAN
(M.Sc., Sorbonne University)

A THESIS SUBMITTED FOR THE DEGREE OF

DOCTOR OF PHILOSOPHY

of the

CENTRE FOR QUANTUM TECHNOLOGIES

NATIONAL UNIVERSITY OF SINGAPORE

2025

Supervisor:
Professor Christian Kurtsiefer

Examiners:
Professor Valerio Scarani
Assistant Professor Di Zhu
Professor Alex Kuzmich, University of Michigan

Declaration

I hereby declare that this thesis is my original work and it has been written by me in its entirety. I have duly acknowledged all the sources of information which have been used in the thesis.

This thesis has also not been submitted for any degree in any university previously.

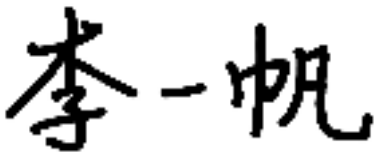

LI Yifan

July 2025

Acknowledgments

I often find myself out of sync with reality and daily life, as if there is a persistent "mismatch" between my desires and my actions. What I long for always feels just out of reach; what I ought to do remains agonizingly one step away. Still, I strive to align myself with the world, seeking a kind of reconciliation, in spirit with the plotline of this thesis: the pursuit of phase-matching. It has taken me a long time and great effort to arrive at where I am now. I've always held the belief that I could achieve what others have, and I constantly search for the optimal path forward. In retrospect, of course, many of those choices and actions were far from right. Although I have taken many wrong turns and squandered a great deal of time, I hope at the very least that my efforts and the time I've invested hold some value, and that I have gained meaningful insights and personal growth from this PhD journey.

First, I would like to express my deepest gratitude to my supervisor, Professor Christian Kurtsiefer, for giving me a second chance to continue my PhD and for providing the freedom to explore every aspect from scratch, from establishing the experimental setup, designing the implementation, to seeking out the relevant theoretical foundations. I am well aware that such freedom can sometimes come with side effects; it often led me to spend time on tedious or seemingly minor matters. Nevertheless, this allowed me to gain a more empirical and comprehensive understanding of experimental work through the process of encountering and solving problems.

I am deeply thankful to Chang Hoong, Boon Long, Lijiong, Xi Jie, Jae Suk, Justin, Adrian, and Peng Kian for their selfless mentoring, generous sharing of experimental skills and knowledge, and their consistent help and support. They always provided valuable suggestions and feedback whenever I encountered experimental problems. Their support was instrumental in enabling me to carry out the experiments and tackle challenges. In particular, I would like to express my sincere appreciation to Xi Jie, who worked closely with me to build the experimental setup and introduced me to the basic experimental procedures when I first joined the group. His guidance helped me settle in quickly. I am also especially grateful to Chang Hoong, who has always been someone I could turn to for help. He consistently provided insightful

and practical advice on the experiments, which greatly assisted me throughout my PhD.

I would also like to thank my fellow lab mates Wen Xin, Zifang, Darren, Vindhiya, and Hou Shun for their company and support throughout this PhD journey. I feel truly honored to have worked alongside you. Your help, both in the lab and in daily life, made this experience more manageable and meaningful.

Contents

Abstract

Correlated photon pairs and multiphoton states from a cold atomic ensemble

by

LI Yifan

Narrowband correlated photon pairs are essential quantum resources for interfacing neutral atom systems and establishing distributed quantum networks. We realized a high-brightness, temporally correlated photon-pair source at near-resonant wavelengths of 780 nm and 795 nm in an optically dense cold ensemble of ^{87}Rb atoms. The source is based on a spontaneous four-wave mixing (SFWM) process employing a double-Λ energy level scheme. We investigated photon-pair generation by varying experimental parameters, including the pump laser intensities and detunings, as well as the optical depth of the atomic cloud. Under optimal conditions, we achieved a measured instantaneous pair rate of up to 5×10^4 counts per second (cps) and an inferred pair generation rate on the order of 10^6 to 10^7 cps. The generated pairs also exhibit a tunable spectral bandwidth ranging from 2 to 20 MHz, arising from the electromagnetically induced transparency (EIT) associated with one of the pump fields. The high brightness of this source and its atomic-transition-compatible bandwidth make it promising for efficient coupling with atomic quantum memories, high-rate entanglement distribution in quantum repeaters, and the generation of non-classical light. Specifically, we observed that the pair rate scales quartically with optical depth, in contrast to the quadratic scaling predicted by independent-emitter models. This finding implies that collective emission plays a key role in photon-pair generation under continuous-wave pumping in a cold atomic cloud.

In addition, the two coupled fields generated via the SFWM process form a two-mode squeezed vacuum state. This state contains both individual photon pairs and multiple indistinguishable pairs within the same spatiotemporal mode. The long coherence time, associated with the narrow spectral bandwidth of our source, enables time-resolved measurements of the joint higher-order correlations that stem from these multi-pair contributions. This characterization relies on identifying multiphoton events distributed across various time bins and detection channels.

Notably, we observed that double-pair correlations distinguish true $|2,2\rangle$ states from accidental and uncorrelated pair coincidences.

Building on the above efficient photon-pair generation, we aimed to produce correlated photon triplets in distinct spectral modes through a spontaneous six-wave mixing (SSWM) process. By introducing an additional pump laser, the first Λ-type transition is replaced with a two-photon excitation, leading to a cascade emission at 776 nm and 780 nm. We proposed an experimentally feasible scheme that satisfies the required phase-matching conditions and introduced an after-pulse detection strategy to decouple the generated photons from the strong pump fields temporally. Preliminary results of detecting one of the generated fields provided encouraging evidence for this process, representing a promising step toward the realization of a practical photon-triplet source.

List of Figures

List of Tables

Chapter 1

Introduction

Neutral atoms offer versatile platforms for studying fundamental atom–light interactions and advancing quantum technologies. For example, neutral atoms trapped in optical tweezers [1–3], where individual atoms can be precisely controlled and addressed, have emerged as one of the most promising candidates for scalable quantum information processing [4] in the near term. These platforms have already demonstrated pioneering achievements, including local entanglement among atoms [5–9] and the simulation of many-body quantum systems [10]. However, the avenue to achieve "quantum supremacy" [11, 12] requires scaling up the size and complexity of quantum systems further. One promising pathway is the development of distributed quantum networks [13–16], where individual systems, like neutral atoms [8, 17], trapped ions [18, 19], atomic ensembles [20], and quantum dots [21–24], serve as quantum nodes, interconnected by photonic messages. In such a scenario, photons act as the flying qubits, which are the carriers of quantum information between spatially separated quantum nodes, allowing long-distance transmission with low loss through fibers.

To efficiently interface quantum systems [25–27], exchange entanglement [13], and transfer quantum information, narrowband photons are particularly crucial. Their narrow spectral bandwidth ensures compatibility with the quantum nodes, such as atomic transitions or cavity resonances, enabling high-fidelity interaction at the single-photon level, and the highly efficient quantum memory [28]. Additionally, their long coherence time supports transmission over extended fiber links without significant decoherence. Furthermore, achieving high-visibility interference in entanglement swapping protocols requires photons to be spectrally pure and indistinguishable [14,

29, 30], criteria that narrowband sources are well suited to meet.

One of the major challenges in building quantum networks is to realize an efficient transfer protocol for quantum information. A trivial idea is to directly deliver a photon emitted by a single atom, which has been entangled with the atom's internal degree of freedom, to interact with another remote atom [31, 32]. However, the photon emission efficiency from single-atom systems falls below the break-even point required for long-distance transmission. Moreover, even if the photon successfully arrives, the probability of interacting with this remote atom is intrinsically limited by the small optical cross-section of atoms in free space [33]. Although cavity QED systems, such as optical or nanofiber cavities [34–36], can significantly enhance the atom-photon coupling strength, their overall efficiencies are still insufficient for direct entanglement operations between two remote atoms mediated by a single emitted photon.

To overcome these limitations, correlated or entangled photon pairs play an important role in establishing scalable quantum networks [13, 16]. They can serve as carriers of quantum information in quantum repeaters, linking individual quantum nodes through entanglement swapping [13, 37, 38]. These repeaters can consecutively extend entanglement over long distances, improving the scalability and reliability of quantum networks. In quantum repeaters [39–41], entanglement between remote atoms is established through photon interference and Bell-state measurements [42] rather than relying on direct interaction with atoms.

Beyond their application in quantum repeaters, correlated photon pairs, especially entangled ones, serve as versatile resources in the realm of quantum optics and quantum information [43]. Owing to their temporal correlations, where the detection of one photon heralds the presence of its partner, they can be utilized as heralded single-photon sources [44]. This heralding mechanism significantly improves the signal-to-noise ratio in practical experiments by providing conditional access to single photons. Temporal correlations also enable some engineering applications, such as clock synchronization [45, 46]. Photon pairs can be further entangled in various degrees of freedom, including polarization [47], time bin [48–50], and others. Since the pioneering Bell tests that verified the violations of Bell inequalities using polarization-entangled photons [51], entangled photon pairs have remained central in foundational studies of quantum entanglement and nonlocality, including a series

of loophole-free experiments [52–54]. These key quantum features, such as the no-cloning theorem [55] and Bell inequality violations, play a central role in QKD protocols [56], including BB84 [57], Ekert91 [58], and others.

A widely adopted method for producing correlated photon pairs is spontaneous parametric down-conversion (SPDC) [59, 60] in nonlinear crystals, where a pump photon spontaneously splits into a pair of lower-energy photons. SPDC-based sources have been extensively used in fundamental quantum experiments and in developing quantum communication systems [61, 62]. However, SPDC sources typically produce photons with a wide bandwidth, associated with short single-photon or biphoton coherence times [60]. Their spectral properties limit their compatibility with quantum network nodes based on atomic transitions, whose linewidths are usually on the order of MHz. Cavity-enhanced SPDC [63] is one of the accessible solutions that enhance the spectral brightness and narrow spectral bandwidths to allow efficient interaction with matter. Inspired by early studies on nonlinear processes in atomic media [64–68], another approach to generate narrowband correlated photon pairs is to employ a spontaneous four-wave mixing (SFWM) parametric process within atomic system, such as hot atomic vapor [69–74] or cold atomic ensembles [75–87]. These experimental investigations primarily implement the ladder-type or double-Λ energy-level scheme. Meanwhile, a series of theoretical studies have been developed to model the emergence of quantum correlations between two coupled fields [79, 80, 88–93]. Hot atomic vapors typically suffer from Doppler broadening due to their thermal motion, which deteriorates the spectral linewidth of generated photons. In contrast, cold atoms prepared by laser cooling have negligible Doppler shifts compared to the intrinsic linewidth of energy levels, thus mitigating the influence of Doppler broadening on the spectral properties and allowing the generation of narrowband correlated photons. The atomic coherence in cold atomic gases enables more controlled engineering and manipulation of coherent light–matter interactions. For example, the atomic population can be prepared in a specific hyperfine ground state, or even within a selected Zeeman sublevel, thereby supporting well-defined coherent processes and enhancing the signal-to-noise ratio. Leveraging the atomic coherence, the two-photon coherence time of biphotons generated from a cold atomic cloud can be extended to the order of microseconds [80, 94, 95], and the biphoton temporal waveform can be shaped through the temporal or spatial modulation [96,

97].

In this project, we develop a cold ^{87}Rb atomic cloud using a magneto-optical trap (MOT), which serves as the atomic medium for implementing parametric nonlinear processes. First, we realize a double-Λ spontaneous SFWM process and demonstrate that it can act as a bright source of narrowband, correlated photon pairs. Their long coherence times facilitate higher-order coherence measurements, enabling the investigation of multiphoton components from this bright source.

1.1 Nonlinear process in atomic media

The nonlinear effect in an atomic medium can be interpreted within the framework of nonlinear optics [98], where the macroscopic dipole moment is given as

$$\mathbf{P} = \varepsilon_0 \left(\chi^{(1)}\mathbf{E} + \chi^{(2)}\mathbf{E}^2 + \chi^{(3)}\mathbf{E}^3 + \dots \right). \tag{1.1}$$

This expression characterizes how the atomic medium responds to the external electric fields through different order susceptibilities. Linear susceptibility $\chi^{(1)}(\omega) = \chi'(\omega) + i\chi''(\omega)$, is related to the refractive index of atomic medium via $n = \sqrt{\chi^{(1)} + 1}$. Its real part describes the dispersion of the field, while its imaginary part accounts for absorption. Near an atomic transition (two-level atom), $\chi^{(1)}(\omega)$ takes the form

$$\chi^{(1)}(\omega) \propto \frac{1}{\omega_0 - \omega - i\gamma}, \tag{1.2}$$

where ω_0 is the transition frequency and γ is the decay rate of the excited state. The linear susceptibility governs the propagation of photons in the cold atomic cloud. Although the SPDC process corresponds to the second-order susceptibility $\chi^{(2)}$ in nonlinear crystals, this process vanishes in systems of neutral atoms due to the inversion symmetry of atoms [98]. The SFWM process in the atomic medium is associated with the third-order susceptibility $\chi^{(3)}$, which characterizes the nonlinear response of the medium with three optical fields: two pump fields and one seed field (or one of the generated fields). Consequently, the SFWM strength, namely pair generation strength, is proportional to $(\chi^{(3)})^2$ [79].

As a parametric process for generating time-correlated photon pairs, commonly referred to as signal (s) and idler (i) photons, SFWM process must satisfy both energy conservation $\omega_1 + \omega_2 = \omega_s + \omega_i$ and the momentum conservation. Within

an atomic medium of length L, the phase mismatch $\Delta\mathbf{k} = \mathbf{k}_1 + \mathbf{k}_2 - \mathbf{k}_s - \mathbf{k}_i$ accumulates along the z-axis (the propagation direction). Each wave-vector is given by $\mathbf{k} = n(\omega)\omega/c$, where $n(\omega)$ is the refractive index. The longitudinal integration over the medium yields a phase

$$\int_{-L/2}^{L/2} dz e^{i\Delta kz} = e^{i\Delta kL/2}\text{sinc}\left(\frac{\Delta kL}{2}\right)L, \tag{1.3}$$

where the first exponential term represents the accumulated phase. Since the pump fields are treated as classical coherent fields, only the accumulated phase from the generated photon $e^{i(\vec{k}_s+\vec{k}_i)L/2}$ contributes to the two-photon wave function amplitude [81]. The phase-matching condition, governed by momentum conservation, is analogous to that in SPDC in nonlinear crystals. In atomic media, however, the refractive index varies near resonance and cam exhibit steep dispersion due to electromagnetically induced transparency (EIT) [99, 100]. Assuming a constant refractive index, it is clear that the simplest way to satisfy phase matching is to employ a collinear configuration, in which the pump fields co-propagate along the same direction. In this case, the generated correlated photons are emitted in the same direction, naturally fulfilling the phase-matching condition. Collinear pump configuration facilitates phase matching; nevertheless, the separation of generated photon pairs from the pump fields needs to be considered. For example, in the ladder-type SFWM processes [82], the photon pair wavelengths are typically far detuned from the pump wavelengths, allowing efficient spectral separation using interference filters. In contrast, in the double-Λ SFWM processes, the frequency separation between the generated photons and the pump fields is typically on the order of the ground-state hyperfine splitting, making spectral separation more challenging.

Another important consideration is the radiation pressure. In the collinear configuration, the unidirectional momentum transfer from the pump beams leads to significant radiation pressure along one direction, potentially pushing the atomic ensemble away. In comparison, using counter-propagating pump beams results in approximately balanced radiation pressure, which helps maintain the atomic cloud over longer timescales.

1.2 Bright narrowband correlated photon pairs

In broadband photon-pair sources, brightness usually refers to how efficiently correlated photon pairs are generated, which is quantified as the number of pairs per unit pump power and unit of bandwidth (e.g. pairs/(mW $\cdot$ MHz)). This metric reflects the strength of spectrally dense photon pairs across a given frequency range [101]. In contrast, for narrowband photon pairs from atomic media, the photon emission bandwidths are limited. As a result, normalizing the generation rate by bandwidth is less meaningful. In such cases, the pair generation rate alone is a practical measure of source brightness.

To enhance the brightness of a photon-pair source based on atomic media, a straightforward method is to increase the number of atoms participating in the SFWM process within the interaction volume. In other words, we have to prepare a "dense" atomic medium. The definition of "dense" here refers to how optically dense an atomic medium is [102], characterized by optical depth (OD). In atomic vapor systems, high optical depth can be realized through increasing the temperature of the atomic vapor, which leads to a broadening of the absorption profile [102]. In the cold atomic ensembles, preparing a dense medium means a large atomic ensemble. The strategies employed in this project to achieve high optical depth, including the use of an elongated atomic cloud and the dark spontaneous-force optical trap technique [103, 104], are detailed in § 2.2. Based on this cold atomic ensemble with large optical depth, we demonstrate an instantaneous photon-pair generation rate on the magnitude of 10^7 pairs/s based on a double-Λ SFWM process from this ^{87}Rb cold atomic ensemble, despite the limited collection volume within the atomic cloud. Figure 1.1 presents a fair comparison with other works, demonstrating that our measured and inferred photon-pair rates are competitive with previously reported results [84, 86]. Moreover, there are strong indications that these rates can be further enhanced by expanding both the spatial collection volume and the interaction region between the atomic cloud and the pump fields. These suggest that such a photon-pair source holds significant promise for generating narrowband correlated photon pairs at a high rate.

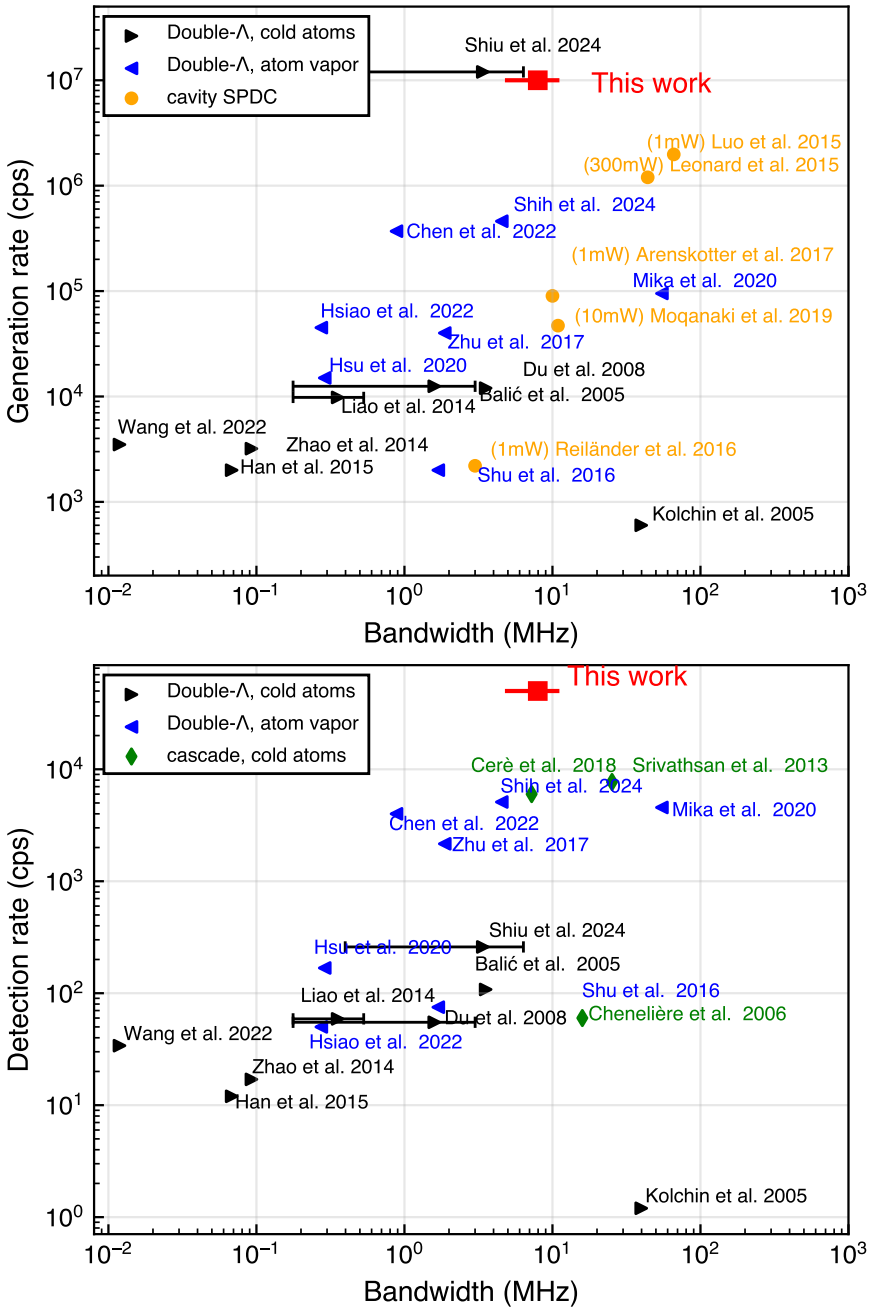

Figure 1.1: Comparison of inferred generation rates and detection rates with previously reported values. Bandwidths are calculated based on the reported coherence times. Some data are referenced from a summary [101].

1.3 Higher-order correlation and multi-photon states

The output state of correlated photon pair sources, such as SPDC or SFWM, is commonly modeled as a two-mode squeezed vacuum state (TMSV) [40, 98]. In the continuous-variable regime, this state approximates an Einstein–Podolsky–Rosen (EPR) entangled state [105–107], characterized by strong quantum correlations in conjugate quadratures [91, 108, 109]. In the Fock state representation, the full two-mode squeezed vacuum state is given by

$$|\psi\rangle = \sqrt{1-\lambda^2}\sum_{n=0}^{\infty}\lambda^n|n\rangle_s|n\rangle_i, \tag{1.4}$$

where $\lambda = \tanh r$ is the pair emission probability amplitude and r is the squeezing parameter, and two modes are referred to as the "signal" and "idler". These terms with $n > 1$ represent the generation of correlated multiphoton states, where multiple photons exist in the same coherence time and occupy the same spatial and spectral mode. This representation highlights the photon-number correlations between the two coupled modes. In the low-gain regime, where the probability of emitting a photon pair is small, the photon state can be well approximated by its biphoton component, which is also the first-order term in a perturbative expansion. This approximation forms the basis for employing such a nonlinear process as a photon-pair source. As the gain increases, higher-order photon-number contributions become significant, leading to multiphoton components that go beyond the ideal single-pair generation. When the number of photon pairs increases exponentially with pump intensity, the system enters the high-gain regime [110, 111], and the resulting photon state is often referred to as twin beams [42, 112]. Further, if feedback exists, the system can reach the stimulated emission regime [110, 113–115], where a laser-like emission of entangled photons emerges [42].

The high-gain SPDC is a standard approach for generating multiphoton states. Owing to its broad spectral bandwidth, achieving a high pair generation probability typically requires strong pumping, often realized by using pulsed lasers that deliver peak powers far exceeding those of continuous-wave sources. However, this requirement can be substantially relaxed when the photons exhibit long coherence times. A coherence time on the order of nanoseconds corresponds to a coherence length

of several meters, much longer than the atomic medium itself, which facilitates the establishment of photon bunching correlations. At the same time, it relaxes the requirements on timing resolution and detector jitter for detectors and time-staggers, enabling time-resolved characterization of higher-order correlations. In this thesis, we generate narrowband correlated photon pairs from a cold atomic ensemble operated near the saturation regime. The photon state is still far from that in the high-gain regime of SPDC, and does not reach the threshold for stimulated parametric oscillation with feedback [116]. Instead, the FWM process operates in the spontaneous regime but still yields a substantial number of multiphoton components, allowing efficient characterization within practical acquisition times. These higher-order terms are essential for probing beyond the second-order correlations, such as the third- and fourth-order temporal correlation functions $g^{(3)}$ and $g^{(4)}$. Measuring these correlations reveals the quantum statistical structure of the generated light fields and provides a clear distinction between genuine multiphoton correlations and uncorrelated backgrounds.

For certain applications, such as the Duan–Lukin–Cirac–Zoller (DLCZ) protocol [14] and heralded single-photon sources, the presence of double-pair components is detrimental. These multiphoton components compromise the fidelity of the stored quantum state and introduce heralding errors, as they violate the single-excitation assumption, which is essential to some quantum communication protocols. In contrast, in other contexts, such as multiphoton interference [42, 117], quantum-enhanced metrology [118, 119], and the generation of multiphoton entangled states [113, 114], these higher-order components can be advantageous, serving as a resource for generating non-classical multiphoton states and multiphoton entanglement.

We investigate the third- and fourth-order correlation functions using a double Hanbury Brown–Twiss (HBT) [120] measurement setup. The joint third-order correlation function across two modes reveals a thermal bunching between correlated pairs. These temporal correlations agree with theoretical predictions based on the Gaussian moment-factoring theorem [121, 122]. From multichannel coincidence measurements, we gain access to photon triplets and quadruplets. Furthermore, by accounting for losses in the atomic ensemble, optical filtering, and detection setup, we estimate the photon quadruplet generation rate and reconstruct the underlying photon states.

1.4 Heralded single photon source

Ideal single photon sources, such as those based on single atoms or single quantum dots [123, 124], exhibit quantum properties of the $|1\rangle$ Fock state, as demonstrated by the photon anti-bunching behavior in second-order correlation functions [125]. However, the practical usability of a single quantum emitter system is always hindered by its low photon emission rate. Time-correlated photon pairs are utilized as heralded single-photon sources to surpass this limitation. One photon of the pair ("signal" photon) acts as the heralding photon. Its detection triggers a single-photon process for the second photon, in applications such as frequency conversion [126, 127] or quantum memory storage [128–130]. Since the probability of generating double pairs scales quadratically with the single-pair generation probability, the heralding mechanism effectively suppresses multi-photon contributions within the heralding window.

The heralded auto-correlation function $g_h^{(2)}(\tau)$ with τ being the relative delay between two idler photons, defined as a conditional analog of second-order auto-correlation $g^{(2)}(\tau)$, was proposed to characterize heralded single photon sources. The measurement is performed using a heralded Hanbury Brown and Twiss (HBT) [120] setup, where idler photons are split into two channels by a 50:50 beam splitter and detected independently by two single-photon detectors. Conceptually, $g_h^{(2)}(\tau)$ is the conditional probability of detecting two photons in the idler mode, given the detection of a heralding signal photon, normalized by the product of conditional single-photon detection probabilities in each idler channel. This interpretation intuitively corresponds to a measurement procedure: upon detection of a signal photon, a heralding interval (comparable to or shorter than the coherence time) is opened, during which two idler photon events are recorded on separate detectors. The two-idler coincidence probability within this window is then normalized by the product of signal-idler coincidence probabilities to yield the heralded auto-correlation function.

In this thesis, we propose a method to directly obtain the two-time heralded auto-correlation function from triple coincidence measurements, eliminating approximations introduced by setting a heralded window. This approach preserves the full timing information and temporal structure relevant to the correlation function,

rather than relying on averaged two-photon probability and normalization factors. We demonstrate this procedure using the timestamp data from correlated photon pairs generated in our cold atomic ensemble and verify its validity. While the method is in principle applicable to SPDC sources, it is particularly crucial for narrowband photon pairs, which inherently exhibit rich two-photon temporal coherence.

1.5 Correlated photon triplet

With the extensive study and broad applications of correlated or entangled photon pairs, the preparation of entanglement among multiple photons [42, 131] has emerged as an appealing yet experimentally challenging frontier in quantum information science, quantum communication, quantum metrology, and quantum imaging. Multipartite entangled states such as the Greenberger–Horne–Zeilinger (GHZ) states [132] and the W states [133] have attracted considerable attention. For instance, multiphoton GHZ states and W states, and other forms of multiphoton entangled states have been experimentally demonstrated by the interferences with the post-selection [133–138], direct double-pair generation in the SPDC process [139, 140], cascaded SPDC [141, 142], and two SPDCs/SFWMs followed by one up-conversion [143–145]. These multiphoton states not only represent an expansion of the Hilbert space, but also exhibit unique quantum features [132], such as inequivalent forms of entanglement [146, 147], which are essential for realizing universal quantum computation and quantum error correction [148].

As an intermediate and experimentally accessible step toward multiphoton entanglement, correlated photon triplets [149] are often regarded as a valuable quantum resource. These triplets refer to three-photon states exhibiting strong temporal and statistical correlations, though not necessarily tripartite entanglement. Such triplets are typically produced via higher-order nonlinear optical processes [150], including third-order SPDC [151–156], cascaded SPDC [157–159] or SFWM [160–162], and double-pair emissions from SFWM or SPDC with appropriate post-selection [114, 163–165]. In particular, the latter approach has been examined in this thesis through the investigation of higher-order correlations and multiphoton states directly emerging from a double-Λ SFWM process. We have demonstrated that the double-pair emission, corresponding to the $|2,2\rangle$ higher-order component in the

two-mode squeezed states, provides an accessible method for generating more than two photons that exhibit temporal correlations. These findings reveal the potential of SFWM in cold atomic ensembles not only for biphoton generation but also as a promising platform for scalable multiphoton quantum sources.

In analogy to higher-order parametric nonlinear processes of SPDC, spontaneous six-wave mixing (SSWM)[166–168] offers an alternative nonlinear approach, particularly in atomic media. Such multi-mode wave mixing processes can be relatively highly efficient due to near-resonance enhancement [66] and EIT [167, 169]. Under this mechanism, the time-energy-entangled W triphotons have been generated from the atomic vapor [170]. Similar to the SFWM process in the cold atomic ensemble, which couples two optical modes and induces quantum correlations between them, we aim to generate quantum correlations among three modes in a near-resonant SSWM process governed by the fifth-order nonlinear susceptibility ($\chi^{(5)}$). In particular, we propose a more intricate atomic excitation scheme that involves multiple coherent drive pathways and cascaded spontaneous emission channels. This process can be viewed as an intersection of a ladder-type SFWM and a double-Λ SFWM process, where the generated photons are spectrally close to the pump fields, enabling experimentally feasible phase-matching conditions. Meanwhile, the pump fields are near-resonant, or even resonant with atomic transitions, enhancing the nonlinear conversion efficiency. In this scheme, three pump fields drive the system, followed by the spontaneous emission of a photon triplet into three distinct optical modes, satisfying both energy and momentum conservation. These three optical modes, initially in the vacuum state, are coupled through atomic coherence, resulting in the generation of time-correlated photon triplets.

In this thesis, we present a theoretical analysis demonstrating the feasibility of such a coherent process in a cold atomic ensemble and propose an experimentally accessible protocol for generating and measuring three-photon correlations. Preliminary observations show a positive indication of photon triplet generation, laying a foundation for further studies of multipartite quantum correlations in atomic systems.

1.6 Thesis Synopsis

The rest of this thesis is organized as follows. In Chapter 2, I review the basic principles of preparing a cold atomic ensemble using a magneto-optical trap and explore techniques for achieving an optically dense atomic cloud. Such a dense medium is advantageous for enhancing the strength of nonlinear processes through the participation of a large number of atoms. I then present an improved absorption imaging method for characterizing such an atomic cloud with a relatively large optical depth. Chapter 3 describes the fundamental experimental components, including laser systems, optical filters, and state preparation techniques, which are essential for the implementation of the experiment. Then, I describe a double-Λ SFWM protocol to realize the generation of the time-correlated photon pairs and characterize the biphoton generation under different experimental parameters to optimize its performance in Chapter 4. In Chapter 5, I focus on the superradiant emission behavior in biphoton generation and present a clear signature of collective emission from the atomic ensemble. In the following Chapter 6, I investigate higher-order photon components, in particular the $|2,2\rangle$ states in the biphoton source, and analyze their temporal higher-order correlation functions between two coupled fields. Building on an efficient method for evaluating the third-order correlation function (triple coincidences), the heralded auto-correlation function, widely used to assess the purity of heralded single-photon sources, is revisited in Chapter 7. The proposed two-time heralded auto-correlation provides a more accurate characterization of the temporal anti-correlation arising from thermal correlations, compared to the widely used version with approximations. In Chapter 8, I further present the realization of correlated photon triplets in three distinct spectral modes via a six-wave mixing process in a cold atomic ensemble, and report some promising preliminary results toward photon triplet generation and measurement. Finally, in Chapter 9, I conclude the thesis and discuss possible directions for future research.

Chapter 2

Elongated magneto-optical trap

In this chapter, I briefly introduce the magneto-optical trap (MOT) setup and describe our efforts to enhance the optical depth through an elongated MOT design.

2.1 Principle of MOT

The principle of a MOT primarily relies on two mechanisms: the cooling process, which cools down the hot atoms emitted from the atomic dispenser and modifies their velocity distribution, and the trapping mechanism, which provides a position-dependent trapping force through a position-dependent Zeeman shift. These two mechanisms together establish the equilibrium state of the cold atomic cloud.

2.1.1 Doppler cooling

Doppler cooling was proposed to cool down neutral atoms by Hänsch and Schawlow [171], and then optical molasses [172] was obtained experimentally in 1985 by Steve Chu et al. [173]. The basic mechanism of cooling down hot atoms is to make the radiation pressure force dependent on the atomic velocity $\mathbf{v}$ through the Doppler shift $-\mathbf{k_L} \cdot \mathbf{v}$. For a plane wave with wave vector $\mathbf{k_L}$ with the saturation parameter s_0, it will apply a radiation pressure [174] on the atoms as

$$\mathbf{F}_{\mathrm{pr}} = \frac{\Gamma}{2}\frac{s_0}{1+s_0}\hbar\mathbf{k}_L \quad \text{where} \quad s_0 = \frac{\Omega_1^2/2}{\delta'^2 + \frac{\Gamma^2}{4}}. \tag{2.1}$$

Here, δ' accounts for the laser detuning from the resonance and the Doppler shift. In the low velocity limit and linear approximation, the radiation pressure displays two components: zero-velocity radiation pressure $\mathbf{F}_{\mathrm{pr}}(\mathbf{v} = \mathbf{0})$ and the velocity-dependent

radiation pressure, which, along one dimension (e.g., the x-axis), can be expressed as:

$$\mathbf{F}_{\rm pr}(\mathbf{v}) \simeq \mathbf{F}_{\rm pr}(\mathbf{v}=\mathbf{0}) - \frac{\alpha}{2} v_x \mathbf{e}_x \,, \tag{2.2}$$

where the friction coefficient α is defined in terms of the saturation coefficient s_0, detuning δ and decay rate Γ as

$$\alpha = -2\frac{s_0}{(1+s_0)^2}\hbar k_L^2 \frac{\delta\Gamma}{\delta^2+\Gamma^2/4} \,. \tag{2.3}$$

As long as the light is red-detuned ($\delta < 0$), the friction force term opposes the direction of the velocity. Microscopically, an atom undergoes fluorescence cycles [172, 175] in which it gains a momentum of $\hbar\mathbf{k}_L$ upon absorbing a photon. Due to the isotropic nature of spontaneous emission, the atom experiences an average momentum change of zero from photon emissions. Through repeated absorption-emission cycles, atoms with higher velocities continually lose momentum until a limiting velocity is reached. When a pair of counter-propagating plane wave cooling lasers with opposite wave vectors $\mathbf{k}_L$ and $\mathbf{k}'_L = -\mathbf{k}_L$ are both negatively detuned from the atomic transition, the zero-order radiation pressure forces terms cancel out, while the first-order terms are asymmetric, leaving a total friction force

$$\mathbf{F}(\mathbf{v}) = \alpha v_x \mathrm{e}_x \,, \tag{2.4}$$

which is proportional to $(\mathbf{k}_L.\mathbf{v})\mathbf{k}_L$, thereby damping the velocity of atoms in the x-axis. Consequently, three pairs of counter-propagating cooling beams allow for decelerations in three dimensions. The lowest achievable temperature in this process is set by the Doppler cooling limit, given by $T_D = \hbar\Gamma/(2k_B)$ at $\delta = -\Gamma/2$, which is approximately $146\,\mu$K for ^{87}Rb atoms. This limit results from an equilibrium between laser cooling and the heating process arising from random absorption and emission [176]. In practice, temperatures lower than the Doppler cooling limit can be achieved experimentally [177], in which the Sisyphus cooling [178] takes effect until the single-photon recoil limit [172]. Further, sub-recoil temperatures can be achieved through techniques such as velocity-selective coherent population trapping (VSCPT) [179], which breaks the absorption–spontaneous emission cycle and transfers cold atoms into dark states; Raman cooling [180], which uses velocity-selective Raman transitions and optical pumping to transfer atoms to lower momentum states;

and resolved-sideband Raman cooling [181], which achieves sub-recoil cooling by transferring atoms to the vibrational ground state of a periodic potential. Compared with these advanced cooling mechanisms, Doppler cooling always serves as a pre-cooling stage in experiments. For our application, achieving an extremely low atomic temperature is not essential, and some methods used to increase the optical depth can compromise the minimum achievable temperature. As a result, Doppler cooling remains the primary cooling mechanism in our setup.

2.1.2 Zeeman shift

The interaction between a position-dependent magnetic field $\mathbf{B}(\mathrm{r})$ and ^{87}Rb neutral atoms with a total angular momentum $\hat{F}$, consisting of a nuclear spin $\hat{I} = 3/2$ and electronic angular moment $\hat{J}$, is given as

$$\hat{V}_m = -\hat{F} \cdot \mathbf{B}(\mathrm{r})\,. \tag{2.5}$$

Correspondingly, the Zeeman sub-levels are shifted by an amount $m_F g_F \mu_B B$ from the hyperfine level when the quantization axis is chosen along the direction of the magnetic field. Figure 2.1 (a) shows the Zeeman shifts of the $|5P_{3/2}, F = 3\rangle$ and $|5S_{1/2}, F = 2\rangle$ energy levels, corresponding to the optical transition used in the laser cooling process. Figure 2.1 (b) illustrates the optical transition from $|m_F = 0\rangle$ ground state in presence of a position-dependent magnetic field $B = b'x$, which varies linearly with the coordinate x. This diagram highlights how the differential Zeeman shift leads to a spatially dependent detuning for counter-propagating $\sigma^{\pm}$ polarized cooling beams, giving rise to a net trapping force for atoms displaced from the trap center.

2.1.3 Trapping forces

The spatial magnetic gradient leads to a position-dependent detuning for circularly polarized cooling light propagating in opposite directions. As a result, atoms experience a net radiation force that depends on their position, forming the trapping force in the MOT mechanism. The required magnetic gradient (typically $1 \sim 30\,\mathrm{G/cm}$) is lower than that in a magnetic trap with trapping potential $V_{\mathrm{trap}} = \mu\mathbf{B}(r)$ in the evaporative cooling of Bose-Einstein preparation [182].

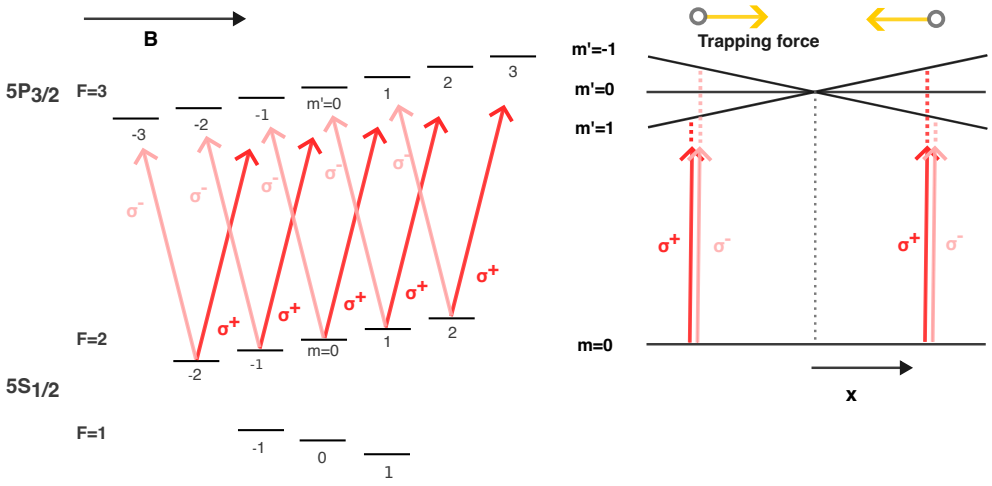

Figure 2.1: (a) Zeeman shifts of $|5P_{3/2}, F = 3\rangle$ and $|5S_{1/2}, F = 2\rangle$, with counter-propagating right and left circularly polarized red-detuned cooling light. The quantization axis is along the magnetic field direction in the x-axis, corresponding to the $x > 0$ position in (b). (b) Position-dependent coupling between the circularly polarized light with excited states, shifted under the position-dependent magnetic fields. The imbalance between σ^+ and σ^+ transitions leads to a trapping force directed to the zero magnetic field point.

For instance, in Figure 2.1 (b) with magnetic gradient along x-axis, red-detuned cooling light is closer to the σ^- transition than the σ^+ transition. Two counter-propagating $\sigma^\pm$ polarized cooling beams lead to a radiation pressure force on the atoms:

$$\mathbf{F}_\pm(x) = \pm\frac{\Gamma}{2}\frac{\Omega^2/2}{\Omega^2/2 + \Gamma^2/4 + (\delta \mp \gamma_m b' x)^2}\hbar\mathbf{k}_L\,. \tag{2.6}$$

Therefore, the net trapping force at low saturation limit $s_0 \ll 1$ in the vicinity of the center [174] is given by

$$\mathbf{F}(x) = -\kappa x\mathbf{e}_x, \quad \kappa = \frac{\gamma_m b'}{k_L}\alpha = -2\frac{s_0}{(1+s_0)^2}\frac{\delta\Gamma}{\delta^2 + \Gamma^2/4}\hbar k_L \gamma_m b'\,. \tag{2.7}$$

This position-dependent trapping force leads to a harmonic potential $\kappa x^2/2$ in the x direction. Further, magnetic gradients in three directions confine the cooled atoms around the zero-field point. The size of a stable MOT in one direction is related to the equilibrium temperature T defined by $1/2\kappa\langle x^2\rangle = 1/2k_B T$. Since the trapping force is proportional to the magnetic field gradient b', as shown in Equation 2.7, the size of the MOT, characterized by the variance of the atomic cloud, is evaluated

through

$$\langle x^2 \rangle = \frac{k_B T}{\kappa} \propto \frac{1}{b'} \,. \tag{2.8}$$

This relationship indicates that the size of the MOT is inversely proportional to the magnetic field gradient in the low-density regime. To elongate the atomic cloud along a specific direction, a reduced magnetic field gradient can be applied along that axis. This forms the basic mechanism of the elongated MOT configuration.

2.1.4 Large density regime

The typical size for MOTs of alkali atoms ranges from microns to millimeters. In the exploration of parametric nonlinear processes in cold atomic ensembles, a dense and large atomic ensemble is always desirable, as we hope to enhance the total interaction probability. However, as the atomic density increases, light-induced interactions become significant, impeding further expansion of the MOT size. In such an optically thick atomic ensemble, a photon scattered from one atom can be reabsorbed by another atom before escaping the system. This emission and reabsorption process induces recoil forces on both atoms in opposite directions, potentially heating the cloud beyond the Doppler cooling limit [183]. A simple evaluation for the maximal density in a plasma-like MOT [174] is given as

$$n_0 = \frac{4}{3\pi} \frac{|\delta|}{\Gamma} \frac{\gamma_m b'}{\Gamma} k_L^2 \,, \tag{2.9}$$

where δ is the cooling laser detuning, Γ is the spontaneous decay rate, $\gamma_m = g_J \mu_B / \hbar$ is the gyromagnetic ratio, and b' is the magnetic gradient rate. It simply indicates that within a limited parameter space, increasing detuning and the magnetic field gradient will enhance the atomic density. The size of the atomic cloud and the atomic density exhibit inverse dependence on the magnetic field gradient, indicating an inherent trade-off between these two parameters in a dense atomic cloud.

In our atomic ensemble, we observe that the system becomes unstable as the MOT size increases. One potential cause is the imperfection in the circular polarization of the cooling laser beams, leading to interference effects. This interference between reflected cooling beams can be observed at the reflected port of a beam splitter, which combines the cooling and repump beams. Another possible reason is the nonlinearity of the restoring force with respect to the distance r from the MOT

center. Ideally, the trapping force should be roughly linear for a small distance r. But in a large MOT, it may instead decrease after a certain distance. This imbalance between the confining force of the MOT and the repulsive interaction associated with multiple scattering of light inside the cold atomic cloud leads to the instability of the MOT size [184].

Several strategies can be used to achieve higher atomic density. One method is creating a dark spot in the cooling beams, where the transverse profile of the cooling laser forms a hole at the center [103, 185, 186]. This results in a small region with no light at the overlap of the six cooling beams. Another approach is dynamic compression [187], where increasing the negative detuning can theoretically increase atomic density, though this may reduce capture efficiency if the detuning is too large. This suggests that the cooling process can be split into two stages: one with smaller detuning for rapid capture and another with standard detuning to enhance atomic density, with the detuning varying over time. Additionally, employing a dark spontaneous-force MOT could further increase atomic density.

2.2 Elongated MOT

To increase the brightness of the photon pair source, a practical approach is to realize a dense atomic ensemble, which is characterized by the on-resonant optical depth (OD) as

$$\mathrm{OD} = n\sigma L\,, \tag{2.10}$$

where n is the atomic density, σ is the on-resonant cross-section, while L is the interaction length. A large optical depth can be realized by increasing the interaction length L, which corresponds to elongating the MOT in the propagation direction. On the one hand, this quantity is proportional to the atomic density and can thus serve as an alternative characterization of the atomic sample's density. On the other hand, the OD provides a metric to distinguish between the single- and multiple-scattering regimes. For resonant light, $\mathrm{OD} \ll 1$ indicates the single-scattering regime, while $\mathrm{OD} \gg 1$ corresponds to the multiple-scattering regime [188].

Inspired by the concept of the 2D MOT [186], a straightforward approach to increasing the optical depth is to extend the length L of the atomic ensemble. This is realized in our experiment by configuring the MOT in an elongated geometry,

achieved through the use of a smaller magnetic field gradient along the elongated axis compared to the transverse directions, as described in Equation 2.8. Although Equation 2.9 suggests that the atomic density decreases linearly with a decreasing magnetic field gradient, in practice, the achievable density is primarily bounded by the multiple scattering limit [103, 185]. This reduction in atomic density is compensated by an increase in interaction length, resulting in an overall enhancement of the optical depth. To achieve the necessary magnetic gradient, a pair of racetrack coils separated by 40 mm is implemented and mounted outside the vacuum chamber, as shown in Figure 2.2. The magnetic field in the x-z plane is simulated in Figure 2.3, showing that the magnetic gradient in the x-axis is smaller than in other directions. To match this configuration, the cooling beams are shaped using a concave lens ($f = -50\,\text{mm}$) and a pair of cylindrical lenses ($f = 75\,\text{mm}$ and $f = 150\,\text{mm}$) to convert a Gaussian beam from the collimator (C280TMD-B) to an elliptical profile, allowing a larger cooling region in x-y direction.

2.3 Dark spontaneous-force optical trap

The density of the MOT is mainly limited by two factors: one is the cold-collision induced losses, in which the collision between ground and excited state transforms certain excitation energy into kinetic energy [103], and the repulsive force caused by the scattering radiation [103, 185]. These two impediments can be mitigated by a dark spontaneous-force optical trap (SPOT), in which the atoms are mainly confined in a hyperfine ground state (dark state) that does not interact with trapping light. The basic idea is to block the central region of the repump laser beam, creating a dark region of repump light at the center of the MOT. In the absence of repump light at the center, the cooled atoms continuously decay into the $|F = 1\rangle$ hyperfine ground state. These atoms become decoupled from the cooling beams, which prevents strong absorption of cooling light. As a result, the repulsive force induced by photon re-scattering and atom collisions is reduced. If the atoms acquire sufficient kinetic energy to escape the confinement region, they quickly enter the outer area where both the cooling and repump beams are present. There, they re-enter the cooling cycle, where they are cooled and confined within the optical trap.

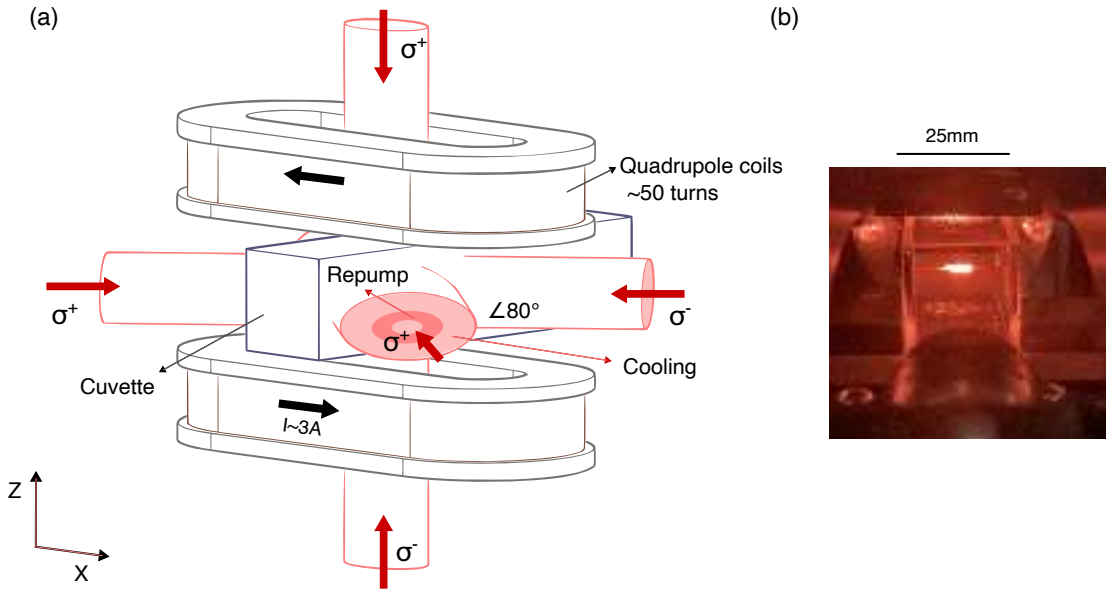

Figure 2.2: (a) Schematic of MOT setup, featuring racetrack-shaped coils, a vacuum chamber, and three pairs of elliptical cooling beams in the x-y plane and z direction. The repump beams are collinear only with the x-y plane cooling beams. Additionally, two elliptical cooling beams in the x-y plane are arranged at an angle of 80° to increase the overlap region and form the elongated MOT. (b) Fluorescence image of the elongated atomic cloud.

2.3.1 Donut-shaped repump beam

The key to establishing a dark SPOT is to create a central region void of a repump field. Vortex beams, such as Laguerre-Gaussian beams LG(n,0), have a donut-shaped intensity profile with a central dark spot of zero intensity. These beams, characterized by a helical phase front, can be generated using a vortex phase plate or a programmable spatial light modulator (SLM). Alternatively, a first-order Bessel beam, known for its non-diffracting nature, also creates a central dark spot and can maintain a consistent intensity profile over a distance. In our setup, we use a pair of axicons (conical lenses) to transform a Gaussian beam into a donut-shaped beam. The resulting pattern is further elongated in the vertical direction to match the elliptical profile of the cooling beam in the x-y plane, ensuring optimal spatial overlap. As shown in Figure 2.5, the hollow region is not perfectly dark; instead, it exhibits ring-shaped intensity fringes due to interference. Both axicons have the

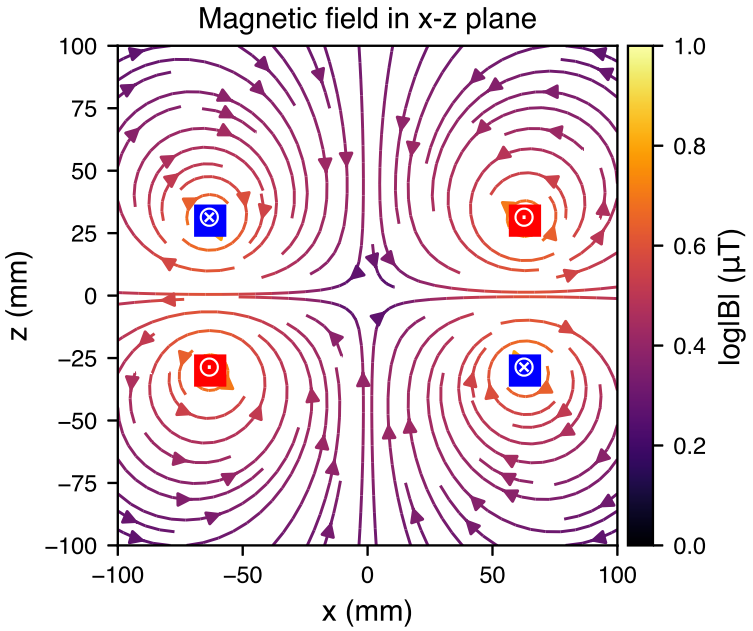

Figure 2.3: Simulation of the magnetic field in the x-z plane involves a coil with 50 turns carrying a current of 2 A. The quadrupole poles are positioned at the coordinates (60 mm, 35 mm), (-60 mm, 35 mm), (-60 mm, -35 mm), and (60 mm, -35 mm).

same diffraction angles; the first axicon generates a ring shape, while the second one converges the diverged ring-shaped distant field in collinear propagation. The distance between the two axicons is adjustable, allowing for control over the donut size.

This donut-shaped repump beam is then combined with an x-y direction input cooling beam. Both beams undergo the same transverse profile shaping by a pair of cylindrical lenses, resulting in an elliptical profile where the horizontal width is twice the vertical height. The shaped repump profile is illustrated in Figure 2.5. The combined cooling and repump beams are then split into two paths, intersecting at the center of the vacuum chamber with an intersection angle of 80°. In the z-direction, only the cooling beam is applied without the repump beam. Consequently, the intersected donut-shaped repump beam forms a void region surrounding the zero-magnetic field point.

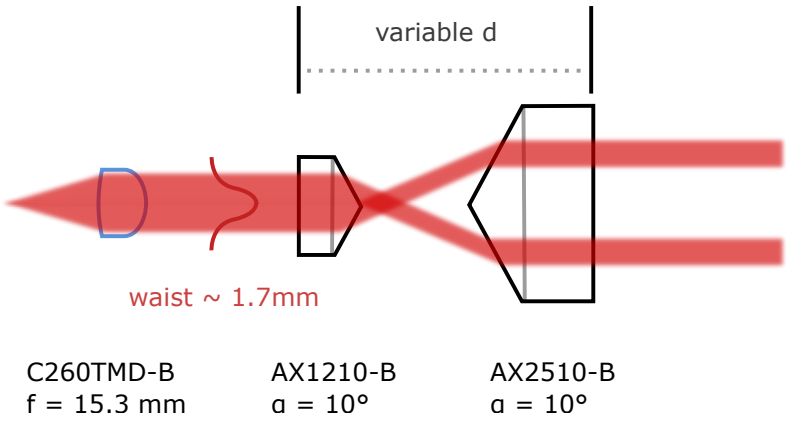

Figure 2.4: A pair of axicons is used to generate a donut-shaped repump beam. The beam collimator with C260TMD-B spherical lens (f=15.3 mm) prepares a Gaussian beam with a waist of 1.7 mm, which is directed into the center of the axicons. Two axicons have a physical angle of 10°, resulting in a 4.6° diffraction angle. The first axicon diffracts the Gaussian beam while the second one converges the diverged light. The distance between two axicons is adjustable to change the size of the donut-shaped profile.

2.4 MOT alignment

As mentioned in § 2.2, anti-Helmholtz coils generate a nearly uniform magnetic field gradient centered at a zero-field point. In practice, this magnetic field gradient is slightly shifted by the Earth's magnetic field (0.25 to 0.65 Gauss). To compensate for this shift, three orthogonal pairs of square Helmholtz coils (around 20 cm wide) surround the anti-Helmholtz coil setup and the mirror system of cooling lasers. These three pairs of coils, driven by the three-channel current source, aim to cancel the Earth's magnetic field at the center of the vacuum chamber and provide the ability to fine-tune the atomic cloud position for better overlap with the pump fields. The x- and y-axis Helmholtz coils each consist of around $40 \sim 50$ turns of copper magnet wires, carrying currents of several hundred mA, which is limited to prevent excessive heating. The z-axis Helmholtz coil is implemented using a 5-turn, 10-channel ribbon cable, allowing installation without disassembling the vacuum setup or existing optics.

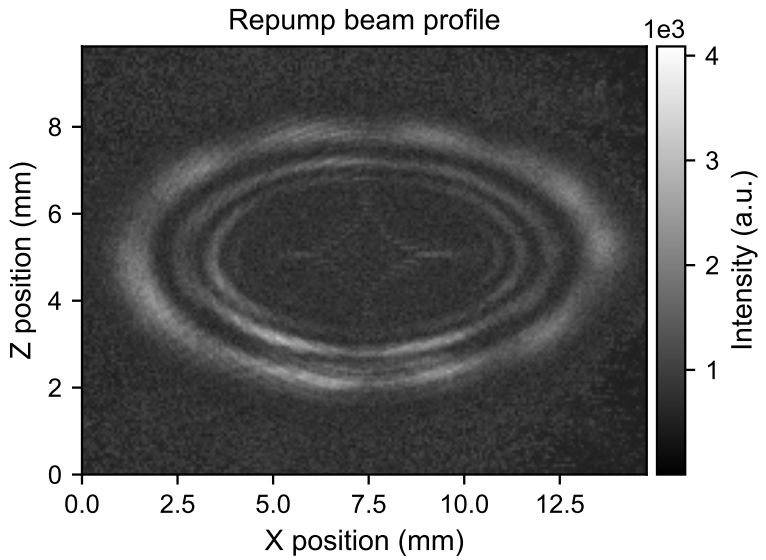

Figure 2.5: Repump beam transverse profile, with a width of around 12 mm and a height of around 6 mm. It is measured after passing through a pair of cylindrical lenses in the x-y axis.

2.4.1 Coarse compensation

Some components of the vacuum system and optical table can become weakly magnetized, giving rise to induced magnetic fields that distort the spatial distribution of the ambient magnetic field. Additionally, the compensation coils in our setup are square and not perfectly identical, making it difficult to generate a perfect uniform magnetic field to fully counteract the Earth's magnetic field over a large area. Consequently, using a magnetic flux sensor to measure the residual magnetic field around the vacuum chamber and determine the appropriate compensation currents in each direction remains challenging due to the complexity of the field distribution and limited spatial access. Our primary objective is to ensure that, within a small central region of the vacuum chamber where the MOT operates, the residual magnetic field is effectively offset, such that the influence of the Earth's magnetic field is negligible. To achieve this, we empirically adjust the compensation currents based on the disappearance behavior of the atomic cloud when the magnetic field gradient is switched off.

Once the three pairs of counter-propagating cooling beams are aligned and intersect at the expected zero-field point (the geometric center of the anti-Helmholtz

coil setup), a small atomic cloud can be observed on the monitor camera when the cooling, repump, and anti-Helmholtz coil currents are properly configured. The following procedure is then implemented to determine the compensation currents:

- Initially set all compensation currents to zero, and prepare a MOT with a small coil current (several hundred mA). In this case, the atomic cloud position is significantly affected by the residual Earth's magnetic fields.
- Quickly switch off the coil current and monitor the atomic cloud's vanishing. In the absence of compensation, the cloud typically disappears rapidly (within < 0.5 seconds) and drifts away along a specific direction.
- Apply a tentative compensation current along one axis, and iteratively adjust it until the atomic cloud no longer exhibits a preferred direction of motion in this axis when the main coil is switched off.
- With appropriate compensation, the cloud expands and vanishes slowly (~ 1 second), indicating the transition from a magnetic field gradient to near-zero magnetic field has minimal pushing force on the atoms, allowing the atomic cloud to expand slightly slower compared to the case without any compensation.

This empirical approach provides a practical method of searching for a starting point for fine-tuning.

2.4.2 Fine-tuning of atomic cloud

The objective of fine-tuning is to enhance the spatial overlap between the atomic cloud, the pump fields, and the collection modes, rather than to further minimize the residual Earth's magnetic field beyond the initial coarse compensation.

The pump beam is aligned to the atomic cloud with the help of an auxiliary probe beam, which is aligned with the 780 nm pump beam. This Gaussian probe, delivered through a Thorlabs C260TMD-B collimator, has a waist large enough to cover the entire atomic cloud and is also used in absorption imaging to characterize the cloud's size and optical depth. In contrast, the pump beam intentionally has a smaller waist than the atomic cloud to ensure efficient interaction. Using the

same optical configuration as the absorption imaging system, a weak probe beam ($\sim 10\,\mu$W), resonant to the $|5S_{1/2}, F = 2\rangle \rightarrow |5P_{3/2}, F = 3\rangle$ D2 line transition, shines on the atomic cloud, resulting in a shallow image on the imaging camera. Initially, the pump beam, generated through a collimator (Thorlabs A375TM-B), is coarsely aligned with the center of this probe beam set to a slightly higher intensity. When both pump and probe beams are derived from the same laser and simultaneously illuminated, a bright spot accompanied by interference fringes becomes visible in the atomic cloud's shadow. This spot serves as a reference for fine alignment, helping to ensure that the pump beam overlaps with the region of maximal optical density.

In the experiment described in Chapter 4, the most critical alignment is the precise overlap between the pump fields and the collection spatial mode. The collection mode is intentionally angled by 1° relative to the pump beams, and both are carefully aligned to intersect at the center of the atomic cloud. Defined by a focused Gaussian beam with a waist of approximately 175 μm at the MOT position, the collection mode is significantly narrower than the pump beam. Its alignment is performed after the pump beams have been aligned, using the established pump path as a reference. Both pump and collection beams are illuminated using resonant 780 nm light from the same source. And the pump intensity is reduced until the bright spot vanishes on the camera, indicating full absorption by the atomic cloud. Meanwhile, the collection beam is set to a slightly higher intensity, allowing a small portion of the light to be transmitted through the cloud.

Under this condition, two bright spots appear on the camera: one corresponding to the direct propagation of the collection beam, which is slightly offset from the MOT center due to the angular deviation, and the other at the pump beam's location. The latter arises because the collection beam locally pushes atoms away at the center of the MOT, thereby allowing partial transmission of the otherwise absorbed pump beam. Once this phenomenon is observed, the collection beam is considered well-aligned with both the pump beam and the atomic cloud, thereby maximizing the effective interaction volume. Furthermore, fine adjustments of the compensation coil current can further optimize the overlap between the collection mode and the atomic cloud, using the single-photon detection rate or photon pair rate as an indicator.

2.5 Atom loading

Sometimes, MOTs are loaded using a Zeeman slower or a 2D MOT to pre-cool atoms from the dispenser. For simplicity, our setup omits this re-cooling stage and directly loads atoms from the background hot Rubidium vapor. Naturally, the presence of hot vapor degrades the vacuum pressure, and collisions with high-kinetic-energy hot atoms can kick trapped atoms out of the MOTs with relatively shallow trapping potential. However, these limitations are acceptable for our investigation of nonlinear processes in cold atomic ensembles.

Our vacuum system, inherited from a previous experimental setup, integrates two dispensers: one has been heavily used over several years, while the other serves as a backup. In Figure 2.6, we characterize the atom emission by monitoring changes in the vacuum chamber pressure, measured using a Varian vacuum gauge. When the dispenser is switched off, the pressure in the vacuum chamber stabilizes at approximately $10^{-8} \sim 10^{-7}$ mbar. When the dispenser is heated by an applied current, ^{87}Rb atoms as well as contamination gases are emitted. The continuous operation of the ion pump helps to clean up the contaminants emitted from the dispenser and maintains the low pressure within the vacuum. To ensure the pressure has reached a stable value, the measurements are recorded 3 minutes after setting a specific dispenser current.

Additionally, we measure the fluorescence of the atomic cloud induced by the cooling light as an indicator to evaluate the size of the atomic cloud. Intuitively, a larger MOT scatters more fluorescence photons from the cooling beam. This fluorescence measurement uses the same 780 nm Stokes collection setup as that employed for the FWM experiment presented in Chapter 4. As illustrated in Figure 2.6, the new backup dispenser requires a lower driving current to achieve similar pressure and the MOT size compared to the old dispenser. Furthermore, the ramp-up increase and ramp-down decrease of the current from a high-value result in different behaviors. This highlights the necessity of activating the release of alkali metals. When restarting the dispenser from a low temperature, it is essential to initially apply a high current, typically around $4 \sim 5$ A for approximately tens of minutes, until additional scattered light is observed along the cooling beam path on the monitoring camera. This initial overheating activates the material,

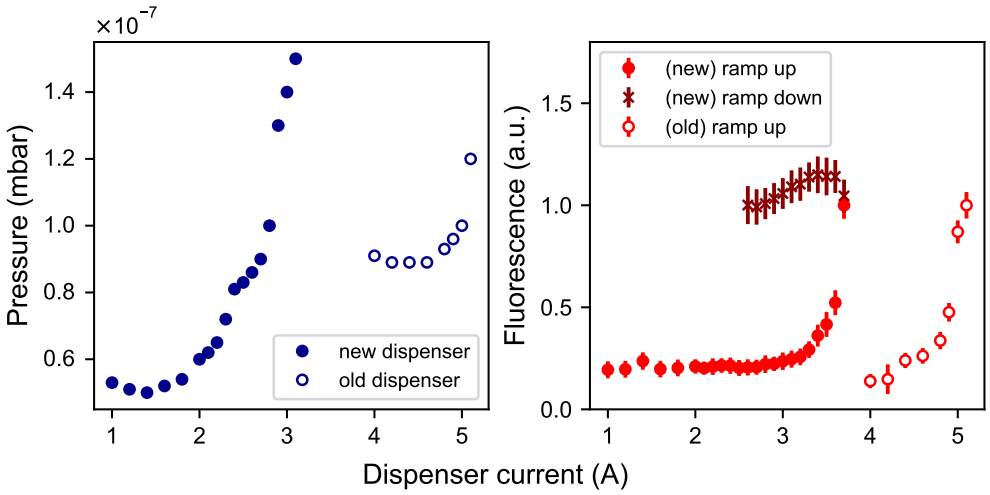

Figure 2.6: Left: Vacuum chamber pressure; Right: cooling-light-induced fluorescence from the atomic ensemble, both as a function of dispenser current. Solid circles represent the preparation of a MOT with a brand-new backup dispenser, while hollow circle dots indicate that the dispenser has been overused over the years.

enabling more stable emission under a relatively low current (around 3.5 A), which supports a consistent rubidium release rate and maintains a stationary MOT size. Unfortunately, repeated on-off cycling of the dispenser, along with prolonged MOT operation time, leads to gradual degradation of the dispenser and deterioration of the vacuum pressure. As a result, sustaining the same MOT size eventually requires a higher operating current as the dispenser ages.

2.6 Absorption imaging of a dense atomic cloud

Ideally, characterizing the atomic density of a cigar-shaped atomic cloud requires a full three-dimensional model of its spatial distribution. However, precise measurement of the longitudinal profile is limited by the lack of an absorption imaging system along the y-axis, while fluorescence imaging from the monitoring camera in this direction evaluates a cloud length of approximately $L \sim 5\,\mathrm{mm}$, with large uncertainty. Given these limitations, we use the optical depth (OD), defined in Equation 2.10, as an effective measure of the number of atoms interacting with the pump light, rather than estimating the atomic density from OD. Along the longest axis, a resonant probe light propagates through the atomic cloud, and the

light intensity change follows the Beer-Lambert law as

$$\frac{dI}{dx} = -n\sigma I\,, \tag{2.11}$$

where n is the atomic number density and σ is the scattering cross-section. In the low intensity regime $I_0 \ll I_{\rm sat} = \hbar\omega\Gamma\pi/3\lambda^2$, the OD is expressed as

$$\mathrm{OD} = \int_0^L n\sigma dz = -\ln\frac{I_t}{I_0} \to -\ln\frac{I_t^m - I_{bg}}{I_0^m - I_{bg}}\,, \tag{2.12}$$

where I_0 and I_t are the initial intensity and transmitted probe intensities, respectively. I_{bg} accounts for the background signal in the measurement and I^m denotes the measured value. For a dense atomic cloud, the probe intensity must be sufficiently high to ensure that $I_t > I_{bg}$, so that the signal-to-noise ratio remains large. When the probe intensity approaches the saturation intensity $I_{\rm sat}$, the scattering cross-section becomes intensity-dependent and is modified as

$$\sigma = \frac{\sigma_0}{1 + s + \delta^2}\,, \tag{2.13}$$

where $\sigma_0 = 3\lambda^2/2\pi$ is the on-resonant cross-section, $\delta = 2\Delta/\Gamma$ is the normalized detuning, and $s = I/I_{\rm sat}$ is the saturation parameter. Taking into account the effects of probe polarization and contributions of different Zeeman sublevel [187, 189], the cross-section σ_0 and saturation factor s are replaced by their effective forms $\sigma_0^{\rm eff} = \sigma_0/\alpha$ and $s^{\rm eff} = I_0/(\alpha I_{\rm sat})$, where $\alpha > 0$ is a correction factor dependent on the atomic transition, probe light polarization and the magnetic field orientation [189]. Since atomic density is not the main focus, we instead characterize the system by the effective OD. The probe beam, sharing the same wavelength (780 nm) and optical path as one of the pumps, provides a practical measure of atom-light interaction. In the following, OD refers to the resonant effective value seen by the 780 nm pump. Under high-intensity illumination, the OD is expressed as

$$\mathrm{OD} = \sigma_0^{\rm eff}\int n(x)dx = -\ln\left(\frac{I_t}{I_0}\right) + \frac{I_0 - I_t}{I_{\rm sat}^{\rm eff}}\,, \tag{2.14}$$

where $I_{\rm sat}^{\rm eff}$ denotes the effective saturation intensity, and the second term accounts for saturation effects of the probe beam. Since the probe intensity is comparable to $I_{\rm sat}$, this correction becomes significant. Accurate OD determination, therefore, requires independent calibration of the correction factor α, or equivalently, $I_{\rm sat}^{\rm eff}$. This

can be achieved by scanning the probe intensity over a wide range [187], or by measuring the momentum imparted to the atomic cloud along the probe direction. In the latter method, the transferred momentum saturates as the scattering rate reaches its maximum [189].

We can bypass the requirement of high-intensity probe light in the absorption imaging for dense atomic clouds by leveraging the detuning dependence of the probe transmission. Starting from the attenuation equation of probe light intensity in an atomic medium,

$$\frac{dI}{dz} = -n\frac{\sigma_0^{\text{eff}}}{1 + s^{\text{eff}} + \delta^2} I \,, \tag{2.15}$$

the transmission intensity I_t, as a function of probe detuning Δ, follows

$$T = \frac{I_t}{I_0} = \exp\left[-\frac{\Gamma^2 \text{OD}(1 + s^{\text{eff}})}{\Gamma^2(1 + s^{\text{eff}}) + 4\Delta^2}\right] \approx \exp\left[-\frac{\Gamma^2 \text{OD}}{\Gamma^2 + 4\Delta^2}\right] . \tag{2.16}$$

This allows us to extract the OD from the transmission profile by scanning the probe detuning under low-intensity conditions ($s^{\text{eff}} \ll 1$). We refer to this method as Detuning-dependent Absorption Imaging (DAI). By scanning the detuning around resonance, a transmission spectrum is obtained at each camera pixel, from which the OD is extracted via fitting to Equation 2.16.

Compared with the conventional absorption imaging methods or their corrected versions, DAI offers several advantages:

- **Non-dependence on the absolute intensity contrast**. The accuracy of conventional OD measurements is limited by the dynamic range of the camera. Most CCD cameras offer 8-bit intensity resolution (or a maximal 16-bit for raw data), which corresponds to a maximal OD at $-\ln(I_t/I_0) \leq \ln(2^{16}) \approx 11$. In contrast, DAI relies on the shape of the detuning-dependent profile rather than absolute intensity difference, thus overcoming this limitation using the camera.

- **Robustness to detector noise**. The conventional method relies on the contrast between the transmitted and incident light. However, when the OD is large, the transmitted light can be extremely weak and dominated by the detector's intrinsic noise. In contrast, the DAI method avoids this issue, as the extracted OD is less affected by detector noise.

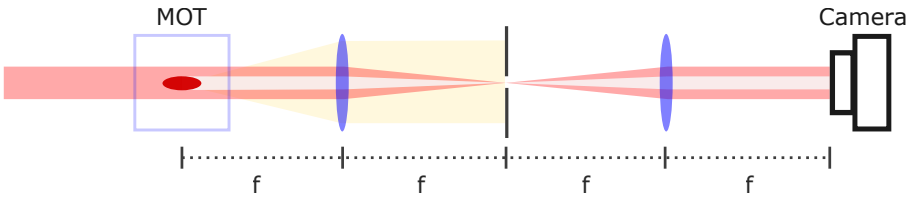

Figure 2.7: Schematic of absorption imaging setup.

- **Random measurement noise averaging out**. The OD is obtained by fitting the transmission curve over several detuning points, which averages out random fluctuations and improves robustness against measurement noise.
- **Tolerant to frequency offsets**. The probe frequency may deviate from atomic resonance by several MHz due to limitations in laser locking. Unlike conventional methods, the DAI approach does not require precise resonance. Instead, it leverages the symmetric transmission profile around resonance, making it robust against probe frequency offsets.

2.6.1 Absorption imaging setup

The DAI setup employs a 4-f configuration (shown in Figure 2.7), in which the MOT, a pair of lenses (each with focal length $f = 200\,\text{mm}$), and a CCD camera (CM3-U3-13S2M) are spaced by one focal length f from one another. A probe Gaussian beam, generated using a collimator (Thorlab C260TMD-B) and aligned with the 780 nm pump laser, is directed along the longitudinal axis of the atomic cloud. The pair of lenses, together with a pinhole placed at the shared focal plane, serves as a spatial filter to suppress divergent fluorescence from the atomic cloud. The CCD camera has a resolution of 1288×960 pixels with a pixel pitch of $3.75\,\mu\text{m}$. Since the 4-f configuration provides a magnification of 1, the size of the absorption shadow recorded on the camera directly corresponds to the actual size of the atomic cloud.

Rather than characterizing the atomic cloud in a continuously running MOT with cooling and repump lasers on, we perform a DAI measurement during a measurement window after a cooling sequence. It provides a more precise characterization of the atomic cloud used in the cooling-measurement sequence. To achieve this, we illuminate the atomic cloud released from the MOT with a probe beam synchronized

with a triggered camera exposure. After turning off the cooling beam and repump beam, the CCD camera is triggered 15 μs in advance before the probe pulse control signal to compensate for the response time of the camera of approximately 12 μs. The camera then opens a 200 μs exposure window, during which only the probe light is recorded. The probe light is pulsed with a duration of 100 μs, ensuring the entire pulse is captured within the exposure window. The intensity of probe light $I \lesssim 0.5\,\mathrm{mW/cm^2}$ is smaller than the saturation intensity $I_{\mathrm{sat}} = 1.67\,\mathrm{mW/cm^2}$.

2.6.2 Results

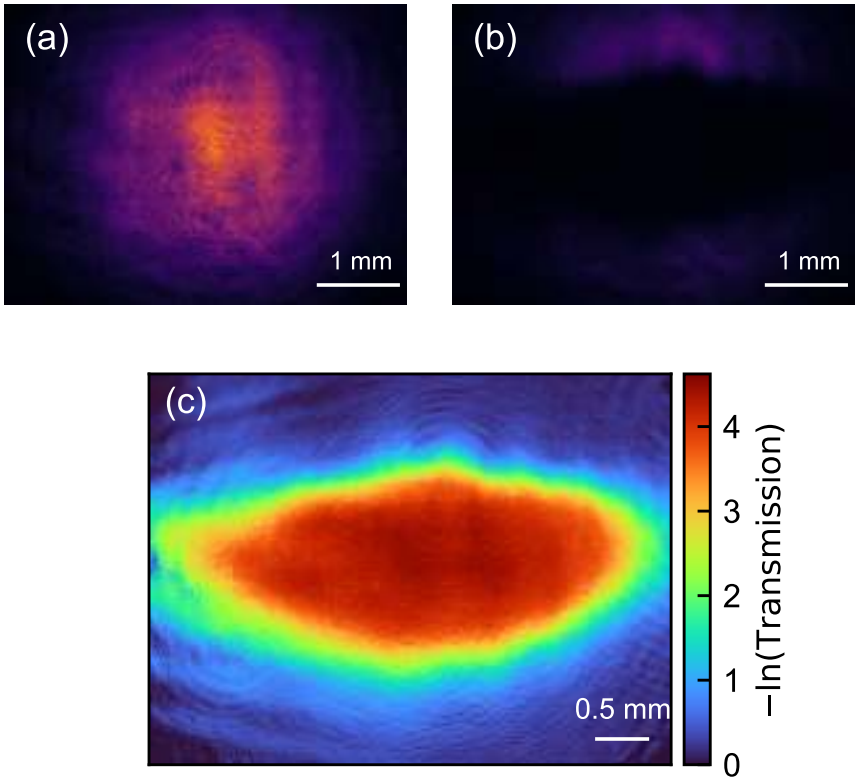

Figure 2.8: (a) Image of incident probe beam. (b) Image of transmitted probe beam through an atomic cloud. (c) Absorption imaging using resonant probe light.

As shown in Figure 2.8, using an image of incident probe light $I_i(y, z)$, a transmit image with the atomic cloud $I_t(y, z)$ and a background image $I_b(y, z)$, we obtain the transmission distribution $T(y, z)$ defined as

$$T(y, z) = \frac{I_t(y, z) - I_b(y, z)}{I_i(y, z) - I_b(y, z)}, \tag{2.17}$$

where the coordinates y, z refer to the cross-section in the y-z plane. The definition of optical depth through $\mathrm{OD} = -\ln(T)$ provides an effective characterization for a small atomic cloud. However, for dense atomic clouds, OD values are limited by the dynamic range of the camera. Using the DAI method described in § 2.6, we record the transmit image under different detuning conditions and extract the OD value from the transmission spectrum for each pixel. The fitted OD at each pixel reconstructs the OD distribution, providing a more precise characterization of the atomic cloud's cross-sectional profile. To simplify the data processing and mitigate anomalies and measurement artifacts, additional data processing steps are implemented. Specifically, every 4×4 block of raw pixels is binned into a single pixel by averaging. Since the DAI method is most effective for large OD values, only pixels with minimal transmission $T < 0.2$ are treated as valid. Furthermore, both the normal absorption images and the reconstructed OD distributions are sensitive to the light interference, often leaving residual interference patterns on the final distribution. To suppress these artifacts, a Gaussian filter with a standard deviation $\sigma = 1$ is applied to the data, smoothing out anomalous pixel values or interference patterns. Figure 2.9 (a) illustrates the $F = 2$ ground state OD distribution following above procedures.

We observe that, due to residual repump light in the central region, the population in the $F = 1$ ground state remains small when only donut-shaped repump beams are applied. Following the approach proposed in Ref. [104], we introduce a resonant 795 nm depumping laser addressing the $|5S_{1/2}, F = 2\rangle \rightarrow |5P_{1/2}, F = 1\rangle$ transition. This depumping beam is aligned collinearly with the donut-shaped repump beam and fills its central void. It is intended to suppress the residual repumping of atoms in the F=2 ground state within the void region, thereby compensating for the repump beam in the intersection area. In our experiment, the optimal power of the depumping laser is approximately 400 μW. A lower intensity is insufficient to compensate for the residual repump field at the center, while a higher intensity disturbs the cooling of the atoms. A proper depumping field enhances the formation of two layers of atom population in the dark SPOT. In the inner area, the population of cold atoms remains in the $F = 1$ dark state, decoupled from the cooling laser, while in the outer layer, where the repump laser is stronger, the atom population predominantly remains in the $F = 2$ ground state, undergoing the cooling cycles.

Figure 2.9 (b) displays the OD distribution after implementing the depumping laser. To transfer all the atoms to the $F = 2$ state for absorption imaging, the repump laser is kept on for an additional 10 μs. Compared to the case without the depumping laser, shown in (a), the depumping laser helps to comply with the criteria of SPOT and increase the central OD from around 40 to a maximum value of 60.

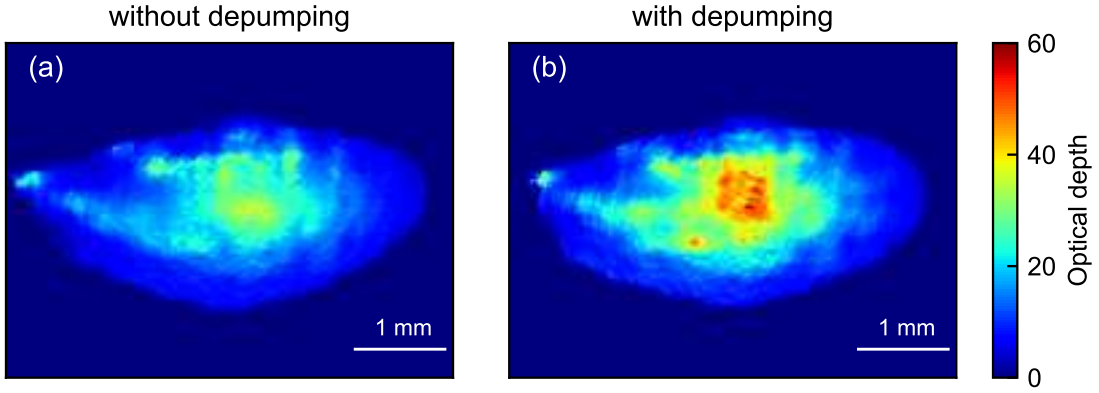

Figure 2.9: (a) Reconstructed OD distribution using DAI method only presence of cooling and 5 mW repump lasers. (b) Reconstructed OD distribution using DAI method with additional 400 μW depumping laser, which is aligned with the void center of the donut-shaped repump beam in the x-y plane.

2.7 Atomic cloud temperature

The velocity distribution of a non-interacting atomic ensemble in thermal equilibrium follows Maxwell-Boltzmann statistics; hence, the temperature of the atomic cloud characterizes the mean kinetic energy of these atoms. For a cloud of N atoms at temperature T, the number of atoms n_i associated with a kinetic energy interval $[E_i, E_i + dE]$ is given by

$$n_i = \frac{N}{Z} \exp\left(-\frac{E_i}{k_B T}\right) dE\,, \tag{2.18}$$

where Z is the partition function and k_B is the Boltzmann constant. Substituting the kinetic energy $E_i = mv^2/2$, the corresponding velocity distribution becomes Gaussian with variance $\sigma_v^2 = k_B T/m$ and can be written as

$$n_i(v) = \frac{NmV}{Z} \exp\left(-\frac{mv^2}{2k_B T}\right) \propto \frac{1}{\sigma_c\sqrt{2\pi}} \exp\left(-\frac{v^2}{2\sigma_v^2}\right)\,. \tag{2.19}$$

When the atomic cloud is released and undergoes free expansion, each atom moves ballistically according to $x = vt + x_0$ where x_0 is the initial position. Assuming the initial position and velocity distributions are uncorrelated, the variance of the cloud size after time t evolves as

$$\sigma^2 = \sigma_0^2 + t^2\sigma_v^2 = \sigma_0^2 + t^2\left(\frac{k_B T}{m}\right), \tag{2.20}$$

where σ_0 is the initial spatial variance of the cloud. This relation forms the basic principle of time-of-flight (TOF) metrology: by imaging the cloud at different expansion times t, one measures the size $\sigma(t)$ of the ensemble. Fitting $\sigma^2(t)$ as a linear function of t^2, the slope yields an estimate of temperature T.

However, measuring the cloud size in a dense atomic ensemble presents additional challenges. In conventional resonant imaging, the high optical depth results in a flat-top absorption profile, which no longer reflects the actual Gaussian distribution of the atoms. Moreover, the standard method of extracting optical depth via the definition $-\ln(T)$, where T is the transmission, fails for dense clouds due to the limited dynamic range imposed by shot noise in high OD regions. Although the DAI method described in § 2.6 can, in principle, recover the OD distribution even for dense clouds, it is resource-intensive and unsuitable for efficient single-shot measurements. Instead, we employ an off-resonant probe light detuned by $\delta/2\pi = 10$ MHz, which reduces absorption in the dense core of the cloud. This enables the quantity $-\ln(T)$ to approximate the Gaussian spatial distribution of the atoms. As shown in Figure 2.10, we image the atomic cloud in the y-z plane (a) immediately after the cooling stage and (b) after 2 ms of free expansion. The spatial distribution broadens over time during expansion. We extract 1D profiles along horizontal and vertical axes from images at different expansion times, and fit these profiles to acquire the time-dependent vertical and horizontal variance σ_V and σ_H, The extracted variances are plotted as a function of expansion time in Figure 2.11. From Figure 2.10 (c) and Figure 2.11 (a), we observe that the horizontal variance, the atomic cloud variance σ_H, exhibits irregular behavior: it decreases slowly and then remains nearly constant. In contrast, Figure 2.11 (b) shows that the vertical variance increases as expected from thermal expansion in Equation 2.20. This anisotropic behavior likely originates from the asymmetric magnetic field gradients along the two axes, which establish different equilibrium conditions and mean velocities. In

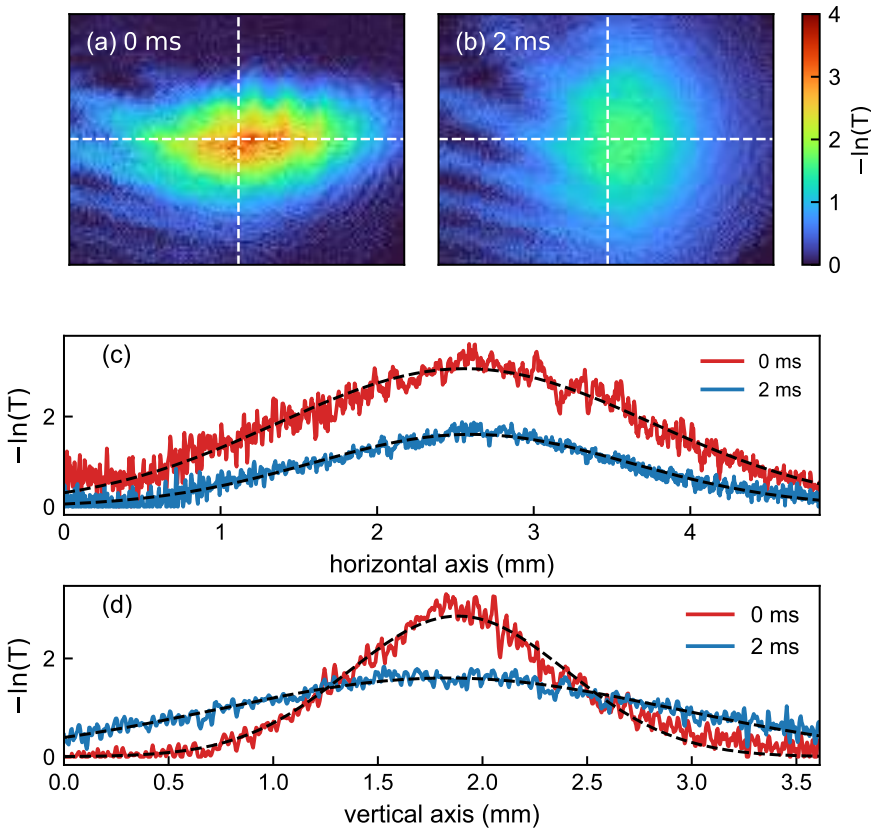

Figure 2.10: (a) Atomic cloud imaging obtained using an off-resonant probe light, evaluated as $-\ln(T)$, taken instantly after atoms are released from the MOT ($t = 0$ ms). (b) Atomic cloud imaging after 2 ms free expansion. (c) Horizontal profile of atomic cloud extracted along a common centerline for $t = 0$ ms and $t = 2$ ms. (d) Vertical profiles through the center point at $t = 0$ ms and $t = 2$ ms. Dotted lines represent their corresponding Gaussian fits.

the horizontal direction, stronger atom loss may occur. Moreover, the current probe beam, limited by its waist, cannot accurately resolve the cloud's expansion in this direction. Consequently, the measured absorption fails to reflect the true thermal distribution, rendering the TOF characterization along the horizontal axis unreliable. In the vertical direction, the fit in Figure 2.11 (b) yields a vertical temperature of around $2.02 \pm 0.08\,\mathrm{mK}$.

This measured temperature in the vertical direction significantly exceeds the Doppler limit of Rubidium atoms. This elevated temperature may be attributed to several factors. Firstly, the atoms are loaded directly from a hot vapor environment, without a prior pre-cooling procedure through a Zeeman slower. Additionally, to

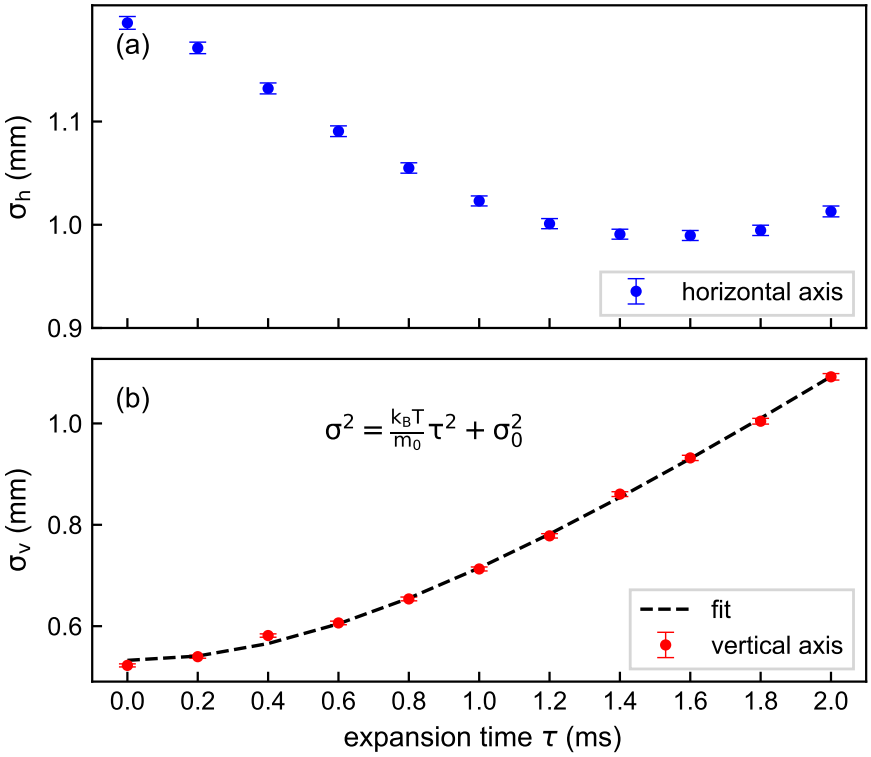

Figure 2.11: (a) Horizontal variance and (b) vertical variance of the atomic cloud as functions of expansion time. The black dashed line represents the fitted curve. Both error bars correspond to the standard deviation from the fitting procedure.

obtain a large atomic cloud, we operate the dispenser at a higher current, which raises the chamber pressure. Thermal coupling with the surrounding hot atoms can lead to an increase in the atomic momentum, shifting the balance between cooling and heating to a higher equilibrium temperature. Furthermore, as noted in [176], the atomic temperature is sensitive to the magnetic field. Therefore, in a large atomic ensemble spanning a relatively wide spatial region, atoms experience different magnetic fields at different positions, resulting in a higher atomic cloud temperature.

Chapter 3

Experimental setup

3.1 Laser system

To interact with cold ^{87}Rb atoms, the linewidth of the pump lasers used in experiments must be narrower than the linewidth of the atomic energy levels (e.g. $2\pi \times 6$ MHz for D2 lines) to resolve the atomic transitions precisely. In the near-infrared wavelength range, at which D1 or D2 lines are located, Ti:sapphire lasers and semiconductor lasers are commonly used. Unlike Ti:sapphire lasers, which typically require high-power optical pump and large setups with extensive gain media and cooling systems, semiconductor lasers (diode lasers) are compact, chip-scale devices that offer high efficiency when driven by a moderate current. They also have a long lifetime and require minimal maintenance. Usually, the semiconductor laser diodes provide MHz or sub-MHz linewidth and output powers of several tens of milliwatts. Furthermore, by integrating the bare diode into an external cavity diode laser (ECDL) system [190] and employing laser locking techniques such as Pound-Drever-Hall (PDH) locking [191] to a high-finesse cavity or atomic reference locking, the laser linewidth can be reduced to several hundred kHz with enhanced frequency and power stability.

In the experiment, most lasers are generated using Distributed Feedback (DFB) lasers and in-house-built ECDL systems based on Fabry-Pérot laser diodes or gain-chip laser diodes. These laser systems typically provide output powers of several tens of milliwatts. A portion of the laser output is used for atomic spectroscopy locking, while the remaining portion serves as the pump or probe lasers.

3.1.1 ECDL

The in-house ECDL adopts the Littrow configuration [190], consisting of a laser diode, a collimating lens (Thorlabs C230TM-B), and a diffraction grating (1800 lines/mm). The first-order diffraction is directed back to the laser diode, providing optical feedback. This configuration forms an external cavity between the grating and the diode, with a length of approximately $1 \sim 2\,\mathrm{cm}$. The cavity modes, combined with the gain profile of the bare laser diode, select a specific spectral mode for lasing, thereby narrowing the spectral linewidth compared to the free-running diode. A piezoelectric actuator mounted on the back of the grating enables fine adjustment of the cavity length, allowing for precise tuning of the cavity mode and, consequently, the laser frequency. Due to the free spectral range of the external cavity, the continuous frequency tuning range of the ECDL is limited to around $7.5 \sim 15\,\mathrm{GHz}$. A larger tuning range often leads to mode hopping, where the lasing shifts from one cavity mode to another. Coarse frequency tuning is achieved by adjusting the grating angle and the diode temperature. Once the laser frequency is close to the target, fine-tuning and modulation are performed by varying the control voltage applied to the piezoelectric actuator. The linewidths of our ECDLs are expected to be around $0.5 \sim 2\,\mathrm{MHz}$ according to previous characterizations [31, 192]. The output beam from the ECDL exits perpendicular to the facet of the bare laser diode and passes through a high-transmission window (B-coated). For certain lasers, a pair of anamorphic prisms is used to reshape the elliptical beam profile into a more circular, Gaussian profile. This beam shaping facilitates efficient coupling into optical fibers.

For downstream applications, an optical isolator is essential to protect the ECDL from back reflections. Reflections from subsequent optical components can couple back into the laser diode along the original beam path, resulting in a feedback that disturbs the ECDL frequency stability. This disturbance can manifest as periodic modulation in the error signal during atomic spectroscopy.

All laser systems are frequency-locked and stabilized to atomic transitions using error signals derived from atomic spectroscopy. Frequency modulation spectroscopy (FMS)[193] (see Figure 3.2) and modulation transfer spectroscopy (MTS)[194–196] (see Figure 3.1) are two Doppler-free techniques commonly used to generate such

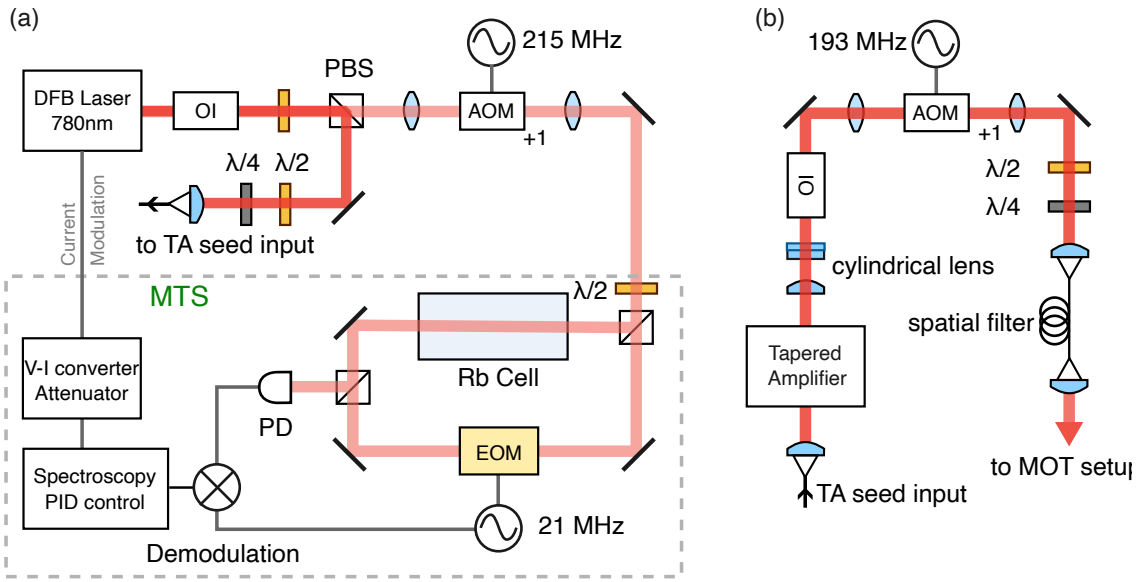

Figure 3.1: Schematic of (a) cooling seed laser and its MTS setup and (b) TA setup of cooling laser. OI: optical isolator; AOM: acousto-optic modulator; PBS: polarizing beam splitter; PD: photodetector.

reference signals. The specific implementation of these spectroscopy methods is described in the subsequent introduction of the laser systems used in the experimental setup.

3.1.2 Cooling laser

The cooling laser requires a total power of hundreds of milliwatts, which cannot be directly provided by a single-mode diode laser. To achieve the necessary power, a tapered amplifier (TA) (see Figure 3.1 (b)) is used to amplify a seed laser while preserving its optical frequency. A 780 nm DFB laser provides roughly 6 mW as seed to the injection TA. The TA is operated at 2.3 A to generate an output power of around 600 mW. The laser output of the TA typically has a narrow elliptical profile, which is reshaped by a pair of cylindrical lenses. After passing through an optical isolator and an AOM, around 150 mW of laser can be coupled into the single-mode fiber. This single-mode fiber also functions as a spatial filter to provide a high-quality Gaussian beam for subsequent shaping of the elliptical cooling beams. A small part of the DFB laser output is first shifted by +215 MHz via an AOM and then used for MTS, such that the original laser is locked to the atomic

transition $|5S_{1/2},\, F = 2\rangle \rightarrow |5P_{3/2},\, F = 3\rangle$ with a $-215\,\mathrm{MHz}$ frequency offset. After amplification, the frequency of the cooling beam is shifted back by another AOM at a frequency of $+193\,\mathrm{MHz}$. The net effect is a detuning of $\Delta/2\pi = -22\,\mathrm{MHz}$ relative to the atomic transition.

Modulation transfer spectroscopy

Modulation transfer spectroscopy (MTS) is employed to provide a Doppler-free, high signal-to-noise spectroscopic reference for stabilizing a laser to the cycling transition $|5S_{1/2},\, F = 2\rangle \rightarrow |5P_{3/2},\, F = 3\rangle$ of ^{87}Rb [197]. Compared to FMS technology, MTS eliminates the residual Doppler-broadened absorption background and offers a flat baseline in the error signal. Consequently, MTS-locked lasers manifest lower frequency noise and reduced frequency drift.

To generate the MTS signal, the laser is split into a relatively strong "pump" and a weak "probe" using a PBS. The "pump" laser is phase-modulated at $f = 21\,\mathrm{MHz}$ using an EOM, while the probe remains unmodulated. After modulation, the "pump" beam contains a carrier and first-order sidebands at $\pm f$. The two beams counterpropagate through a Rubidium vapor cell. Near resonance, the "pump" field periodically modulates the atomic population and coherence at the modulation frequency. This leads to an imbalance in the sideband absorption for the "pump" field. In the presence of a third-order susceptibility $\chi^{(3)}$ near resonance, an atomic medium results in a four-wave mixing process involving both "pump" and "probe" fields. Through this nonlinear interaction, the atomic modulation is transferred to the "probe" mode by generating a conjugate component, resulting in a phase and amplitude modulation at $f = 21\,\mathrm{MHz}$ frequency component.

The transmitted probe light is detected by a photodiode (Si PIN, S5971, 100 MHz bandwidth), and the resulting signal is mixed with the original RF signal in a home-built FM demodulation board. This demodulation yields a near-symmetric dispersive error signal centered on the atomic resonance. By adjusting the demodulation phase, the output can represent either the in-phase or quadrature component. In our implementation, the FM demodulation board does not specify a fixed demodulation phase; instead, the phase is empirically optimized to search for a proper slope across the zero-crossing of the error signal, ensuring stable laser locking. MTS provides strong signals only for nearly closed cycling transitions, which support efficient

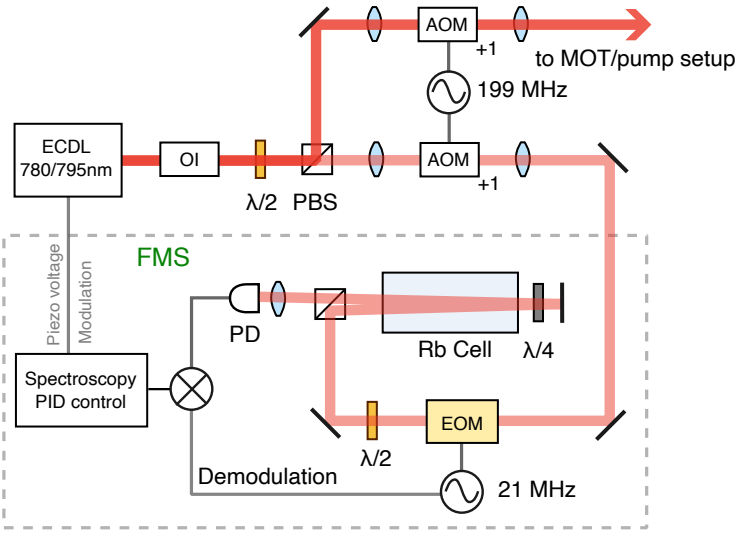

Figure 3.2: Schematic of repump laser (or 795 nm coupling laser) with FMS setup. For the 795 nm coupling laser, two AOMs are driven with 205 MHz RF signal.

optical pumping and strong nonlinear effects. In contrast, transitions originating from the $F = 1 \rightarrow F'$ manifold, particularly $F' = 0, 1, 2$, do not support MTS signal generation. This limitation arises because the excited states can decay to both $F = 1$ and $F = 2$ ground states. Atoms initially in $F = 1$ are optically pumped and accumulated in $F = 2$ ground state, thereby breaking the resonance condition.

3.1.3 Repump laser

The repump laser is provided by an in-house ECDL based on a laser diode (Thorlab L785P090), whose frequency is resonant to the $|5S_{1/2},\ F = 1\rangle \rightarrow |5P_{3/2},\ F = 2\rangle$ transition. A portion of the light is first shifted by +199 MHz for FMS locking. The remaining light is shifted back to resonance using the +1 diffraction order of another AOM to enable switch-on/off control. The laser module ultimately delivers approximately 8 mW of repump light to the MOT setup.

Frequency modulation spectroscopy

The frequency modulation spectroscopy (FMS) is an effective technique for generating error signals for most non-forbidden atomic transitions, even in the presence of an absorption profile background, making it suitable for a wide range of applications.

In the FMS setup, a portion of the laser serves as the probe light, which

is modulated by a home-built electro-optic modulator (EOM) at a modulation frequency of $f = 21\,\mathrm{MHz}$. This modulation creates sidebands around the carrier frequency, and imbalanced absorption of these sidebands by the atomic transitions in the rubidium vapor cell generates a modulation on this frequency component. The probe light is initially polarized to either horizontal (H) or vertical (V) polarization using a polarization beam splitter (PBS). After passing through the rubidium cell, the light encounters a quarter-wave plate (QWP) and a mirror, which reflects the probe light. The double-pass QWP is set to convert the probe light to the opposite polarization (from H to V or V to H), enabling it to exit through the orthogonal port of the PBS instead of being reflected back along its incident path. The forward and backward probe light beams overlap but are slightly misaligned from perfect collinearity to avoid interference between the incident and reflected light, which would cause periodic modulation in the error signal. Since the incident and reflected probe lights counter-propagate in different directions, this allows the Doppler shifts to cancel out, as the frequency shifts due to atomic motion are equal and opposite for the two beams. Therefore, it provides a Doppler-free error signal for different hyperfine transitions.

The transmitted light from the PBS is then detected by a photodiode (Si PIN, S5971, 100 MHz bandwidth). The detected signal is mixed with the modulation signal and demodulated to extract its amplitude modulation applied to these frequency components. Although the error signals for the hyperfine transitions are Doppler-free, they are still applied on a residual Doppler-broadened absorption background, making it difficult to accurately lock a laser to an atomic transition. As a result, when using FMS, the laser may sometimes exhibit a fixed offset ($< 5\,\mathrm{MHz}$) relative to the atomic transition.

3.1.4 The 780 nm laser

One of the pump lasers used in the experiment described in Chapter 4 is a 780 nm distributed feedback (DFB) diode laser to address the D2 line of ^{87}Rb. This laser also serves as a probe in certain characterization measurements. It is frequency-stabilized using FMS, as illustrated in Figure 3.3. It allows rapid frequency adjustment to address different atomic transitions from the $F = 1$ or $F = 2$ state, while avoiding

the mode hopping often encountered in the frequency detuning of the ECDL. The pumping beam used in the experiment is obtained from the first diffraction order of an AOM, driven by a fixed RF signal at +180 MHz. This frequency is kept constant to maintain a consistent and stable output, avoiding misalignment due to changes in the diffraction angle. Frequency tunability of the pumping laser is achieved via a separate spectroscopy AOM, which shifts the frequency of the laser used in FMS by the first diffraction order. The RF signal for this AOM is tunable within a range of $140 \sim 230$ MHz, which provides a detuning range of $\Delta/2\pi$ between +40 to −50 MHz relative to the atomic transition frequency. Once the laser is locked, we can still fine-tune its frequency by updating the spectroscopy AOM's RF frequency in small steps. This gradual adjustment enables smooth transfer to the target detuning while maintaining stable laser locking and power output.

3.1.5 The 795 nm laser

Another pump laser, tuned to the D1 line of ^{87}Rb, is a 795 nm in-house ECDL constructed using a Thorlabs LD808-SA100 diode. It is frequency-locked using FMS in a configuration similar to that used for the repump laser (see Figure 3.2), and delivers an output power of approximately 12 mW. As an alternative, another laser diode (Qphotonics QLD-790-80S) was also tested to evaluate its suitability as a replacement for the now-obsolete LD808. However, this diode exhibited issues with power stability in the ECDL configuration, as its output power degraded over time.

3.1.6 The 776 nm laser

The 776 nm laser is used to realize the two-photon excitation to $5D_{3/2}$ or $5D_{5/2}$ hyperfine states. Bare laser diodes centered at 776 nm are not readily available. Therefore, we employ L795P090 and LD785-SH300 diodes in ECDL configurations and tune them toward the target wavelength of 776 nm by adjusting the injection current and temperature. Both laser diodes operate far from their center wavelengths, requiring precise adjustment of the diffraction grating angle. As a result, they are more prone to mode hopping. The LD785-SH300 requires relatively low temperatures ($\lesssim 18\,^{\circ}$C) and low driving currents ($\lesssim 150$ mA) to achieve this wavelength. Using their output as the seed, we also implemented a master–slave

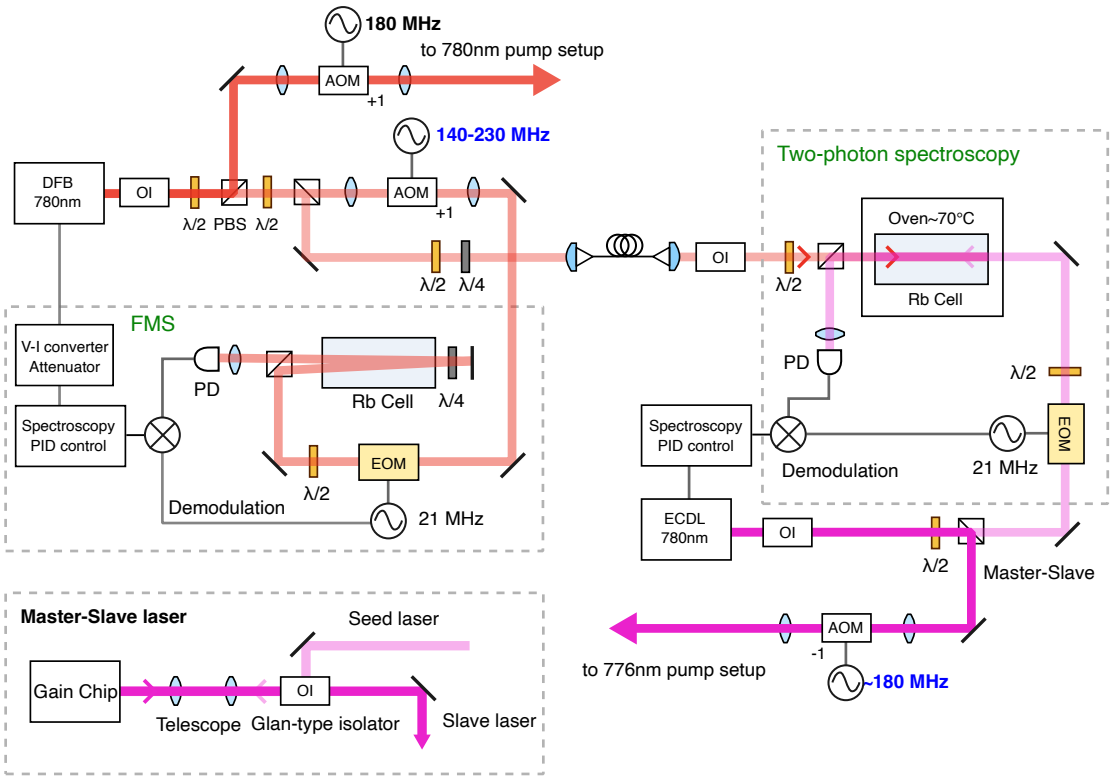

Figure 3.3: Schematic of the 780 nm pumping laser with its FMS setup, and the 776 nm driving laser with its two-photon spectroscopy setup. To increase the available power of the 776 nm laser, a gain chip laser is employed in a master-slave configuration, where it is frequency-locked to the seed laser using injection locking.

configuration (see Figure 3.3) with a gain chip laser diode (EYP-RWE-0780-02000-1300-SOT12-0000). However, this configuration is highly sensitive to mode matching between the seed laser's beam profile and the slave laser's output mode. We realize such spatial mode matching by the telescopic layout of the lens to adjust the seed beam size. Due to the limited stability of telescope optics and mirrors on the optical table, maintaining good mode matching proved challenging. We consistently observed unstable output power caused by misalignment and degradation over time. Therefore, we utilized the direct output from the ECDL based on L795P090 laser diode, which provides 8 mW of usable power.

Two-photon spectroscopy

As illustrated in Figure 3.3, a 776 nm laser is frequency-locked using two-photon spectroscopy, enabling access to the two-photon processes $5S_{1/2} \rightarrow 5D_{3/2}$ or $5D_{5/2}$

transitions, with a 780 nm laser. Since the two-photon transition probability is much smaller than that of one-photon resonant absorption, a relatively high atomic vapor density is required to achieve observable signal strength. The rubidium vapor cell is heated to approximately 70 °C, which can increase the atomic density to $10^{11} \sim 10^{12}$atoms/cm^3, significantly boosting two-photon transition efficiency [102]. In the experiment, the 780 nm laser is detuned from the atomic D2 transition (e.g., $|5S_{1/2},\, F = 1\rangle \rightarrow |5P_{3/2},\, F = 2\rangle$ or $|5S_{1/2},\, F = 2\rangle \rightarrow |5P_{3/2},\, F = 3\rangle$) by over hundreds of MHz, and has a power of approximately 2 mW. A portion of the 776 nm laser, also with a power of around 2 mW, is first modulated by an EOM and then counter-propagates and spatially overlaps with a 780 nm beam inside the vapor cell. The two beams are linearly polarized along orthogonal directions, allowing efficient separation using a PBS. After passing through the vapor cell, the transmitted 776 nm light is detected by a photodiode. The detected signal is demodulated with the same EOM drive frequency to generate a dispersion-like two-photon error signal, which is used to stabilize the 776 nm laser frequency precisely to the two-photon resonance condition. In practice, the hyperfine level splitting within $5D_{3/2}$ or $5D_{5/2}$ excited states is relatively small, resulting in closely spaced error signals in the two-photon spectroscopy. Consequently, to accurately reach the desired two-photon resonance condition, it is always necessary to implement the fine tuning of the RF drive frequency applied to the switch AOM of the 776 nm laser. Since the principle of two-photon spectroscopy is similar to that of FMS, the error signal is imposed on a non-zero absorption background. To achieve a stable, drift-free error signal for laser locking, several conditions must be carefully controlled. Maintaining this stability requires avoiding saturation effects at various stages, including the photodiode saturation, the optical absorption saturation in the rubidium cell, and the EOM modulation saturation. These considerations require stable laser power for both 780 and 776 nm lasers, as well as a stable atomic density through precise temperature control. Additionally, the polarization of the 776 nm laser must align with the EOM modulation axis to avoid the degradation of the error signal.

3.1.7 Laser control

Each AOM is driven by an RF signal generated by a direct digital synthesis (DDS) card and amplified by an RF amplifier (Mini-circuits ZHL-1-2W). Dedicated DDSs are employed to generate continuous RF signals for atomic spectroscopy, avoiding signal jitter or instability caused by the control disturbances. To minimize cross-talk and prevent unwanted resonances, the RF frequencies are intentionally set to different values rather than a simple center modulation frequency of 200 MHz. Each laser system is typically equipped with a pair of AOMs: one, referred to as the "Spectroscopy AOM", provides a frequency-shifted beam used for atomic spectroscopy; the other, called "Switch AOM" compensates for the frequency offset and controls the laser's on/off switching function. By programming the output RF signal of DDS, we can precisely control the switching and amplitude/frequency modulation of the AOMs, enabling operations such as ramping down the repump laser. Each DDS is triggered by a multi-channel pattern generator. According to characterization measurements, the total delay from the pattern generator output to the final AOM control of the laser beam is approximately 120 ns.

In addition to laser control, this multi-channel pattern generator also governs the main experimental sequence described in § 3.2 by generating the corresponding control signals in NIM logic level. These signals are used for tasks such as defining the measurement window of the coincidence counting module to exclude photon events during the cooling stage, triggering the timestamp card, and controlling the operation of the absorption imaging camera.

3.2 Control sequence and state preparation

In a MOT, the cooling and repump beams must remain continuously on to maintain the cold atomic cloud in equilibrium, resulting in strong fluorescence that makes the cloud visible to the naked eye. However, this fluorescence significantly hampers the implementation of nonlinear optical processes and the detection of generated photons. To overcome this, the SFWM process is carried out in a sequential scheme, in which each cooling stage is followed by a measurement window. During the measurement window, the cooling and repump beams are switched off, preparing most atoms in a specific ground state as the initial condition for the nonlinear

interaction and eliminating background fluorescence.

After the cooling and repump lasers are switched off, the majority of atoms are optically pumped into the hyperfine ground state $|5S_{1/2}, F = 2\rangle$, with their population thermally distributed among the Zeeman sublevels. This corresponds to a mixed state of multiple Zeeman levels, rather than a well-defined Zeeman manifold. Although a residual magnetic field remains, it induces only a small Zeeman splitting on the order of sub-MHz, much smaller than the natural linewidth of the $|5S_{1/2}, F = 2\rangle$ excited state. The residual magnetic field has a negligible effect on the spectral properties of the generated photons. As a result, the SFWM process can be treated as a parametric interaction involving only the hyperfine levels. Moreover, actively switching off the coil current would require additional wait time for its decay, which leads to atom loss due to ballistic expansion. Thus, we maintain the magnetic field gradients during the measurement window.

Once released from the MOT and without additional trapping mechanisms such as a far-off-resonance trap (FORT), the atomic cloud undergoes ballistic expansion at an expansion rate determined by its temperature, causing a gradual reduction in optical depth. The measurements of fluorescence illuminated by pump lasers indicate that the atomic cloud could support the nonlinear interaction with pump fields for several milliseconds after release. To ensure a relatively stable optical depth during the SFWM process, we set the measurement window to $500\,\mu$s, following a cooling stage of at least 5 ms.

3.2.1 Atomic state preparation in F = 2

Based on the empirical observation, a cooling stage requires a duration of at least 5 ms, otherwise, the atomic ensemble becomes significantly reduced in size. The schematic in Figure 3.4 shows the timing of the control sequence. At the beginning of each cooling stage, an optional substage spanning several hundred microseconds is introduced, during which the cooling laser detuning is altered to $\Delta/2\pi = -10\,\text{MHz}$. This smaller detuning enhances the interaction between the cooling light and atoms, accelerating the recapture and reloading of the expanded atomic cloud into the MOT. Following this, the detuning is switched back to $\Delta/2\pi = -22\,\text{MHz}$ for standard cooling, until the atomic ensemble reaches thermal equilibrium and a

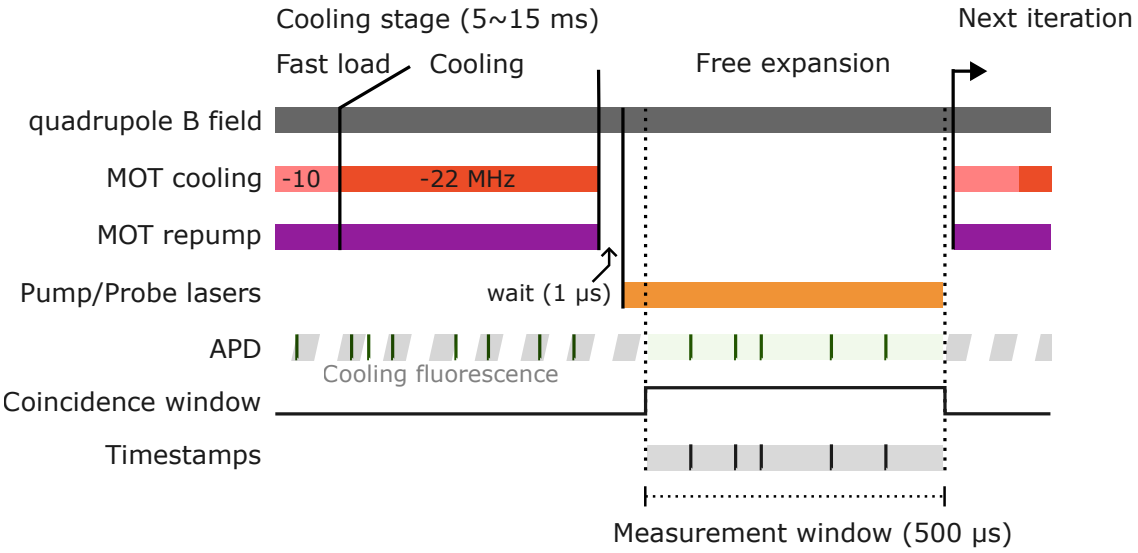

Figure 3.4: Experimental timing sequence for consecutive cooling, state preparation in the F=2 ground state, and photon detection control during the measurement stage. After the cooling phase, atoms are initially prepared in the $|5S_{1/2}, F = 2\rangle$ state.

stable size. Then, after the cooling and repump lasers are switched off, the atomic cloud is released and begins to expand during the measurement window. Before the atomic ensemble becomes too dilute to sustain efficient nonlinear interaction, the measurement window is closed, and the cooling cycle is restarted to recapture and re-cool atoms for the next sequence.

In our setup, the single-photon avalanche photodiodes (APDs) operate in continuous mode rather than in the gated acquisition mode. The built-in gate function of these modules (Excelitas SPCM series), which modulates the bias voltage, can introduce instability in photon counting and lead to spurious coincidences in correlation measurements. Under this configuration, even with spectral filtering by etalons, the strong residual fluorescence during the cooling phase can still saturate the APDs. Therefore, a short delay of 1 μm between switching off the cooling beams and initiating the pump pulses is introduced. This delay allows the Excelitas APDs to recover from saturation as their dead time is approximately $20 \sim 40$ ns. Additionally, this delay ensures that all cooling and repump beams are fully extinguished, considering the $120 \sim 300$ ns DDS control and AOM delay and the $10 \sim 100$ ns rise/fall time of the AOMs, which depends on the specific beam size through the AOM.

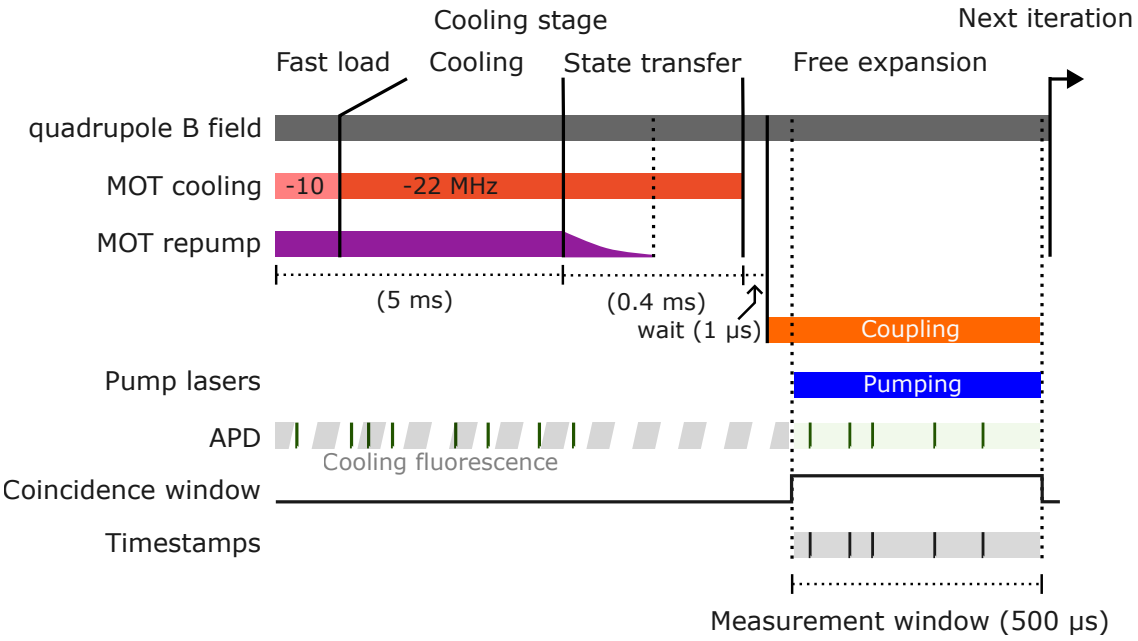

Figure 3.5: Experimental timing sequence illustrating the consecutive cooling, state transfer, and measurement stages, along with the corresponding photon detection control sequence. After a cooling and state transfer phase, atoms are initially prepared in $|5S_{1/2}, F = 1\rangle$.

To filter out photon events from cooling fluorescence, a coincidence gating signal (in NIM logic) defines the valid detection window and performs an AND Boolean operation with the single-photon pulses. These logic operations typically introduce additional jitter of less than 1 ns, which is acceptable for our experimental requirements and compatible with the 2 ns resolution of the timestamp card. In this way, we implement a post-selected gate scheme, ensuring that photon events occurring during the measurement phase are time-tagged.

3.2.2 Atomic state preparation in F = 1

The double-Λ SFWM scheme requires the atomic ensemble to be initially prepared in the ground state $|5S_{1/2}, F = 1\rangle$. Accordingly, the experimental sequence (refer to Figure 3.5), in addition to the MOT preparation and control steps described in § 3.2.1, exclusively includes a state transfer stage following the cooling stage. This stage aims to transfer the atomic population from the $F = 2$ ground state to the $F = 1$ ground state. State initialization can be achieved via optical pumping or

stimulated Raman adiabatic passage (STIRAP). In the optical pumping scheme, a depumping beam drives the $F = 2 \rightarrow F' = 2$ transition, allowing atoms to spontaneously decay into the target $F = 1$ state with minimal scattering. The STIRAP protocol could employ a pair of two-photon resonant pulses in a Λ-type three-level system to adiabatically transfer the population from the $F = 2$ state to the $F = 1$ state without populating the intermediate state. However, both techniques require additional laser beams in the setup. Instead, we adopt a simplified approach by reusing the cooling light as a depumping beam. In the absence of the repump light, atoms in the $F = 2$ state interact with the cooling beam and spontaneously decay either to $F = 1$ or back to $F = 2$. Once atoms fall into the $F = 1$ "dark state", they decouple from the cooling cycle and are no longer trapped or re-cooled. As a result, the MOT fluorescence diminishes, and the trap vanishes within a few milliseconds. However, if this process is limited to a short duration (hundreds of microseconds), significant atomic expansion is avoided, and atoms are effectively transferred to the $F = 1$ ground state.

In our implementation, the state transfer stage spans $400\,\mu$s and consists of two substages: 1. During the first $200\,\mu$s, the repump intensity is ramped down, while the MOT remains active. During this phase, the recycling and cooling efficiency decrease as the repump field weakens. 2. In the following substage, the repump beam is fully switched off, while the cooling beams remain on. Throughout these two substages, atoms are continuously pumped by the cooling light while the repump field diminishes, leading to a progressive transfer of population from the $F = 2$ to the $F = 1$ ground state. A small fraction of atoms remaining in $F = 2$ during the residual cooling phase maintains limited cooling and trapping, thereby suppressing excessive atomic expansion. The optimal duration of the transfer stage is determined by measuring the optical depth as a function of the total cooling time (see Figure 3.6). It shows that after $400\,\mu$s cooling time, including $200\,\mu$s ramp-down of the repump field, the majority of atoms have been transferred into the $F = 1$ ground state. We note that, due to the counter-propagating σ^+ - σ^- polarization configuration of the cooling beams, unlike the single-polarization used in optical pumping, the transferred population remains distributed among Zeeman manifolds in a mixed state.

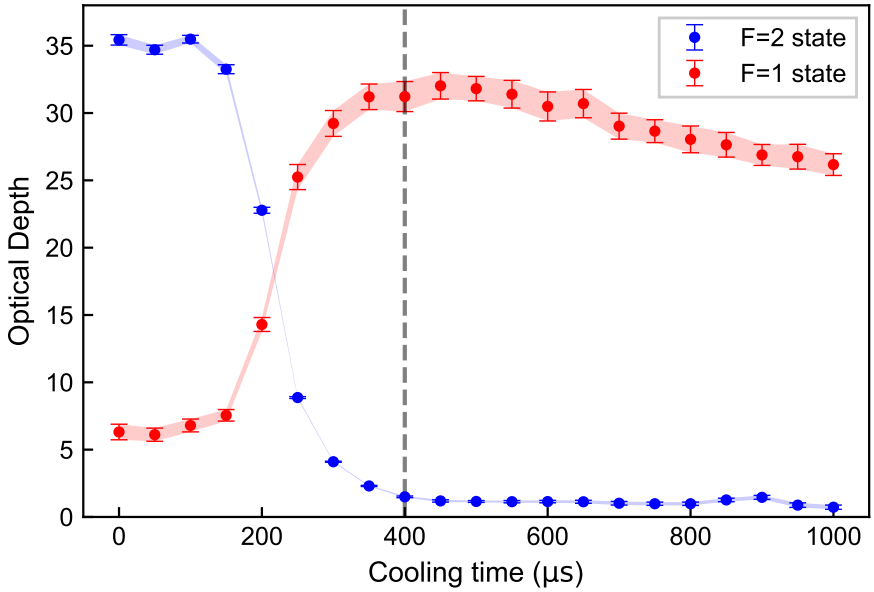

Figure 3.6: Optical depths of $F = 2$ (blue) and $F = 1$ (red) ground states as a function of cooling time during the state transfer stage. The optical depths are extracted from fits to the transmission spectra, with the error bars representing the standard deviations from the fitting procedure.

3.2.3 Control of optical depth

To prepare atomic clouds with different optical depths, we can adjust parameters such as the dispenser current and cooling light intensity to modify the size of the prepared cold atomic sample. However, these methods do not consistently reach the target value, and the characterization of optical depth and the practical implementation require a time-consuming process. In contrast, since the free expansion of the atomic cloud gradually reduces the atomic density, controlling the expansion time provides a more reliable and reproducible way to tune the optical depth. Figure 3.7 characterizes the dependence of optical depth on the expansion time, showing an approximately exponential decay. Therefore, by introducing an additional wait time between the release from the MOT and the measurement window, a wide range of atomic cloud sizes with well-defined optical depths can be accessed consistently.

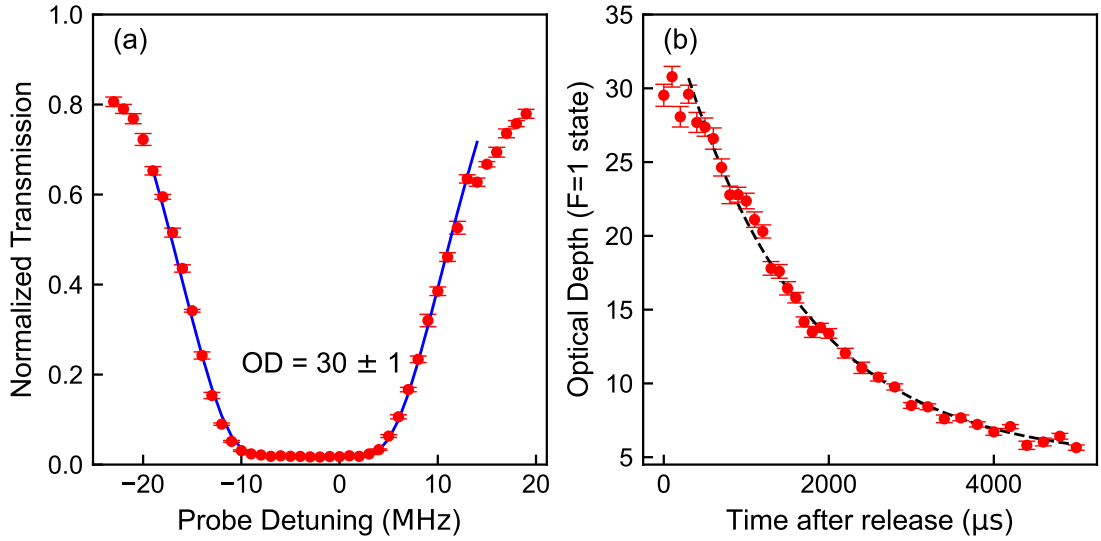

Figure 3.7: (a) Transmission spectrum as a function of probe detuning, measured immediately after release from the MOT. The center detuning is offset due to the frequency shift introduced by the atomic spectroscopy laser locking. (b) Optical depth of the $F = 1$ ground state as a function of expansion time after release from the MOT, following the control sequence described in Figure 3.5.

3.3 Fabry-Pérot cavity filters

Due to scattering of the pump laser from mirror surfaces and multiple reflections between glass interfaces within the vacuum chamber, a low-intensity background of the pump light extends beyond the main beam profile. Despite spatial separation by 1°, a substantial fraction of these stray pump photons is still coupled into the collection single-mode fiber, significantly exceeding the count rate of the Stokes or anti-Stokes photons. To suppress this background, we employ a Fabry–Pérot cavity as a frequency filter to selectively transmit the desired photons.

Air-spaced Fabry–Pérot cavities with piezo-tuned mirrors often require active locking, while thermally expandable spacer designs [198] need precise mode matching. In contrast, our filters employ a monolithic design (etalon) consisting of either a plano-convex or plano-plano substrate with high-reflectivity coatings on both surfaces. The center transmission of the cavity can be tuned via thermal expansion by stabilizing the etalon temperature. Once thermal equilibrium is reached, the transmission peak of the etalon can be aligned to the desired frequency with high precision. Based on

long-term observations, this temperature-controlled approach ensures stable filtering without significant frequency drift or stress-induced birefringence [199], allowing us to neglect such effects in practice.

Theoretically, the transmission of a planar Fabry-Pérot cavity with respect to the frequency ν is given by the Airy function:

$$T(\nu) = \frac{T_{\max}}{1 + F \sin^2\left(\frac{\pi\nu}{\Delta\nu_{\mathrm{FSR}}}\right)}, \quad F = \frac{4R}{(1-R)^2}\,. \tag{3.1}$$

Here, $T_{\max}$ is the maximal transmission and F is the finesse coefficient, which relates to the cavity finesse $\mathcal{F} = \Delta\nu_{\mathrm{FSR}}/\Delta\nu_{\mathrm{FWHM}}$ via $\mathcal{F} = \pi\sqrt{F}/2$. The free spectral range (FSR) $\nu_{\mathrm{FSR}} = c/(2nL)$ depends on the cavity length L and material refractive index n. In the ideal case, we hope for the etalon to exhibit maximal transmission at the frequency of the target photons, while the pump photons, which need to be suppressed, fall midway between two adjacent transmission peaks. This condition is satisfied when the FSR equals twice the frequency separation between the target and pump photons. In our system, this frequency separation approximately corresponds to the ground-state hyperfine splitting of ^{87}Rb, which is 6.8 GHz. Therefore, the optimal FSR for 780 nm and 795 nm etalons is 13.6 GHz.

3.3.1 Alignment

For a plano-plano cavity, any Gaussian beam can achieve the mode matching in principle without requiring additional focusing optics. In contrast, for convex–convex or plano–convex cavities, the input beam must be appropriately focused to match the cavity mode and mitigate coupling losses due to spatial mismatch. The required focal length of the mode-matching lens for a convex-type cavity is given by

$$f = \left(\frac{\pi^2 w_{\mathrm{in}}^4 d(r-d)}{n^2\lambda_0^2}\right)^{1/4} - d(n-1) \approx \left(\frac{\pi^2 w_{\mathrm{in}}^4 d(r-d)}{n^2\lambda_0^2}\right)^{1/4}, \tag{3.2}$$

in which w_{in} is the input beam waist, r is the curvature of the convex cavity surface, d is the distance from the convex surface to the desired beam focus inside the cavity, n is the refractive index of etalon material, and λ_0 is the vacuum wavelength. This expression is derived by matching the curvature of the Gaussian beam to the cavity mode inside the material. The approximation in Equation 3.2 holds when the cavity

length is much smaller than the required focal length, such that the little shift due to the refractive index of the cavity material can be neglected.

In our case, the 795 nm etalon consists of two coated planar surfaces and therefore does not require additional spatial mode matching. The input beam is a Gaussian mode with a waist of 0.74 mm. The 780 nm etalon uses a plano-convex design with a $R = 95\%$ reflective coating and a cavity length of 6.35 mm with a convex surface curvature $r = 50\,\text{mm}$. To simplify the optical setup, spatial mode matching is achieved by adjusting the position of the aspheric lens in a collimator (Thorlab A375TM-B, $f = 7.5\,\text{mm}$). This cavity requires a beam waist of approximately $w_0 \approx 53\,\mu\text{m}$ at the planar surface, calculated from

$$w_0 = \sqrt{\frac{\lambda_0 d}{\pi n} \cdot \sqrt{\frac{r}{d} - 1}}\,. \tag{3.3}$$

With an initial Gaussian beam waist of $2.5\,\mu\text{m}$ (half of mode field diameter of fiber), the required distance from the aspheric lens to the cavity surface is $s \approx 110\,\text{mm}$, such that the beam focuses at the etalon's planar surface. To achieve this focusing condition, the fiber-lens separation is increased to 7.85 mm beyond the nominal focal length of the collimator. The same type of collimator is used for collecting the transmitted light, placed symmetrically at a distance s after the cavity to enhance the coupling efficiency. The 776 nm etalon is a convex-convex etalon with surface curvature $r = 200\,\text{mm}$ and a length of 20 mm. According to Equation 3.2, cavity mode matching is realized through a pair of additional convex lenses with a focal length $f \approx 400\,\text{mm}$, separated by a distance of $2f$, for a input Gaussian beam with a waist of 1.09 mm. The cavity is positioned at the focal point, where the beam curvature matches the cavity mode.

Once the optical components are coarsely positioned according to the theoretical values, the system can be fine-tuned by optimizing the light transmission. This is done by monitoring the transmitted light intensity and observing the transverse mode profile with a camera placed after the cavity. A prerequisite for effective alignment is that the probe light frequency is sufficiently close to the cavity resonance. By iteratively adjusting the cavity position, its orientation, and the angle of the incident probe beam, the transmitted beam can be tuned to exhibit a clean TEM_{00} mode, indicating approximate mode matching. Further optimization is performed by maximizing the transmitted intensity. Once optimal mode matching is achieved,

sweeping the probe laser frequency near resonance results in variations in transmitted intensity without altering the transverse mode displayed in the camera.

3.3.2 Characterization

Table 3.1 summarizes the characterization of the three etalons. Here, the measured extinction ratios are obtained by evaluating the attenuation of the pump laser when the etalon transmission is aligned with the target frequency, using the formula ER = $\log_{10}(P_{\text{in}}/P_{\text{out}})$. This measurement typically overestimates the theoretical extinction ratio, as it includes additional loss contributions from scattering, absorption, and mode mismatch. Therefore, it reflects the overall attenuation of the pump field passing through the cavity, rather than the ideal ratio between maximum and minimum transmission.

Filter	Type	Length	R	FSR	FHWM (MHz)		Extinction (dB)	
		(mm)	(%)	(GHz)	theo	meas	max	meas
780 nm	Plano-Convex	6.35	95	16.3	265	275	32	32~34
795 nm	Plano-Plano	3	97	34.5	334	345	36	34~40
776 nm	Convex-Convex	20	97	5.2	50	55	36	34~40

Table 3.1: Characterization of filter etalons. Theoretical values above are calculated based on a refractive index of $n = 1.45$ for fused silica.

Table 3.2 presents the coupling efficiencies in the filtering system. After passing through the etalons, the transmitted photons are coupled into single-mode fibers for downstream. Based on long-term observations, the plano-plano etalon suffers from the transverse mode's distortion, leading to large coupling efficiency fluctuations over time. This instability is attributed to non-uniform changes in etalon length caused by temperature fluctuations. In contrast, the plano-convex etalon exhibits better stability and resilience against temperature variations.

3.3.3 Detection and overall efficiencies

The overall transmission efficiencies for the Stokes and anti-Stokes channels are composed of multiple factors. They include the transmission through one layer of

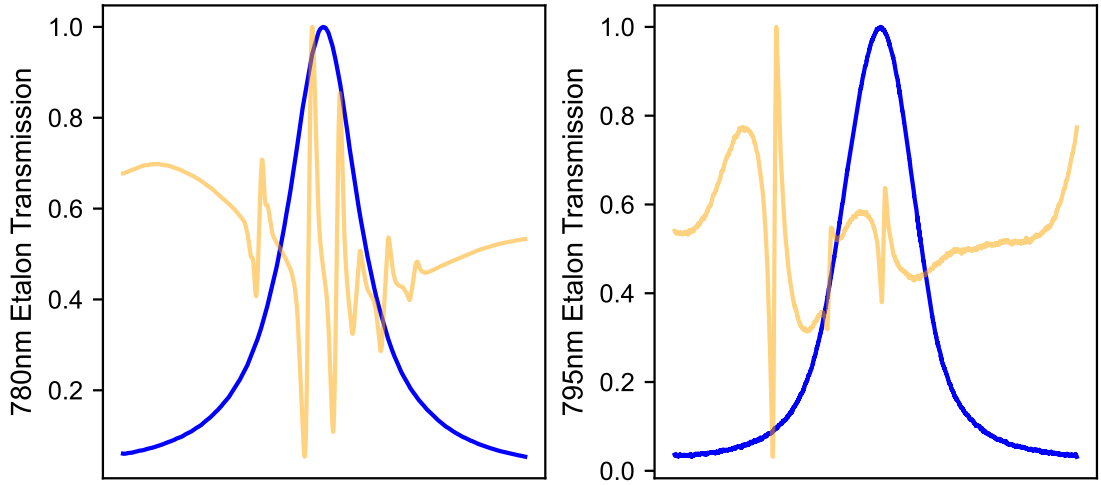

Figure 3.8: Transmission profiles of the 780 nm and 785 nm etalons, with the frequency axis calibrated via atomic spectroscopy.

Filter	Cavity T (%)	Fiber coupling efficiency (%)	Total T (%)
780 nm	85	67	57
795 nm	80	65 $\sim$ 80	52 $\sim$ 64
776 nm	60	50	30

Table 3.2: Characterization of maximal transmission and coupling efficiencies of etalon setups. The transmission of 795 nm is taken as (61 ± 5) % in the following analysis based on in-situ characterization performed before the experiment.

vacuum chamber of 94 %, spatial coupling between mutually coupled collimators 70 %, etalon transmission measured to be (57 ± 2) % for Stokes channel and (61 ± 5) % for anti-Stokes channel, and fiber transmission which accounts for approximately 1.2 dB insertion loss due to fiber mating sleeves. The insertion loss from fiber mating sleeves is evaluated based on a measured transmission of approximately 75 % per sleeve, with two sleeves used per channel. The larger uncertainty in the anti-Stokes efficiency arises from the instability of the plano-plano etalon. Combining these factors, the overall transmission efficiencies are estimated to be (21 ± 2) % for the Stokes photons and (23 ± 5) % for the anti-Stokes photons at the output of the optical system before detection. After spectral filtering, photons are recoupled into single-mode fibers and detected by the Excelitas single-photon detectors with an expected

Application	Serial	Connection	η (%)	Dark count (cps)
780 nm (pair)	SPCM-AQRH-54	free-space	65	$\sim$ 100 (nominal)
795 nm (pair)	SPCM-AQR-15	free-space	65	$\sim$ 50 (nominal)
double-HBT	SPCM-800-10-FC	fiber	70	$\sim$ 1500
double-HBT	SPCM-800-10-FC	fiber	70	$\sim$ 1500

Table 3.3: Datasheet of single-photon detectors.

detection efficiency of about 60 %. This figure also accounts for certain coupling losses caused by the free-space coupling to these detectors. Consequently, including the detector efficiency, the total system detection efficiencies are approximately (12.6 ± 1.0) % for the Stokes channel and (13.8 ± 3.0) % for the anti-Stokes channel. These overall efficiencies will be used to infer the photon pair generation rate.

Chapter 4

Time-correlated photon pairs

In this chapter, I first present the theoretical framework of spontaneous four-wave mixing (SFWM) based on the double-Λ energy-level structure in a cold atomic ensemble. I subsequently analyze the temporal cross-correlations between two coupled optical fields. Finally, I provide a detailed characterization of the resulting narrowband photon-pair source, including its spectral features, correlation properties, and its generation efficiency under different pump conditions.

4.1 Theory

The double-Λ SFWM process is implemented based on the D1 and D2 lines of ^{87}Rb atoms, where the pump and generated fields are spectrally separated by the ground-state hyperfine splitting. Following the cooling stage and state transfer stage, the majority of atoms in a MOT are initially prepared in the ground state $|5S_{1/2}, F = 1\rangle$. After the atom cloud is released from the MOT, continuous-wave pump fields drive the atomic ensemble during the SFWM interaction window, before the cold atoms leave the interaction region. During this stage, two pump fields counter-propagate through the atomic cloud, enabling efficient nonlinear interaction and photon-pair generation. One of the pump fields, referred to as the "pumping" field (ω_p), is detuned by Δ_p from the $|5S_{1/2}, F = 1\rangle \rightarrow |5P_{3/2}, F = 2\rangle$ transition on the D2 line, while the other, termed the "coupling" field (ω_c), is resonant with the $|5S_{1/2}, F = 2\rangle \rightarrow |5P_{1/2}, F = 2\rangle$ transition on the D1 line.

Under these two near-resonant optical drives, the system forms a double-Λ configuration involving spontaneous transitions along two decay paths: the Stokes mode (ω_s), corresponding to $|5P_{3/2}, F = 2\rangle \rightarrow |5S_{1/2}, F = 2\rangle$, and the anti-Stokes mode (ω_{as}), corresponding to $|5P_{1/2}, F = 2\rangle \rightarrow |5S_{1/2}, F = 1\rangle$. These two optical

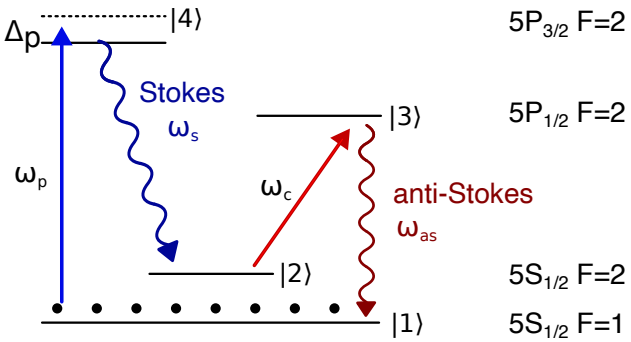

Figure 4.1: Energy levels and closed transitions involved in the double-Λ SFWM process.

modes are coupled via the nonlinear four-wave mixing interaction, leading to the spontaneous generation of time-correlated photon pairs from vacuum fluctuations. This process arises from the third-order nonlinear susceptibility $\chi^{(3)}$ of the atomic medium.

In atomic systems, operating under resonant or near-resonant conditions significantly enhances the nonlinear susceptibility, enabling efficient frequency conversion [65, 200]. Notably, the double-Λ configuration has been shown to exhibit superior nonlinear optical properties [66, 68, 201, 202]. The two coupled fields undergo exponential amplification with a gain coefficient proportional to the third-order susceptibility, surpassing the effects of linear absorption. This enhancement originates from atomic interference effects, which suppress absorption while boosting near-resonant nonlinear response, enabling efficient parametric gain [68]. Under strong nonlinear amplification, if the generated photons provide feedback that stimulates the nonlinear process, the atomic system can even undergo mirrorless optical parametric oscillation [116].

4.1.1 Hamiltonian

In the rotating frame, the interaction Hamiltonian of a single atom coupled with two electromagnetic fields, pumping ω_p and coupling fields ω_c, under rotating wave

approximation, is given by

$$\begin{aligned}\hat{H} = -\hbar\Big(&\Delta_p\hat{\sigma}_{44} + \delta_{as}\hat{\sigma}_{33} + (\delta_{as} - \Delta_c)\hat{\sigma}_{22} + \Omega_p\hat{\sigma}_{41} + \Omega_c\hat{\sigma}_{32} \\ &+ g_{42}\hat{a}_s\hat{\sigma}_{42} + g_{31}\hat{a}_{as}\hat{\sigma}_{31}\Big) + \text{H.c.}\,,\end{aligned} \tag{4.1}$$

where Δ_p is the detuning of the pumping field from the $|1\rangle \leftrightarrow |4\rangle$ transition (notation defined in Figure 4.1), Δ_c is the detuning of the coupling field compared to $|2\rangle \leftrightarrow |3\rangle$ transition, and δ_{as} denotes the anti-Stokes detuning from the transition $|1\rangle \leftrightarrow |3\rangle$. The detuning δ_s represents the Stokes detuning from a center frequency $\omega_{s0} = \omega_{42} + \Delta_p$. Due to the energy conservation in the parametric process $\omega_{as} + \omega_s = \omega_p + \omega_c$, the Stokes photon detuning is givne by $\delta_s = -(\delta_{as} - \Delta_c)$, and Stokes and coupling fields are linked via a virtual level detuned from $|2\rangle$ by $\delta_{as} - \Delta_c$ (see the $\hat{\sigma}_{22}$ term in Equation 4.1). In practice, that coupling field is resonant to the transition frequency as $\Delta_c = 0$, $\delta_s = \delta_{as}$. For the classical driving terms, the Rabi frequencies of the pump and coupling fields are given by $\Omega_p = d_{14}\mathcal{E}_p/\hbar$ and $\Omega_c = d_{23}\mathcal{E}_c/\hbar$, respectively, where d_{jk} represents the transition dipole moment between state $|j\rangle$ and $|k\rangle$, and the complex electric field amplitudes $\mathcal{E}_{p/c}$ are defined as $\mathcal{E}_{p/c} = 2E_{p/c}$. In the interaction terms, $g_{jk} = d_{jk}\sqrt{\omega_{s,as}/2\hbar\varepsilon_0 V}$ is the single-photon coupling strength between the Stokes (anti-Stokes) field and the corresponding atomic transition, with ε_0 being the vacuum permittivity and V being the interaction volume.

The above Hamiltonian describes the microscopic dynamics of the nonlinear interaction at the single-atom level. To capture the photon states from an ensemble of atoms, we now introduce an effective Hamiltonian that characterizes the nonlinear process between the pump fields and the generated fields, mediated by the atomic nonlinear susceptibility. We consider an elongated atomic cloud with its longest dimension of length L along the z-axis (x-axis in MOT geometry axis definition). In counter-propagating configuration, the relatively strong pumping and coupling fields are treated as classical fields with opposite wavevectors k_p and $-k_c$, propagating in opposite directions along the z-axis; their positive frequency components are given by

$$\begin{aligned}E_p^{(+)}(z,t) &= E_p e^{i[k_p z - \omega_p t]}\,, \\ E_c^{(+)}(z,t) &= E_c e^{i[-k_c z - \omega_c t]}\,.\end{aligned} \tag{4.2}$$

On the other hand, the generated Stokes and anti-Stokes modes are quantized and denoted by their positive-frequency components as

$$\begin{aligned}\hat{E}_s^{(+)}(z,t) &= \frac{1}{\sqrt{2\pi}}\int d\omega_s \sqrt{\frac{\hbar\omega_s}{2\varepsilon_0 cA}}\,\hat{a}_s(\omega_s)e^{i(k_s z-\omega_s t)}\,,\\ \hat{E}_{as}^{(+)}(z,t) &= \frac{1}{\sqrt{2\pi}}\int d\omega_{as} \sqrt{\frac{\hbar\omega_{as}}{2\varepsilon_0 cA}}\,\hat{a}_{as}(\omega_{as})e^{i(-k_{as} z-\omega_{as} t)}\,,\end{aligned} \tag{4.3}$$

where A denotes the single-mode cross-section area, ε_0 is the vacuum permittivity and c is the speed of light in the vacuum. The operators $\hat{a}_s(\omega_s)$ and $\hat{a}_{as}(\omega_{as})$ represent the photonic annihilation operators for the Stokes and anti-Stokes modes, respectively, and obey standard bosonic commutation relations. Macroscopically, in the interaction picture, the effective Hamiltonian describing such a nonlinear interaction takes the form of

$$\hat{H}_I(t) = \frac{\epsilon_0 A}{4}\int_0^L dz\chi^{(3)}E_p^{(+)}E_c^{(+)}\hat{E}_{as}^{(-)}\hat{E}_s^{(-)} + \text{H.c.}\,, \tag{4.4}$$

where $\chi^{(3)}$ represents the third-order nonlinear susceptibility to Stokes (or anti-Stokes). In the frequency domain, the interaction Hamiltonian is given by

$$\hat{H}_I = \frac{i\hbar L}{2\pi}\int d\omega_{as}d\omega_s\Psi(\omega_{as},\omega_s)\hat{a}_{as}^{\dagger}(\omega_{as})\hat{a}_s^{\dagger}(\omega_s)e^{-i(\omega_p+\omega_c+\omega_s-\omega_{as})t} + \text{H.c.} \tag{4.5}$$

Here, $\Psi(\omega_{as},\omega_s) = \kappa(\omega_{as},\omega_s) * \Phi(\Delta\vec{k})$ denotes the two-photon wavefunction, comprising the nonlinear parametric coupling coefficient $\kappa(\omega_{as},\omega_s)$ and the phase matching term $\Phi(\omega_{as})$. The nonlinear parametric coupling characterizes the strength of the interaction mediated by the third-order susceptibility as

$$\kappa(\omega_{as},\omega_s) = \frac{-i\sqrt{\omega_{as}\omega_s}}{2c}\chi^{(3)}(\omega_{as},\omega_s)\,. \tag{4.6}$$

As described in § 1.1, the two-photon state includes a longitudinal phase-matching function given by

$$\Phi(\Delta\vec{k}) = \text{sinc}\left(\frac{\Delta\vec{k}L}{2}\right)e^{i(\vec{k}_{as}+\vec{k}_s)L/2} \tag{4.7}$$

where $\Delta\vec{k}$ refers to the phase mismatching. In this case, since the pump and phase-matched fields are all near-axis, we approximate the phase mismatch as $\Delta k = (\vec{k}p + \vec{k}c - \vec{k}s - \vec{k}as)\cdot\hat{z} \approx k_p - k_c - k_s + k_{as}$.

4.1.2 Biphoton state

The evaluation of this interaction Hamiltonian $\hat{H}_I$ leads to the generation of a two-photon state in the Stokes and anti-Stokes modes, evolving from an initial vacuum state $|\psi(t_0)\rangle = |0\rangle$, as

$$|\psi(t)\rangle = \mathcal{T} \exp\left(-\frac{i}{\hbar}\int_{t_0}^{t} \hat{H}_I(t')dt'\right)|0\rangle\,, \tag{4.8}$$

where $\mathcal{T}$ represents the normalization and $|\psi(t_0)\rangle$ refers to the initial state. In the first-order perturbation expansion, the steady state is expressed as

$$|\psi(t)\rangle = -\frac{i}{\hbar}\int_0^t dt\hat{H}_I|0\rangle \propto |0\rangle + a_{as}^{\dagger}a_s^{\dagger}|0\rangle\,. \tag{4.9}$$

As the vacuum state is not detectable, the target state is the two-photon component of the wavefunction [81], given by

$$|\Psi\rangle = L\int dw_{as}\kappa(\omega_{as},\omega_s)\Phi(\Delta\vec{k})a_{as}^{\dagger}(\omega_{as})a_s^{\dagger}(\omega_s)|0\rangle\,. \tag{4.10}$$

The energy conservation $\omega_c + \omega_p - \omega_{as} - \omega_s = 0$ constrains the spectral bandwidth of two-photon state, allowing the joint spectral amplitude to be described by a single parameter, either ω_{as} or ω_s. In the two-photon joint detection measurement, the rapidly oscillating phase factor $e^{i(\omega_c+\omega_p)t}$ ($e^{i(\omega_s+\omega_{as})t}$) in the longitudinal phase-matching function is not temporally resolved. Consequently, the relevant quantity is the two-photon wavefunction envelope $\psi(\tau = t_{as} - t_s)$ in time domain, which is given by the the Fourier transformation of the product of two spectral components: the nonlinear coupling coefficient $\kappa(\omega_{as})$ and the longitudinal detuning function $\Phi(\omega_{as})$ as

$$\psi(\tau) = \frac{L}{2\pi}\int \mathrm{d}\omega_{as}\kappa(\omega_{as})\Phi(\omega_{as})e^{-i\omega_{as}\tau}\,. \tag{4.11}$$

This two-photon wavefunction envelope is manifested in the unnormalized second-order Glauber correlation function [203] between the two conjugate modes, which characterizes the joint detection probability as

$$\begin{aligned} G^{(2)}(t_{as},t_s) &= \langle\Psi|\hat{a}_s^{\dagger}(t_s)\hat{a}_{as}^{\dagger}(t_{as})\hat{a}_{as}(t_{as})\hat{a}_s(t_s)|\Psi\rangle \\ &\approx |\psi(t_{as},t_s)|^2 + R_{as}R_s\,, \end{aligned} \tag{4.12}$$

where $R_{as}R_s$ accounts for the uncorrelated coincidence background arising from two detection channels. The total photon-pair emission rate, obtained by integrating

the correlated part of the two-photon joint probability over the relative delay time is given by

$$R = \int d\tau |\psi(\tau)|^2 \,. \tag{4.13}$$

Accordingly, in the coincidence count measurement where a Stokes photon is detected at time t_s and anti-Stokes at time t_{as}, the detected photon pair rate R is evaluated through the coincidence histogram over a total measurement time T_m as

$$R \approx \frac{1}{T_m} \sum_n (N^{(2)}(nt_b) - N_{bg}^{(2)}) \,, \tag{4.14}$$

where $N^{(2)}(\tau)$ represents the discrete coincidence count histogram as a function of time delay τ, $N_{bg}^{(2)}$ denotes the accidental coincidence counts per bin, and t_b is the time bin width. This background level can be estimated either by $R_s R_{as} t_b T_m$ or by averaging the coincidence counts at a large time delay, where no photon correlation is expected. This photon pair rate can act as a figure of merit for characterizing the brightness of photon-pair sources. In contrast, the photon coincidence rate $R_{cc}(\tau)$ [81] describes the instantaneous pair detection rate per time bin and is given by

$$R_{cc} \approx G^{(2)}(\tau) t_b \,. \tag{4.15}$$

This quantity primarily reflects the temporal structure of the photon correlations and is commonly used to visualize the two-photon wavepacket.

4.1.3 Nonlinear susceptibility

As shown in Equation 4.11, the two-photon wave function is partially determined by the third-order nonlinear susceptibility $\chi^{(3)}$. This quantity characterizes the macroscopic strength of the parametric four-wave mixing process in the atomic medium, while also being fundamentally governed by the microscopic atomic coherence, including the excitation and decay dynamics of the atomic levels. These microscopic processes determine the natural spectral linewidth of the generated biphotons through the intrinsic linewidths of the atomic transitions. Based on the SFWM scheme illustrated in Figure 4.1, and under the assumption of a weak pump field and a sufficiently strong coupling field such that the atomic population remains primarily in the $F = 1$ ground state, the generation of correlated Stokes and anti-Stokes fields, as well as their temporal correlations, originates from the

third-order nonlinear susceptibility $\chi^{(3)}$. This susceptibility gives rise to higher-order polarization terms that drive the emission in both the Stokes and anti-Stokes modes, which are given by

$$\begin{aligned} \mathcal{P}_s &= \varepsilon_0 \chi_s^{(1)} \mathcal{E}_s + \varepsilon_0 \chi_s^{(3)} \mathcal{E}_{as}^* \mathcal{E}_p \mathcal{E}_c \exp(i\delta\vec{k}\vec{r}) \,, \\ \mathcal{P}_{as} &= \varepsilon_0 \chi_{as}^{(1)} \mathcal{E}_{as} + \varepsilon_0 \chi_{as}^{(3)} \mathcal{E}_s^* \mathcal{E}_p \mathcal{E}_c \exp(i\delta\vec{k}\vec{r}) \,, \end{aligned} \tag{4.16}$$

where $\mathcal{E}_s^*$ and $\mathcal{E}_{as}^*$ denote the complex conjugates of the Stokes and anti-Stokes field amplitudes, respectively, while $\mathcal{E}_p$ and $\mathcal{E}_c$ represent the complex amplitudes of the pump and coupling fields. As derived in § C.2, the third-order nonlinear susceptibility associated with the anti-Stokes field [81, 88, 93, 202, 204] is given by

$$\begin{aligned} \chi_{as}^{(3)}(\delta_{as}) &= \frac{N\mu_{13}\mu_{32}\mu_{24}\mu_{41}}{\varepsilon_0\hbar^3} \frac{1}{(\Delta_p + i\gamma_{14})} \frac{1}{|\Omega_c|^2 - (\delta_{as} + i\gamma_{12})(\delta_{as} + i\gamma_{13})} \\ &= \frac{N\mu_{13}\mu_{32}\mu_{24}\mu_{41}}{\varepsilon_0\hbar^3} \frac{1}{(\Delta_p + i\gamma_{14})} \frac{1}{(\delta_{as} - \frac{\Omega_e}{2} + i\gamma_e)(\delta_{as} + \frac{\Omega_e}{2} + i\gamma_e)} \,. \end{aligned} \tag{4.17}$$

Here, μ_{ij} demotes the electrical dipole matrix elements $\langle i|\hat{\mathbf{d}}|j\rangle$ between states i and j. The nonlinear spectrum is centered at the resonance $\omega_{0as} = \omega_{31}$ ($\Delta_c = 0$) with the detuning $\delta_{as} = \omega_{as} - \omega_{0as}$. The effective coupling Rabi frequency is given by $\Omega_e = \sqrt{|\Omega_c|^2 - (\gamma_{13} - \gamma_{12})^2}$ where $\gamma_e = (\gamma_{13} + \gamma_{12})/2$ is the effective dephasing rate and γ_{13} and γ_{12} are the decay rates between $|3\rangle \to |1\rangle$ and $|2\rangle \to |1\rangle$ transitions. This third-order nonlinear susceptibility $\chi_{as}^{(3)}(\delta_{as})$ exhibits two key spectral features. Apart from the overall prefactor, the term $1/(\Delta_p + i\gamma_{14})$ corresponds to a far-detuned response near the excited state $|4\rangle$. The remaining structure arises from Autler–Townes splitting (ATS) [205] induced by the coupling field. This splitting results in a spectral doublet separated by Ω_e with a linewidth of $2\gamma_e$ caused by the dressing of atomic levels with a strong coupling field. In the presence of the ATS, two SFWM pathways contribute to biphoton generation. One channel produces anti-Stokes photons at $\omega_{0as} + \Omega_e/2$, which, by energy conservation, pairs with Stokes photons at $\omega_{42} + \Delta_p - \Omega_e/2$. The other channel generates anti-Stokes photons at $\omega_{0as} - \Omega_e/2$, associated with Stokes photons at $\omega_{42} + \Delta_p + \Omega_e/2$. These two SFWM channels interfere, leading to oscillating behavior in the two-photon wave function. Since the third-order polarizations in the Stokes and anti-Stokes modes are coupled through a parametric nonlinear process, their third-order susceptibilities exhibit similar spectral splitting structures, as shown in Equation C.37.

4.1.4 Linear susceptibility

The linear susceptibilities of the anti-Stokes and Stokes fields determine their respective refractive indices during propagation, thereby governing the dispersion and absorption (or gain) experienced by each field in the medium. In the SFWM, both generated fields are sufficiently weak to satisfy the weak probe approximation, allowing their propagation to be described by linear response theory [98].

For the anti-Stokes field, which interacts with a coupling field in a three-level Λ-type atomic configuration, the linear susceptibility exhibits features such as electromagnetically induced transparency (EIT) [99] and ATS, depending on the strength of the coupling field and the optical depth of the atomic ensemble. These effects appear in the transmission spectrum as a narrow transparency window in the EIT regime, or as an absorption doublet in the ATS regime.

4.1.4.1 Anti-Stokes field

In a three-level Λ-type system, the linear susceptibility for anti-Stokes field arises from the coherence between states $|3\rangle$ and $|1\rangle$, characterized by the density matrix $\hat{\rho}_{31}$ as

$$\hat{\rho}_{31} \approx \frac{-\Omega_{as} \cdot (\delta_{as} + i\gamma_{12})}{|\Omega_c|^2 - (\delta_{as} + i\gamma_{13})(\Delta_c + \delta_{as} + i\gamma_{12})}\,, \tag{4.18}$$

where Ω_{as} and Ω_c refer to the Rabi frequency of the weak anti-Stokes field and coupling field, respectively. The anti-Stokes detuning is defined as $\delta_{as} = \omega_{as} - \omega_{0as}$, where ω_{0as} is the center frequency of the anti-Stokes transition. The linear polarization is given by $P_{as} = N\mu_{13}\hat{\rho}_{31} = \varepsilon_0\chi_{as}\mathcal{E}_{as}$ yielding a linear susceptibility (see Equation C.36) as

$$\chi^{(1)}_{as}(\delta_{as}) = \frac{N|\mu_{13}|^2}{\varepsilon_0\hbar} \cdot \frac{(\delta_{as} + i\gamma_{12})}{|\Omega_c|^2 - (\delta_{as} + i\gamma_{13})(\Delta_c + \delta_{as} + i\gamma_{12})}\,. \tag{4.19}$$

This susceptibility exhibits a distinct behavior depending on the strength of the coupling field. In the strong coupling regime ($|\Omega_c| \gg \gamma_{13}, \gamma_{12}$), the excited state splits into two dressed states. In the weak coupling, destructive quantum interference between the coupling and anti-Stokes channels induces EIT, resulting in a spectral transparency window for anti-Stokes fields [99]. Near this transparency window, the refractive index changes rapidly with frequency (i.e., large dispersion), leading to a steep slope of the real part of susceptibility. The imaginary part of the linear

susceptibility represents the absorption in the atomic medium. The corresponding transmission spectrum of the anti-Stokes field through a medium of length L is given by

$$T(\delta_{as}) = \exp(-\alpha L) = \exp\Big(- k \cdot \mathrm{Im}[\chi(\delta_{as})] L \Big) \,, \tag{4.20}$$

where $k = \omega_{as}/c$ is the wavevector. For comparison, the imaginary part of the susceptibility for a two-level system without the coupling field is

$$\mathrm{Im}[\chi_0(\delta_{as})] = \frac{N|\mu_{13}|^2}{\varepsilon_0 \hbar} \cdot \frac{\gamma_{13}}{\delta_{as}^2 + \gamma_{13}^2} \,, \tag{4.21}$$

yielding an absorption profile characterized by the on-resonance optical depth OD as

$$\begin{aligned} \mathrm{OD} &= k \cdot \mathrm{Im}[\chi_0(0)] \cdot L \,, \\ \ln T(\delta_{as}) &= -\mathrm{OD} \frac{\gamma_{13}^2}{\delta_{as}^2 + \gamma_{13}^2} \,. \end{aligned} \tag{4.22}$$

Correspondingly, in the three-level system with the presence of the coupling field, the transmission spectrum of a weak probe on the anti-Stokes mode becomes

$$\begin{aligned} \ln T(\delta_{as}) &= -\mathrm{OD} \cdot \frac{\mathrm{Im}[\chi(\delta_{as})]}{\mathrm{Im}[\chi_0(0)]} \\ &= -\mathrm{OD} \cdot \gamma_{13} \cdot \mathrm{Im}\left[\frac{(\delta_{as} + i\gamma_{12})}{|\Omega_c|^2 - (\delta_{as} + i\gamma_{13})(\Delta_c + \delta_{as} + i\gamma_{12})} \right] . \end{aligned} \tag{4.23}$$

In the weak coupling field limit, $|\Omega_c|^2 \ll \gamma_{13}^2$, the transmission exhibits a narrow transparency window in the absorption profile [206] as

$$\ln T(\delta_{as}) \approx -\mathrm{OD} \cdot \frac{\delta_{as}^2 + \gamma_{12}\gamma_{\mathrm{EIT}}}{\delta_{as}^2 + \gamma_{\mathrm{EIT}}^2} \,, \tag{4.24}$$

with the EIT linewidth given by $\gamma_{\mathrm{EIT}} = \gamma_{12} + |\Omega_c|^2/\gamma_{13}$. In a dense medium, the transmission at zero detuning is approximated as

$$T(0) \approx \exp\left(-\mathrm{OD} \cdot \frac{\gamma_{13}\gamma_{12}}{|\Omega_c|^2 + \gamma_{13}\gamma_{12}} \right) , \tag{4.25}$$

which indicates that the transparency depth is determined by both the optical depth and the Rabi frequency of the coupling field in the weak coupling regime. At a fixed optical depth, the transparency depth grows with increasing Rabi frequency of coupling fields. However, as Ω_c increases further, ATS begins to dominate the spectral response, and the approximation in the weak coupling limit no longer

holds. In this context of the double-Λ SFWM, the biphoton generation benefits from the EIT effect, which facilitates resonant anti-Stokes photon propagation through the medium by suppressing absorption [79]. Photon-pair generation in SFWM can be viewed as a competition between the nonlinear process governed by third-order nonlinear susceptibility $\chi^{(3)}$ and the propagation loss determined by the linear susceptibility $\chi^{(1)}$. As the coupling field intensity increases, the system typically transitions from EIT to the ATS regime. In the ATS regime, the nonlinear susceptibility $\chi^{(3)}$ exhibits a spectral gain doublet, while the linear susceptibility simultaneously shows an absorption doublet at the corresponding dressed states, with a reduction of absorption between them. The generated anti-Stokes photons are not exactly situated at the center of the transparency window. The escape of correlated photon pairs from the atomic cloud results from the competition between the nonlinear generation spectrum and the atomic absorption profile. In addition to background photons arising from incoherent scattering in each mode, this competition fundamentally limits the purity and heralding efficiency of the generated photon pairs.

In addition to the absorption influenced by the imaginary part of the anti-Stokes susceptibility, the dispersion relation of the medium is determined by the real part, which further affects the group velocity. The group velocity v_g of the anti-Stokes field is defined as

$$v_g = \frac{d\omega}{dk} = \left(\frac{d}{d\omega}\left[\frac{n(\omega)\omega}{c}\right]\right)^{-1} = \frac{c}{n(\omega) + \omega\frac{dn}{d\omega}}\,. \tag{4.26}$$

where $n(\omega)$ is the refractive index as a function of anti-Stokes field frequency. Near the EIT resonance, the refractive index exhibits a steep frequency dependence due to the rapid variation in the real part of the linear susceptibility $d\mathrm{Re}[\chi^{(1)}(\delta_{as})]/d\omega$. As a result, the group velocity of the anti-Stokes field is given by

$$v_g \approx \frac{c}{1 + \frac{1}{2}\mathrm{Re}[\chi^{(1)}(\delta_{as})] + \frac{\omega_{as}}{2}\frac{d\mathrm{Re}[\chi^{(1)}(\delta_{as})]}{d\omega_{as}}}\,, \tag{4.27}$$

which can be further approximated as

$$v_g \approx \frac{2c\gamma_{\mathrm{EIT}}}{\omega\chi_0} = \frac{2|\Omega_c^2|L}{\gamma_{13}\mathrm{OD}}\,, \tag{4.28}$$

where $\chi_0 = N|\mu_{13}|^2/(\varepsilon_0\hbar\gamma_{13}) = \mathrm{OD}/(kL)$ is the resonant susceptibility in the absence of the coupling field. Neglecting the imaginary part of the wavevector, the

longitudinal detuning function in the two-photon wave function in Equation 4.11 can be written as

$$\Phi(\omega_{as}) \approx \text{sinc}\left(\frac{\omega_{as}L}{2v_g}\right)\exp\left(i\frac{\omega_{as}L}{2v_g}\right). \tag{4.29}$$

Depending on which component dominates in Equation 4.11, the biphoton characteristics in double-Λ SFWM are classified into two regimes. One regime is governed by the intrinsic nonlinear susceptibility of the medium, while the other is dominated by the group delay imposed through the phase-matching condition associated with slow light propagation.

4.1.4.2 Stokes field

The Stokes field arises from the $|4\rangle \rightarrow |2\rangle$ transition, and its linear polarization is described by $\hat{P}s = N\mu_{24}\hat{\rho}_{42}$. Consequently, the linear susceptibility associated with the Stokes field can be expressed as (see Equation C.34 and Equation C.36)

$$\chi_s^{(1)}(\delta_s) = \frac{N|\mu_{24}|^2(\delta_s - i\gamma_{13})/(\varepsilon_0\hbar)}{|\Omega_c|^2 - (\delta_s - i\gamma_{13})(\delta_s - i\gamma_{12})} \cdot \frac{|\Omega_p|^2}{(\Delta_p + i\gamma_{14})(\Delta_p - i\gamma_{24})}, \tag{4.30}$$

where Ω_p and Ω_c are the Rabi frequencies of pumping and coupling fields, respectively; γ_{jk} is the transition rate from state $|k\rangle$ to $|j\rangle$. The first term reflects the influence of the coupling fields, arising from the fact that the Stokes and anti-Stokes fields are coupled and therefore share detuning constraints due to energy conservation. The second term accounts for the off-resonant excitation of state $|4\rangle$ by the far-detuned pump field. This real part of $\text{Im}[\chi_s(\delta_s)] < 0$ represents the Raman gain for the Stokes field [93], as a portion of the pump photons are converted into Stokes photons. Within the framework of linearization of atomic coherence (see § C.2), no coherence terms exist in the absence of both the pump fields and the generated quantized fields. This linear susceptibility, associated with the atomic coherence $\hat{\rho}_{42}$, thus characterizes the initial establishment of atomic coherence in the SFWM process. Subsequent coherences are built upon this initial coherence, which is driven by the interaction between the pump field and the generated Stokes field.

In practice, the pump fields are typically operated with a large single-photon detuning $\Delta_p \gg |\Omega_p|$, which significantly suppresses the population in the excited state $|4\rangle$ and thereby minimizes spontaneous emission. As a result, the absorption experienced by the Stokes photons propagating through the atomic cloud becomes

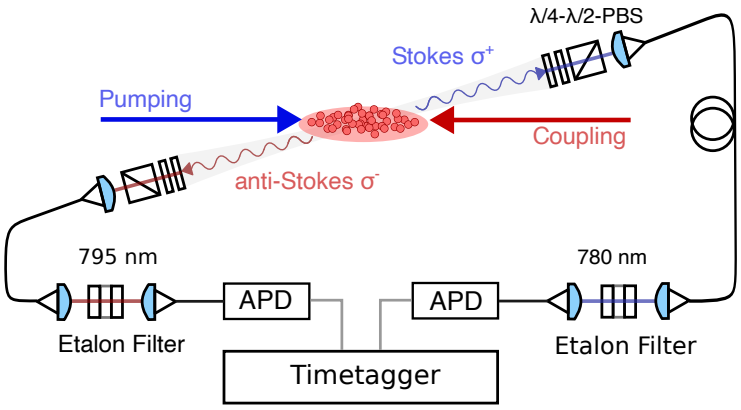

Figure 4.2: Schematic representation of the experimental setup. The pumping beam and coupling beam counter-propagate along the longest axis of a cigar-shaped atomic ensemble, with a collection path angled by approximately 1°.

negligible compared to the Raman gain. In this regime, the Stokes photons experience negligible absorption and dispersion as they propagate through the medium.

4.2 Experimental setup

The experimental protocol involves double-Λ atomic energy levels driven by the "pumping" field and the "coupling" field, with frequencies denoted as ω_p and ω_c, respectively. As illustrated in Figure 4.1, the pumping laser is detuned by Δ_p from the $|5S_{1/2}, F = 1\rangle \leftrightarrow |5P_{3/2}, F = 2\rangle$ transition and the coupling laser is initially resonant to the $|5S_{1/2}, F = 2\rangle \leftrightarrow |5P_{1/2}, F = 2\rangle$ transition. The polarizations of the pump fields are adjusted by optimizing the pair rate under a fixed polarization filter configuration. The experimental setup, depicted in Figure 4.2, employs a backward-propagation configuration where the coupling beam and pumping beam, each with a waist of roughly 830 μm (Gaussian beam from A375TMB collimators), counter-propagate collinearly. This configuration minimizes residual Doppler effects and facilitates spatial discrimination of the generated photons from the pump fields. These two pump fields align with the elongated axis of the ^{87}Rb atomic ensemble, characterized in § 2.6. The control sequence follows the implementation in § 3.2.2, which prepares the majority of atoms in the $|5\mathrm{S}_{1/2}, F = 1\rangle$ ground state during the measurement stage.

4.2.1 Collection mode

The collection path diverges from the pumping and coupling beam by a small angle of roughly 1° and uses a focused Gaussian mode with an estimated waist of around 175 μm, which spatially overlaps with the pump region in the atomic ensemble. In our setup, scattered photons from surfaces of the vacuum chamber and pump-beam optics introduce significant laser leakage into the collection mode. A smaller deviation angle leads to increased collection of these laser leakage photons. To mitigate this, the deviation angle is carefully optimized to maximize the pair detections. This optimization represents a trade-off between reducing laser leakage and making the collection closer to the parallel axis of the pump beams. Considering the diffraction effects arising from the coupling between the optical field mode and the elongated atomic ensemble [207], the directional emission is characterized by the Fresnel number:

$$F = \frac{\pi w^2}{L\lambda}\,, \tag{4.31}$$

where w is the pump beam waist, $L \approx 5\,\mathrm{mm}$ is the length of atomic cloud, and λ is the wavelength. Here $\lambda = 780\,\mathrm{nm}$ is used for simplicity. If $F < 1$, the emission supports sustaining a single mode, but it strongly diverges in the transverse direction due to diffraction. In contrast, for a large Fresnel number ($F \gg 1$), several diffraction-limited modes can be supported within a geometrical angle $\theta_G = w/L$, and each mode propagating close to the cylinder axis occurs in a small diffraction angle of $\theta_D = \lambda/w$. In our setup, we estimate a Fresnel number of $F \approx 550$, allowing off-axis modes within a geometrical angle of $\theta_G \approx 0.166\,\mathrm{rad}$ (9.5°) and a diffraction angle of $\theta_D \approx 0.9\,\mathrm{mrad}$. The collection mode, being a focused Gaussian beam, has a divergence angle

$$\theta \approx \frac{\lambda}{\pi w_0} \approx 1.42\,\mathrm{mrad}\,, \tag{4.32}$$

which is close to the diffraction angle permitted by the atom cloud coupling geometry. This implies that the collection setup effectively captures emission from a near-axis spatial single-diffraction mode, which guarantees the spatial mode purity of the photon pair source. As shown in § E.1, the phase mismatch reaches a minimum when the Stokes photon emission angle is approximately 3.5° under a counter-propagating configuration, assuming a constant refractive index within the atomic cloud. This result, together with geometry diffraction calculations, highlights the feasibility of

collecting correlated photon pairs emitted in spatial modes deviating from the pump beam directions. The collection strategy relies on aligning the Gaussian collection mode with the single diffraction modes. Misalignment between them would lead to reduced collection efficiency.

The experimental configuration corresponds to the photon collection from an interaction volume of approximately $5 \times 10^{-4}\,\mathrm{cm}^3$ in the atomic cloud. With the theoretical cross-section being $\sigma_0 = 3\lambda^2/2\pi \approx 2.9 \times 10^{-13}\,\mathrm{m}^2$ and atomic cloud length $L \approx 5\,\mathrm{mm}$, the atom density is approximated to $2 \times 10^{10}\,\mathrm{atoms/cm}^3$ for an optical depth of 30, resulting in a total atom number around 10 million. The number of participating atoms imposes an upper limit on the photon pair generation rate that can be collected within the designated spatial mode. From the perspective of photon scattering, the single-atom scattering rate is given by

$$R_{\mathrm{sc}} = \frac{\Gamma}{2} \cdot \frac{s_0}{1 + s_0 + \left(\frac{2\Delta}{\Gamma}\right)^2}\,, \tag{4.33}$$

where Γ is the spontaneous emission rate, s_0 is the on-resonance saturation factor defined as $s_0 = I/I_s$, and Δ is the detuning of the light field from the atomic transition. For a typical laser intensity of 1 mW and detuning $\Delta = 2\pi \times 40\,\mathrm{MHz}$, the resulting photon scattering rate into the collection solid angle can be coarsely estimated to be on the order of 10^7 counts per second. This provides a rough estimate of the photon generation rate relevant to our collection geometry.

4.2.2 Polarization control

Before coupling into the single-mode fibers, photons are filtered through polarization filters composed of a quarter-wave plate (QWP), a half-wave plate (HWP), and a polarizing beam splitter (PBS). The Stokes polarization filter is set to transmit right circular polarization (σ^+) in the atomic frame, while the anti-Stokes filter is set to transmit left circular polarization (σ^-) in the same frame. The pump and coupling fields are initially prepared with horizontal linear polarization and converted to circular polarization using a quarter-wave plate (QWP). To maximize the photon pair rate, the QWP in the pump path is finely adjusted while keeping the filter polarization settings fixed. This approach minimizes disturbances to the collection mode alignment caused by mechanical vibrations during manual wave plate

adjustment. The polarization calibration and the optimization of the pump field polarization to maximize the photon pair generation rate are detailed in Appendix A. The maximum pair generation rate is achieved when the pump and coupling fields are roughly polarized opposite to the circular polarizations selected by their corresponding filters: the pump field is closer to σ^- when the Stokes filter selects σ^+, and the coupling field is closer to σ^+ when the anti-Stokes filter selects σ^-. This apparent mismatch between the pump field polarization and the detected photon polarization can be attributed to the Faraday effect in the cold atomic ensemble [208]. When near-resonant or resonant light propagates through a magnetized atomic medium, the Zeeman-split σ^+ and σ^- transitions exhibit different complex polarizabilities, resulting in unequal refractive indices and absorption. This birefringence leads to a rotation of the linear polarization plane, potentially converting an initially circularly polarized beam into elliptical polarization. In the experimental setup, after the polarization filters, the collected photons undergo spectral filtering via temperature-controlled fused-silica etalons, which are designed to suppress the laser leakage photons and any incoherent scattering photons from the atomic ensemble in other spectral modes. These etalons transmit photons centered at the target frequencies ω_s and ω_{as}. Their characterization is presented in § 3.3.2.

The dependence of pair rate on the polarization can be reflected through the EIT transmission of the anti-Stokes field in the presence of the coupling field. As shown in Figure 4.3, we measured the transmission of an anti-Stokes probe field injected along the collection path, while varying the polarization and intensity of the coupling field. The anti-Stokes probe is generated by phase modulating a small portion of the coupling beam by a phase modulator, with the modulation frequency swept around the ground-state hyperfine splitting ($\sim 6.8\,\mathrm{GHz}$). This ensures that the probe remains phase-coherent with the coupling field, and it corresponds to one sideband of the modulated coupling light. The modulated probe light propagates through the atomic cloud, after which the etalon filters placed in the collection path suppress unwanted spectral components, allowing selective measurement. In the weak coupling regime, the EIT transparency window does not display a high peak, which may suggest that there exists a large dephasing in our atomic cloud. In the strong coupling regime, both the width and depth of the transparency window increase with the coupling strength, associated with the emergence of

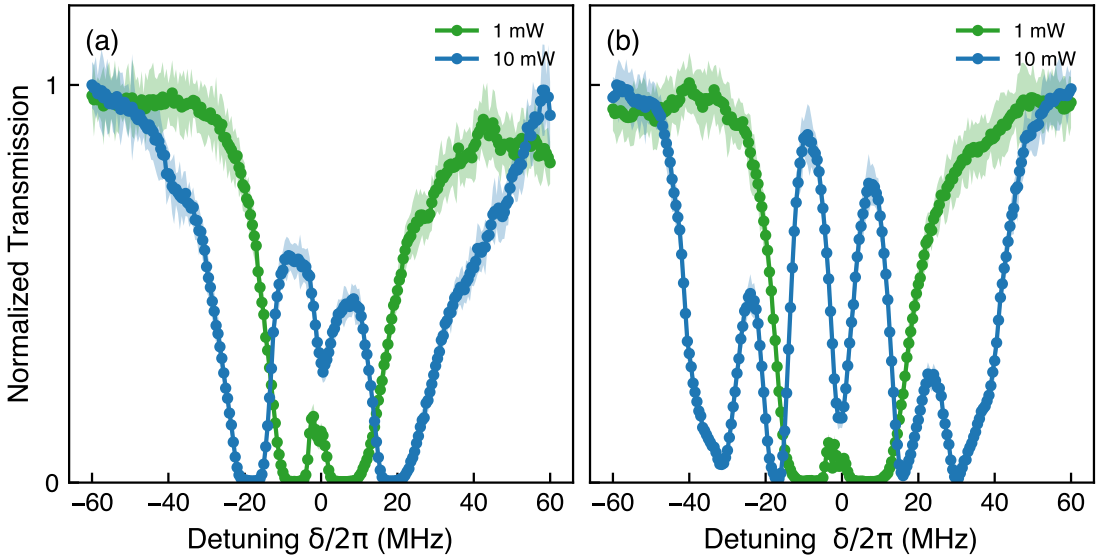

Figure 4.3: Transmission of anti-Stokes probe beam in presence of the coupling field: (a) The coupling field has the same σ^- polarization as the polarization filter. (b) The polarization of the coupling field is adjusted to reach the maximal pair rate. The labels denote the power of the coupling field employed.

the ATS splitting. At zero detuning, however, we observe enhanced absorption, especially under the configuration that yields the maximum pair generation rate (see Figure 4.3 (b)). This behavior may be attributed to electromagnetically induced absorption (EIA) [209], where quantum interference between excitation pathways becomes constructive—rather than destructive—as a result of the multi-Zeeman-level structure of the atomic system.

4.3 Pair characterization

In this section, I demonstrate the characteristics of the photon-pair source under specific experimental conditions. The pump and coupling field powers are set to $P_p \simeq 250\,\mu\text{W}$ and $P_c \simeq 7.7\,\text{mW}$, respectively. The pump field is detuned by $\Delta_p/2\pi = +40\,\text{MHz}$ from the $|5S_{1/2}, F = 1\rangle \rightarrow |5P_{3/2}, F = 1\rangle$ transition, while the coupling field is resonant ($\Delta_c/2\pi = 0$) with the $|5S_{1/2}, F = 2\rangle \rightarrow |5P_{3/2}, F = 2\rangle$ transition. The results presented under these conditions represent typical, though not optimized, performance of the correlated photon-pair source. Measurements

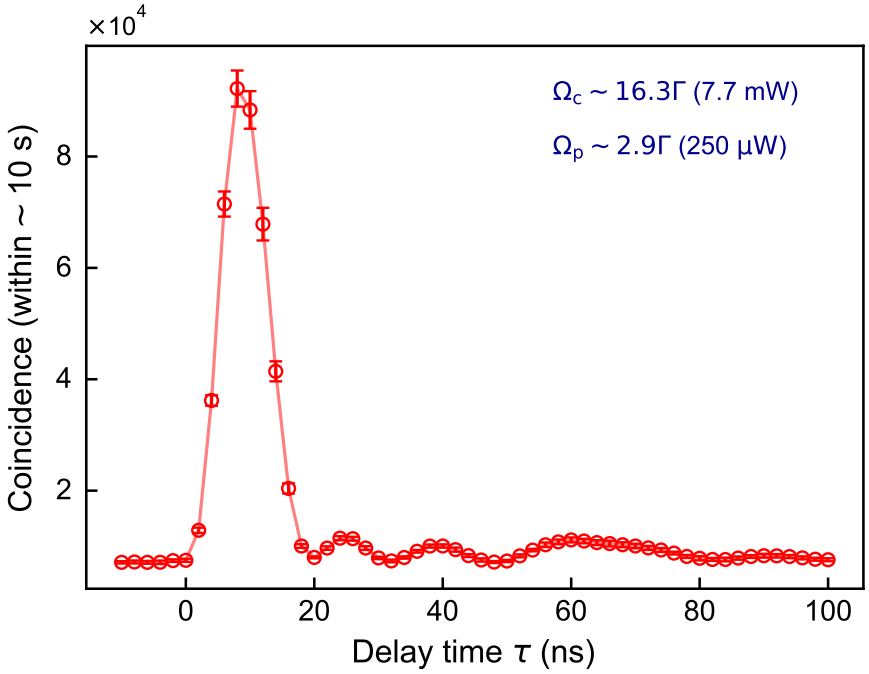

Figure 4.4: Coincidence histogram between the Stokes and anti-Stokes channels accumulated over approximately 10 s of valid measurement time. The error bar is evaluated via 6 repeated measurements.

corresponding to the maximum pair generation rate and highest correlation are discussed in detail in § 4.4.

4.3.1 Cross-correlation

As defined in Equation 4.12, the second-order cross-correlation function between Stokes and anti-Stokes photons is determined by the two-photon wave function $\Psi(\tau)$. It can be measured via coincidence detection between the conjugate modes. The corresponding normalized cross-correlation function is given by

$$g^{(2)}_{\text{as-s}}(\tau) = \frac{G^{(2)}_{\text{as-s}}(\tau)}{R_s R_{as}} \,. \tag{4.34}$$

This function signifies the strong temporal correlation between conjugate photons, where the detection of a Stokes photon precedes the detection of its paired anti-Stokes photon within the coherence time. In data processing, the two-photon coincidence counts $N^{(2)}_{\text{as-s}}(\tau)$ are obtained by using the detection events of Stokes photons as triggers. For each trigger, the arrival time of the corresponding anti-Stokes photon

is recorded relative to the trigger time and accumulated into a histogram over delay time bins. This coincidence histogram $N^{(2)}_{\text{as-s}}(\tau)$ is proportional to second-order cross-correlation function $G^{(2)}_{\text{as-s}}(\tau)$. The uncorrelated (accidental) coincidence count per bin is given as $R_s R_{as} t_b T_m$ where R_s and R_{as} are the single-count rates for the Stokes and anti-Stokes photons, respectively; t_b is the time-bin width, and T_m is the total measurement duration. The number of correlated photon pairs is evaluated as the excess counts above the flat accidental background, as described in Equation 4.14. Normalizing the coincidence histogram by the average accidental coincidence yields the second-order cross-correlation function $g^{(2)}_{\text{as-s}}(\tau)$.

The instantaneous single-count rates are measured to be $(5.60 \pm 0.02) \times 10^5$ cps for Stokes photon and $(6.63 \pm 0.24) \times 10^5$ cps for the anti-Stokes channels. Since we observed that the correlated photon pairs are concentrated within the first oscillation peak, as shown in Figure 4.4, we define a coincidence window of $t_c = 22\,\text{ns}$. The total pair rate within this window is measured to be $(4.42 \pm 0.16) \times 10^4$ cps.

As the heralding efficiency is defined as the probability that the heralded photon is detected given that a heralding photon has been detected, it can be expressed as the ratio between the coincidence count rate and the single-count rate:

$$\eta_{s(as)} = \frac{R_c}{R_{s(as)}}\,. \tag{4.35}$$

The heralding efficiencies for the Stokes and anti-Stokes channels are measured to be $(6.6 \pm 0.3)\%$ and $(5.6 \pm 0.1)\%$, respectively. The heralding efficiency is upper-bounded by the overall transmission and detection efficiency of heralded photons. In practice, this efficiency is further degraded by incoherent scattering and dark counts in single-photon detectors, which contribute to uncorrelated photon events and reduce the heralding efficiency.

4.3.2 Generation characterization

In a simple model that accounts for collection and detection losses while neglecting detector dead time, the overall detection efficiency $\eta_{s(as)}$ for the Stokes (anti-Stokes) channel is expressed as $\eta_{s(as)} = \eta_{\text{trans}}\eta_{\text{detect}}$, where η_{trans} includes losses from coupling, filtering, and optics, and η_{detect} is the detector's quantum efficiency. Let R_p denote the photon pair generation rate, and R_{is} (R_{ias}) the rate of incoherently scattered photons in the Stokes (anti-Stokes) channel. The dark count rates of the detectors

in these two channels are denoted by R_{ds} and R_{das}, respectively. The photon events induced by pump laser leakage are relatively constant under fixed pump field conditions and are largely insensitive to the collection and transmission efficiency, as they occur far detuned from the filter transmission peak. Therefore, we incorporate the contribution from pump leakage into the effective dark count rate, as it behaves as a quasi-constant background under steady pump power. This implies that the effective dark count rate here is higher than the nominal dark counts of single-photon detectors. In the following, a superscript "m" is used to denote the experimentally measured values of the corresponding rates. In this modeling, the measured single-count rates and pair rates are linked to the generation rates as

$$\begin{aligned} R_s^m &= \eta_s(R_p + R_{is}) + R_{ds}\,, \\ R_{as}^m &= \eta_{as}(R_p + R_{ias}) + R_{das}\,, \\ R_p^m &= \eta_s\eta_{as}R_p\,. \end{aligned} \tag{4.36}$$

The detected pair rate is not affected by the incoherently scattered photon events and dark count events, given that they are measured above the accidental coincidence background. Therefore, the pair generation rate is simply evaluated with the overall detection efficiencies listed in § 3.3.3 as

$$R_p = \frac{R_p^m}{\eta_s\eta_{as}} \approx (2.2 \pm 0.6) \times 10^6 \text{ cps}\,. \tag{4.37}$$

The measured dark count rates are 1.5×10^3 cps in the Stokes channel and 8×10^3 cps in the anti-Stokes channel under the given pump power and polarization setting, both approximately two orders of magnitude lower than the respective single-photon count rates. Consequently, the contributions from detector dark counts and residual laser leakage are negligible and excluded from the analysis for simplicity. Under this approximation, the pair ratio, defined as the ratio between the photon pair generation rate and the total single-photon generation rate, is given by

$$\begin{aligned} r_s &= \frac{R_p}{R_p + R_{is}} \approx (47 \pm 13)\ \%\,, \\ r_{as} &= \frac{R_p}{R_p + R_{ias}} \approx (46 \pm 17)\ \%\,. \end{aligned} \tag{4.38}$$

This pair ratio quantifies the fraction of photon pairs in the Stokes and anti-Stokes modes, reflecting the presence of incoherent components in the source. It should be

noted that this parameter depends on the evaluation of the optical transmissions. The overall detection efficiencies used here may be underestimated, and absorption or spatial losses within the atomic cloud are not accounted for in this preliminary analysis. Since the incoherent and coherent components share similar spectral properties, characterizing the incoherent contribution is challenging. In § 6.7.1, we show that, under specific assumptions, the overall efficiency can be evaluated by analyzing triple and quadruplet coincidence measurements.

4.3.3 Coincidence-to-accidental ratio

The coincidence-to-accidental ratio (CAR) quantifies the ratio of correlated photon pairs to uncorrelated (accidental) pairs within a specified coincidence window. A larger coincidence window inevitably lowers the CAR due to the increased contribution of accidental coincidences. In our analysis, we employ a coincidence window of 22 ns, yielding a CAR of

$$\mathrm{CAR} = \frac{R_p^m}{R_p^m + R_a^m} \approx 5.01 \pm 0.03\,. \tag{4.39}$$

The CAR depends on the single-photon count rates and increases as the pump power decreases, since lower power reduces accidental coincidences more significantly than true coincidences. As the CAR is partially reflected by the degree of violation of the Cauchy–Schwarz inequality: a stronger violation indicating a higher CAR, its detailed characterization under varying experimental conditions is omitted in the following.

4.3.4 Violation of Cauchy-Schwarz inequality

The non-classical nature of correlated photon pairs is evidenced by the violation of the Cauchy-Schwarz inequality [210]. Considering a two-mode photon state ρ_{ab}, it can be represented by a P-representation as

$$\rho_{ab} = \int d^2\alpha d^2\beta P(\alpha,\beta)|\alpha,\beta\rangle\langle\alpha,\beta|\,, \tag{4.40}$$

where $|\alpha\rangle$ and $|\beta\rangle$ are coherent states in two photonic modes associated with creation operators $a^\dagger$ and $b^\dagger$. If the quasi-probability $P(\alpha,\beta)$ is positive semi-definite, the two-mode state is considered to be classical. In such cases, the square of joint

detection probability in two modes is always less than or equal to the product of individual two-photon detection probabilities, and the correlation functions satisfy the following inequality

$$\langle a^\dagger b^\dagger b a\rangle^2 \leq \langle a^{\dagger 2} a^2\rangle \langle b^{\dagger 2} b^2\rangle \,. \tag{4.41}$$

This relation directly follows from the classical Cauchy–Schwarz inequality applied to a positive probability distribution. For correlated photon pairs in two modes, the violation of this inequality is quantified using the normalized second-order correlation functions

$$\frac{[g^{(2)}_{\text{as}-\text{s}}(\tau)]^2}{g^{(2)}_{\text{s}}(0) g^{(2)}_{\text{as}}(0)} \,, \tag{4.42}$$

where the numerator is the square of the cross-correlation function between Stokes and anti-Stokes modes, while the denominator is the product of their auto-correlation functions. In the worst case, the denominator reaches its maximum with $g^{(2)}_{\text{s}}(0) \approx g^{(2)}_{\text{as}}(0) \approx 2$, as shown in § 4.3.6. Under the above experimental condition, we observe a violation by a factor of 38.3 ± 0.3. A large violation factor typically indicates strong nonclassicality and is generally observed at low pair generation rates (see § 4.4) and low dark count. This observation is consistent with theoretical analyses, which show that the violation parameter is influenced by the mean photon number, the presence of incoherent background, and dark counts [211].

4.3.5 Modulation of two-photon wavefunction

Figure 4.5 displays that the two-photon wavefunction can be modulated by the intensity of the coupling field. As the pump field power decreases, the two-photon coherence time broadens, consistent with the increase in single-photon coherence discussed in § 4.4.2. Within an experimental range of $0.5 \sim 10\,\text{mW}$ for the coupling field, the two-photon wavefunction remains approximately consistent with the theoretical form derived from Autler–Townes splitting:

$$g^{(2)}_{\text{as-s}}(\tau) \sim 1 + A \exp(\Gamma\tau)(1 - \cos(\Omega_{\text{eff}}\tau))\Theta(\tau) \,, \tag{4.43}$$

where Γ denotes the decay rate of the exponential decay envelope, Ω_{eff} is the effective Rabi frequency associated with ATS splitting as described in § 4.1.3 and $\Theta(\tau)$ is Heaviside step function, reflecting the time ordering where the Stokes photon precedes the anti-Stokes photon. Further reduction of the coupling field power

leads to a degradation in the overall SFWM efficiency in our case. With a strong coupling field, the measured two-photon wavefunction exhibits a faster decay than the predicted exponential decay with a natural decay rate. This discrepancy is attributed to the collective emission effect, which is further investigated in Chapter 5. As the coupling field power decreases, the slow light effect becomes more pronounced, leading to a reduced group velocity of the anti-Stokes photon and hence a longer two-photon coherence time. In this regime, phase-matching terms increasingly dominate the shape of the two-photon wavefunction, resulting in a slower decay rate. During the alignment procedure, we find that at certain deviation angles between the collection mode and the pump field, correlated photon pairs with longer two-photon coherence times can be observed. However, under these conditions, both the pair detection rate and heralding efficiency are suboptimal. This suggests that the slow-light effect is highly sensitive to the angle between the collection and pump fields, or equivalently, the effective optical depth along the collection direction and the spatial overlap between the pump beams and the collection mode.

4.3.6 Auto-correlation

Light scattered by a macroscopic atomic cloud exhibits a finite coherence time, reflecting temporal fluctuations in its intensity. The loss of their coherence arises from two mechanisms [212] depending on the saturation of drive fields. In the weak drive regime, atoms scatter light elastically. The finite cloud temperature induces a broadening of the spectrum through the Doppler effect, resulting in a temperature-dependent coherence time $\tau_c^T \propto 1/\sqrt{T}$, often referred to as thermal coherence. At a temperature of 2 mK, the thermal time due to Doppler broadening is approximately $\tau_c^T \approx 245\,\mathrm{ns}$. In contrast, in the strong-drive regime, spontaneous emission dominates, and the coherence timescale is set by zero-point fluctuations associated with the radiative transition [212]. Despite their different physical origins, both mechanisms lead to a zero-delay $g^{(2)}(0) = 2$ in the limit of a large atom number $N \gg 1$. The preceding part discusses the coherence of photon emission from a linear optical process. In contrast, the SFWM is a higher-order nonlinear optical process, where photon emission in two coupled optical modes cannot be simply regarded as two successive Raman scattering events. Instead, the nonlinear interaction generates

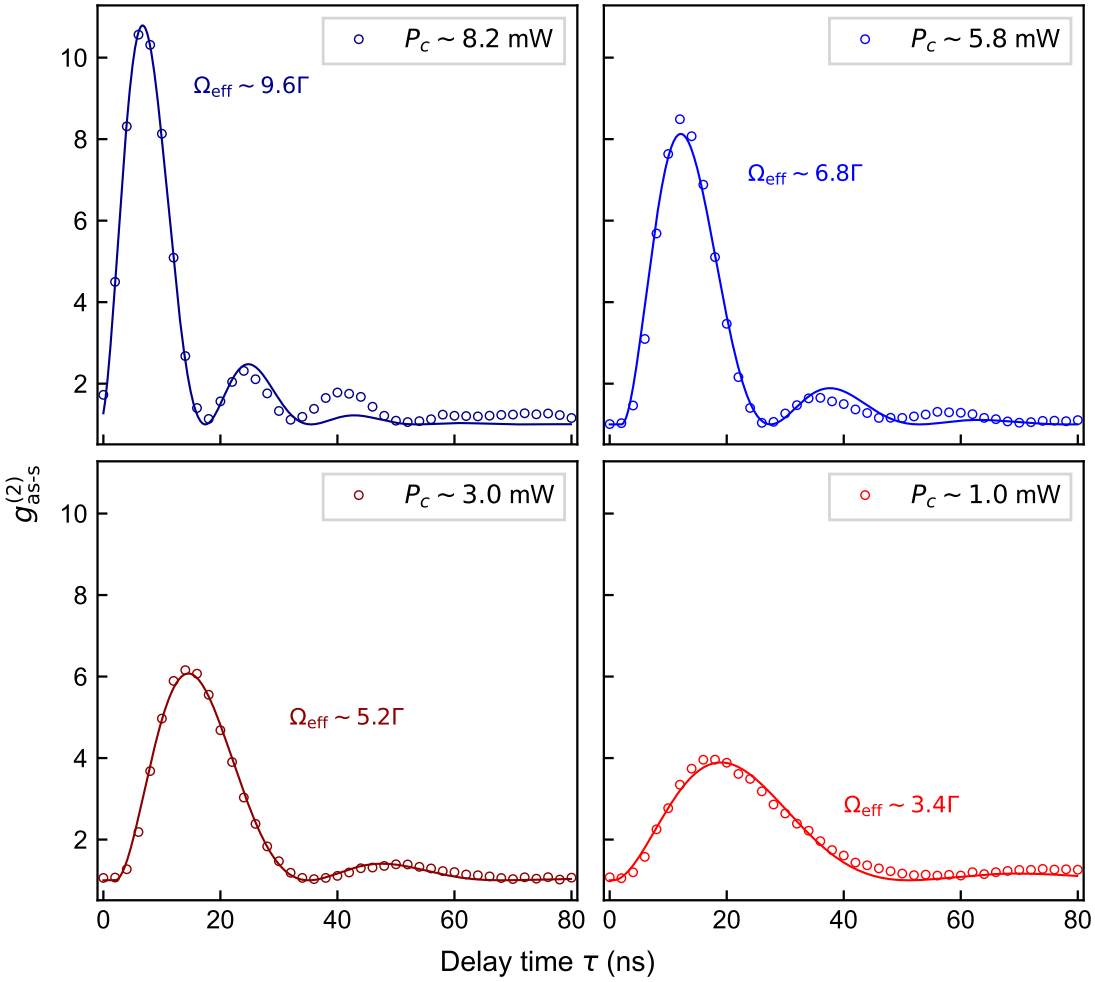

Figure 4.5: Cross-correlation function $g^{(2)}_{\text{as-s}}(\tau)$ under different coupling field powers with same pumping field power of $P_p \simeq 500\,\mu$W and OD = 30. The dashed lines represents the fit with model $\exp(-\Gamma\tau)(1-\cos(\Omega_{\text{eff}}\tau))$.

a TMSV state in the Stokes and anti-Stokes modes. The thermal properties in each mode arise from the amplification of vacuum fluctuations and the entanglement generated between the modes [213]. After tracing out the idler (anti-Stokes) mode in Equation 1.4, the reduced state of the signal (Stokes) mode is given by

$$\rho_s = (1-\lambda^2)\sum_{n=0}^{\infty}\lambda^{2n}|n\rangle\langle n|\,, \tag{4.44}$$

which corresponds to a thermal state with a Bose–Einstein photon number distribution.

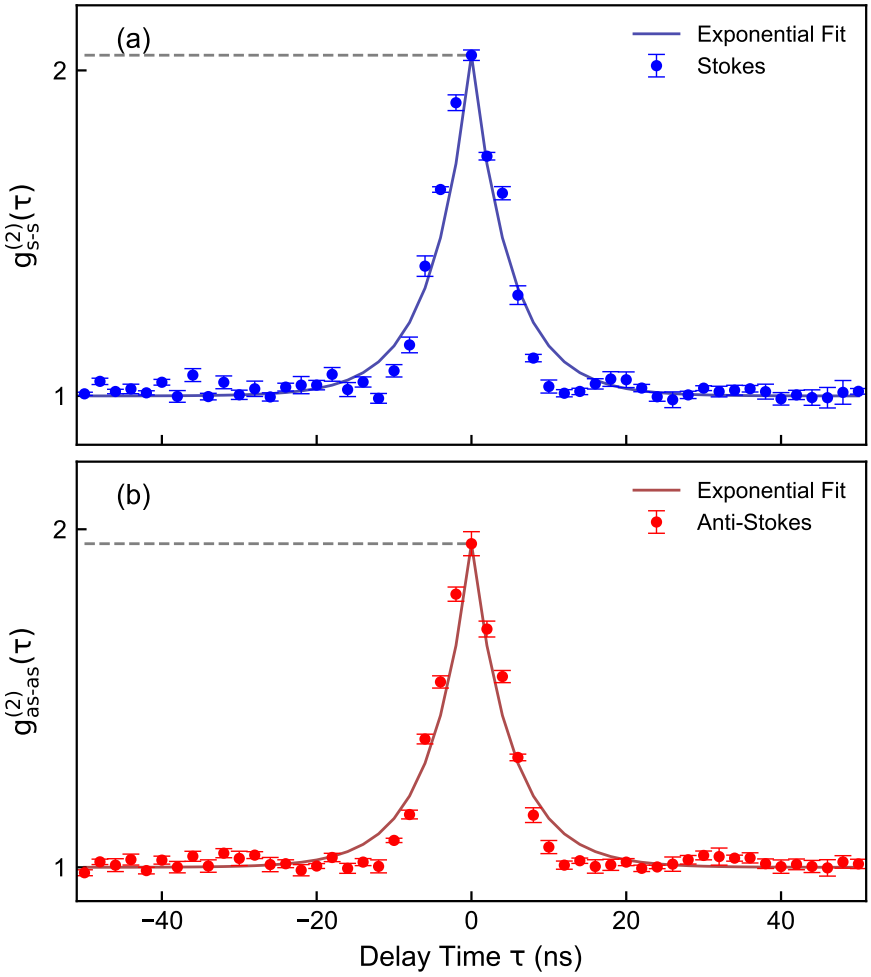

Figure 4.6: Auto-correlation of (a) Stokes field and (b) anti-Stokes field.

In our experimental settings, the pump field operates well below saturation with an effective saturation parameter $s_p \approx 0.1$ ($P_p \approx 250\,\mu\text{W}, \Delta_p = 2\pi \times 40\,\text{MHz}$), while the coupling field has a resonant saturation parameter of $s_c \approx 540$ ($P_c \approx 8\,\text{mW}$). The saturation intensity for ^{87}Rb is used as $I_{\text{sat}} = 1.37\,\text{mW/cm}^2$. The auto-correlation for each mode is achieved through a Hanbury Brown and Twiss (HBT) setup, which splits the collected photons in the single mode by a 50:50 fiber-based beam splitter and performs the coincidence counting between these two split channels. As shown in Figure 4.6, both the Stokes and anti-Stokes modes exhibit a second-order autocorrelation value of $g^{(2)}(0) \approx 2$, consistent with thermal photon statistics. This measurement reflects the mode purity of the emission, as a lower degree of purity (i.e., multimode contributions) typically reduces the observed $g^{(2)}(0)$ value. The

temporal width of the autocorrelation peak is found to be narrower than the intrinsic lifetime of the atomic level, i.e., $\Delta\tau < 1/\Gamma$, indicating that the temporal coherence of the photons is shorter than the natural atomic emission timescale. Furthermore, the shape of the measured correlation waveform deviates slightly from both an exponential decay, associated with a Lorentzian spectrum, and a Gaussian profile, which is expected for ideal thermal light with a Gaussian spectral distribution [214, 215]. This deviation suggests the presence of an additional mechanism shaping the temporal correlations in the single-mode emission, beyond what is predicted by standard thermal light models. As discussed earlier, both spontaneous emission and SFWM can give rise to similar values of $g^{(2)}(0)$ at zero delay. Therefore, the observation of $g^{(2)}(0) \approx 2$ is not a definitive and exclusive signature of photon bunching due to pair correlations. In particular, under conditions where spontaneous Raman scattering contributes photons to each mode, thermal statistics may arise independently in the Stokes and anti-Stokes channels, yielding $g^{(2)}(0) \approx 2$, imposed on the photon statistics of the underlying TMSV state. To verify the presence of pair-wise correlations, we aim to investigate higher-order temporal correlations, as discussed in Chapter 6.

4.4 Pump power and detuning dependence

4.4.1 Pumping field dependence

We investigate the dependence of photon pair generation on both the pump field detuning and pump power. The pump power is controlled by varying the RF drive amplitude of the AOM used for switching the laser, while the detuning is tuned by slowly sweeping the RF frequency of a separate spectroscopy AOM. This configuration allows fine frequency adjustment over a narrow range without disrupting the laser frequency lock. A key advantage of this approach is that the switching AOM remains unaffected during detuning sweeps, ensuring relatively stable output across different detuning settings.

In Figure 4.8 (a) and (b), the single-photon count rates in the Stokes and anti-Stokes channels exhibit a Lorentzian dependence on the pumping field detuning Δ_p. At resonance, the light-atom interaction strength is enhanced, leading to strong

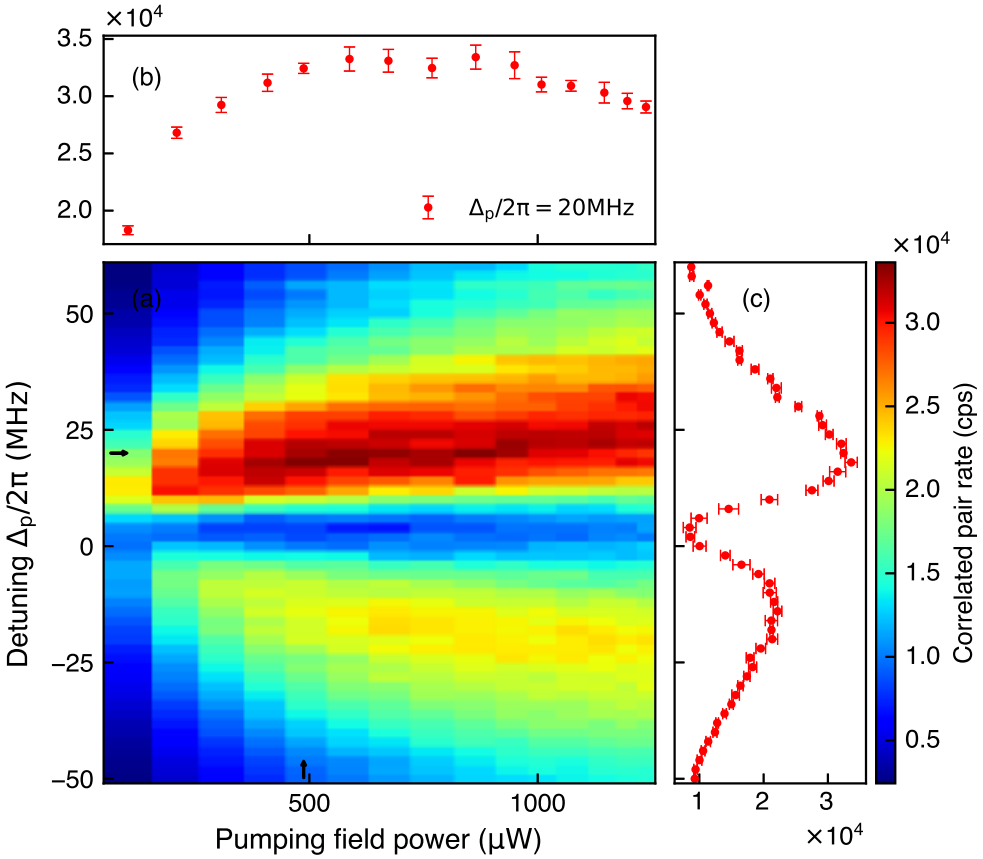

Figure 4.7: (a) Correlated photon pair rates as a joint function of pumping field power and its detuning from $|5S_{1/2}, F = 1\rangle \rightarrow |5S_{3/2}, F = 2\rangle$ transition. The coupling field is kept on resonance with a fixed power of approximately 8.5 mW. (b) Profile at $\Delta_p/2\pi = 20$ MHz, showing the dependence on pumping field power. (c) Profile at a pumping field power of 500 μW, showing the dependence on pumping field detuning Δ_p.

spontaneous emission and absorption. In contrast, Figure 4.7 illustrates that the photon pair generation does not reach maximum at zero detuning. Instead, the peak occurs at a positive detuning, where spontaneous emission and absorption are suppressed, and atomic coherence is better maintained. This suggests that resonance degrades coherence and weakens the efficiency of coherent nonlinear processes. While resonance enhances the light-matter interaction strength and the frequency conversion, it simultaneously increases incoherent processes such as spontaneous Raman scattering and absorption, which counteract the generation of correlated photon pairs.

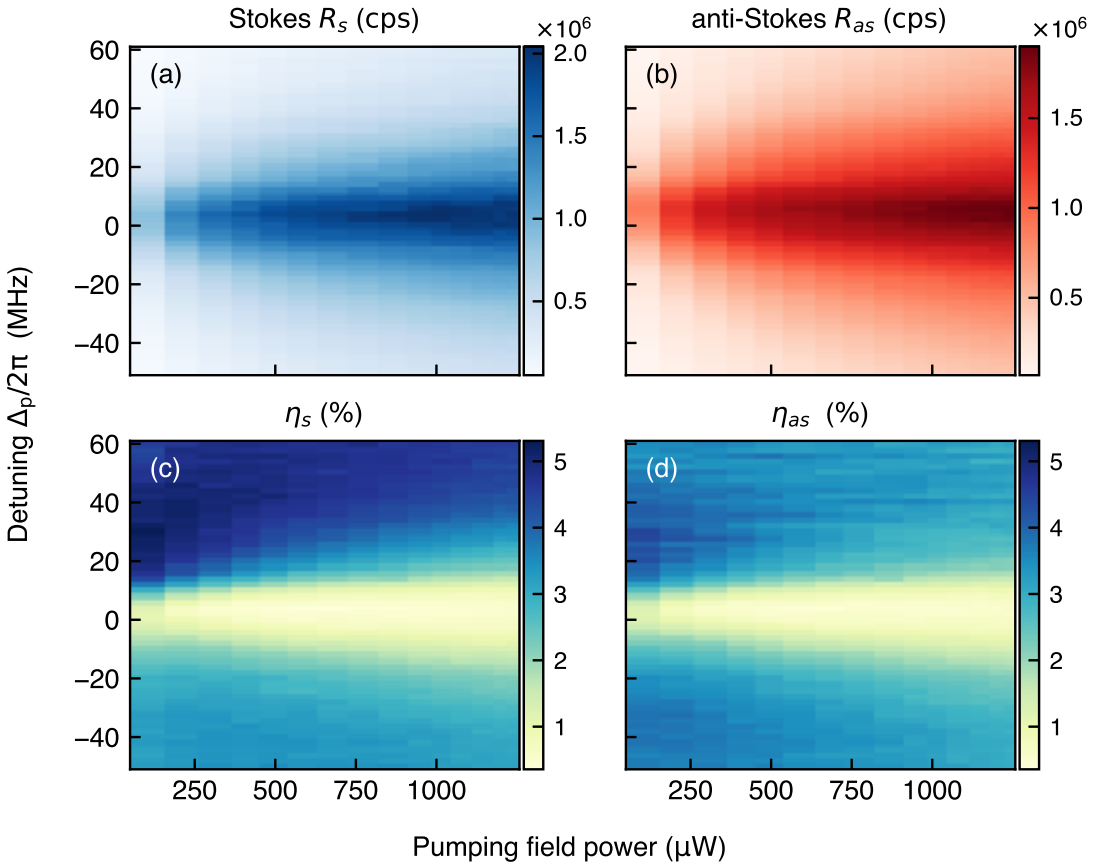

Figure 4.8: (a) Stokes single-photon count rate, (b) anti-Stokes single-photon count rate, (c) heralding efficiency of the Stokes mode, and (d) heralding efficiency of the anti-Stokes mode, plotted as joint functions of the pump field power and its detuning.

As shown in Figure 4.8 (c), the biphoton generation spectrum exhibits an asymmetric profile with respect to the pump detuning, where positive detuning yields a higher correlated photon pair rate than negative detuning. This asymmetry may arise from an enhanced SFWM process due to the excitation pathway interference near the positively detuned $|5S_{1/2}, F = 1\rangle \rightarrow |5P_{3/2}, F = 2\rangle$ transition, or from improved satisfaction of phase-matching conditions. However, the exact origin of this asymmetry remains unclear.

4.4.2 Coupling field dependence

By varying the coupling field power from 1 mW to 8.5 mW under different pumping field power conditions, Figure 4.9 (a) reveals a saturation behavior in the correlated photon pair generation rate. Once the coupling field power becomes sufficiently strong, the pair generation efficiency is primarily determined by the pumping field power, and further increases in the coupling field power do not enhance the generation rate. However, as shown in Figure 4.9 (b), the non-classicality of the generated photons, as indicated by the violation of the Cauchy–Schwarz inequality, improves with increasing coupling field power and decreasing pumping field power. Figure 4.9 (c) and (d) show the heralding efficiencies for the Stokes and anti-Stokes photons, respectively, which indirectly reflect the evolution of incoherent scattering with increasing field strengths. The heralding efficiency of the Stokes photons increases with coupling field power, indicating that the strong coupling field suppresses incoherent components in the Stokes mode. In contrast, when the coupling field power reaches the saturation regime, the heralding efficiency of the anti-Stokes photons deteriorates, suggesting that excessive pumping field may introduce incoherent contributions into the anti-Stokes mode.

The effect of the coupling field intensity is also reflected in the two-photon (see Figure 4.5) and single-photon coherence times. According to the Wiener-Khinchin theorem [216], for a stationary random electric field, the power spectral density is the Fourier transform of its first-order correlation function as

$$S_E(\omega) = \int_{-\infty}^{\infty} \langle E^*(t)E(t+\tau)\rangle e^{-i\omega\tau} d\tau \,. \tag{4.45}$$

For classical (thermal) light fields that are stationary and exhibit Gaussian statistics, the first-order coherence function is further related to the intensity auto-correlation via the Siegert relation [214, 217]:

$$g^{(2)}(\tau) = 1 + |g^{(1)}(\tau)|^2 \,. \tag{4.46}$$

However, these relations do not directly apply to the TMSV state generated via the SFWM process. In general, extracting the spectral bandwidth from the temporal coherence requires that the photon wave packets be transform-limited, i.e., their temporal duration Δt and spectral bandwidth $\Delta\nu$ satisfy the time-bandwidth

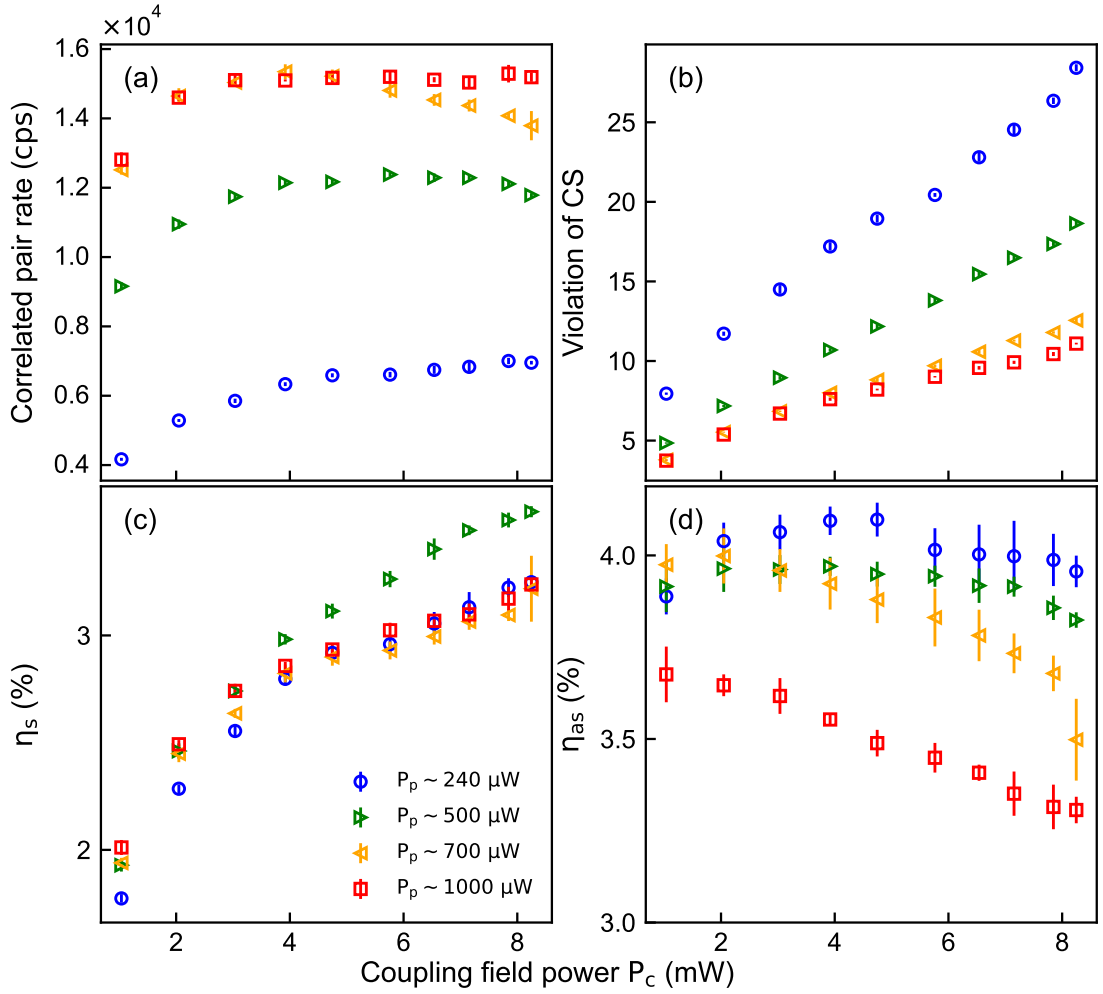

Figure 4.9: (a) Correlated photon-pair rate (b) Violation of Cauchy–Schwarz inequality (c) Stokes efficiency (d) anti-Stokes efficiency as a function of coupling field power under different pumping field power.

uncertainty limit. To verify whether a photon state is transform-limited, a full characterization of its joint spectral and temporal properties is necessary. Srivathsan et al. [82] has shown that transform-limited photon pairs can be generated from cold atomic ensembles. In our case, we observe changes in the width of the temporal auto-correlation function and use the associated coherence time to estimate an effective bandwidth. However, this approach implicitly assumes that the photons are transform-limited. Since we do not directly verify this assumption (e.g., through joint spectral and temporal characterization), the inferred bandwidth cannot be

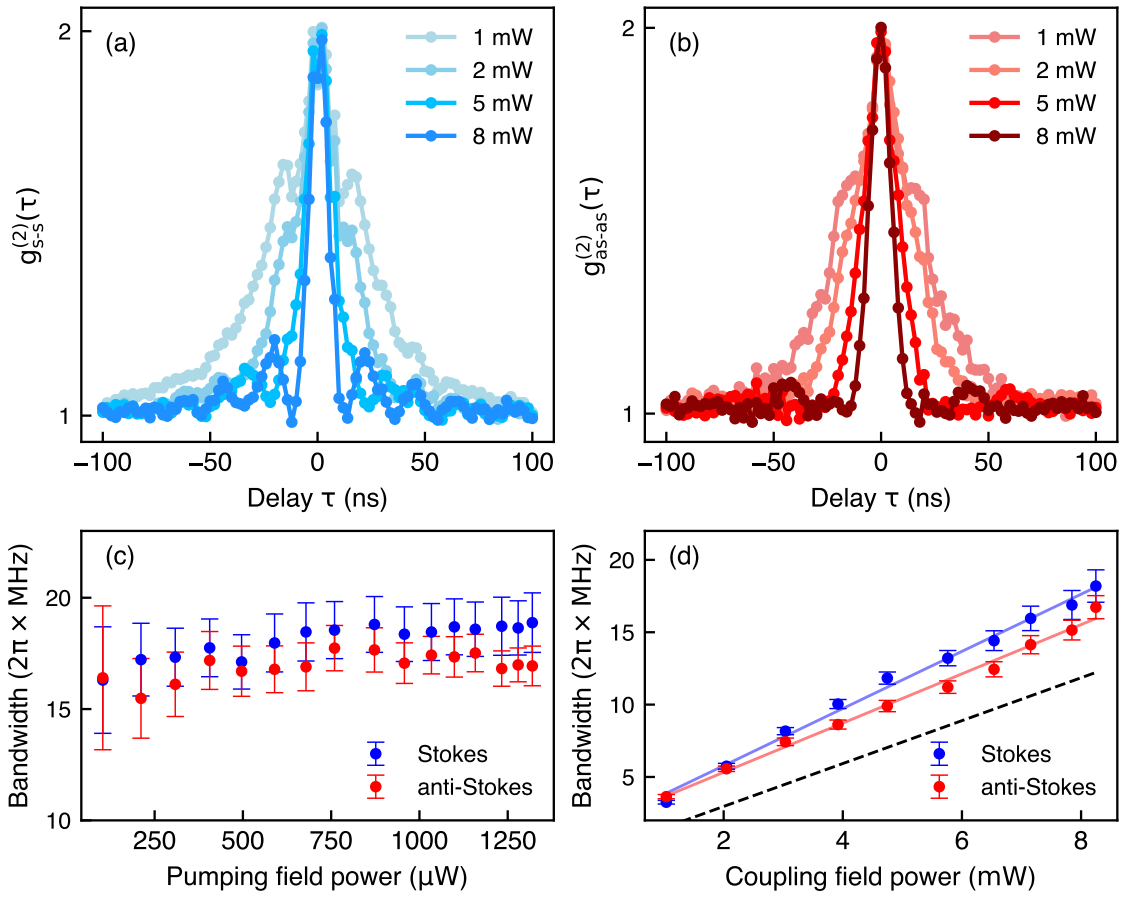

Figure 4.10: (c) Bandwidths $(1/\tau)$ in each mode as a function of pumping field power, while maintaining the coupling field power at a constant level of 8.5 mW and the pumping field detuning at $\Delta_p/2\pi = -50$ MHz (d) Bandwidths with respect to the coupling field power with experimental condition of $\Delta_p/2\pi = -50$ MHz and $P_p \approx 800\,\mu$W. The solid lines are linear fits for the data, while the dashed black line represents the theoretical group-delay bandwidth $\Delta\omega_g$ with parameters $\gamma_{13} = 2\pi \times 3$ MHz and OD = 30.

rigorously interpreted as the true spectral bandwidth. Instead, it should be regarded as an approximate or effective value derived from temporal coherence properties.

For generality, the coherence time is conventionally defined as the full width at half maximum (FWHM) of the auto-correlation function with respect to the relative time delay. Figure 4.10 (a) and (b) illustrate the broadening of the auto-correlation in the Stokes and anti-Stokes modes, with the decrease of the coupling field power. This behavior arises because the coupling field determines the EIT bandwidth that limits the coherence of anti-Stokes photons, and, due to energy conservation, similarly

affects the Stokes photons. Figure 4.10 (c) reveals that the photon-pair bandwidths (defined as $1/\tau$, with τ being the coherence time) remain largely unchanged with varying pumping power, indicating that the coherence is primarily governed by the coupling field. In contrast, Figure 4.10 (d) shows a clear linear dependence of the bandwidth on coupling power: as the coupling field power increases from 1 mW to 8.5 mW, the spectral bandwidths vary from sub-natural linewidth around $2\pi \times 3$ MHz to $2\pi \times 17.5$ MHz, corresponding to the single-photon coherence time changing from 53 ns to 10 ns. This dependence on the coupling field power follows a similar trend to the theoretical prediction of the group delay bandwidth, given by $\Delta\omega_g \simeq 0.88/\tau_g$, where the group delay time τ_g is characterized by [81]

$$\tau_g \approx \frac{2\gamma_{13}\mathrm{OD}}{|\Omega_c|^2}\,. \tag{4.47}$$

Figure 4.11 (a)-(c) illustrate the dependence of correlated photon pair generation on the coupling field detuning Δ_c, while the pumping field detuning is held constant at $\Delta_p/2\pi = -50$ MHz. As a coupling field detuning range from -40 MHz to 40 MHz, the correlated photon pair rate exhibits only moderate variation. This limited sensitivity to Δ_c may be attributed to power broadening effects. Notably, the maximum correlated photon pair rate is observed at approximately $\Delta_c/2\pi = -25$ MHz, indicating a red shift from the expected resonance. This red shift may be related to the collective (cooperative) Lamb shift, a phenomenon arising from average dipole-dipole interactions. The collective Lamb shift has been previously observed in hot atomic vapors [218, 219] and extended samples of cold atoms [220, 221], which has been theoretically investigated [222–225]. In our setup, the current laser configuration limits the accessible detuning range at constant laser power, preventing a broader investigation. Within the explored detuning range, the effect of the etalon bandwidth is negligible, as its transmission profile is significantly broader than the frequency shifts under consideration.

The second-order cross-correlation function $g^{(2)}_{\text{as-s}}(\tau)$ exhibits different waveforms when the coupling field is detuned, as shown in Figure 4.12 (a) and (b). Compared to the resonant case, the waveform shows a slower decaying envelope and reduced visibility of quantum beating. This behavior can be qualitatively understood as follows: Under a resonant coupling field in the ATS regime, two FWM pathways on the two dressed states contribute equally. One generating a pair of $\bar{\omega}_s + \Omega_e/2$

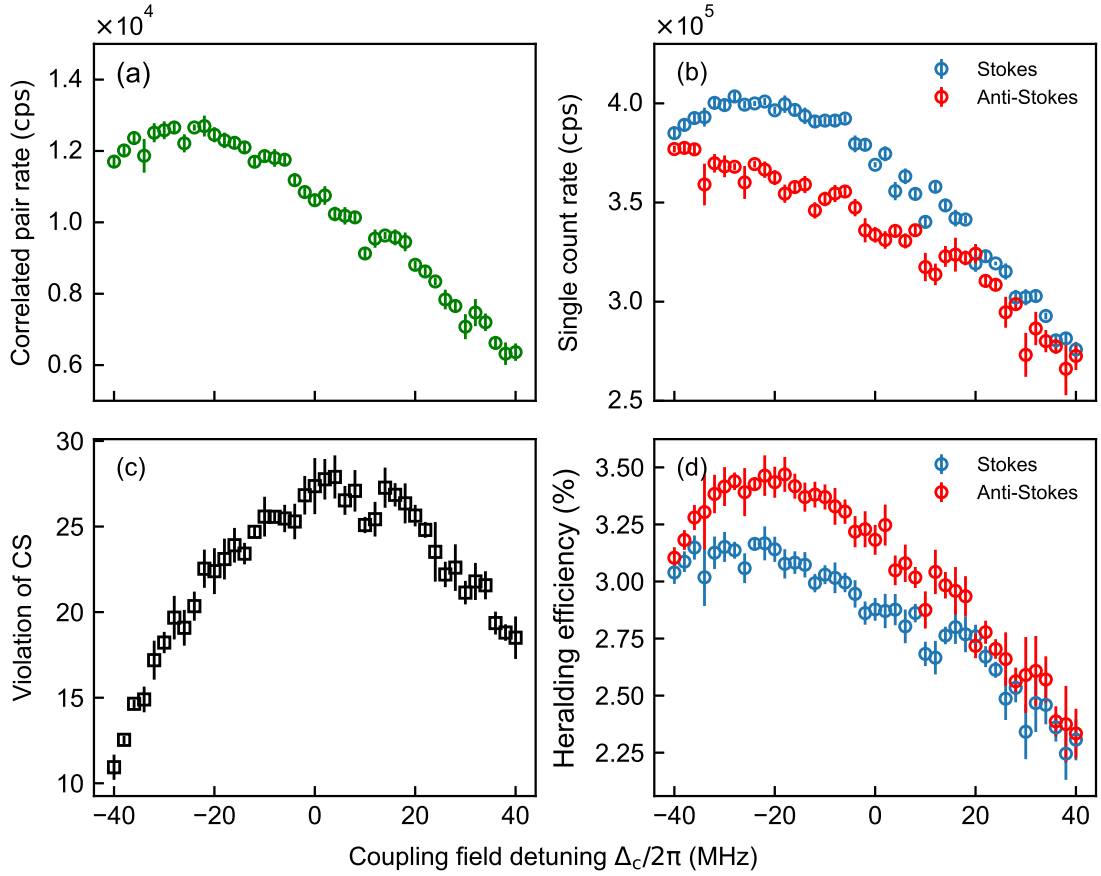

Figure 4.11: (a) Correlated photon-pair rate, (b) single-photon count rate, (c) Cauchy–Schwarz inequality violation factor, and (d) heralding efficiencies for the Stokes and anti-Stokes modes. The measurements are taken at a pump detuning of $\Delta_p/2\pi = -50\,\mathrm{MHz}$, with pump and coupling powers of $P_p \approx 700\,\mu\mathrm{W}$ and $P_c \approx 8.5\,\mathrm{mW}$, respectively.

and $\bar{\omega}_{as} - \Omega_e/2$, and the other at $\bar{\omega}_s - \Omega_e/2$ and $\bar{\omega}_{as} + \Omega_e/2.$, where $\bar{\omega}_s$ and $\bar{\omega}_{as}$ are the center frequencies of the Stokes and anti-Stokes modes, and Ω_e denotes the energy splitting between the dressed states. Interference between these two frequency components leads to quantum beating in the temporal waveform. When the coupling field is detuned, one of the SFWM channels becomes stronger and dominates the generation process, while the other is suppressed. The symmetry between the two FWM pathways is broken, leading to diminished quantum beating and a distorted temporal profile. Figure 4.12 (a) shows that such interference enhances the two-photon coherence to a certain extent. This indicates that the

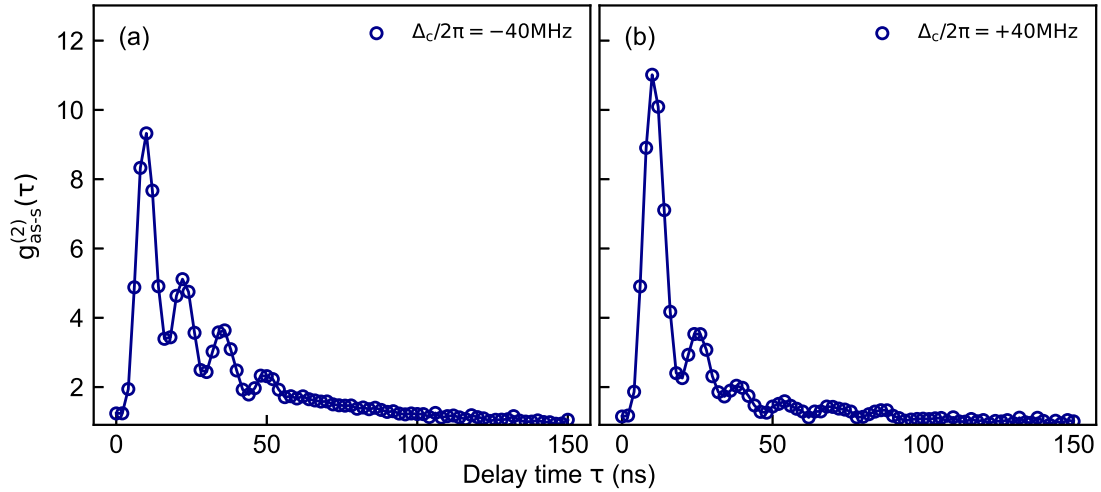

Figure 4.12: Normalized cross-correlation functions of coupling field detuning (a) $\Delta_c/2\pi = -40\,\mathrm{MHz}$ and (b) $\Delta_c/2\pi = 40\,\mathrm{MHz}$.

detuning of the coupling field serves as a useful degree of freedom for tailoring the temporal two-photon waveform. Additionally, the results in Figure 4.11 suggest that an appropriate choice of detuning can enhance pair generation efficiency, owing to quantum interference between two asymmetric decay channels [226].

4.5 Summary

Our experimental results demonstrate the generation of narrowband, highly bright correlated photon pairs from a cold atomic ensemble. The relatively low detected pair rate is mainly limited by the overall system loss of about 80% in the current collection and filtering setup. This can be further improved experimentally, while the detection efficiency can also be enhanced by employing superconducting nanowire single-photon detectors (SNSPDs), which offer state-of-the-art detection efficiencies exceeding 95% for near-infrared photons. These improvements can both enhance the detection of photon pairs. Meanwhile, the inferred photon-pair generation rate indicates that the nonlinear process can occur efficiently near the saturation regime of photon scattering. Although we have prepared a relatively dense atomic cloud with an optical depth of about 30 for the $F = 1$ ground state, this value has not yet reached the highest optical depths reported for cold atomic

systems. Further improvement of the optical depth would enhance the nonlinear interaction strength and thus the photon-pair generation efficiency. In the current experimental configuration, we collect photons from a single diffraction-limited spatial mode, which overlaps only with a limited portion of the entire atomic cloud. Starting from the goal of maximizing the effective interaction and atom number contributed to the collection, one could redesign the atomic cloud preparation and collection geometry, which is expected to yield a significantly brighter photon-pair source.

Chapter 5

Superradiance in biphoton generation

5.1 Introduction

Spontaneous emission from a dilute ensemble of atoms is often treated as an incoherent process, where each atom radiates independently and the total radiation emission rate (intensity) scales linearly with the number of emitters N. This simplified picture, however, overlooks the fact that atoms establish correlations by interacting with a shared radiation field. Such interactions can lead to a cooperative phenomenon known as "superradiance" first introduced by Dicke in 1954 [227]. In superradiance, atomic dipoles synchronize through their common coupling to the light field. This collective behavior results in a dramatically enhanced emission rate, which can scale as N^2, especially during the initial stage of the radiation burst. This contrasts with the linear scaling observed in incoherent emission. Consequently, at the peak of the superradiant burst, the collective decay rate can reach up to $N\Gamma$, where Γ is the single-atom decay rate, resulting in a much shorter emission duration of approximately τ_{sp}/N [207, 227–229].

Superradiance is most intuitively understood in systems where all atoms are confined within a volume much smaller than the emission wavelength ($d \ll \lambda$), ensuring that emitted photons cannot distinguish between individual atoms [227]. In this regime, atomic excitations become effectively indistinguishable, and quantum coherence leads to the formation of collective states, referred to as Dicke states. Within this framework, excitations are shared among all atoms in a coherent superposition. Symmetric states, which are invariant under particle exchange, result

in constructive interference of the decay pathways and thus facilitate spontaneous emission. Conversely, anti-symmetric Dicke states, which change sign under particle exchange, exhibit destructive interference, suppressing emission and effectively trapping the excitation. This phenomenon is known as subradiance, the counterpart to superradiance. Theoretical and experimental studies have significantly broadened the scope of superradiance beyond the idealized condition of small volume and population inversion. Cooperative emission has been investigated in ordered atomic systems, such as atomic chains and arrays with sub-wavelength spacing [230–234], and even in large, disordered atomic samples [231, 235–242] that do not strictly meet the original Dicke state assumptions. A collective phenomenon is not confined to neutral atoms, and it has also been observed in other systems composed of a few emitters, including trapped ions [243], superconducting qubits [244], Rydberg gas [245, 246], and free electrons [247]. Furthermore, superradiant behavior can manifest even at the single photon level [75, 224, 231, 239, 248–253]. Although superradiance is often explored in two-level systems, it has also been observed in multilevel configurations. Examples include cascade emission [254–257] and Raman-based schemes, such as those employed in the Duan-Lukin-Cirac-Zoller (DLCZ) protocol for quantum memories [14, 75, 250, 258]. Furthermore, collective emission properties have also been reported in photon pairs generated via parametric processes [77, 82]. These experimental findings indicate that superradiance is a widely observed phenomenon in photon emission across various systems.

We investigate narrowband correlated photon pairs generated from a cold, elongated atomic ensemble. To align with the framework of extended systems [228], photon collection is performed along a phase-matched spatial mode oriented along the longest axis of the atomic cloud, with a slight deviation from the counter-propagating pump fields. To suppress diffraction-related effects, such as slow-light propagation under EIT conditions, which can obscure the observation of collective emission features [228], we employ a strong coupling laser and operate the double-Λ SFWM process in the ATS regime. Under these conditions, we observe that the photon pair generation rate scales quartically with the atom number, following a clear N^4 dependence. Concurrently, the single-photon rate in each mode exhibits a quadratic dependence on N, scaling as N^2. In our experiment, the atom number N is characterized by the resonant optical depth, defined as $\mathrm{OD} = n\sigma L$, where n is

the atomic density, σ is the resonant absorption cross-section, and L is the atomic medium length. To the best of our knowledge, this N^4 scaling has not been predicted by existing models. We tentatively interpret this observation as the product of two distinct quadratic dependencies on the atom number: one arising from the third-order nonlinear susceptibility, which is predicted to scale quadratically with N in photon-pair generation [79], and the other from a superradiant enhancement in the emission of the correlated photon pairs. Additionally, we observe that the decay rate, reflected in the envelope of the two-photon wavefunction in the ATS regime, exhibits an approximately linear dependence on the atom number. This behavior is consistent with key signatures of superradiant emission: the enhancement of decay rate.

Our results show that correlated photon pairs inherit these collective properties, influencing both the SFWM strength and the shape of the two-photon wavefunction. We find that collective emission is feasible under continuous-wave (CW) pumping, a configuration distinct from conventional superradiance experiments, which typically employ pulsed excitation to prepare an initial population inversion and subsequently observe a burst-like decay. Moreover, the demonstration of CW superradiant behavior opens up new possibilities for developing CW superradiant lasers. Such lasers aim to achieve ultra-narrow linewidths and spectral purity far exceeding that of conventional lasers [259–263].

5.2 Theory

Although the Dicke model does not fully describe the dynamics of superradiant biphoton generation in a cold atomic ensemble, it nevertheless provides valuable insight into the observed atom-number scaling. Let us consider the spontaneous emission of an ensemble of N two-level atoms with ground state $|g\rangle$ and excited state $|e\rangle$. Each atom (i) has Pauli operators $\sigma_+^{(i)} = |e_i\rangle\langle g_i|, \sigma_-^{(i)} = |g_i\rangle\langle e_i|, \sigma_z^{(i)} = |e_i\rangle\langle e_i| - |g_i\rangle\langle g_i|$. Because the atoms couple indistinguishably to a single electromagnetic mode, we introduce collective spin operators that sum over all atoms, including their phase factors

$$\hat{S}^{\pm} = \sum_{i=1}^{N} \sigma_{\pm}^{(i)} \exp(\pm i\mathbf{kr_i}),\ \hat{S}_z = \sum_{i=1}^{N} \sigma_z^{(i)} \exp(i\mathbf{kr_i}),\tag{5.1}$$

In the interaction picture, the collective atom–photon Hamiltonian [207, 264, 265] under the rotating wave approximation is given as

$$\hat{H} = -\hbar\Delta\hat{S}_z - \sum_{\mathbf{k}} \hbar(g_{\mathbf{k}}\hat{S}^+\hat{a}_{\mathbf{k}} + g^*_{\mathbf{k}}\hat{a}^\dagger_{\mathbf{k}}\hat{S}^-)\,, \tag{5.2}$$

where $\hat{a}^\dagger_{\mathbf{k}}$ ($\hat{a}_{\mathbf{k}}$) is the creation (annihilation) operator for a quantum field in the mode $\mathbf{k}$ with frequency $\omega_{\mathbf{k}}$, and $\Delta = \omega_{\mathbf{k}} - \omega_a$ is the field detuning from atomic transition ω_a. The single-photon coupling strength is given as $g_{\mathbf{k}} = i\sqrt{\frac{2\pi\hbar\omega_{\mathbf{k}}}{V}}\langle e|\hat{d}|g\rangle$ where $\hat{d}$ is the electric dipole moment vector of the two-level system. Consequently, the dynamics of the atomic density ρ is governed by the following Lindblad master equation

$$\frac{\mathrm{d}\rho}{\mathrm{d}t} = -\frac{\mathrm{i}}{\hbar}[\hat{H},\rho] + \frac{\Gamma}{2}\left(2\hat{S}^-\rho\hat{S}^+ - \hat{S}^+\hat{S}^-\rho - \rho\hat{S}^+\hat{S}^-\right)\,. \tag{5.3}$$

Here, the first term represents the Hamiltonian dynamics, while the second term is the dissipator describing collective spontaneous emission at a collective decay rate Γ. In the Dicke state model, the system size is assumed to be smaller than the wavelength, i.e., $V \ll \lambda^3$. The state evolution of an ensemble of indistinguishable two-level atoms is restricted to $N+1$ permutation-symmetric states labeled by the number of excitations m, as $|s = N/2, m\rangle$ with $-N/2 \le m \le N/2$. These are simultaneous eigenstates of $\hat{S}_z$ and $\hat{S}^2$, where the latter is defined as $\hat{S}^2 = 1/2(\hat{S}^+\hat{S}^- + \hat{S}^-\hat{S}^+) + 1/4\hat{S}_z^2$. The eigenvalue equations are given as

$$\begin{aligned} \hat{S}_z|s,m\rangle &= 2m|s,m\rangle\,, \\ \hat{S}^2|s,m\rangle &= s(s+1)|s,m\rangle\,. \end{aligned} \tag{5.4}$$

Here, the quantum number m represents half of the population inversion (i.e., $m = (N_e - N_g)/2$). When $m = N/2$, all atoms are in the excited states ($N_e = N, N_g = 0$), corresponding to the maximal population inversion. When $m = 0$, half of the atoms are excited and half are in the ground state ($N_e = N_g = N/2$).

Under the resonance condition ($\Delta = 0$), the intensity of the emission into a unit solid angle around the direction $\mathbf{k}$ is expressed in terms of the correlation of the collective atomic operators (refer to § D.1) as

$$\frac{\mathrm{d}}{\mathrm{d}t}\langle a^+_{\mathbf{k}}a_{\mathbf{k}}\rangle = I_{\mathbf{k}}(t) = I_{\mathrm{sp}}\langle\hat{S}^+(t)\,\hat{S}^-(t)\rangle\,, \tag{5.5}$$

where I_{sp} is the intensity of the isotropic spontaneous decay per unit solid angle. If the system is initially in the state $|S = N/2, m = 0\rangle$, half of the atoms are in the

excited states and the other half are in the ground states. The radiation intensity in this case is

$$I_{\mathbf{k}} = I_{\mathrm{sp}} \frac{N}{2} \left(\frac{N}{2} + 1 \right) \approx I_{\mathrm{sp}} \frac{N^2}{4} \,. \tag{5.6}$$

It reveals that the emission intensity is proportional to N^2 when the wavefunction of N identical atoms forms a Dicke state. This state is fully symmetric under particle exchange and exhibits nonzero atom-atom correlation, $\langle \hat{S}^+ \hat{S}^- \rangle$. Although derived from Dicke state modeling, the characteristic N^2-scaling of emission intensity also applies to more general systems beyond the strict Dicke assumption. In general, the emission intensity is governed by a macroscopic atom-atom correlation that accounts for interference between radiation from distinct atoms:

$$\langle \hat{S}^+ \hat{S}^- \rangle = \sum_{i \neq j} e^{i\mathbf{k}\cdot(\mathbf{r}_i - \mathbf{r}_j)} \langle \sigma_+^{(i)} \sigma_-^{(j)} \rangle \,, \tag{5.7}$$

which reflects the emergence of effective atom-atom interactions through the shared coupling to the electromagnetic vacuum. This collective atom-atom correlation is critically dependent on the system's geometric configuration and diffraction effect [207, 228], especially in large atomic ensembles. For example, in specific geometries such as pencil-shaped atomic clouds, superradiant emission can be effectively characterized by an effective atom number $\tilde{N} = \mu N$ [264], where the geometrical factor μ accounts for the coupling to the diffraction modes of the radiation field [228]. The dissipative Dicke model [264], within the spin-wave and mean-field approximations, is valid for describing extended ensembles of randomly distributed emitters, such as our elongated atomic cloud.

5.2.1 SFWM strength

The SFWM strength is determined by the third-order nonlinear susceptibility $\chi^{(3)}$. As detailed in Equation 4.17, the macroscopic $\chi^{(3)}$ arises from the sum of individual atomic contributions. Therefore, assuming that SFWM processes in different emitters occur independently and without collective enhancement, $\chi^{(3)}$ scales linearly with the total atom number N.

Consequently, the photon pair generation rate R_p, or equivalently the spectral density, is proportional to $|\chi^{(3)}|^2$, which implies an ideal scaling of $R_p \propto N^2$. This quadratic dependence on atom number is typically observed at low optical depths

(OD), where OD is proportional to N in a given interaction volume. Kolchin et al. [79] predict that the spectral density of photon pair generation scales quadratically with atom number when the phase-matching term $\kappa(\delta_{as})$ dominates the two-photon wavefunction. However, this scaling transitions to a linear dependence in the group-delay regime. Furthermore, their model indicates that incoherent scattering, attributed to Langevin noise fluctuations, can cause the observed scaling to deviate from these theoretical predictions. In the following section, we present our experimental observations, which notably differ from this theoretical prediction.

5.3 Results

In this section, we present experimental results that demonstrate superradiant emission within our photon-pair generation process. Key observations supporting this include a significant nonlinear scaling of the pair generation rate with optical depth, and enhancement of photon pairs within the two-photon coherence time, both of which are hallmarks of the collective effects inherent to superradiance. These findings indicate that superradiant emission plays a crucial role in enhancing the underlying nonlinear interaction strength and, consequently, the pair emission rate.

5.3.1 Optical depth dependence

Figure 5.1 presents the dependence of the correlated photon-pair rate and the single-photon count rate on the resonant optical depth. The optical depth is controlled by adjusting the free expansion time of the atomic cloud after its release from the MOT, a process detailed in § 3.2.3. Once the target OD is reached, a $200\,\mu$s measurement window is initiated. During this period, a CW pump beam is applied, and the generated Stokes and anti-Stokes photons are collected. Within this short window, the optical depth remains approximately constant throughout the data acquisition. During the photon-pair generation process, the experimental parameters are as follows: the pumping field is detuned by $\Delta_p/2\pi = -50\,\mathrm{MHz}$ from the atomic resonance and has a power of around $500\,\mu$W; the coupling field is on resonance with a power of $8.5\,\mathrm{mW}$.

To determine the optical depth for each data point, we perform an independent calibration by fitting the transmission spectrum of a weak probe field as a function

of detuning from the $5S_{1/2}, F = 1\rangle \rightarrow 5P_{3/2}, F = 2\rangle$ transition. The probe propagates through the same spatial mode used for photon collection, ensuring that the measurement reflects only the atoms contributing to the collected signal. Therefore, this procedure provides a practical and consistent measure of the atom number participating in the SFWM process within the collection mode, rather than the total atom number in the entire atomic cloud.

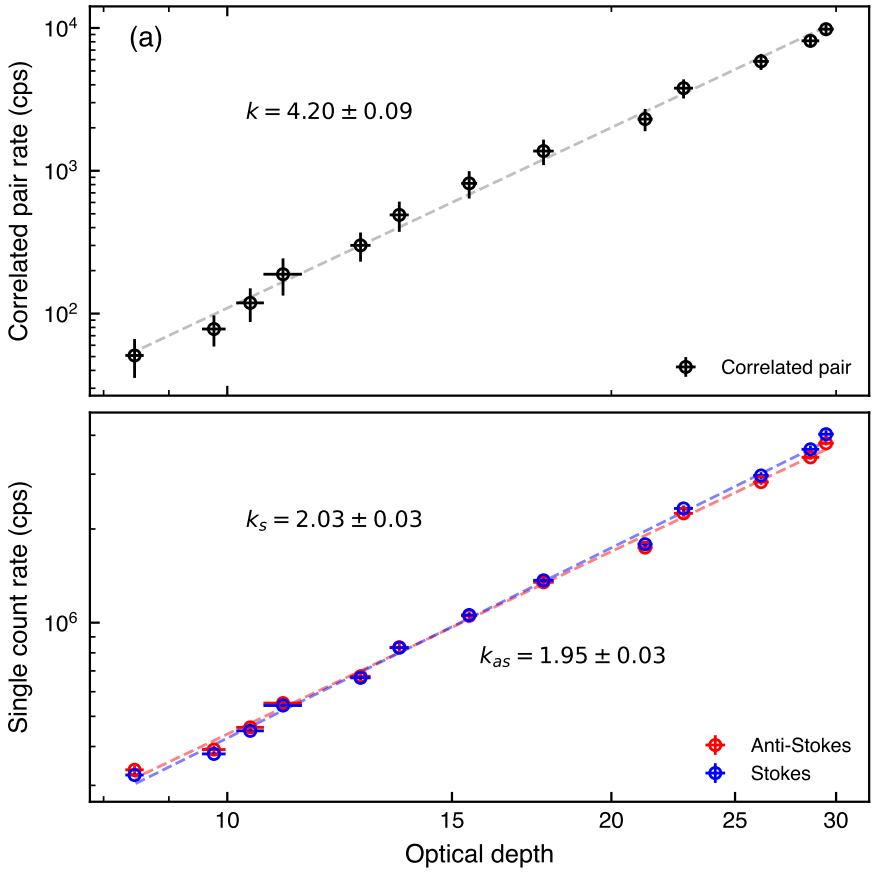

Figure 5.1: (a) Correlated photon pair rate and (b) single-count rates in Stokes and anti-Stokes modes as a function of optical depth. The x- and y-axes are shown on a logarithmic scale.

In contrast to the quadratic scaling predicted in § 5.2.1, the logarithmic scaling analysis in Figure 5.1 displays a different behavior. A power-law fit to the correlated photon-pair rate yields a slope of approximately 4.20 ± 0.09, indicating that the correlated pair rate, measured within a 22 ns coincidence window, corrected for uncorrelated background, scales nearly as OD^4, rather than quadratically as initially

expected. This quartic dependence suggests that the pair generation benefits from the collective emission enhancement based on the quadratic scaling with $(\chi^{(3)})^2$. In comparison, the single-count rates for Stokes and anti-Stokes photons show fitted slopes of 2.02 ± 0.03 and 1.95 ± 0.03, respectively, which deviate from the linear scaling expected from an independent emitter model. These results indicate that both Stokes and anti-Stokes emissions exhibit collective behavior, scaling approximately as OD^2.

5.3.2 Suppression of Rabi oscillation

We investigated whether signatures of superradiant emission manifest in the two-photon wavefunction. To minimize propagation effects such as slow light, the coupling field is set to a high intensity, leading to a two-photon wavefunction characterized by damped Rabi oscillations. The data for this analysis is the same as that used for the optical depth dependence study presented in Figure 5.1.

The influence of superradiance on Rabi oscillations has been explored previously. For instance, Ferioli et al. [241] suggested that superradiance can modify spontaneous emission and further the behavior of Rabi oscillations. In their experiments using pulsed excitation, collective Rabi oscillations were observed in the photons scattered along the pencil-shaped atomic cloud. Notably, the ratio of peak to steady-state emission rates increased with atom number, providing strong evidence of enhanced collective interactions. In a subsequent study, the same group [264] reported a reduction of the frequency and amplitude of the oscillations as the atom number increases. Although our system, a dense, elongated atomic cloud in free space, differs from their pencil-shaped atomic clouds confined in dipole traps (with waists smaller than the wavelength), their observations inspired us to investigate the collective effect through the Rabi oscillation features displayed in the two-photon wavefunction.

The two-photon wavefunction, represented by the normalized cross-correlation function between the Stokes and anti-Stokes photons, shows a key deviation from the theoretical prediction: the damped oscillatory waveform follows a decay envelope with a decay rate significantly larger than the natural linewidth. As shown in Figure 5.2 (a), the decay rate Γ_1, extracted by fitting two peak points with an exponential envelope, certainly captures the initial decay behavior but does not

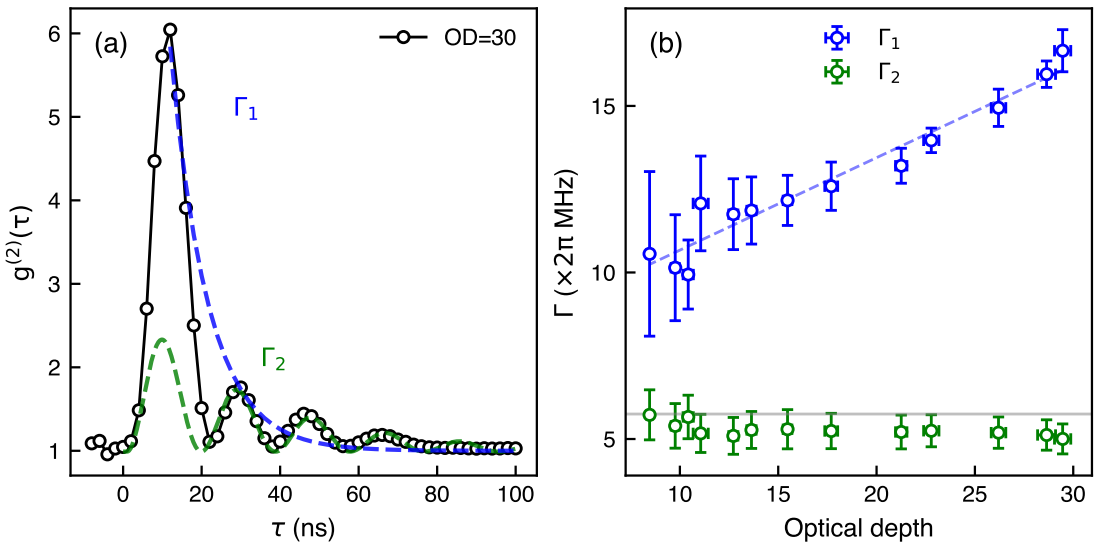

Figure 5.2: (a) Cross-correlation function and two fits to the two-photon wavefunction. The decay rate Γ_1 is extracted by fitting an exponential envelope to the first two oscillation peaks. The decay rate Γ_2 is obtained by fitting an exponentially decaying oscillation to the remaining peaks, excluding the first one. (b) Extracted decay rates as a function of optical depth. The blue dashed line shows a linear fit to Γ_1, yielding a slope of 0.28 ± 0.02. The solid grey line indicates the natural linewidth $2\pi \times 5.75\,\mathrm{MHz}$ as reference. The error bar of Γ_1 is evaluated from 23 repeated measurements, while the error bar of Γ_2 is obtained from the standard deviation of the fit.

account for the remaining oscillations. In contrast, the decay rates Γ_2 extracted by fitting the subsequent oscillations (excluding the first peak) reflect the long-time exponential envelope of the damped Rabi oscillation. The dependence of these decay rates on optical depth is shown in Figure 5.2 (b): Γ_1 increases roughly linearly with optical depth, whereas Γ_2 remains constant, and matches the natural linewidth of the D1 line of ^{87}Rb. Therefore, the fitted waveform using Γ_2 (green dashed line) in Figure 5.2 (a) is much closer to the expected theoretical waveform with natural damping. However, the experimental data show that the first peak is significantly broader than the expected Rabi period, and the number of photon pairs within this first peak (22 ns coincidence window) is much higher than that predicted by a model with a natural exponential decay envelope. This observation suggests a collective emission burst occurring on a timescale shorter than the two-photon coherence time. Such a burst is consistent with the hallmark features of superradiant emission,

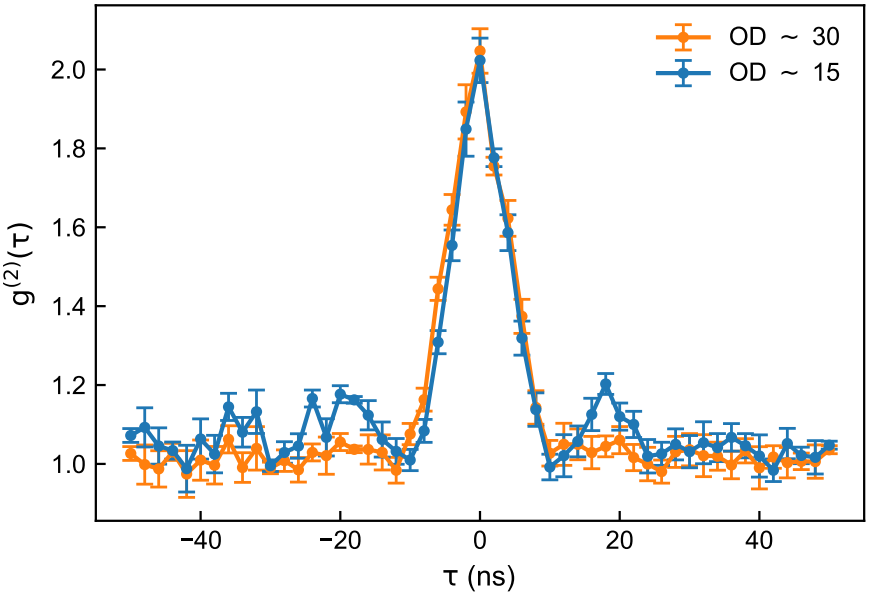

Figure 5.3: Intensity auto-correlation for Stokes field under different optical depths. Experimental conditions are given as $\Delta_p/2\pi = 40\,\mathrm{MHz}$, $P_p \approx 300\ \mu\mathrm{W}$ and $P_c \approx 8.5$ mW.

where collective dynamics evolve faster than the spontaneous relaxation of individual atoms [207], leading to intense and rapid radiation in the early stages of the emission process [228].

This suppression of Rabi oscillations is also reflected in the autocorrelation measurements. Under the experimental conditions of $\Delta_p/2\pi = 40\,\mathrm{MHz}$, pumping laser power $P_p \approx 300\,\mu\mathrm{W}$ and coupling field power $P_c \approx 8.5\,\mathrm{mW}$, varying the optical depth range from 5 to 30 does not lead to significant changes in the zero-delay intensity correlation $g^{(2)}(0)$ and its full width at half maximum (FWHM) for either Stokes or anti-Stokes modes. Notably, at high optical depth, the sideband structure of the Stokes field is strongly suppressed, as shown in Figure 5.3.

Our steady-state SFWM experiment with a large atomic ensemble operates under distinct drive conditions: the pumping field remains in the unsaturated ($s_{\mathrm{p,eff}} \ll 1$), while the coupling field is strongly saturated ($s_{\mathrm{c,eff}} \gg 1$). In this scenario, we observe intensity auto-correlations for both the Stokes and anti-Stokes modes, with $g^{(2)}(0) \approx 2$. These auto-correlation results are consistent with the thermal statistics of a two-mode squeezed vacuum (TMSV) state after tracing over one mode. The TMSV state arises from an effective macroscopic model, in which the atom-light

interaction is effectively involved in a nonlinear coupling strength between two optical modes. However, this framework does not explicitly capture how microscopic nonlinear processes of individual atoms contribute to the build-up of autocorrelation. However, this framework fails to explain how the autocorrelation arises from the nonlinear dynamics of individual atoms at the microscopic level. On the other hand, a zero-delay intensity of $g_N^{(2)}(0) \approx 2 - 2/N$ is also predicted in the large atom number limit as a signature of the superradiance [265–267]. As discussed in Appendix D, the derivation of intensity correlations in collective emission from randomly distributed emitters relies on the spin-wave approximation, where the dipole amplitude of a given atom depends on its position only through a phase factor [264]. This approximation is similarly employed in the modeling of the spontaneous emission [212]. Given that a second-order correlation of $g^{(2)} = 2$ can be interpreted by various mechanisms and is not unique to collective emission, whether the observed intensity auto-correlation can be attributed to collective behavior remains an open question.

5.4 Summary

In conclusion, we have observed several nontrivial features in biphoton generation from a cold atomic cloud that deviate from previous theoretical predictions. In particular, the quartic scaling of the correlated photon pair rate with optical depth serves as a compelling hallmark of collective emission in an extended, disordered atomic system. This superradiance arises from the coupling between the atomic ensemble and radiation modes, which is influenced by the geometry of the cloud. This work introduces a novel platform for investigating superradiant behavior through correlated photon pairs, offering an alternative to traditional pulsed excitation schemes. This approach may enhance the signal-to-noise ratio or mitigate the ring-down or after-pulse effects of optical pulsed excitation. Furthermore, this biphoton generation scheme is not confined to a disordered system. Its potential extension to ordered or small-scale atomic configurations offers a new paradigm for studying steady-state collective emission.

Chapter 6

Higher-order correlations and multiphoton

Nonclassical multiphoton states of light are essential resources for quantum computing [268], quantum communication [137], and quantum lithography [269, 270]. These states exhibit distinct coherence and entanglement properties, such as photon-number squeezing (in either single-mode or two-mode configurations) [40, 98], multiphoton quantum interference [42, 117], and even multipartite entanglement [42, 132, 133]. This chapter presents our investigation into the direct characterization of multiphoton states such as the $|2,2\rangle$ state, a representative example of multiple pair generation in a bright, narrowband correlated photon-pair source based on SFWM in a cold atomic ensemble. Our primary focus is on the higher-order temporal correlations between two coupled modes.

6.1 Introduction

In the discrete photon-number basis, the single-mode Fock states have defined photon numbers in individual modes. Multi-mode states $|n,m\rangle$ represent well-defined photon numbers in distinct modes and can exhibit quantum correlations between these modes. For example, the simplest case, $|1,1\rangle$, is typically referred to as a correlated photon pair; the $|2,2\rangle$ state, in contrast, exemplifies a correlated four-photon state, with two photons in each of the two distinct modes. While SPDC and SFWM processes are most commonly employed as sources of correlated photon pairs, the quantum states they produce naturally include higher-order components, which correspond to the simultaneous generation of multiple indistinguishable pairs. Arising from higher-order terms in the interaction Hamiltonian, these multi-pair

contributions carry nontrivial correlations beyond independent pairwise emission. Therefore, they provide a valuable resource for exploring the dynamics and statistics of nonclassical multiphoton states.

Due to the inherently low pair-generation probability of SPDC under continuous-wave (CW) pumping, multi-pair components are typically accessed by operating in a high-gain regime [110, 111, 271, 272] using pulsed excitation. This approach necessitates high instantaneous pump powers, often orders of magnitude greater than those used in CW experiments. When the pulse duration is shorter than or comparable to the coherence time ($\tau_c \sim 100$ fs to a few ps), the mean photon number per pulse increases significantly, representing a high probability of multi-pair generation. However, the short coherence time relative to detector timing resolution generally precludes the detailed resolution of temporal structures within these higher-order correlations.

Our narrowband correlated photon-pair source, characterized by its long coherence time and high brightness, allows for the observation of rich temporal features within higher-order correlations, overcoming limitations of other approaches. Unlike pulsed excitation schemes where photon states are confined to brief pulse durations, our CW-pumped SFWM process generates stationary coupled fields, manifesting as a continuous flux of photons. Consequently, characterizing joint higher-order correlation functions necessitates identifying multiphoton events across various time bins and detection channels. We have developed a statistical method to solve this problem instead of same-time-bin coincidence measurements. This method can be naturally extended to arbitrary orders of cross-time-bin coincidences, allowing for a more complex characterization of multi-channel correlations.

From the perspective of two coupled fields, the macroscopic SFWM process can be described by an effective two-mode interaction Hamiltonian [40, 98]. This Hamiltonian, which acts on the two field modes, is given by

$$\hat{H}_{\text{eff}} = i\hbar\kappa(\hat{a}_{as}^{\dagger}\hat{a}_{s}^{\dagger} - \hat{a}_{as}\hat{a}_{s})\,, \tag{6.1}$$

where κ is the effective nonlinear parametric coupling coefficient between the two coupled modes, and $\hat{a}_s$ ($\hat{a}_{as}$) is the annihilation operator for the Stokes (anti-Stokes) mode. When pump fields are on, the system evolves under the corresponding unitary

operator as follows

$$|\psi(t)\rangle = \exp\left(-\frac{i}{\hbar}\hat{H}_{\text{int}}t\right)|0,0\rangle\,. \tag{6.2}$$

With the squeezing parameter $r = \kappa t$, such a unitary evolution is equivalent to a two-mode squeezing operator $\hat{S}(r)$, expressed by

$$\hat{S}(r) = \exp\left(r\hat{a}_{as}^{\dagger}\hat{a}_{s}^{\dagger} - r\hat{a}_{as}\hat{a}_{s}\right)\,. \tag{6.3}$$

Applying this squeezing operator to the initial vacuum states of the Stokes and anti-Stokes modes leads to the generation of a two-mode squeezed vacuum (TMSV) state [40, 273, 274], which is also referred to as an entangled two-mode Gaussian state [274], and can be expressed in the Fock basis as

$$|\psi\rangle = \sqrt{1-\lambda^2}\sum_{n=0}^{\infty}\lambda^n|n\rangle_s|n\rangle_{as}\,, \tag{6.4}$$

where λ refers to the single-pair probability amplitude, related to the squeezing parameter by $\lambda = \tanh r$. The states $|n,n\rangle$ represent the number state with the same number of photons n in each mode. The TMSV state is a pure and quadrature (EPR-type) entangled state with thermal reduced state [274, 275]. The first-order term $|1,1\rangle$ refers to the correlated photon pair from such a process. In contrast, the second-order term $|2,2\rangle$ represents the simultaneous generation of two photon pairs, which are not independent but exhibit nontrivial correlations inherent to the quantum nature of the squeezing process.

6.2 Experimental protocols

To investigate multiphoton events and higher-order correlations, one approach is to employ photon-number-resolving detectors in each mode to obtain the photon number distribution. An alternative method is to split the photons using beam splitters and detect them with single-photon detectors, which can detect only one photon event at a time. As shown in Figure 6.1, the experimental setup builds upon the photon pair collection scheme described in Chapter 4, replacing single-mode photon detection with Hanbury Brown and Twiss (HBT) [120] type configurations for each mode. Specifically, after passing through the etalon filters, the collected light in each mode (Stokes and anti-Stokes) is split by a 50:50 beam splitter, and the two outputs from this splitter are each directed to separate single-photon detectors.

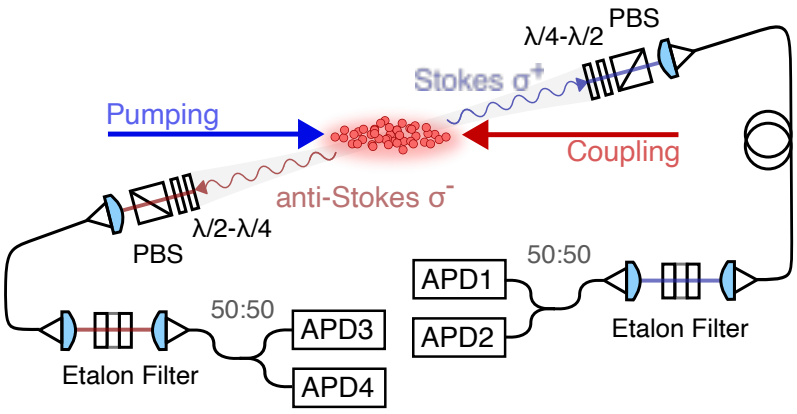

Figure 6.1: Schematic of the experimental setup, including the counter-propagating pump, phase-matched collection, and Hanbury Brown–Twiss (HBT) configurations for photon correlation measurements.

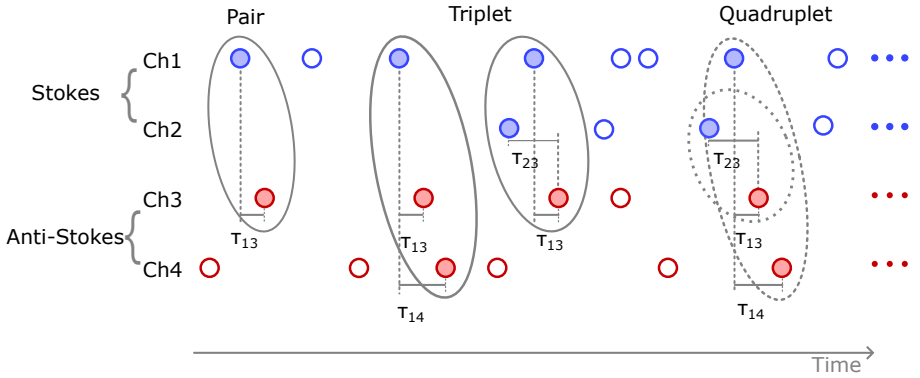

Figure 6.2: Schematic of multifold coincidence searching.

6.3 Algorithm for multifold coincidences

In contrast to broadband photon pairs, which are typically measured as coincidences within the same time bin, narrowband photon pairs exhibit long coherence times. This extended coherence often results in the constituent photons of a pair being detected in different time bins. To obtain the joint higher-order correlation functions, our method first efficiently identifies two-fold coincidences between selected channel pairs using a sliding time window. Subsequently, it extends the search to higher-order coincidences (e.g., three-fold or four-fold) by filtering candidate events based on these initially identified pairs. This hierarchical approach significantly reduces the computational complexity compared to a brute-force, full combinatorial search.

As shown as Figure 6.2, pairwise coincidences between two channels are determined as follows: a photon event in one channel (the 'trigger' channel) initiates a search for corresponding photon events in the other channel (the 'target' channel) within a predefined analysis interval $[\tau_a, \tau_b]$ relative to the trigger time. This interval is chosen to be larger than the two-photon coherence time to capture the pair's temporal features. If a photon is found in the target channel within this interval, a pair event is registered with their respective timestamps, (t_1, t_3), where t_1 is the trigger time and t_3 is the time of the coincident photon in the target channel. A histogram of the relative delays $(t_3 - t_1)$ for all such registered pairs yields the two-fold coincidence distribution. Triplet coincidences are identified by finding specific overlaps between previously identified pair events. For example, to identify a triplet involving channels 1, 3, and 4, we would look for two pair events, such as (t_1, t_3) (linking channels 1 and 3) and (t_1', t_4) (linking channels 1 and 4). If these two pairs share the same trigger photon in channel 1 (i.e., $t_1 = t_1'$), a triplet event is recorded as (t_1, t_3, t_4).

Quadruplet events are constructed in a similar hierarchical manner. For instance, a quadruplet can be identified by finding a coincidence between an established triplet (t_1, t_3, t_4) and an additional pair event, defined as (t_2, t_3'). If this triplet and pair share a common photon in one of their constituent channels (e.g., if $t_3 = t_3'$ for a photon in channel 3), they are grouped into a quadruplet event, such as (t_1, t_2, t_3, t_4).

By extending this algorithmic approach, N-fold coincidences can be efficiently identified and analyzed. It is important to note, however, that due to the finite width of the analysis interval, the adequate search volume for higher-order coincidences experiences an edge effect which reduces the accessible volume from the ideal $(\tau_b - \tau_a)^{N-1}$ parameter space for N-fold coincidences. To mitigate this effect when characterizing temporal features, the analysis interval is typically chosen to be significantly larger than the relevant correlation times.

6.4 Joint third-order correlation

Higher-order coherences of optical fields usually reflect their multiphoton contributions. In our multi-mode system, we use the term "joint" to emphasize that these correlations describe multiphoton events where cross-correlations between coupled

modes (Stokes and anti-Stokes) and auto-correlations within the same mode (either of them) are simultaneously relevant. Such a correlation function is measured using triple-coincidence counting across three detection channels, and they are classified into two scenarios: (i) two anti-Stokes photons heralded by a single Stokes photon, and (ii) two Stokes photons heralded by a single anti-Stokes photon. For instance, the joint third-order correlation for scenario (i) is expressed as

$$g^{(1,2)}(t_3,t_4,t_s)=\frac{\langle\hat{E}_s^{(-)}(t_s)\hat{E}_{as}^{(-)}(t_3)\hat{E}_{as}^{(-)}(t_4)\hat{E}_{as}^{(+)}(t_4)\hat{E}_{as}^{(+)}(t_3)\hat{E}_s^{(+)}(t_s)\rangle}{\langle\hat{E}_s^{(-)}(t_s)\hat{E}_s^{(+)}(t_s)\rangle\langle\hat{E}_{as}^{(-)}(t_3)\hat{E}_{as}^{(+}(t_3)\rangle\langle\hat{E}_{as}^{(-)}(t_4)\hat{E}_{as}^{(+)}(t_4)\rangle}\,, \tag{6.5}$$

where $\hat{E}_{s(as)}^{(-)}(t_i)$ denotes the negative-frequency component of the corresponding field, while the subscript of t_i refers to the detection channels. Under conditions of CW pumping and single-photon level detection, the joint third-order correlation function can be expressed in terms of photonic field operators and formulated as a function of two relative time delays:

$$g^{(1,2)}(\tau_{3\text{-}s},\tau_{4\text{-}s})=\frac{\langle\hat{a}_{as}^{\dagger}(t_4)\hat{a}_{as}^{\dagger}(t_3)\hat{a}_s^{\dagger}(t_s)\hat{a}_s(t_s)\hat{a}_{as}(t_3)\hat{a}_{as}(t_4)\rangle}{\langle\hat{a}_s^{\dagger}(t_s)\hat{a}_s(t_s)\rangle\langle\hat{a}_{as}^{\dagger}(t_3)\hat{a}_{as}(t_3)\rangle\langle\hat{a}_{as}^{\dagger}(t_4)\hat{a}_{as}(t_4)\rangle}\,, \tag{6.6}$$

where $\hat{a}_{s(as)}(t_i)$ denotes the annihilation operators for the Stokes (anti-Stokes) mode measured in channel i. This function reflects the photon bunching at the third-order level. As a comparison, for classical thermal light, the normalized third-order correlation function is $g^{(3)}=3!=6$ [276]. In contrast, for quantum sources like squeezed light, the joint triplet coincidences can reveal deviations from these classical statistics, indicating the presence of multiphoton correlations in non-classical light.

6.4.1 Theory

The TWSV state is also termed as a zero-mean-field Gaussian state [274, 275], as its Wigner function is also Gaussian [275]. According to Wick's probability theorem (or Isserlis' theorem) [122], for such a state, all even-order operator moments are entirely determined by the second-order moments (covariance matrix). Let $\hat{a}_s$ and $\hat{a}_{as}$ denote the annihilation operators for the Stokes and anti-Stokes modes, respectively. These bosonic field operators obey the following commutation relations:

$$[\hat{a}_j(t_1),\hat{a}_j^{\dagger}(t_2)]=\delta(t_1-t_2)\,,\ j\in\{s,as\}\,, \tag{6.7}$$

where δ_{jk} is the Kronecker delta function. For an ideal TMSV state, which possesses a joint Gaussian spectral profile, the expectation values of second-order field moments (expectation value of photon number) are identical for either the Stokes or anti-Stokes mode. In other words, the photons in the two modes are perfectly paired. Neglecting the rapidly oscillating terms, we define the first-order correlation function as $R(\tau)$, such that:

$$\begin{aligned} R(\tau) := \langle \hat{a}_s^\dagger(t+\tau)\hat{a}_s(t)\rangle = \langle \hat{a}_{as}^\dagger(t+\tau)\hat{a}_{as}(t)\rangle\,, \\ \langle \hat{a}_s(t+\tau)\hat{a}_s(t)\rangle = \langle \hat{a}_{as}(t+\tau)\hat{a}_{as}(t)\rangle = 0\,. \end{aligned} \tag{6.8}$$

At zero delay $\tau = 0$, the value of $R(\tau)$ corresponds to the mean photon number in that mode. This value also represents the intrinsic single-channel photon rate (or flux) from the source, before accounting for detection efficiency. At the far-delay regime where $\tau > t_c$, $R(\tau) = 0$, indicating that the photons are uncorrelated beyond the coherence time t_c. On the other hand, between two coupled modes, phase-sensitive cross-correlations are denoted as

$$\begin{aligned} C(\tau) := \langle \hat{a}_s(t)\hat{a}_{as}(t+\tau)\rangle\,, \\ C^*(\tau) := \langle \hat{a}_{as}^\dagger(t)\hat{a}_s^\dagger(t+\tau)\rangle\,, \\ \langle \hat{a}_{as}^\dagger(t+\tau)\hat{a}_s(t)\rangle = \langle \hat{a}_s^\dagger(t)\hat{a}_{as}(t+\tau)\rangle = 0\,. \end{aligned} \tag{6.9}$$

If the TMSV state has symmetry in the joint spectral function, then $\langle \hat{a}_s(t)\hat{a}_{as}(t+\tau)\rangle = \langle \hat{a}_{as}(t+\tau)\hat{a}_s(t)\rangle$. With the help of the Gaussian moment-factoring theorem [121, 122], the intensity cross-correlation between two coupled modes, i.e, the expectation value of a normally ordered fourth-order moment, can be expressed in terms of second-order moments as

$$\begin{aligned} G^{(2)}_{as\text{-}s}(\tau) =& \langle \hat{a}_{as}^\dagger(t+\tau)\hat{a}_s^\dagger(t)\hat{a}_s(t)\hat{a}_{as}(t+\tau)\rangle \\ =& \langle \hat{a}_{as}^\dagger(t+\tau)\hat{a}_s^\dagger(t)\rangle\langle \hat{a}_s(t)\hat{a}_{as}(t+\tau)\rangle \\ &+ \langle \hat{a}_{as}^\dagger(t+\tau)\hat{a}_s(t)\rangle\langle \hat{a}_s^\dagger(t)\hat{a}_{as}(t+\tau)\rangle \\ &+ \langle \hat{a}_{as}^\dagger(t+\tau)\hat{a}_{as}(t+\tau)\rangle\langle \hat{a}_s^\dagger(t)\hat{a}_s(t)\rangle \\ =& R^2(0) + C^*(\tau)C(\tau)\,, \end{aligned} \tag{6.10}$$

where $C^*(\tau)C(\tau) = |C(\tau)|^2$ is two-photon interference in coupled modes, analogous to the two-photon interference in a single mode [277]. The joint third-order correlation involving one Stokes channel and two anti-Stokes channels, which experimentally corresponds to measuring triple coincidences across these three channels,

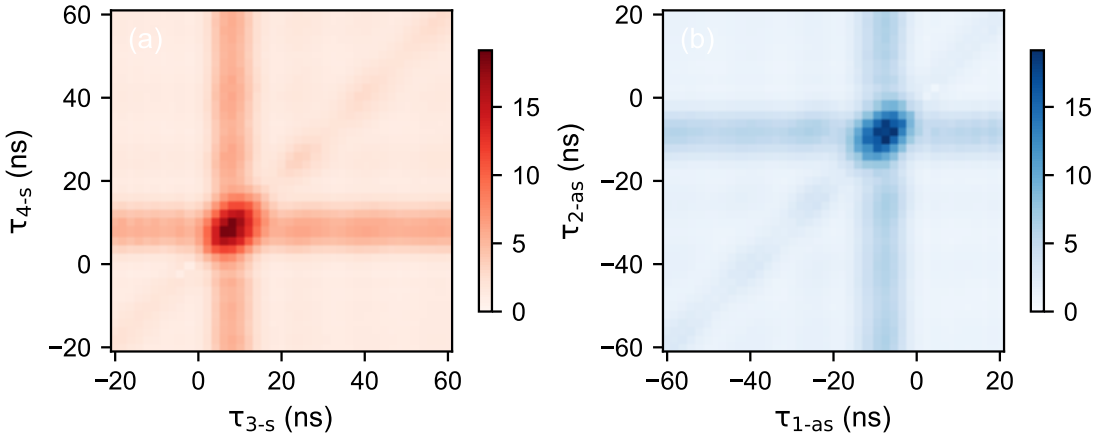

Figure 6.3: Normalized joint third-order correlations: (a) correlation between two anti-Stokes photons, heralded by a Stokes photon; (b) correlation between two Stokes photons, inversely heralded by an anti-Stokes photon.

is theoretically predicted as

$$\begin{aligned} G^{(1,2)}(\tau_{3\text{-}s}, \tau_{4\text{-}s}) =& R(0)[R^2(0) + |R(\tau_{3\text{-}4})|^2] \\ &+ R(0)[|C(\tau_{3\text{-}s})|^2 + |C(\tau_{4\text{-}s})|^2] \\ &+ 2\mathrm{Re}\{C(\tau_{3\text{-}s})C^\star(\tau_{4\text{-}s})R(\tau_{3\text{-}4})\}\,. \end{aligned} \tag{6.11}$$

Here, the superscript $(1,2)$ indicates that the joint third-order correlation involves two distinct modes, rather than representing a third-order correlation within a single mode. Among these decomposed terms, the first term represents entirely uncorrelated coincidences, incorporating the thermal components present in the anti-Stokes mode. The second set of terms describes uncorrected coincidences between a correlated pair (e.g., one Stokes and one anti-Stokes photon) and uncorrelated single counts in the remaining anti-Stokes channel. The final term signifies the contribution from double-pair correlations. The joint third-order correlation function for the case of one anti-Stokes photon and two Stokes photons yields a similar decomposition with inverse timing order.

6.4.2 Results

To maximize the collection of multiphoton events, we set the pump field power to approximately $800\,\mu$W with a detuning of $\Delta_p/2\pi = +40\,$MHz, and the coupling

field power to about 8.5 mW. Under these conditions, the measured cross-correlation between Stokes and anti-Stokes photons reaches a maximum value of $g^{(2)}_{as\text{-}s} \simeq 5.5$. We then recorded photon detections continuously for 2550 s ($\simeq 0.7$ h) to accumulate sufficient statistics for constructing higher-order correlation functions. Figure 6.3 displays the joint third-order correlation functions for the case of one Stokes photon, two anti-Stokes photons, and that of one anti-Stokes photon, two Stokes photons. Under these conditions, the measured cross-correlation between Stokes and anti-Stokes photons reaches a maximum value of $g^{(1,2)}_{\max} \simeq 18.5$ and $g^{(2,1)}_{\max} \simeq 19.2$, respectively, significantly exceeding the classical threshold $g^{(3)} = 6$. Meanwhile, the two-dimensional correlations show pronounced horizontal and vertical ridges, indicating strong cross-correlations between the heralding photon and its partner, and a weaker diagonal ridge, characteristic of thermal correlations within the heralded mode.

In the example shown in Figure 6.4, the observed triple coincidences are consistent with the prediction from Equation 6.11. The flat background given by $R_a = R_s R_3 R_4 t_b^2$ corresponds to $R^3(0)$, while the diagonal features represents the thermal properties of uncorrelated photons as $R_a g^{(2)}_{as}(\tau_{3\text{-}4})$. Besides the sum of two ridges, which matches the term of $R(0)[|C(\tau_{3\text{-}s})]^2 + |C(\tau_{4\text{-}s})]^2]$, the area of high coincidence counts within coherence time is further contributed by the interference term $2\mathrm{Re}\{C(\tau_{3\text{-}s})C^*(\tau_{4\text{-}s})R(\tau_{3\text{-}4})\}$ in Equation 6.11, which represents the correlation between photon pairs, corresponding to $2R_a(g^{(2)}_{as\text{-}s}(\tau) - 1)\sqrt{g^{(2)}_{as}(\tau) - 1}$. These triplet counts represent the direct measurement of $|1, 2\rangle$ triplets from the four-photon state $|2, 2\rangle$ across three detection channels. For correlated photon pairs exhibiting thermal statistics, the predicted ratio between maximal triplet counts and counts along the horizontal or vertical ridges is $4[(g^{(2)}_{as\text{-}s} - 1) + g^{(2)}_{as\text{-}as}]/g^{(2)}_{as\text{-}s} \simeq 4$ [278]. This ratio directly reflects the correlation between photon pairs. In contrast to the second-order auto-correlation function, which may be dominated by thermal statistics arising from incoherent scattering components, the third-order correlation provides direct evidence for the presence of genuine photon-pair correlations. In other words, the correlated photon pairs cannot be treated as independent events following Poissonian statistics. Instead, the pairs themselves exhibit thermal statistics.

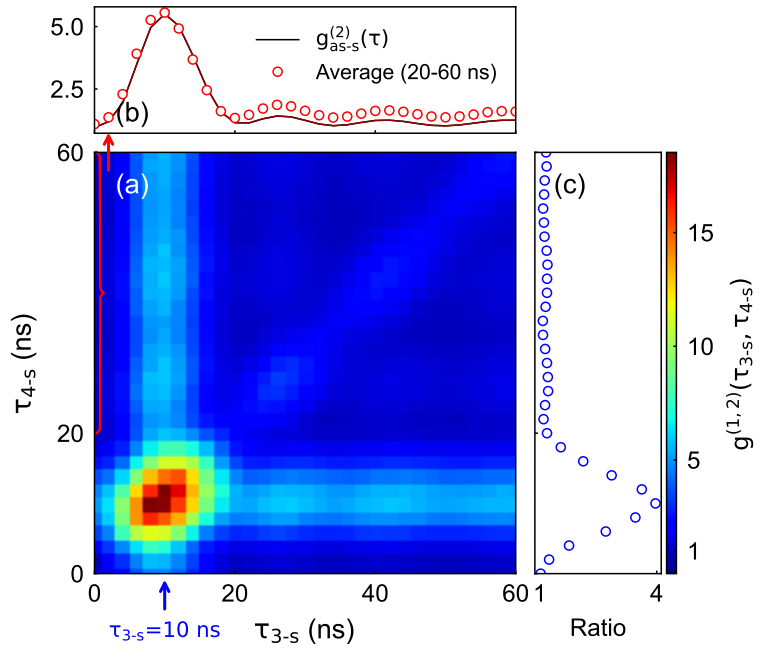

Figure 6.4: (a) Normalized triplet coincidence, heralded by Stokes photons, as a function of time delay $\tau_{3\text{-}s}$ and $\tau_{4\text{-}s}$. The data is acquired over 0.7 hours. The normalization factor is the accidental triplet rate $R_s R_3 R_4 t_b^2 T_m$, with the time bin being $t_b = 2\,\text{ns}$. (b) Red dots: Mean normalized triplet count, averaged over $\tau_{4\text{-}s}$ from 20 ns to 60 ns. Solid line: normalized cross-correlation function $g^{(2)}_{as,s}(\tau_{3\text{-}s})$ between Stokes and Ch3. (c) Ratio of normalized triple coincidence peak value to the average value along the vertical ridge away from the peak. Blue dots: triple coincidences at $\tau_{3\text{-}s} = 10\,\text{ns}$, normalized by the ridge counts over $\tau_{4\text{-}s}$ from 20 ns to 60 ns.

6.5 Joint fourth-order correlation

To obtain further insight into the multiphoton correlation in such a photon pair source, we extend the analysis from the joint third-order correlation to the joint fourth-order correlation, capturing the full statistics of four-photon coincidences across two coupled modes. The joint fourth-order correlation function, denoted by the superscript $(2,2)$ to indicate two-photon detection in each of the two distinct modes, is given as

$$g^{(2,2)}(\tau_{21}, \tau_{41}, \tau_{31}) = \frac{\langle \hat{a}^\dagger_{as}(t_4)\hat{a}^\dagger_{as}(t_3)\hat{a}^\dagger_s(t_2)\hat{a}^\dagger_s(t_1)\hat{a}_s(t_1)\hat{a}_s(t_2)\hat{a}_{as}(t_3)\hat{a}_{as}(t_4)\rangle}{\langle \hat{a}^\dagger_s(t_1)\hat{a}_s(t_1)\rangle\langle \hat{a}^\dagger_s(t_2)\hat{a}_s(t_2)\rangle\langle \hat{a}^\dagger_{as}(t_3)\hat{a}_{as}(t_3)\rangle\langle \hat{a}^\dagger_{as}(t_4)\hat{a}_{as}(t_4)\rangle}\,, \tag{6.12}$$

where the relative delays $\tau_{21} = t_2 - t_1$, $\tau_{41} = t_4 - t_1$ and $\tau_{31} = t_3 - t_1$ are defined under the CW pumping condition. This normalized fourth-order correlation captures the four-photon correlations, enabling direct measurement of the $|2,2\rangle$ component in the photon-pair source with the accidental measurement of four photons. For simplicity, we focus on the unnormalized fourth-order correlation function $G^{(2,2)}(\tau_{21}, \tau_{41}, \tau_{31})$ in the following analysis.

6.5.1 Theory

The joint fourth-order correlation exhibits a more intricate structure, comprising combinations of second-order moments based on Wick's theorem [122]. Under the same mechanism detailed in § 6.4.1, the fourth-order correlation $G^{(2,2)}(\tau_{21}, \tau_{41}, \tau_{31})$ factors into second-order moments, yielding non-zero contributions as

$$
\begin{aligned}
G^{(2,2)}(\tau_{21}, \tau_{41}, \tau_{31}) = {} & R^4(0) \quad \text{(i)} \\
& + R^2(0) \left[|R(\tau_{43})|^2 + |R(\tau_{21})|^2 \right] \quad \text{(ii)} \\
& + |R(\tau_{43})|^2 |R(\tau_{21})|^2 \quad \text{(iii)} \\
& + R^2(0) \left[|C(\tau_{23})|^2 + |C(\tau_{24})|^2 + |C(\tau_{13})|^2 + |C(\tau_{14})|^2 \right] \quad \text{(iv)} \\
& + R(0) \operatorname{Re} \{ R(\tau_{34}) [C^*(\tau_{13}) C(\tau_{14}) + C^*(\tau_{23}) C(\tau_{24}) \\
& \qquad + C^*(\tau_{14}) C(\tau_{13}) + C^*(\tau_{24}) C(\tau_{23})] \} \quad \text{(v)} \\
& + R(0) \operatorname{Re} \{ R(\tau_{21}) [C^*(\tau_{13}) C(\tau_{23}) + C^*(\tau_{23}) C(\tau_{13}) \\
& \qquad + C^*(\tau_{14}) C(\tau_{24}) + C^*(\tau_{24}) C(\tau_{14})] \} \quad \text{(vi)} \\
& + |C(\tau_{13})|^2 |C(\tau_{24})|^2 + |C(\tau_{14})|^2 |C(\tau_{23})|^2 \quad \text{(vii)} \\
& + \operatorname{Re} \{ C^*(\tau_{24}) C^*(\tau_{13}) C(\tau_{14}) C(\tau_{23}) + C^*(\tau_{14}) C^*(\tau_{23}) C(\tau_{13}) C(\tau_{24}) \} \quad \text{(viii)} \\
& + \operatorname{Re} \{ R(\tau_{34}) R(\tau_{21}) [C^*(\tau_{24}) C(\tau_{13}) + C^*(\tau_{14}) C(\tau_{23}) \\
& \qquad + C^*(\tau_{23}) C(\tau_{14}) + C^*(\tau_{13}) C(\tau_{24})] \} \quad \text{(ix)} \,. \qquad (6.13)
\end{aligned}
$$

These terms arise from all possible pairwise contractions and reflect the Gaussian statistical nature of the underlying fields. In the above expansion, the terms can be interpreted as follows: Terms (i), (ii), and (iii) refer to the accidental coincidence background arising from uncorrelated single-photon events and thermal photon bunching. Terms (iv) represent accidental quadruplet events, consisting of correlated photon pairs in two channels, while the remaining detection channels

register uncorrelated single-photon events. Terms (v) and (vi) represent path interference in the HBT setup involving three distinct paths for the four-photon states. Terms (vii) correspond to two independent and uncorrelated photon pairs detected without interference. Terms (viii) describe the purely fourth-order interference terms, revealing the four-photon coherence in the TMSV state. They arise when two photon pairs are indistinguishable in all degrees of freedom, leading to path superposition between the detection combinations (1,3)-(2,4) and (1,4)-(2,3). Additionally, terms (ix) capture the more complicated hybrid interference structure for the double-pair states in the double-HBT setup. These interference terms require that the phase coherence between two pairs in $|2,2\rangle$.

In this paragraph, we aim to distinguish several photon states and identify the corresponding expected observations for each. If the output state is strictly modeled as a pure two-photon state $|1,1\rangle$ in two modes, the four-fold coincidences cannot be observed, as only two photons are present within the coherence time. In this case, all fourth-order interference terms vanish. Such a pure two-photon state, without contributions from multi-pair components, can be realized using a single emitter, where multi-pair emission is strictly prohibited and photon anti-bunching in each single mode is exhibited. If photon pairs are emitted independently, originating from different spatial or spectral modes, or from temporally separated events beyond the coherence time, then such pairs are distinguishable. The fourth-order interference terms will cancel due to a lack of phase coherence and mutual indistinguishability. Consequently, these contributions do not appear in multiphoton coincidence measurements. In contrast, if the photon state can be modeled as the TMSV state, higher-order coherence emerges, and multiphoton interference effects can be observed in the multifold coincidence measurements.

6.5.2 Results

In Figure 6.5, quadruple coincidence counts are displayed as a function of τ_{21}, τ_{31}, and τ_{41}, and they are presented without normalization due to low counts. In slices at fixed τ_{21}, particularly around $\tau_{21} \approx 0$, the quadruple coincidences have a similar structure as seen in triple coincidences. As τ_{21} deviates away from zero, these quadruplet events become progressively uncorrelated. With a 20 ns coincidence

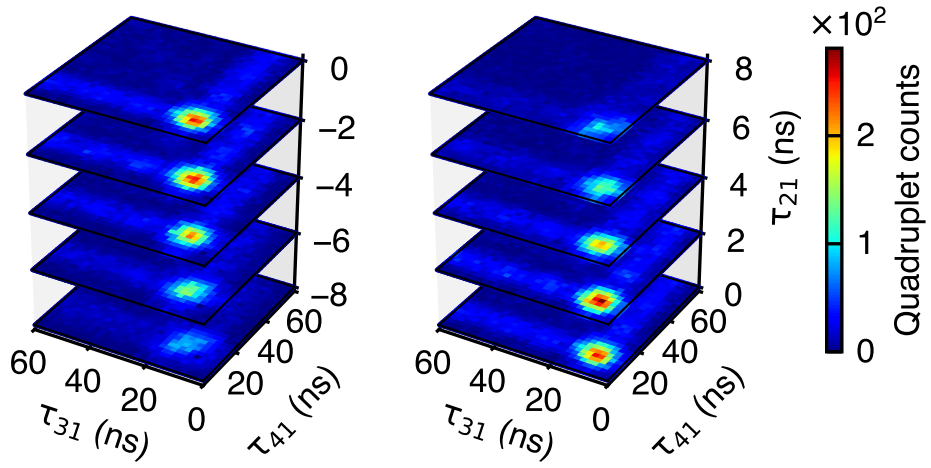

Figure 6.5: Unnormalized quadruple coincidences. Each panel shows four-fold coincidences from a detection in each channel with a fixed delay τ_{21} (in 2 ns time bins), plotted as a function of the delays τ_{31} and τ_{41}. The full set of panels spans different values of τ_{21}.

window applied to each mode, the observed bunched quadruple coincidences result from all terms in Equation 6.5.1, encompassing both accidental and interference contributions. These give rise to a rich temporal structure across the three-delay parameter space. As shown in § 6.7.2, the factorization of higher-order correlations into two-point correlations (i.e., the expectation values of second-order operator moments) provides a method to analyze accidental contributions in the overall coincidence measurements. After subtracting these accidental contributions, the remaining residuals correspond to genuine photon pair correlations or direct detections of the $|2,2\rangle$ photon number states. These residuals can then be used to reconstruct the pure photon state emitted by the source.

6.6 Multifold coincidence rate

The properties of the TMSV state are encoded in the ratio of single-pair to double-pair generation probabilities. To explore this, we measure multifold coincidence rates using a 20 ns coincidence window, without correcting for accidentals. Figure 6.6 shows how single-photon count rates and multiphoton coincidence rates vary with the power of the pumping field (780 nm), which primarily determines the strength of the SFWM process. A significant observation is that the multifold coincidence

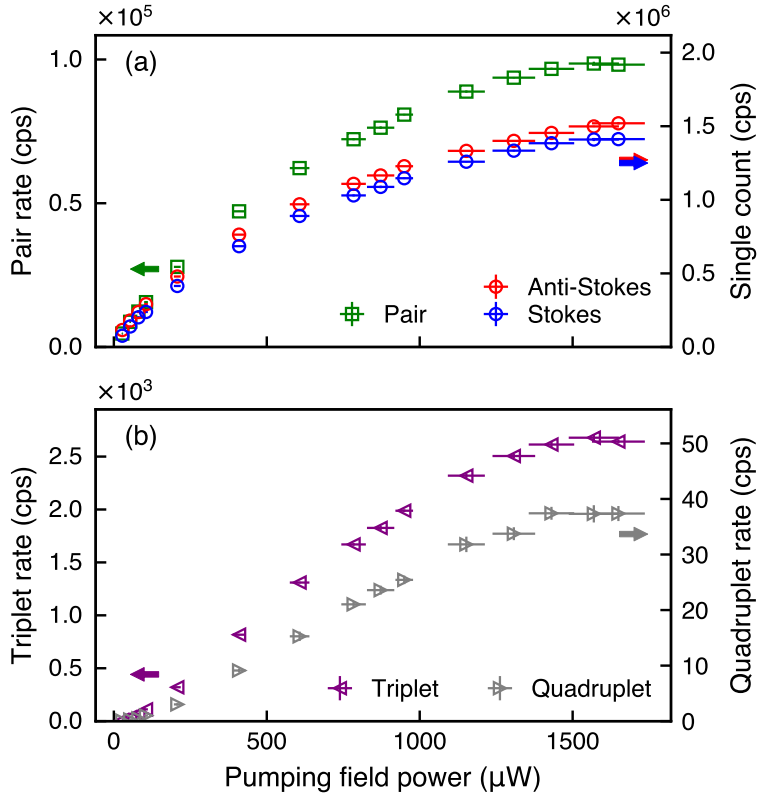

Figure 6.6: (a) Single count rates in Stokes and anti-Stokes channels (right axis) and photon pair rate (left axis) as functions of pumping field power. (b) Photon triplet rates across three detector channels (left axis) and photon quadruplet rate (right axis) as functions of pumping field power. The detuning of the 780 nm pumping field is $\Delta_p/2\pi = +40\,\mathrm{MHz}$, while the coupling field is resonant with a power of 8.5 mW. The atomic cloud has OD $\simeq 30$.

rates saturate as the single-photon count rate reaches saturation. In the weak power regime, both the single-photon count rate and the pair rate scale linearly with the power of the pump field, before gradually saturating. In contrast, the triplet and quadruplet rates scale quadratically with the pumping field power and then also exhibit saturation.

Because the detection efficiencies act as a constant linear factor on the detection channels, the intrinsic power-law scaling between single-pair and double-pair generation is preserved in the measured multifold coincidence rates. Accordingly, we plot these coincidence rates against the single-count rates in each channel, using logarithmic scales on both axes, as shown in Figure 6.7. The photon pair rates $R_p = R_{13} + R_{14} + R_{23} + R_{24}$ scale approximately linearly with the single-

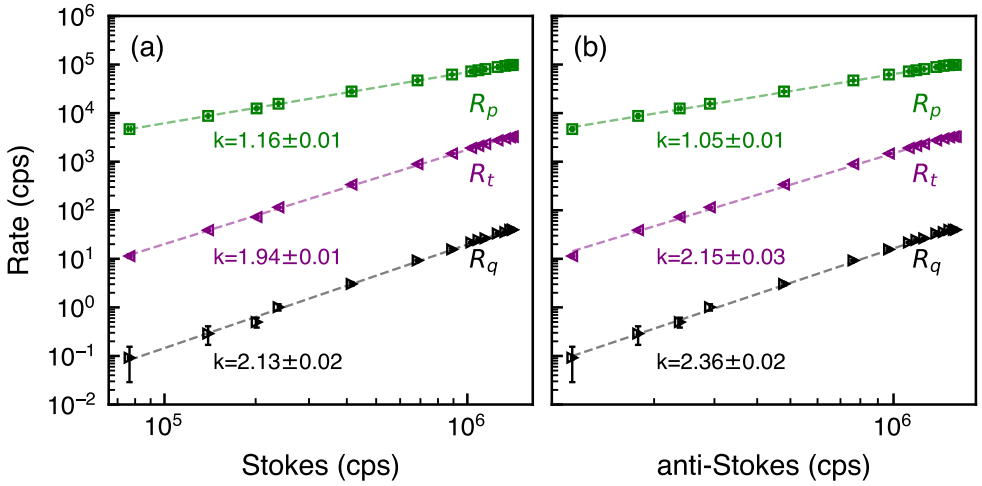

Figure 6.7: Detected photon pair rate R_p, photon triplet rate R_t, and photon quadruplet rate R_q relative to (a) the single count rate R_s in the Stokes mode and (b) the single count rate R_{as} in the anti-Stokes mode. Both axes are plotted on a logarithmic scale. The variation in the single count rates is achieved by varying the power of the pumping laser while keeping the other parameters constant. Photon-pair, triplet, and quadruplet rates are defined within a 20 ns coincidence window, without correcting for accidental coincidences.

count rates, with fitted slope parameters of (1.16 ± 0.01) for the Stokes channel R_s and (1.05 ± 0.01) for the anti-Stokes channel R_{as}. The photon triplet rates $R_t = R_{134} + R_{234} + R_{123} + R_{124}$ indicate an exponent of (1.94 ± 0.01) for R_s and an exponent of (2.15 ± 0.03) for R_{as}. Finally, the photon quadruplet rates $R_q = R_{1234}$ exhibit power-law scaling with exponents of (2.13 ± 0.02) for the Stokes mode and (2.35 ± 0.02) for the anti-Stokes mode, respectively. The exponents of R_t and R_q concerning the single-count rates are both close to 2, as expected from the fact that triplet and quadruplet photons originate from the $|2, 2\rangle$ component of the TWSV state, which scales quadratically with the single-pair emission probability.

6.7 Reconstruction of the photon state

The output state from the SFWM process is, in principle, a pure quantum state rather than a mixed one. Reconstructing this state and quantifying its properties involve analyzing the generation rates of both single-photon pairs and photon quadruplets, based on the measured detection rates and corrections for accidental

contributions. Accurate inference of the initial quantum state requires careful consideration of experimental imperfections, including optical losses and non-unit detection efficiencies. Therefore, correcting for these losses is essential for reliably determining the intrinsic generation probabilities of single- and multi-photon pairs.

6.7.1 Loss modeling

Dark counts from the detectors and incoherently scattered photons from the atomic cloud contribute solely to a flat accidental background in coincidence measurements (neglecting the thermal correlation of incoherently scattered photons). As a result, the measured correlated photon pairs remain unaffected by these sources of noise, and only the overall detection efficiencies are involved in the final detection statistics. Referring to the theoretical treatment of imperfections in single-photon detectors [211], we can model the detection of a single photon in channel k using the following measurement operator:

$$\hat{D}(\eta_k) = \mathbb{1} - (1-\eta_k)^{\hat{a}^\dagger \hat{a}}\,. \tag{6.14}$$

Here, we use $\hat{a}$ to denote the annihilation operator for the Stokes mode, and $\hat{b}$ for the anti-Stokes mode in the following analysis. η_k denotes the total transmission and detection probability in channel k, which incorporates the transmission in the collection and filtering setup, 50% splitting efficiency of the beamsplitter, and quantum efficiency of the detector in this channel. Using this model, the probability of getting a click in this detector is expressed as $\mathrm{Tr}[\hat{D}(\eta_k)\hat{\rho}]$, where $\hat{\rho}$ is the density operator representing the initial photon state.

The detection of the correlated photon pair in one Stokes and one anti-Stokes detection channel is modeled as

$$\begin{aligned}\hat{D}_{\mathrm{s}}(\eta_k)\hat{D}_{\mathrm{as}}(\eta_l) &= \hat{D}_{\mathrm{s}}(\eta_k) \otimes \hat{D}_{\mathrm{as}}(\eta_l) \\ &= (\mathbb{1} - (1-\eta_k)^{\hat{a}^\dagger \hat{a}}) \otimes (\mathbb{1} - (1-\eta_l)^{\hat{b}^\dagger \hat{b}})\,.\end{aligned} \tag{6.15}$$

The detection of thermally correlated photon pairs in two channels of the same mode is evaluated using the normal-ordered approximation of the operator function $f(\hat{a}^\dagger\hat{a})$, given by

$$\begin{aligned}f(\hat{a}^\dagger\hat{a}) &= 1 - :(1-\eta)^{\hat{a}^\dagger\hat{a}}: \\ &= 1 - :e^{\hat{a}^\dagger\hat{a}\ln(1-\eta)}: \quad \approx 1 - :e^{-\eta\hat{a}^\dagger\hat{a}}:\,.\end{aligned} \tag{6.16}$$

Thus, the detections for thermally-correlated Stokes photon pairs in channels 1 and 2, and anti-Stokes photon pairs in channels 3 and 4, are respectively given by:

$$\begin{aligned}\hat{D}_{\mathrm{s}}(\eta_1)\hat{D}_{\mathrm{s}}(\eta_2) &= \mathbb{1} - (1-\eta_1)^{\hat{a}^\dagger\hat{a}} - (1-\eta_2)^{\hat{a}^\dagger\hat{a}} + (1-\eta_1-\eta_2)^{\hat{a}^\dagger\hat{a}} \\ \hat{D}_{\mathrm{as}}(\eta_3)\hat{D}_{\mathrm{as}}(\eta_4) &= \mathbb{1} - (1-\eta_3)^{\hat{a}^\dagger\hat{a}} - (1-\eta_4)^{\hat{a}^\dagger\hat{a}} + (1-\eta_3-\eta_4)^{\hat{a}^\dagger\hat{a}}\,.\end{aligned} \tag{6.17}$$

For a photon triplet consisting of two photons in the Stokes mode (detected in channels 1 and 2) and one photon in the anti-Stokes mode (detected in channel 3 or 4), the corresponding detection operator is given by:

$$\begin{aligned}\hat{D}_{\mathrm{s}}(\eta_1)\hat{D}_{\mathrm{s}}(\eta_2)\hat{D}_{\mathrm{as}}(\eta_l) &= \hat{D}_{\mathrm{s}}(\eta_1)\hat{D}_{\mathrm{s}}(\eta_2) \otimes \hat{D}_{\mathrm{as}}(\eta_l) \\ &= \mathbb{1} - (1-\eta_1)^{\hat{a}^\dagger\hat{a}} - (1-\eta_2)^{\hat{a}^\dagger\hat{a}} + (1-\eta_1-\eta_2)^{\hat{a}^\dagger\hat{a}} \\ &\otimes (\mathbb{1} - (1-\eta_l)^{\hat{b}^\dagger\hat{b}}\,.\end{aligned} \tag{6.18}$$

On the other hand, for a photon triplet consisting of two photons in the anti-Stokes mode (detected in channels 3 and 4) and one photon in the Stokes mode (detected in channel l = 1 or 2), the corresponding detection operator is given by:

$$\begin{aligned}\hat{D}_{\mathrm{s}}(\eta_k)\hat{D}_{\mathrm{as}}(\eta_3)\hat{D}_{\mathrm{as}}(\eta_4) &= \hat{D}_{\mathrm{s}}(\eta_k)\hat{D}_{\mathrm{as}}(\eta_3)\hat{D}_{\mathrm{as}}(\eta_4) \\ &= (\mathbb{1} - (1-\eta_k)^{\hat{a}^\dagger\hat{a}} \\ &\otimes \mathbb{1} - (1-\eta_3)^{\hat{b}^\dagger\hat{b}} - (1-\eta_4)^{\hat{b}^\dagger\hat{b}} + (1-\eta_3-\eta_4)^{\hat{b}^\dagger\hat{b}}\,.\end{aligned} \tag{6.19}$$

The detection of a photon quadruplet across four channels is modeled as follows:

$$\begin{aligned}&\hat{D}_{\mathrm{s}}(\eta_1)\hat{D}_{\mathrm{s}}(\eta_2)\hat{D}_{\mathrm{as}}(\eta_3)\hat{D}_{\mathrm{as}}(\eta_4) \\ &= \hat{D}_{\mathrm{s}}(\eta_1)\hat{D}_{\mathrm{s}}(\eta_2) \otimes \hat{D}_{\mathrm{as}}(\eta_3)\hat{D}_{\mathrm{as}}(\eta_4) \\ &= \mathbb{1} - (1-\eta_1)^{\hat{a}^\dagger\hat{a}} - (1-\eta_2)^{\hat{a}^\dagger\hat{a}} + (1-\eta_1-\eta_2)^{\hat{a}^\dagger\hat{a}} \\ &\otimes \mathbb{1} - (1-\eta_3)^{\hat{b}^\dagger\hat{b}} - (1-\eta_4)^{\hat{b}^\dagger\hat{b}} + (1-\eta_3-\eta_4)^{\hat{b}^\dagger\hat{b}}\,.\end{aligned} \tag{6.20}$$

Up to this point, we have established the operator representations for two-, three-, and four-fold coincidence measurements. Taking into account the detection paths in the double-HBT setup and the detection efficiencies, the measured coincidence probabilities correspond to the expectation values of these operators evaluated on the underlying photonic state. Assuming a pure quantum state, and without imposing any prior assumptions on the probability amplitudes of single- or double-pair emission, we arrive at a general form of the multiphoton state as

$$\sqrt{a_0}|0,0\rangle + \sqrt{a_1}|1,1\rangle + \sqrt{a_2}|2,2\rangle\,. \tag{6.21}$$

The correlated photon quadruplet detection probability is given as

$$P_{1234} = 4a_2\eta_1\eta_2\eta_3\eta_4\,. \tag{6.22}$$

The correlated photon triplet detection probabilities are

$$\begin{aligned} P_{123} &= 2a_2\eta_1\eta_2(2-\eta_3)\eta_3\,, \\ P_{124} &= 2a_2\eta_1\eta_2(2-\eta_4)\eta_4\,, \\ P_{134} &= 2a_2\eta_3\eta_4(2-\eta_1)\eta_1\,, \\ P_{234} &= 2a_2\eta_3\eta_4(2-\eta_2)\eta_2\,. \end{aligned} \tag{6.23}$$

The correlated photon pair probabilities are

$$\begin{aligned} P_{13} &= \eta_1\eta_3(a_1 + (2-\eta_1)(2-\eta_3)a_2)\,, \\ P_{14} &= \eta_1\eta_4(a_1 + (2-\eta_1)(2-\eta_4)a_2)\,, \\ P_{23} &= \eta_2\eta_3(a_1 + (2-\eta_2)(2-\eta_3)a_2)\,, \\ P_{24} &= \eta_2\eta_4(a_1 + (2-\eta_2)(2-\eta_4)a_2)\,. \end{aligned} \tag{6.24}$$

Here, $\eta_i, i \in \{1,2,3,4\}$ denotes the overall detection efficiency in each channel, which accounts for losses from collection, coupling, and detection. These efficiencies are evaluated through dedicated loss measurements. This efficiency can be further refined to include transmission losses within the atomic cloud, characterized by factors $(1-\eta_s)$ for the Stokes mode and $(1-\eta_{as})$ for the anti-Stokes mode. These additional losses contribute to the total transmission efficiency and can be inferred experimentally through measurements of photon triplets and quadruplets.

6.7.2 Accidentals and corrections

In the detection model, the detection probability of two photons between channel i and j corresponds to the correlated photon pair above the flat accidental coincidences. Correspondingly, it is corrected from the two-fold coincidence count rate by $R_iR_jt_c$, where $R_{i(j)}$ is the single-count rate in $i(j)$ modes and t_c is the coincidence window. The detection of photon triplets in channels i, j_1, j_2 (j_1, j_2 are two detection channels in the same mode) corresponds to the two-photon interference term in Equation 6.11. Thus, the correlated triplet rate is given by

$$c_{i,j_1,j_2} = R_{i,j_1,j_2} - R_iR_{j_2}R_{j_2}t_c^2 - (c_{j_1,j_2}R_i + c_{i,j_2}R_{j_1} + c_{i,j_1}R_{j_2})t_c\,, \tag{6.25}$$

where c_{j_1,j_2} represents the thermally-correlated pair rate and $c_{i,j_1(j_2)}$ denotes the correlated pairs between channels i and $j_1(j_2)$.

To determine the true photon quadruplet rate, c_q, accidental coincidences must be subtracted. Firstly, terms involving the single count rates are identified as accidental contributions. Second, accidental coincidences arising from thermally correlated pairs and individual correlated pairs also need to be corrected. As a result, the corrected photon quadruplet rate c_q is given by

$$\begin{aligned} c_q = c_{1234} &= R_{1234} \\ &- t_c^3 R_1 R_2 R_3 R_4 \quad \text{(i)} \\ &- t_c^2 (c_{12} R_3 R_4 + c_{34} R_1 R_2) \quad \text{(ii)} \\ &- t_c^2 (c_{13} R_2 R_4 + c_{14} R_2 R_3 + c_{23} R_1 R_4 + c_{24} R_1 R_3) \quad \text{(iv)} \\ &- t_c (c_{12} c_{34} + c_{13} c_{24} + c_{14} c_{23}) \quad \text{(iii), (vii)} \\ &- t_c (c_{123} R_4 + c_{124} R_3 + c_{134} R_2 + c_{234} R_1) \quad \text{(v), (vi)}\,, \end{aligned} \tag{6.26}$$

where c_{12} and c_{34} refer to the thermally-correlated pairs, and other c_{ij} represent the correlated pairs between different channels. c_{ijk} accounts for the correlated photon triplet rate corrected by the above correction procedures. The labels after each term correspond to various orders of accidental contribution, identified in the joint fourth-order correction function. Consequently, interference terms arising from coherent double-pair emissions, corresponding to (viii) and (ix) in Equation 6.5.1, remain in the corrected quadruplet rate. These surviving terms signify the direct detection of the genuine four-photon component of the TMSV state, as a signature of multiphoton interferences and nonclassical correlations.

At fixed pump and coupling powers of $800\,\mu$W and $10\,$mW, respectively, and with a pump detuning of $\Delta_p/2\pi = +40\,$MHz, the mean single-count rates are $R_s = (1.04 \pm 0.07) \times 10^6\,$cps for the Stokes channel and $R_{as} = (1.10 \pm 0.06) \times 10^6\,$cps for the anti-Stokes channel. After applying the relevant corrections, the correlated photon pair detection rate is given by $c_p = (4.85 \pm 0.08) \times 10^4\,$cps. The detection rate of correlated photon triplets consisting of one Stokes photon and two anti-Stokes photons in Ch3 and Ch4 is $c_{134} + c_{234} = (251 \pm 30)\,$cps, while the rate for triplets consisting of two Stokes photons in Ch1 and Ch2 and one anti-Stokes photon is $c_{123} + c_{124} = (246 \pm 21)$ cps. The correlated photon quadruplet rate after

accidental-subtraction is found to be $c_q = (3.0 \pm 1.0)$ cps.

Based on the loss model presented in § 6.7.1, the generation rates (generation probabilities) for $|1,1\rangle$ and $|2,2\rangle$ components can be evaluated based on the detection rates and the overall detection efficiencies, including the transmission and detection efficiency in each channel. The overall efficiencies in each channel are given as $\eta_1 \approx 0.078, \eta_2 \approx 0.083, \eta_3 \approx 0.080, \eta \approx 0.067$. In general, the inference of the intrinsic generation rate is sensitive to the estimation of the overall detection efficiencies. However, by examining the mismatch between the observed photon triplet and quadruplet count rates, one can infer the additional transmission factors that are not captured by the calibration of overall detection efficiencies. These include, for instance, residual absorption in the atomic cloud, unaccounted spatial mismatching, additional optical losses in the collection paths, and the overestimation of the detection efficiencies. These additional transmission efficiencies are evaluated as $\eta_1' \approx 0.30$, $\eta_2' \approx 0.28$, $\eta_3' \approx 0.32$, and $\eta_4' \approx 0.33$, for each detection channels, respectively. In this case, the four-photon state is expected to be generated at an initial rate of around $(2.3 \pm 0.9) \times 10^6$ cps within the volume defined by the collection mode. Meanwhile, the single-pair generation rate is evaluated to be $(1.2 \pm 0.4) \times 10^7$ cps. Modeling the photon source as a pure state, as given in Equation 6.7.1, the quantum state can be approximated as

$$|\Psi\rangle \approx \sqrt{0.703}|0,0\rangle + \sqrt{0.251}|1,1\rangle + \sqrt{0.046}|2,2\rangle. \tag{6.27}$$

The probability of double-pair emission, P_2, is approximately equal to the square of the single-pair emission probability, P_1, i.e., $P_2 \approx P_1^2$, consistent with the photon-number statistics of a TMSV state.

6.8 Summary

The multiple-channel coincidence search techniques we developed allow us to investigate higher-order temporal correlations in a correlated photon-pair source generated via the SFWM process in a cold atomic ensemble. In the joint third-order correlation functions, pair–pair correlations appear above the uncorrelated background, providing direct evidence that the measured photon pairs exhibit thermal bunching. In the joint fourth-order correlation functions, aside from complex

accidental and uncorrelated contributions, the residual quadruplet events provide a direct measurement of the photon-quadruplet state, corresponding to the higher-order components of a two-mode squeezed vacuum state. Both higher-order correlations are in good agreement with the predictions of the quantum Gaussian factoring theorem. The long coherence time of these photon pairs, resulting in a coherence length larger than the atomic cloud, allows us to take advantage of this property to investigate temporal higher-order correlations based on the photon statistics. Our observations provide further insight into how correlations build up among the photon pairs.

Chapter 7

Heralded single-photon source

This chapter investigates the application of narrowband correlated photon pairs as heralded single-photon sources. Commonly used single-variable heralded autocorrelation measurements can be limited in fully characterizing these sources, primarily due to the approximations [279] involved. To overcome these limitations, we introduce a two-time heralded autocorrelation function derived from triple coincidence measurements, providing a more comprehensive insight into the source's temporal properties.

7.1 Introduction

Correlated photon pairs provide a practical and widely adopted basis for generating heralded single photons. Unlike genuine single-photon sources, these heralded single-photon sources exhibit anti-correlation [87, 280] via conditional preparation: the detection of one "idler" photon from a pair projects its partner "signal" into a single-photon state. This projection, in turn, suppresses coincident detections within the heralded channel, leading to a low value for the heralded second-order correlation function.

The temporal characteristics of these photon pairs, particularly their coherence time (t_c), significantly impact their detection. For example, SPDC or SFWM processes in nonlinear materials non-deterministically generate broadband photons with coherence times on the order of sub-nanoseconds or even shorter. Such short coherence times pose challenges for detectors and time-tagging devices, whose temporal resolutions are often insufficient to resolve the photons' temporal structure. In contrast, the correlated photon pairs we generate in a cold atomic ensemble (see Chapter 4) exhibit significantly longer coherence times. Depending on the

relationship between the photon coherence time t_c and the minimal resolvable time bin δt, two measurement scenarios arise: if $t_c \lesssim \delta t$, pair coincidence detection is defined as two photons arriving within the same time bin; if $t_c > \delta t$, the heralded photons are distributed within a two-photon coherence window that spans several bins.

The heralded autocorrelation function $g_h^{(2)}(\tau)$, as the conditional analog of the second-order autocorrelation $g^{(2)}(\tau)$, was proposed to characterize the purity of heralded single photon sources [281–283]. A high single-photon purity minimizes the error of quantum communications [14, 40] and quantum computation [284, 285]. This quantity is usually measured using a heralded HBT setup [120]. In this configuration, signal photons are directed to a 50:50 beam splitter, with the outputs monitored by two detectors (channels 1 and 2). The corresponding idler photon is detected by a third detector, with its arrival time denoted as t_i. The heralded autocorrelation function, $g_h^{(2)}(0)$, quantifies the conditional probability of detecting two photons in the signal mode, given the detection of an idler photon.

The measurement strategy depends on the relation between photon coherence time and detector resolution. For photon pairs with coherence times shorter than the detector timing resolution (e.g., under pulsed or CW pumping), coincidences are registered within a single time bin, and the accuracy of $g_h^{(2)}(0)$ is mainly limited by the detector's jitter and the time-tagging device's resolution. Conversely, for correlated photon pairs with coherence times that are resolvable by the detection system, it always introduces a procedure described as follows: Upon detection of an idler photon, a heralding interval, equal to or shorter than the coherence time, is opened. Two-photon events in the idler channels (1 and 2) occurring within this interval are recorded. The probability of such an event, often expressed as a function of the relative delay τ between the two idler photons, is then normalized by the product of the idler-signal probabilities (idler-ch1 and idler-ch2) [279, 281, 286, 287].

The heralding window is not essential for data processing, as heralded autocorrelation is fundamentally a third-order (triple) coincidence. Conventional $g_h^{(2)}(\tau)$ uses a single time delay, τ, representing the separation between the two signal photons (conditioned on an idler photon). This approach, however, often involves averaging and normalization approximations. In contrast, a two-time heralded autocorrelation function, by retaining both signal photon delays relative to the heralding photon,

preserves the complete temporal structure of the two-photon coherence. It is crucial for narrowband photon pairs whose coherence spans multiple resolvable time bins.

Some studies [288–290] claim extremely low values of heralded autocorrelation $g_h^{(2)}(0)$. However, such values are often dominated by averaging over the two-photon delay and the cross-correlation in the normalization. Moreover, due to differences in the approximations and definitions adopted across studies, these reported $g_h^{(2)}(0)$ values are not directly comparable. In contrast, the two-time heralded autocorrelation can provide a more standardized and consistent framework for characterizing the degree of anti-correlation.

7.2 Analysis

We assume that the signal photon is delayed by a time t_c relative to the idler photon, where t_c denotes the two-photon coherence time. This convention also applies to SPDC sources with symmetric temporal correlations, where an artificial offset of $t_c/2$ can be introduced to redefine the temporal ordering between the idler and signal photons. The correlated photon pairs are generated under continuous-wave conditions and measured using a heralded HBT setup. The idler photons detected and time-tagged at t_i serve as the heralding, while the two signal photons are detected and tagged at t_1 and t_2 in two detectors, respectively. The heralded autocorrelation [281, 283] for such a heralded single-photon source is given by

$$g^{(2)}(t_1, t_2|t_i) = \frac{\langle a_s^\dagger(t_1) a_s^\dagger(t_2) a_s(t_2) a_s(t_1)\rangle_{\mathrm{pm}}}{\langle a_s^\dagger(t_2) a_s(t_2)\rangle_{\mathrm{pm}} \langle a_s^\dagger(t_2) a_s(t_2)\rangle_{\mathrm{pm}}}, \tag{7.1}$$

where $\hat{a}_s$ denotes the annihilation operators in the signals mode and $\langle\cdot\rangle_{\mathrm{pm}}$ represents the expectation value under post-measurement triggered by a detection of a signal photon, defined as

$$\langle X\rangle_{\mathrm{pm}} = \frac{\langle a_i^\dagger(t_i) X a_i(t_i)\rangle}{\sqrt{a_i^\dagger(t_i) a_i(t_i)}}\,. \tag{7.2}$$

As a result, the $g^{(2)}(t_1, t_2|t_i)$ can be expressed in terms of conditional probabilities, or equivalently, as ratios of joint probabilities involving detection events at times

t_1, t_2, and the heralding time t_i, given by

$$\begin{aligned} g^{(2)}(t_1, t_2|t_i) &= \frac{P(t_1, t_2|t_i)}{P(t_1|t_i)P(t_2|t_i)} \\ &= \frac{P^{(3)}(t_i, t_1, t_2)P_i(t_i)}{P^{(2)}(t_i, t_1)P^{(2)}(t_i, t_2)}\,, \end{aligned} \tag{7.3}$$

where $P^{(3)}(t_i, t_1, t_2)$ is the triple coincidence probability density, $P_i(t_i)$ is the single-photon probability density in idler mode, and $P^{(2)}(t_i, t_1)$ and $P^{(2)}(t_i, t_2)$ are the pair coincidence probability densities between signal and channels 1 and 2, respectively. We are interested in these probabilities relative to the idler photon, defining relative delays as $\tau_{1i} \equiv t_1 - t_i$ and $\tau_{2i} \equiv t_2 - t_i$. Under the stationary field condition, the joint probabilities can be expressed as: $P^{(3)}(\tau_{1i}, \tau_{2i}) = TP^{(3)}(t_i, t_i + \tau_{1i}, t_2 + \tau_{2i})$ and $P^{(2)}(\tau_{ji}) = TP^{(2)}(t_i, t_i + \tau_{ji})$ where T is the integration range over t_i and $j \in \{1, 2\}$. Accordingly, the heralded second-order autocorrelation function is expressed as

$$g_h^{(2)}(\tau_{1i}, \tau_{2i}) = \frac{N^{(1,2)}(\tau_{i1}, \tau_{i2})N_i(t_i)}{N^{(2)}(\tau_{1i})N^{(2)}(\tau_{2i})}\,, \tag{7.4}$$

where $N_i(t_i)$ is the total number of idler detection events, $N^{(2)}(\tau_{ji})$ is the pair coincidence counts between idler and channel j, and $N^{(1,2)}(\tau_{1i}, \tau_{2i})$ is the triple coincidence counts. Additionally, the superscript "(1,2)" indicates that the triple coincidences s occur across both modes, rather than within a single mode. These coincidence counts correspond to experimentally measured histograms across the three detection channels, with a time bin width of δt over the total measurement time T, defined as

$$\begin{aligned} N^{(2)}(\tau_{ji}) &= T\int_0^{\delta t} P(\tau_{ji} + \tau)d\tau\,, \\ N^{(1,2)}(\tau_{1i}, \tau_{2i}) &= T\iint_0^{\delta t} P(\tau_{1i} + \tau_1\tau_{2i} + \tau_2)d\tau_1 d\tau_2\,. \end{aligned} \tag{7.5}$$

As shown in Equation 7.4, the heralded autocorrelation function is fully determined by the measured triple- and pair-coincidence counts, with the only approximation arising from averaging over finite time bins. Triple-coincidence measurements were introduced in Chapter 6. Here, we use experimental data from our correlated photon-pair source to illustrate the standard procedure for extracting the heralded autocorrelation function, as detailed below:

Firstly, we select a large analysis window $[-T_a, T_a]$ which is several times larger than the coherence time t_c. This window is chosen as a trade-off between capturing

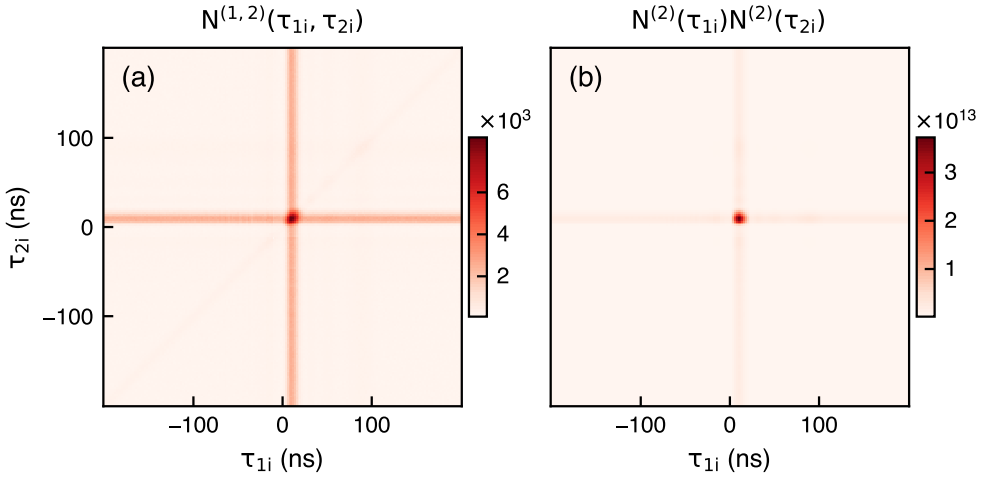

Figure 7.1: (a) Triple coincidence counts as a function of two delays τ_{1i} and τ_{2i}. (b) Product of pair coincidences $N^{(2)}(\tau_{1i})N^{(2)}(\tau_{2i})$ as a function of the same delay parameters.

all relevant features and facilitating data processing. Secondly, pair coincidences $N(\tau_{1i})$ and $N(\tau_{2i})$ within this analysis window are obtained through the two-fold coincidence measurement. The triple-coincidence events are then identified by finding overlapping pair-coincidence events that share the same time tag in the idler channel, within the selected analysis window, as described in Chapter 6. The resulting triple coincidences $N^{(1,2)}(\tau_{1i}, \tau_{2i})$ are then binned into a two-dimensional histogram over $\tau_{1i}/\tau_{2i} \in [-T_a, T_a]$ (see Figure 7.1 (a)). Thirdly, to construct the denominator, we compute, for each bin, the product of the pair-coincidence counts $N^{(2)}(\tau_{1i})$ and $N^{(2)}(\tau_{2i})$ (see Figure 7.1 (b)). Finally, the two-time heralded autocorrelation is calculated by multiplying the triple-coincidence count by the total count from the heralding signal channel, and then dividing this product by the product of the two relevant signal-idler pair coincidence counts. The result is presented in Figure 7.2.

This two-time heralded autocorrelation function shows, in the time domain, the transition from thermal bunching (a maximum value of 2 along the diagonal) to anti-correlation ($g_h^{(2)}(\tau_{1i}, \tau_{2i}) < 1$) as the signal-idler delay approaches the two-photon coherence time along the diagonal axis. Compared to the other uncorrelated regions, the anti-correlation region shows anti-bunching behavior in the heralded condition. This is a direct visualization of the statistical nature of the heralded photons. Correspondingly, the strongest anti-correlation is reflected as the deepest

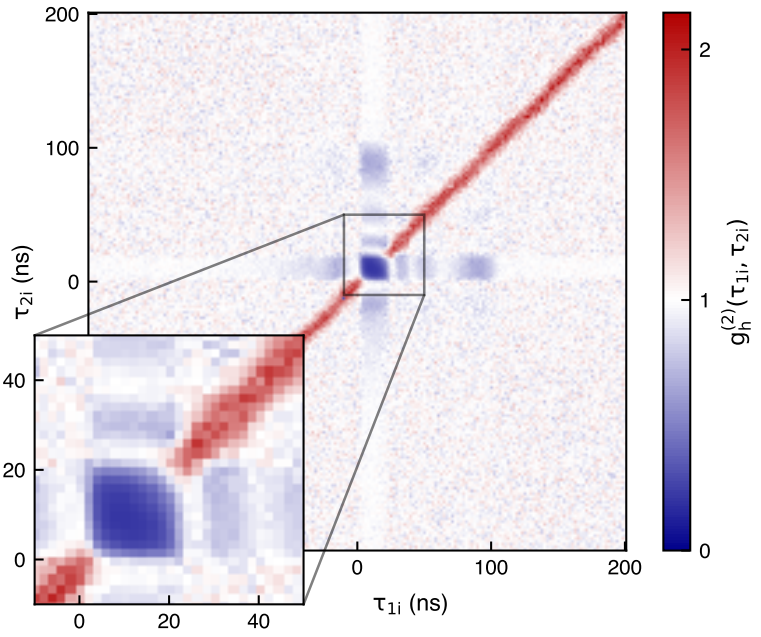

Figure 7.2: Two-time heralded autocorrelation $g_h^{(2)}(\tau_{1i}, \tau_{2i})$ as a function of two delay times relative to signal photons. The vertical and horizontal ridges (appearing as white regions) correspond to areas of high event rates, indicating an enhanced signal-to-noise ratio. Oscillatory patterns in these ridges are attributed to the temporal oscillatory tail in the two-photon wavefunction.

dip $g_h^{(2)}(\tau_{1i} = 10\,\text{ns}, \tau_{2i} = 10\,\text{ns}) \approx 0.21$ in the two-dimensional plot.

7.3 Approximations

In the following, we examine widely used approximations and averaging procedures used in the characterization of heralded single-photon sources, and analyze how they affect the observed minimum in the anti-correlation dip, often referred to as the degree of anti-correlation and the purity of the heralded photon. We show that these approximations effectively correspond to an approximation treatment of the two-time heralded autocorrelation function, leading to a partial loss of temporal information.

First, we consider the timing uncertainty introduced by detector jitter, the finite response function of single-photon detectors, and the time resolution of both the detectors and the time-taggers. The overall effect can be modeled by an effective response function $u(t)$; therefore, the measured coincidences are the convolution of

this response function with the true photon arrival-time probability as

$$\begin{aligned}\tilde{P}^{(2)}(\tau_{ji}) &= P^{(2)}(\tau_{ji}) * [u * u](\tau_{ji})\,, \\ \tilde{P}^{(3)}(\tau_{1i}, \tau_{2i}) &= P^{(3)}(\tau_{1i}, \tau_{2i}) * [u * u](\tau_{1i}) \cdot [u * u](\tau_{2i})\,,\end{aligned} \tag{7.6}$$

where $[u * u](\tau_{ji})$ denotes the convolution of the response functions of two detectors along a single time-delay dimension. In the case of triple coincidence, the effective response function becomes a product of two such convolutions, since the triplet event corresponds to the intersection of two pairwise coincidences sharing a common idler detection time. These response functions result in a broadening and flattening of coincidence profiles. In the case where detector jitter is negligible ($t_r \ll \tau_c$), the response function can be approximated by a delta function $\delta(t)$, and the measured signal-idler coincidences faithfully closely reflect the true temporal correlations. This approximation is valid in our characterization of narrowband photon pairs, where the influence of the detector response function is negligible. When $t_r \gtrsim \tau_c$, the shape of the measured coincidences is dominated by the detector response rather than the intrinsic temporal structure of the second-order correlations.

Under a simplified model, we assume that the true cross-correlation has a characteristic width t_c, while each detector has a square response function $u(t)$ of width $t_r = rt_c$. Under this approximation, the detector response smears the coincidence profile, leading to a broadening by convolution and a suppression of the peak amplitude by approximately a factor of r. Since the measured triple coincidence involves smearing along two independent time-delay axes, the peak is suppressed by a factor of approximately r^2. As a result, the dip of the heralded autocorrelation is not significantly affected by the reduction of the cross-correlation due to the detectors' responses. Instead, the primary effect of the response functions is to broaden the measured temporal profile, effectively extending the observed coherence time, and further enlarging the anti-correlation region.

Apart from the systematic errors introduced by the detection system, heralded autocorrelation functions are commonly expressed in a single-delay form [31, 87, 287, 291], which is equivalent to a specific approximation of the full two-time heralded autocorrelation function. In Equation 7.4, the triple coincidence term $N^{(1,2)}(\tau_{i1}, \tau_{i2})$ in the numerator, representing the two-photon coincidence in the idler mode heralded by a signal photon, is often reduced to a single-variable function characterized by

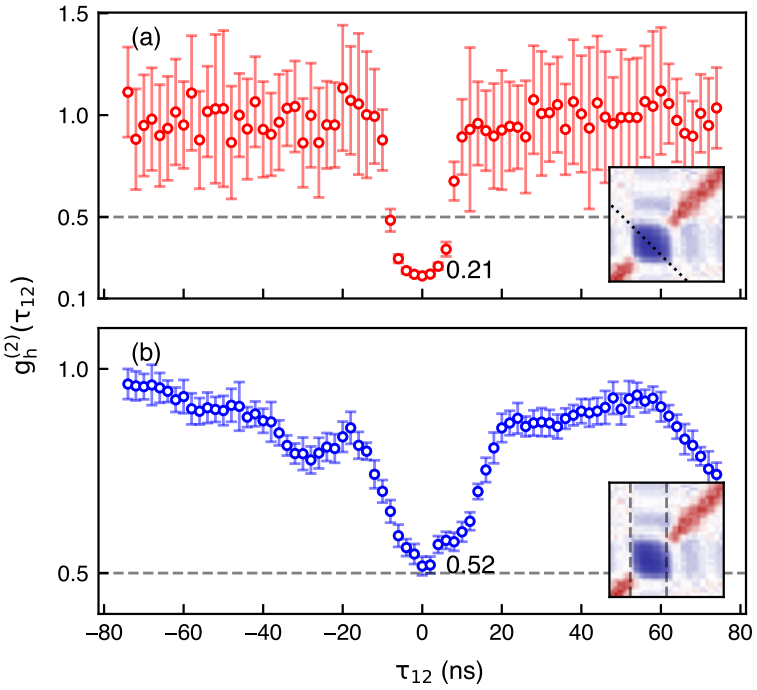

Figure 7.3: (a) A diagonal trace of the two-time heralded autocorrelation, plotted as a function of the relative delay between idler photons in channel 1 and channel 2. The error bars are evaluated from 15 subsets of the total coincidence data. (b) Single-delay heralded autocorrelation under approximations over all heralded idler photon events within a coincidence window of 20 ns between signal and channel 1 of idler. Insets show the corresponding regions in the full two-time heralded autocorrelation map.

the relative delay τ_{12} as

$$N^{(1,2)}(\tau_{12}) \approx T_m \int_0^{t_c} d\tau_{i1} P(t_i, t_1 = \tau_{1i} + t_i, t_2)\,. \tag{7.7}$$

This approximation corresponds to an experimental implementation in which, upon detection of a heralding idler photon, a coincidence window of width t_c is applied to one of the signal channels (denoted as ch1). Photon events registered in ch1 within this window are then correlated with photon events in the other signal channel (ch2) to measure $N^{(1,2)}(\tau_{12})$, where τ_{12} is the delay between detections in ch1 and ch2. Figure 7.3 (b) illustrates the result of such an averaging procedure, where a window is applied to one signal channel. In this scenario, the resulting single-delay heralded autocorrelation function, $g_h^{(2)}(\tau_{12})$, exhibits a dip value of approximately 0.52. This contrasts with the dip value of 0.21 observed in the diagonal trace of the

full two-time heralded autocorrelation function shown in Figure 7.3 (a). This reveals that averaging within the coherence time, especially for bright, narrowband photon pairs, can introduce significant error in the characterization of anti-correlation.

In certain scenarios, the denominator in Equation 7.4 is also approximated [31], where the two-variable function is reduced to a single-variable form as $D(\tau_{12}) \approx N^{(2)}(\tau_{1i})N^{(2)}(\tau_{2i})$, which facilitates the acquisition of single-delay heralded autocorrelation with respect to the delay time τ_{12}. The approximation is usually applied as

$$\begin{aligned} D(\tau_{12}) &\approx \int_0^{\tau_c} N_{1i}^{(2)}(\tau_{1i}) N_{2i}^{(2)}(\tau_{1i}+\tau_{12}) d\tau_{1i} \\ &\approx \int_0^{\tau_c} N_{2i}^{(2)}(\tau_{2i}) N_{1i}^{(2)}(\tau_{2i}+\tau_{12}) d\tau_{2i}\,, \end{aligned} \tag{7.8}$$

which corresponds to a diagonal averaging over the two-dimensional histogram of the denominator in Figure 7.1 (b) within a coherence time window of τ_c horizontally or vertically. Under this approximation, the shape of the heralded autocorrelation is primarily determined by the shape of the averaged denominator function. Since the cross-correlation function exhibits rich temporal structure within the coherence time, rather than a flat profile, this averaging smears out the fine features of temporal correlations, distorting the resulting heralded autocorrelation. In contrast, a bin-by-bin mapping preserves the temporal resolution.

7.4 Summary

In this work, we present a comprehensive characterization of the anti-correlation behavior of heralded single-photon sources using triple coincidences, beyond the conventional pair-coincidence-based approach in heralded gates. Unlike the single-variable formulations that rely on approximations and averaging, the two-time characterization preserves the full temporal correlation structure, providing a standardized and more informative description of the photon statistics. This framework also offers a clear illustration of the transition from thermal statistics to anti-correlated behavior induced by the heralding mechanism.

Chapter 8

Correlated photon triplet

As shown in the previous chapter, we have developed a bright, correlated photon-pair source based on a double-Λ energy scheme. Building on this efficient SFWM process, we extend this scheme to realize a spontaneous six-wave mixing (SSWM) process to generate photon triplets in three distinct spectral modes, which arise from a $\chi^{(5)}$ nonlinear susceptibility of atomic media. Although such a higher-order nonlinear process is intrinsically less efficient than SFWM, the exceptional brightness of our photon-pair source implies that the photon triplet is measurable within reasonable integration times in our setup. This chapter details these protocol enhancements and presents preliminary results toward realizing a practical photon-triplet source.

8.1 Theory

A SSWM process is driven by three pump fields, each resonant or near-resonant with a specific atomic transition, which coherently excite the atomic ensemble from their ground states. The atoms undergo spontaneous emission through intended pathways, emitting three spectrally distinct, time-correlated photons, whose frequencies satisfy the energy conservation with the pump fields. We propose a SSWM process based on the explored double-Λ SFWM scheme in which all atoms are initially prepared in the ground state $|5S_{1/2}, F = 1\rangle$. This ground-state initialization maximizes the available population for the parametric process and suppresses the unwanted spontaneous emission or absorption. To introduce a new pump field, a two-photon excitation to $|5D_{5/2}, F = 3\rangle$ state interpolates the first coherent Λ Raman process in the original double-Λ SFWM, followed by a cascade emission through $|5D_{5/2}, F = 3\rangle \rightarrow |5P_{3/2}, F = 2\rangle \rightarrow |5S_{1/2}, F = 2\rangle$, which emits a 776 nm "idler" and 780 nm "signal" photon. The atoms in $|5S_{1/2}, F = 2\rangle$, un-

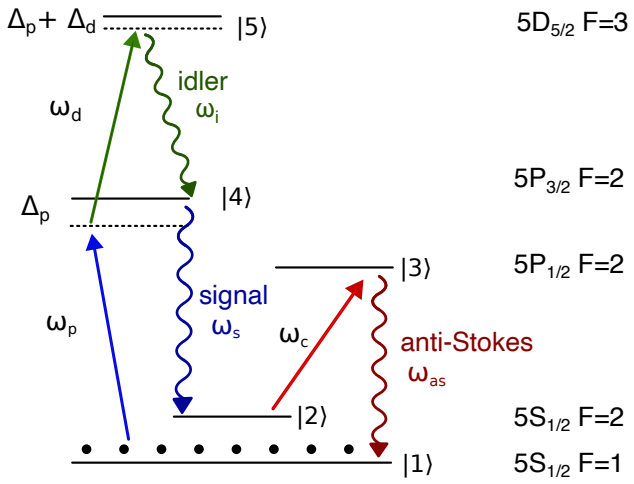

Figure 8.1: Energy levels involved in the SSWM process. Emission pathways not contributing to the SSWM are omitted for clarity.

dergo a second coherent Raman transition ("second Λ" in SFWM) in the presence of a strong coupling field, emitting an "anti-Stokes" photon resonant to $|5P_{1/2}, F = 2\rangle \rightarrow |5S_{1/2}, F = 1\rangle$ transition. The pump fields associated with the three decay pathways establish a closed-loop parametric cycle that returns the atomic ensemble to its original ground state manifold. Compared to earlier approaches [292], two features greatly enhance transmission and phase matching: (i) Since the majority of atoms remain in the $|5S_{1/2}, F = 1\rangle$ ground state, the absorption for generated fields "idler" and "signal" is minimal, therefore facilitating their transmission in the atomic ensemble. (ii) The electromagnetically induced transparency (EIT) [79], created by the coupling field, opens a transparency window for the anti-Stokes photons, allowing them to propagate with reduced absorption. By choosing the $|5D_{5/2}, F = 3\rangle \rightarrow |5P_{3/2}, F = 2\rangle \rightarrow |5S_{1/2}, F = 2\rangle$ coherent cascade emission (776 nm and 780 nm) rather than the alternative $|5D_{5/2}, F = 3\rangle \rightarrow |5P_{1/2}, F = 2\rangle \rightarrow |5S_{1/2}, F = 2\rangle$ route (762 nm and 795 nm), all three generated fields are slightly detuned from the pump frequencies. These pump conditions enable near-collinear phase matching and straightforward near-axis collection of photon triplets. In contrast, the 762 nm and 795 nm cascade emission channels would require large off-axis emission angles, complicating experimental alignment. The $5D_{5/2}$ excited state is chosen over $5D_{3/2}$, because $5D_{3/2}$ decays predominantly via the $5P_{1/2}$ intermediate state [293, 294], while the $5D_{5/2}$ level

decays mainly through $5P_{3/2}$ [295]. Consequently, routing the cascade through $5P_{3/2}$ allows the emission path with a high emission probability and fulfills the phase-matching requirements.

8.1.1 Hamiltonian

We consider the interaction between a single atom and multiple electromagnetic fields, including three classical pump fields and three quantized modes that give rise to correlated photon triplets. By neglecting collective effects from an atomic ensemble, the single-atom Hamiltonian incorporating all six fields can capture the essential dynamics of photon triplet generation. The classical fields consist of a pumping field at frequency ω_p, detuned by Δ_p from the atomic transition $|1\rangle \rightarrow |4\rangle$; the driving field at ω_d, detuned by Δ_d from the transition $|4\rangle \rightarrow |5\rangle$; and the coupling field at ω_c, detuned by Δ_c from the transition $|2\rangle \rightarrow |3\rangle$. Correspondingly, the effective two-photon detuning from $|1\rangle \rightarrow |5\rangle$ is given as $\Delta_p + \Delta_d$. Meanwhile, the cascade decay and Raman process generate three fields: the idler photon (frequency ω_i), the signal photon (frequency ω_s), and an anti-Stokes photon (frequency ω_{as}). These three fields constitute the targeted, mutually coupled modes in the SSWM protocol, with energy conservation given by $\omega_p + \omega_d + \omega_c = \omega_i + \omega_s + \omega_{as}$. The anti-Stokes field is defined to be associated with a δ_{as} from the atomic resonance $|3\rangle \rightarrow |1\rangle$, and this detuning δ_{as} serves as a variable characterizing the nonlinear spectral response of the system. For simplicity, the idler field detuning is fixed to $\delta_i = \Delta_p + \Delta_d$, compared to the $|5\rangle \rightarrow |4\rangle$ transition. Additionally, the signal field exhibits a detuning of $\delta_s = -(\delta_{as} - \Delta_c)$ with respect to the transition $|4\rangle \rightarrow |2\rangle$. In the rotating frame with rotating wave approximation, the effective interaction Hamiltonian is expressed as

$$\begin{aligned}\hat{H} = -\hbar\Big(&\Delta_p\hat{\sigma}_{44} + (\Delta_p + \Delta_d)\hat{\sigma}_{55} + \delta_{as}\hat{\sigma}_{33} + (\delta_{as} - \Delta_c)\hat{\sigma}_{22} + \Omega_p\hat{\sigma}_{41} + \Omega_d\hat{\sigma}_{54} + \Omega_c\hat{\sigma}_{32} \\ &+ g_{42}\hat{a}_s\hat{\sigma}_{42} + g_{54}\hat{a}_i\hat{\sigma}_{54} + g_{31}\hat{a}_{as}\hat{\sigma}_{31}\Big) + \text{H.c.}\,.\end{aligned} \tag{8.1}$$

In addition to the terms given in Equation 4.1, the driving-field Rabi frequency is given by $\Omega_d = d_{45}\mathcal{E}_p/\hbar$ and the interaction between the idler photon and atomic transition $|5\rangle \rightarrow |4\rangle$ is parametrized by the coupling strength g_{54}. This Hamiltonian

describes the interaction of a single atom with three classical pump fields and three generated fields, and can be extended to the collective form for the entire atomic ensemble, as detailed in Equation C.15.

8.1.2 Correlations

As the number of involved energy levels increases, an analytic treatment becomes intractable, so we turn to numerical simulations to explore the temporal correlations. The key quantity for photon-triplet detection is the third-order time-delayed correlation function [203] of the three generated field modes, which is defined as

$$G^{(3)}(\tau_s, \tau_{as}) = \langle \hat{a}^\dagger_{as}(t_i + \tau_{as})\hat{a}^\dagger_s(t_i + \tau_s)\hat{a}^\dagger_i(t_i)\hat{a}_i(t_i)\hat{a}_s(t_i + \tau_s)\hat{a}_{as}(t_i + \tau_{as})\rangle \,. \quad (8.2)$$

Under the input-output formalism [98], a photon field $\hat{a}_{\text{out}}$ radiated from an atomic transition $|j\rangle \to |i\rangle$ can be simply expressed as

$$\hat{a}_{\text{out}}(t) = \sqrt{\gamma}\hat{\sigma}_{ij}(t) + \hat{a}_{\text{in}}(t) \,, \quad (8.3)$$

where $\hat{a}_{\text{in}}(t)$ denotes the input vacuum field and γ represents the coupling rate between the light field and atoms. Assuming the vacuum contribution is negligible for detection, the output field operator is approximately proportional to the atomic coherence operator as $\hat{a}(t) \propto \hat{\sigma}_{ij}$. Accordingly, the photon triplet correlation function $G^{(3)}(\tau_s, \tau_{as})$ is proportional to the following expectation value of atomic operator moments:

$$\langle \hat{\sigma}^\dagger_{13}(t_i + \tau_{as})\hat{\sigma}^\dagger_{24}(t_i + \tau_s)\hat{\sigma}^\dagger_{45}(t_i)\hat{\sigma}_{45}(t_i)\hat{\sigma}_{24}(t_i + \tau_s)\hat{\sigma}_{13}(t_i + \tau_{as})\rangle \,, \quad (8.4)$$

where $\tau_s = t_s - t_i$ denotes the time delay between the signal and idler photons, while $\tau_{as} = t_{as} - t_i$ denotes the delay between the anti-Stokes and idler photons. As depicted in Figure 8.2, the numerical simulation of temporal correlations among these atomic operators reveals the structure of the three-field cross-correlation, $G^{(3)}(\tau_s, \tau_{as})$, as a consequence of sequential photon emissions. This two-time correlation function is primarily characterized by an exponential decay with increasing idler-signal delay time (τ_s), a feature originating from the cascade emission process. Concurrently, it exhibits a damped Rabi oscillation with increasing delay between anti-Stokes and signal photons ($\tau_{as\text{-}s} = \tau_{as} - \tau_s$), arising from Autler–Townes splitting [205]

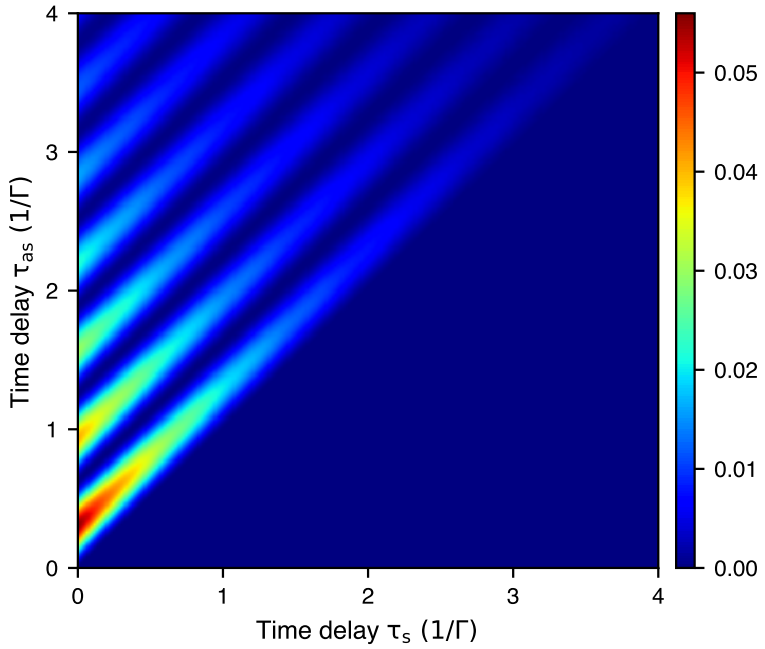

Figure 8.2: Time-dependent correlations among three atomic transitions, as described in Equation 8.4. The simulation parameters are set to $\Delta_p = 15\Gamma$, $\Delta_d = -15\Gamma$, $\Omega_p = 0.5\Gamma$, $\Omega_d = \Gamma$ and $\Omega_c = 5\Gamma$, where Γ is the spontaneous emission rate of the D2 line of ^{87}Rb.

in the presence of a strong coupling field. These features directly stem from the ordered emission of idler, signal, and anti-Stokes photons within the atomic coherence time. Because our effective Hamiltonian does not include additional potential decay pathways, such as the cascade via $|5P_{3/2}, F = 3\rangle$, and different Zeeman sublevels, interference among these unmodeled pathways could introduce extra quantum beats into the measured temporal correlations.

8.2 Phase matching condition

Efficiently generating and detecting correlated photon triplets requires careful configuration of the pump field geometry and collection modes, ensuring the phase-matching condition. Without phase matching, the output fields can rapidly dephase with atomic polarizations, resulting in destructive interference and low conversion efficiency [68]. For practical feasibility, we aim for a near-axis arrangement for both the pumping and the collection of the three generated spatial modes. The near-axis

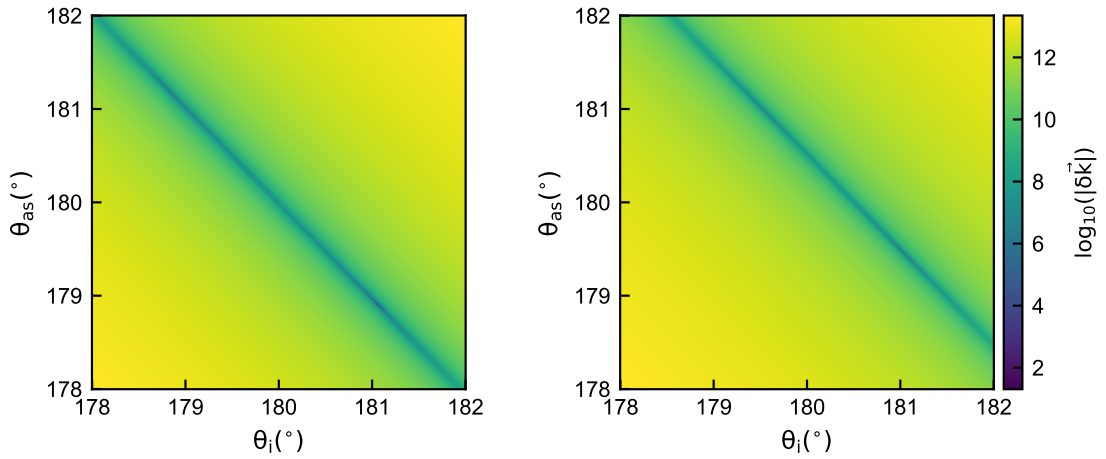

Figure 8.3: Phase mismatching $|\delta\vec{k}|$ for counter-propagating pumping ($\theta_p = 0°$) and coupling ($\theta_c = 180°$) fields, with the signal photon collection fixed at $\theta_s = 1°$. (Left) idler photon angle $\theta_d = 179°$. (Right) idler photon angle $\theta_d = 179.5°$.

configuration is primarily enabled by the choice of decay pathway that produces 776 nm (idler), 780 nm (signal), and 795 nm (anti-Stokes) photons, as their spectral proximity to the respective pump fields facilitates near-collinear phase-matching. The phase-matching condition is evaluated by minimizing the following mismatch term:

$$|\delta\vec{k}| = |\vec{k}_p + \vec{k}_d + \vec{k}_c - (\vec{k}_i + \vec{k}_s + \vec{k}_{as})|\,, \tag{8.5}$$

where we assume a refractive index of unity for all generated fields. This assumption is reasonable because the majority of atoms remain in the $|5S_{1/2}, F = 1\rangle$ ground state, which is decoupled from the idler and signal photons. Meanwhile, the anti-Stokes photon propagates within a transparency window created by the strong coupling field. With a strong coupling field applied, the "slow light" effect [296] is suppressed, and the corresponding refractive index change for the anti-Stokes field is consequently neglected.

In particular, we assume the pumping and coupling fields are counter-propagating, with $\theta_p = 0°$ and $\theta_c = 180°$, which is similar to the counter-propagating configuration in the SFWM. Additionally, the signal photon is collected using the same spatial collection mode as the Stokes photon in the SFWM process, with $\theta_s \approx 1°$. The phase mismatching term $|\delta\vec{k}|$ within limited idler and anti-Stokes emission angles is

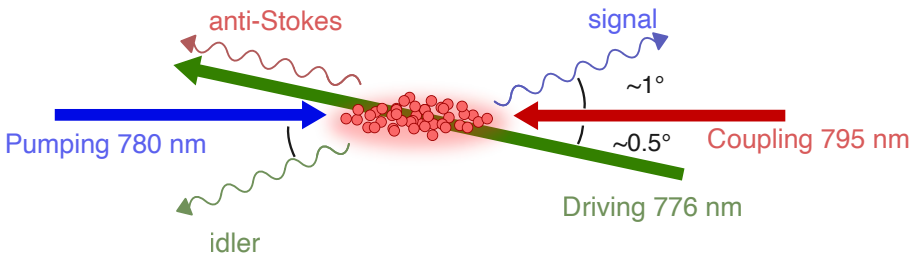

Figure 8.4: The geometry of the pump fields and the collection spatial mode for the three generated photons.

presented in Figure 8.3, while its minimum is determined using a global minimization function. Under conditions where the signal photon collection angle is $\theta_s = 1°$ and the driving field angle is $\theta_d = 179°$, the minimal phase mismatch ($|\delta\vec{k}| < 1\,\mathrm{rad}\cdot\mathrm{m}^{-1}$) due to the geometry of pump lasers and generated photons is achieved when the idler photon angle is $\theta_i \approx 178.95°$ and the anti-Stokes photon angle is $\theta_{as} \approx 181.07°$. Consequently, the phase-matched idler photon is collected nearly collinearly with the driving field. Although a temporal separation strategy allows the idler photon to be identified within the after-pulse measurement window, the driving field's spectral proximity to the 776 nm etalon filter's peak transmission results in substantial leakage, which poses a damage hazard to the single-photon detectors. Alternatively, when the driving field is slightly tilted by half of the signal collection mode ($\theta_d = 179.5°$), the phase mismatch term reaches its minimum ($|\delta\vec{k}| < 1\,\mathrm{rad}\cdot\mathrm{m}^{-1}$) at $\theta_i \approx 181.07°$ and $\theta_{as} \approx 179.41°$. In this configuration (see Figure 8.4), the idler photon is collected from a spatial mode opposite to the signal photon, while the phase-matched anti-Stokes photon remains approximately collinear with the driving field. A 795 nm etalon filter can then strongly attenuate the driving field. This approach facilitates the spatial separation of the generated photons from the nearby pump fields, preventing excessive optical power from reaching the single-photon detectors.

8.3 After-pulse measurement

In the SSWM schemes, the two-photon detuning $\Delta_c + \Delta_d$ is kept close to zero to enhance the cascade emission. This two-photon excitation is mediated by a virtual intermediate level rather than an exact atomic energy level. Therefore, the single-photon detuning, Δ_p, must be sufficiently large to suppress spontaneous emission

from the intermediate state and maintain the atomic coherence. On the other hand, while the cascade emission produces resonant photon pairs, a large single-photon detuning Δ_p facilitates the spectral separation of the generated photons from the pump fields. It is crucial for distinguishing the idler photon from the driving field. However, for fixed pumping and driving field intensities, the two-photon excitation probability $P_{|5\rangle}$ scales inversely with the square of the single-photon detuning as

$$P_{|5\rangle} \propto \left| \frac{\Omega_p \Omega_d}{\Delta_p} \right|^2 . \tag{8.6}$$

Consequently, increasing the detuning reduces the two-photon excitation probability, thereby lowering the efficiency of the SSWM process. To address this trade-off, we propose an after-pulse measurement strategy. This approach leverages the approximately 238 ns lifetime of the excited $5D_{5/2}$ state [294]. By using pulsed pumping and driving lasers for the two-photon excitation to the $5D_{5/2}$ state, the long lifetime ensures that the excited state persists even after the pump fields are switched off. Consequently, cascade emission can occur within a clear detection window following the laser pulses. This after-pulse measurement temporally decouples the generated cascaded photon pairs from the pump fields, enabling the use of a relatively small single-photon detuning to enhance the two-photon excitation probability. Furthermore, this method significantly increases the signal-to-noise ratio for the correlated photons within the after-pulse measurement window, as laser leakage is substantially reduced.

To validate the effectiveness of this after-pulse measurement strategy, we implemented a ladder-type SFWM process in a pulsed pump configuration to verify that the cascaded photon pairs can maintain temporal correlation in the absence of the pump fields. Initially, atoms are prepared in the $|5S_{1/2}, F = 2\rangle$ ground state. The pumping field is detuned by $\Delta_p/2\pi \simeq 100$ MHz from the $|5S_{1/2}, F = 2\rangle \rightarrow |5P_{3/2}, F = 3\rangle$ atomic transition. The driving field is tuned to compensate for this detuning, coupling the $|5P_{3/2}, F = 3\rangle$ state to the $|5D_{5/2}, F = 3\rangle$ (or $F = 4$) state. The hyperfine states of $5D_{5/2}$ are not perfectly resolved in our two-photon spectroscopy, so the laser is occasionally locked to a random hyperfine state. As shown in Figure 8.5, a pulsed pumping field with a 100 ns width and a pulsed driving laser with a 150 ns width are used. The actual pulse width is slightly broader than the predefined values. The driving laser precedes the pumping field by 50 ns; this timing is chosen

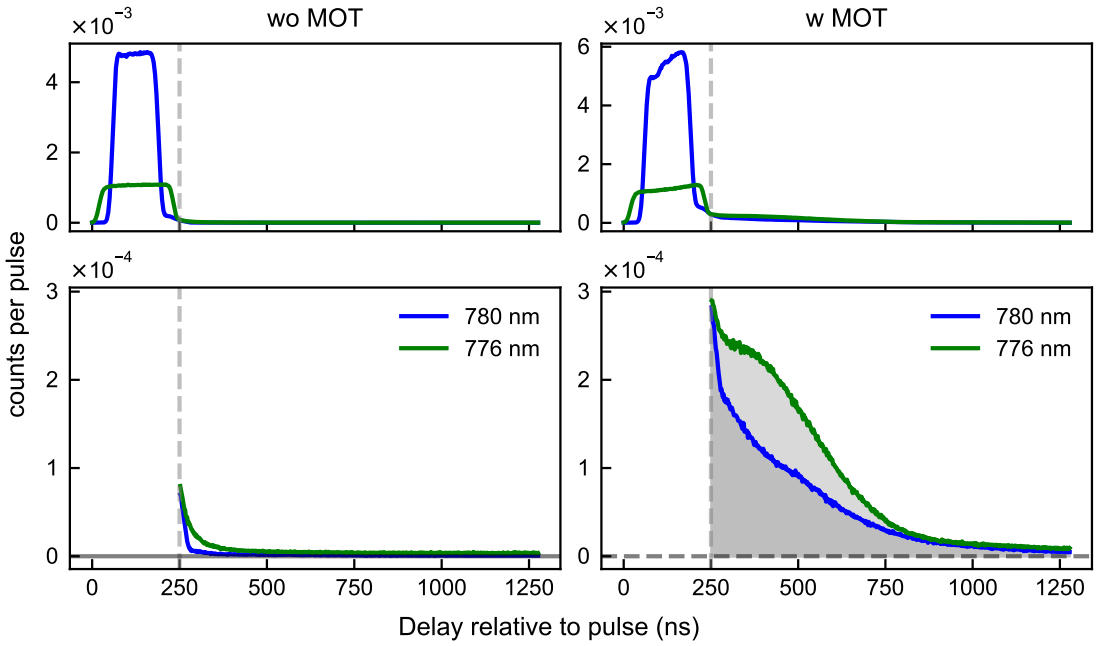

Figure 8.5: (Left) Laser leakage from the pulsed pump and driving fields, along with background counts within the measurement window in the absence of the atomic cloud. (Right) Laser leakage during pulsed excitation, along with cascaded photons within a window starting at 250 ns.

to ensure good overlap and further effective two-photon excitation rather than population transfer to the intermediate state. This configuration ensures that the pulses overlap temporally and spatially with the atomic ensemble in a counter-propagating geometry. In the collection setup, the generated 780 nm photons are collected at an angle of approximately 1° relative to the pump beam, which corresponds to the same collection mode as the Stokes photons in a double-Λ SFWM configuration. The generated 776 nm photons are collected at approximately 181°, which is the same collection mode as the anti-Stokes photons in a double-Λ SFWM scheme and is thus opposite to the 780 nm photon collection direction. The corresponding etalon filters are adjusted to match the frequencies of these target photons. Under the pulsed configuration, the generated photons at 776 nm and 780 nm are no longer stationary fields. We investigate their temporal correlations through two-time coincidence measurements. Figure 8.6 presents the coincidence counts between the 776 nm and 780 nm photons within the measurement window, accumulated over approximately

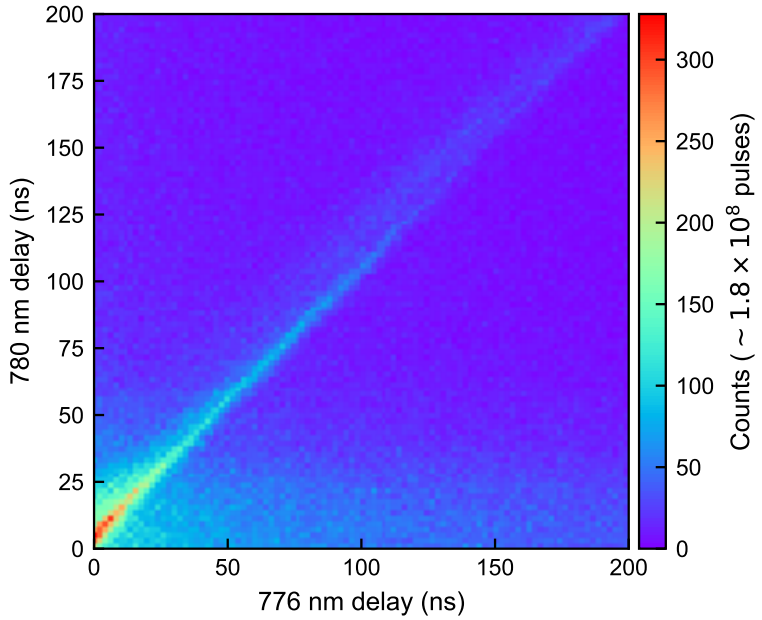

Figure 8.6: The photon count distribution within the after-pulse measurement window, accumulated over approximately 1.8×10^8 pulses. The plot represents the two-time correlation between 776 nm and 780 nm photons, with both delay times defined relative to the start of the after-pulse window.

1.8×10^8 pulses. The delay times for both photon detection events are measured relative to the start of this measurement window. The diagonal counts exceeding the background level in Figure 8.6 indicate strong temporal correlations between the 776nm and 780nm photons detected within the after-pulse measurement window. This result demonstrates the successful generation of correlated photon pairs from cascade emission and the detection in a time window separated from the excitation pulses, underscoring the after-pulse strategy's ability to mitigate pump leakage during measurement and enhance the signal-to-noise ratio.

8.4 Preliminary results

Based on our previous SFWM studies, we now implement the pulsed pump configuration and apply the "after-pulse" detection strategy. The pump (776 nm) and driving (795 nm) fields have overlapped 100 ns and 150 ns pulse envelopes, respectively. In comparison, the coupling field (795 nm) remains continuously on to provide a continuous-wave pump condition for the subsequent step of Raman

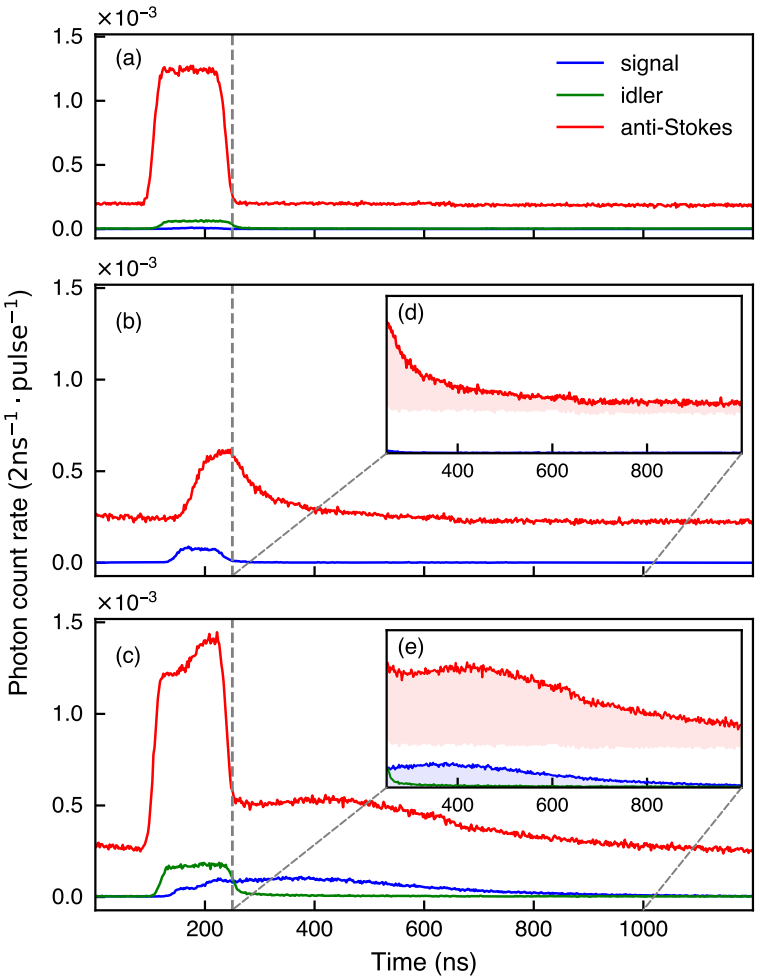

Figure 8.7: Photon counts per pulse in the signal (blue), idler (green), and anti-Stokes (red) channels under different conditions. (a) Laser leakage measured in the absence of the atomic ensemble. (b) Photon background arising from SFWM driven by the pumping and coupling fields, with the driving field off. (d) Inset to (b): Zoom into the after-pulse window (250–1000 ns), showing residual SFWM counts. (c) Photon counts from the cascade emission and Raman process in the SSWM process, including the noise photon counts mentioned above, with pumping, driving, and coupling fields all active. (e) Inset to (c): Zoom into the after-pulse window (250–1000 ns), showing collected photons from the SSWM process within the after-pulse window.

emission. The single-photon detuning is set to $\Delta_p/2\pi \approx -100\,\mathrm{MHz}$, while both the two-photon and coupling-field detunings are set to zero. In our geometry, the pump and coupling beams counter-propagate ($\theta_p = 0°, \theta_c = 180°$), and the driving field is roughly aligned at $\theta_d = 179°$. We collect "signal" photons at around 1°

(same spatial mode as Stokes photon in SFWM experiment), and "idler" photons at around 181° (backward relative to "signal"), and "anti-Stokes" photons from a spatial mode $\theta_c = 179°$ which aligns with the driving beam. Each channel passes through an etalon filter tuned to its target frequencies.

Figure 8.7 (a) shows laser leakage in the signal (blue), idler (green), and anti-Stokes (red) channels with no atoms present. Specifically, during the excitation pulse, the anti-Stokes collection mode overlaps the driving beam, resulting in extra photons confined within the pulse duration. The background originates from the leakage of the strong CW coupling field. Figure 8.7 (b) illustrates the scenario where the driving field pulses are turned off. In this case, photon counts in the "signal" and "anti-Stokes" channels (above the background) originate from a weak double-Λ SFWM process driven by the pump and coupling fields. This residual SFWM also contributes additional counts in the after-pulse measurement window, as evidenced by the exponential decay envelopes. Figure 8.7 (c) illustrates the collected photons in the presence of pulsed pump and driving fields, along with a continuous-wave coupling field. Within the after-pulse window, when the pump and driving fields are no longer present, signal photons originating from cascade emission and anti-Stokes photons from a subsequent Raman process can be detected. Due to the limited attenuation of the 795 nm etalon filters for 776 nm photons, additional photon events detected in the "anti-Stokes" channel may include both 795 nm and residual 776 nm photons from cascade emission. However, in the current unoptimized setup, the "idler" collection mode fails to capture the idler photon from the cascade. These observations suggest that further optimization of the collection geometry, particularly for the idler and anti-Stokes modes, is necessary to resolve the temporal correlations among the three photons. In the next step, the alternative collection configurations described above should be experimentally tested. Once sufficient photon counts are detected in all three modes within the after-pulse measurement window, an analysis analogous to that in Figure 8.6 should be carried out to investigate the temporal correlations among the three collected photons. This will help verify the existence of temporal correlations and provide experimental evidence for the generation of correlated photon triplets.

8.5 Summary

Detecting correlated photon triplets from a SSWM process in an atomic ensemble presents two significant challenges: first, achieving an experimentally feasible phase-matching condition for the pump fields and the generated photons; and second, effectively detecting the generated photons while distinguishing them from strong pumping fields.

To address the first challenge, we have developed a composite SSWM process by integrating a cascade emission within a double-Λ SFWM configuration. This approach enables us to select spontaneous decay pathways with frequencies close to those of the pump fields, thereby allowing for near-collinear pump and collection geometries. For the second challenge, we leverage the long lifetime of the $5D_{5/2}$ excited state and propose an after-pulse measurement strategy. This configuration temporarily separates the generated photons from the pumping fields. This approach has been validated by a successful implementation in a ladder-type SFWM process, where temporally correlated photons were resolved in the two-time correlation function.

Although correlated photon triplets were not observed in the preliminary experiment, the detection of intermediate signal photons within an after-pulse measurement window indicates the presence of a ladder-type SFWM process. The occurrence of these signal photons depends on the presence of pulsed pump and drive fields, as well as the continuous-wave coupling field. Further improvements will focus on fine-tuning the collection angles near the theoretically predicted phase-matching conditions to resolve temporal correlations among photons in the three distinct spectral modes. These initial observations underscore the strong potential for generating and detecting correlated photon triplets from a cold atomic ensemble.

Chapter 9

Conclusion and Outlook

An optically dense, elongated atomic cloud provides a promising platform for realizing complex nonlinear processes with the assistance of rich atomic energy levels, such as spontaneous four-wave mixing (SFWM) and six-wave mixing (SSWM). These processes can generate correlated photon pairs and photon triplets, respectively. Compared to spontaneous parametric down-conversion (SPDC) sources, the generated photons are spectrally narrowband and naturally compatible with atomic transitions, making them well-suited for applications in quantum networks involving interacting neutral atom nodes.

First, the large number of atoms interacting with the pump fields within the optically dense medium enables efficient generation of correlated photon pairs. To enhance the collection efficiency and spatial mode purity of the photon pairs, we collect only a single diffraction mode, thereby realizing a bright, narrowband source of correlated photon pairs. In Chapter 4, we characterize the properties of correlated photon pairs under various experimental parameters, including the intensity and detuning of the pump fields. The results show that the pair generation efficiency and the spectral properties of the photon pairs depend sensitively on these driving conditions, highlighting the potential for spectral engineering via the near-resonant linear susceptibility of the atomic cloud. In Chapter 5, we further investigate the collective nature of the photon-pair emission. Notably, we observe that the photon-pair rate scales quartically with the optical depth (or atom number), and the decay rate of the two-photon wavefunction increases with increasing optical depth, both of which are hallmarks of superradiant emission. These observations deviate from the quadratic scaling predicted by models based on independent atomic emitters, highlighting the role of collective effects. Importantly, the detection of a heralding

photon in one mode conditions the emission of its partner photon in a distinct mode, enabling the extraction of the heralded photon's temporal characteristics via the second-order correlation function under the continuous-wave steady-state driving condition. It suggests that correlated photon pairs offer a unique perspective on the dynamics of photon emission, such as collective emission in extended atomic systems, in contrast to conventional superradiance studies based on pulsed excitation and decay-time measurements.

In the SFWM process, the effective Hamiltonian theoretically gives rise to a two-mode squeezed vacuum state, indicating the presence of both photon pairs and multi-pair components. However, the statistics and higher-order temporal correlations of these multiphoton states have not been widely explored experimentally. Leveraging our narrowband and bright source of correlated photon pairs generated from a cold atomic ensemble, we investigate the joint third- and fourth-order temporal correlations between the coupled modes using a double Hanbury Brown–Twiss (HBT) measurement in Chapter 6. Both correlation functions exhibit photon bunching behaviors consistent with theoretical predictions based on Gaussian moment factoring. In particular, the joint third-order correlation reveals clear evidence of double-pair interference, manifesting as a bunching beyond what is expected from independent photon-pair statistics. Additionally, loss analysis allows us to reconstruct the underlying pure state, which closely matches a two-mode squeezed vacuum state with moderate pair generation probability, confirming the validity of a macroscopic effective Hamiltonian for an ensemble of non-interacting atoms.

Furthermore, motivated by the successful detection of correlated photon pairs in the double-Λ SFWM process, we extend our investigation to the realization of correlated photon triplets via a SSWM process. To this end, we introduce systematic improvements to the experimental protocol, including phase-matched pump and collection geometries, temporal filtering, and measurement strategies designed to overcome the challenges associated with triplet generation and detection in Chapter 8. Theoretical analysis and preliminary results indicate strong potential for generating time-correlated photon triplets in distinct optical modes via a SSWM process in a cold atomic ensemble.

This thesis summarizes our efforts in generating a bright, narrowband correlated photon pair source, exploring higher-order correlations across coupled modes and

multiphoton states, and advancing toward the realization of photon triplets using a cold atomic ensemble. Together, these studies demonstrate the potential of cold atomic ensembles as a versatile platform for photon-state engineering and the generation of non-classical light. Additionally, using experimentally measured photon correlation data, we verify specific theoretical models and gain insight into the structure and dynamics of higher-order quantum correlations for the photon-pair source. These results lay the foundation for future developments in quantum nonlinear optics and open pathways toward quantum networks and other scalable quantum photonic applications.

Bibliography

[1] D. Barredo, V. Lienhard, S. De Leseleuc, T. Lahaye, and A. Browaeys, "Synthetic three-dimensional atomic structures assembled atom by atom", Nature **561**, 79–82 (2018).

[2] D. Bluvstein, H. Levine, G. Semeghini, T. T. Wang, S. Ebadi, M. Kalinowski, A. Keesling, N. Maskara, H. Pichler, M. Greiner, et al., "A quantum processor based on coherent transport of entangled atom arrays", Nature **604**, 451–456 (2022).

[3] C. Sheng, J. Hou, X. He, K. Wang, R. Guo, J. Zhuang, B. Mamat, P. Xu, M. Liu, J. Wang, et al., "Defect-free arbitrary-geometry assembly of mixed-species atom arrays", Physical Review Letters **128**, 83202 (2022).

[4] L. Henriet, L. Beguin, A. Signoles, T. Lahaye, A. Browaeys, G.-O. Reymond, and C. Jurczak, "Quantum computing with neutral atoms", Quantum **4**, 327 (2020).

[5] E. Urban, T. A. Johnson, T. Henage, L. Isenhower, D. Yavuz, T. Walker, and M. Saffman, "Observation of rydberg blockade between two atoms", Nature Physics **5**, 110–114 (2009).

[6] L. Isenhower, E. Urban, X. Zhang, A. Gill, T. Henage, T. A. Johnson, T. Walker, and M. Saffman, "Demonstration of a neutral atom controlled-NOT quantum gate", Physical Review Letters **104**, 10503 (2010).

[7] T. Graham, M. Kwon, B. Grinkemeyer, Z. Marra, X. Jiang, M. Lichtman, Y. Sun, M. Ebert, and M. Saffman, "Rydberg-mediated entanglement in a two-dimensional neutral atom qubit array", Physical Review Letters **123**, 230501 (2019).

[8] H. Levine, A. Keesling, A. Omran, H. Bernien, S. Schwartz, A. S. Zibrov, M. Endres, M. Greiner, V. Vuletić, and M. D. Lukin, "High-fidelity control and entanglement of rydberg-atom qubits", Physical Review Letters **121**, 123603 (2018).

[9] H. Levine, A. Keesling, G. Semeghini, A. Omran, T. T. Wang, S. Ebadi, H. Bernien, M. Greiner, V. Vuletić, H. Pichler, et al., "Parallel implementation of high-fidelity multiqubit gates with neutral atoms", Physical Review Letters **123**, 170503 (2019).

[10] H. Bernien, S. Schwartz, A. Keesling, H. Levine, A. Omran, H. Pichler, S. Choi, A. S. Zibrov, M. Endres, M. Greiner, et al., "Probing many-body dynamics on a 51-atom quantum simulator", Nature **551**, 579–584 (2017).

[11] S. Boixo, S. V. Isakov, V. N. Smelyanskiy, R. Babbush, N. Ding, Z. Jiang, M. J. Bremner, J. M. Martinis, and H. Neven, "Characterizing quantum supremacy in near-term devices", Nature Physics **14**, 595–600 (2018).

[12] F. Arute, K. Arya, R. Babbush, D. Bacon, J. C. Bardin, R. Barends, R. Biswas, S. Boixo, F. G. Brandao, D. A. Buell, et al., "Quantum supremacy using a programmable superconducting processor", Nature **574**, 505–510 (2019).

[13] J. I. Cirac, P. Zoller, H. J. Kimble, and H. Mabuchi, "Quantum state transfer and entanglement distribution among distant nodes in a quantum network", Physical Review Letters **78**, 3221 (1997).

[14] L.-M. Duan, M. D. Lukin, J. I. Cirac, and P. Zoller, "Long-distance quantum communication with atomic ensembles and linear optics", Nature **414**, 413–418 (2001).

[15] H. J. Kimble, "The quantum internet", Nature **453**, 1023–1030 (2008).

[16] A. Reiserer and G. Rempe, "Cavity-based quantum networks with single atoms and optical photons", Reviews of Modern Physics **87**, 1379–1418 (2015).

[17] J. P. Covey, H. Weinfurter, and H. Bernien, "Quantum networks with neutral atom processing nodes", npj Quantum Information **9**, 90 (2023).

[18] I. V. Inlek, C. Crocker, M. Lichtman, K. Sosnova, and C. Monroe, "Multi-species trapped-ion node for quantum networking", Physical Review Letters **118**, 250502 (2017).

[19] J. M. Pino, J. M. Dreiling, C. Figgatt, J. P. Gaebler, S. A. Moses, M. Allman, C. Baldwin, M. Foss-Feig, D. Hayes, K. Mayer, et al., "Demonstration of the trapped-ion quantum CCD computer architecture", Nature **592**, 209–213 (2021).

[20] K. Hammerer, A. S. Sørensen, and E. S. Polzik, "Quantum interface between light and atomic ensembles", Reviews of Modern Physics **82**, 1041–1093 (2010).

[21] D. Loss and D. P. DiVincenzo, "Quantum computation with quantum dots", Physical Review A **57**, 120 (1998).

[22] L. Childress, M. Gurudev Dutt, J. Taylor, A. Zibrov, F. Jelezko, J. Wrachtrup, P. Hemmer, and M. Lukin, "Coherent dynamics of coupled electron and nuclear spin qubits in diamond", Science **314**, 281–285 (2006).

[23] V. Schäfer, C. Ballance, K. Thirumalai, L. Stephenson, T. Ballance, A. Steane, and D. Lucas, "Fast quantum logic gates with trapped-ion qubits", Nature **555**, 75–78 (2018).

[24] W. Huang, C. Yang, K. Chan, T. Tanttu, B. Hensen, R. Leon, M. Fogarty, J. Hwang, F. Hudson, K. M. Itoh, et al., "Fidelity benchmarks for two-qubit gates in silicon", Nature **569**, 532–536 (2019).

[25] C. Junge, D. O'shea, J. Volz, and A. Rauschenbeutel, "Strong coupling between single atoms and nontransversal photons", Physical Review Letters **110**, 213604 (2013).

[26] V. Leong, M. A. Seidler, M. Steiner, A. Cerè, and C. Kurtsiefer, "Time-resolved scattering of a single photon by a single atom", Nature Communications **7**, 13716 (2016).

[27] Y.-S. Chin, M. Steiner, and C. Kurtsiefer, "Nonlinear photon-atom coupling with 4pi microscopy", Nature Communications **8**, 1200 (2017).

[28] H. P. Specht, C. Nölleke, A. Reiserer, M. Uphoff, E. Figueroa, S. Ritter, and G. Rempe, "A single-atom quantum memory", Nature **473**, 190–193 (2011).

[29] H. Takesue and B. Miquel, "Entanglement swapping using telecom-band photons generated in fibers", Optics Express **17**, 10748–10756 (2009).

[30] Y. Xue, A. Yoshizawa, and H. Tsuchida, "Polarization-based entanglement swapping at the telecommunication wavelength using spontaneous parametric down-conversion photon-pair sources", Physical Review A **85**, 32337 (2012).

[31] G. Kaur Gulati, "Narrowband photon pairs from a cold atomic vapour fro interfacing with a single atom", (2015).

[32] V. Leong, "Interfacing a single atom with single photons", (2016).

[33] C. H. Chow, "Control and manipulation of single atoms for interfacing with light", PhD thesis (National University of Singapore, 2023).

[34] C. H. Nguyen, A. N. Utama, N. Lewty, and C. Kurtsiefer, "Operating a near-concentric cavity at the last stable resonance", Physical Review A **98**, 63833 (2018).

[35] S. Kato and T. Aoki, "Strong coupling between a trapped single atom and an all-fiber cavity", Physical Review Letters **115**, 93603 (2015).

[36] K. P. Nayak, J. Wang, and J. Keloth, "Real-time observation of single atoms trapped and interfaced to a nanofiber cavity", Physical Review Letters **123**, `10.1103/PhysRevLett.123.213602` (2019).

[37] M. Żukowski, A. Zeilinger, M. A. Horne, and A. K. Ekert, ""event-ready-detectors" bell experiment via entanglement swapping", Physical Review Letters **71**, 4287–4290 (1993).

[38] J.-W. Pan, D. Bouwmeester, H. Weinfurter, and A. Zeilinger, "Experimental entanglement swapping: entangling photons that never interacted", Physical Review Letters **80**, 3891–3894 (1998).

[39] H.-J. Briegel, W. Dür, J. I. Cirac, and P. Zoller, "Quantum repeaters: the role of imperfect local operations in quantum communication", Physical Review Letters **81**, 5932–5935 (1998).

[40] N. Sangouard, C. Simon, H. De Riedmatten, and N. Gisin, "Quantum repeaters based on atomic ensembles and linear optics", Reviews of Modern Physics **83**, 33–80 (2011).

[41] K. Azuma, S. E. Economou, D. Elkouss, P. Hilaire, L. Jiang, H.-K. Lo, and I. Tzitrin, "Quantum repeaters: from quantum networks to the quantum internet", Reviews of Modern Physics **95**, 10.1103/RevModPhys.95.045006 (2023).

[42] J.-W. Pan, Z.-B. Chen, C.-Y. Lu, H. Weinfurter, A. Zeilinger, and M. Żukowski, "Multiphoton entanglement and interferometry", Reviews of Modern Physics **84**, 777–838 (2012).

[43] D. Bouwmeester, J.-W. Pan, K. Mattle, M. Eibl, H. Weinfurter, and A. Zeilinger, "Experimental quantum teleportation", Nature **390**, 575–579 (1997).

[44] B. Lounis and M. Orrit, "Single-photon sources", Reports on Progress in Physics **68**, 1129–1179 (2005).

[45] J. Lee, L. Shen, A. N. Utama, and C. Kurtsiefer, "Absolute clock synchronization with a single time-correlated photon pair source over a 10 km optical fibre", Optics Express **30**, 18530 (2022).

[46] C. Spiess, S. Töpfer, S. Sharma, A. Kržič, M. Cabrejo-Ponce, U. Chandrashekara, N. L. Döll, D. Rieländer, and F. Steinlechner, "Clock synchronization with correlated photons", Physical Review Applied **19**, 054082 (2023).

[47] P. G. Kwiat, K. Mattle, H. Weinfurter, A. Zeilinger, A. V. Sergienko, and Y. Shih, "New high-intensity source of polarization-entangled photon pairs", Physical Review Letters **75**, 4337–4341 (1995).

[48] J. D. Franson, "Bell inequality for position and time", Physical Review Letters **62**, 2205–2208 (1989).

[49] J. Brendel, N. Gisin, W. Tittel, and H. Zbinden, "Pulsed energy-time entangled twin-photon source for quantum communication", Physical Review Letters **82**, 2594–2597 (1999).

[50] I. Marcikic, H. De Riedmatten, W. Tittel, H. Zbinden, M. Legré, and N. Gisin, "Distribution of time-bin entangled qubits over 50 km of optical fiber", Physical Review Letters **93**, 180502 (2004).

[51] A. Aspect, J. Dalibard, and G. Roger, "Experimental test of bell's inequalities using time- varying analyzers", Physical Review Letters **49**, 1804–1807 (1982).

[52] G. Weihs, T. Jennewein, C. Simon, H. Weinfurter, and A. Zeilinger, "Violation of bell's inequality under strict einstein locality conditions", Physical Review Letters **81**, 5039–5043 (1998).

[53] L. K. Shalm, E. Meyer-Scott, B. G. Christensen, P. Bierhorst, M. A. Wayne, M. J. Stevens, T. Gerrits, S. Glancy, D. R. Hamel, M. S. Allman, K. J. Coakley, S. D. Dyer, C. Hodge, A. E. Lita, V. B. Verma, C. Lambrocco, E. Tortorici, A. L. Migdall, Y. Zhang, D. R. Kumor, W. H. Farr, F. Marsili, M. D. Shaw, J. A. Stern, C. Abellán, W. Amaya, V. Pruneri, T. Jennewein, M. W. Mitchell, P. G. Kwiat, J. C. Bienfang, R. P. Mirin, E. Knill, and S. W. Nam, "Strong loophole-free test of local realism", Physical Review Letters **115**, 250402 (2015).

[54] M. Giustina, M. A. M. Versteegh, S. Wengerowsky, J. Handsteiner, A. Hochrainer, K. Phelan, F. Steinlechner, J. Kofler, J.-Å. Larsson, C. Abellán, W. Amaya, V. Pruneri, M. W. Mitchell, J. Beyer, T. Gerrits, A. E. Lita, L. K. Shalm, S. W. Nam, T. Scheidl, R. Ursin, B. Wittmann, and A. Zeilinger, "Significant-loophole-free test of bell's theorem with entangled photons", Physical Review Letters **115**, 250401 (2015).

[55] W. K. Wootters and W. H. Zurek, "A single quantum cannot be cloned", Nature **299**, 802–803 (1982).

[56] V. Scarani, H. Bechmann-Pasquinucci, N. J. Cerf, M. Dušek, N. Lütkenhaus, and M. Peev, "The security of practical quantum key distribution", Reviews of Modern Physics **81**, 1301–1350 (2009).

[57] C. H. Bennett and G. Brassard, "Quantum cryptography: public key distribution and coin tossing", Theoretical Computer Science **560**, 7–11 (2014).

[58] A. K. Ekert, "Quantum cryptography based on bell's theorem", Physical Review Letters **67**, 661–663 (1991).

[59] S. E. Harris, M. K. Oshman, and R. L. Byer, "Observation of tunable optical parametric fluorescence", Physical Review Letters **18**, 732–734 (1967).

[60] C. Couteau, "Spontaneous parametric down-conversion", Contemporary Physics **59**, 291–304 (2018).

[61] Y. Shi, S. Moe Thar, H. S. Poh, J. A. Grieve, C. Kurtsiefer, and A. Ling, "Stable polarization entanglement based quantum key distribution over a deployed metropolitan fiber", Applied Physics Letters **117**, 124002 (2020).

[62] L. Shen, C. H. Chow, J. Y. X. Peh, X. J. Yeo, P. K. Tan, and C. Kurtsiefer, "Distributing polarization entangled photon pairs with high rate over long distance through standard telecommunication fiber", Physical Review Applied **18**, 44075 (2022).

[63] O. Slattery, L. Ma, K. Zong, and X. Tang, "Background and review of cavity-enhanced spontaneous parametric down-conversion", Journal of Research of the National Institute of Standards and Technology **124**, 124019 (2019).

[64] C. K. Hong and L. Mandel, "Theory of parametric frequency down conversion of light", Physical Review A **31**, 2409–2418 (1985).

[65] M. Jain, H. Xia, G. Y. Yin, A. J. Merriam, and S. E. Harris, "Efficient nonlinear frequency conversion with maximal atomic coherence", Physical Review Letters **77**, 4326–4329 (1996).

[66] M. D. Lukin, P. R. Hemmer, M. Löffler, and M. O. Scully, "Resonant enhancement of parametric processes via radiative interference and induced coherence", Physical Review Letters **81**, 2675–2678 (1998).

[67] M. D. Lukin, A. B. Matsko, M. Fleischhauer, and M. O. Scully, "Quantum noise and correlations in resonantly enhanced wave mixing based on atomic coherence", Physical Review Letters **82**, 1847–1850 (1999).

[68] M. Lukin, P. Hemmer, and M. Scully, "Resonant nonlinear optics in phase-coherent media", in *Advances in Atomic Molecular and Optical Physics*, Vol. 42 (Elsevier, 2000), pp. 347–386.

[69] S. D. Jenkins, D. N. Matsukevich, T. Chanelière, S.-Y. Lan, T. A. B. Kennedy, and A. Kuzmich, "Quantum telecommunication with atomic ensembles", Journal of the Optical Society of America B **24**, 316 (2007).

[70] Y.-S. Lee, S. M. Lee, H. Kim, and H. S. Moon, "Highly bright photon-pair generation in doppler-broadened ladder-type atomic system", Optics Express **24**, 28083 (2016).

[71] J. Park, T. Jeong, H. Kim, and H. S. Moon, "Time-energy entangled photon pairs from doppler-broadened atomic ensemble via collective two-photon coherence", Physical Review Letters **121**, 263601 (2018).

[72] C. Shu, P. Chen, T. K. A. Chow, L. Zhu, Y. Xiao, M. Loy, and S. Du, "Subnatural-linewidth biphotons from a doppler-broadened hot atomic vapour cell", Nature Communications **7**, 12783 (2016).

[73] J. Park, T. Jeong, and H. S. Moon, "Spectral–temporal biphoton waveform of photon pairs from cascade-type warm atoms", Scientific Reports **10**, 16413 (2020).

[74] H. Jeong, H. Kim, and H. S. Moon, "High-performance telecom-wavelength biphoton source from a hot atomic vapor cell", Advanced Quantum Technologies **7**, 2300108 (2024).

[75] A. Kuzmich, W. P. Bowen, A. D. Boozer, A. Boca, C. W. Chou, L.-M. Duan, and H. J. Kimble, "Generation of nonclassical photon pairs for scalable quantum communication with atomic ensembles", Nature **423**, 731–734 (2003).

[76] V. Balić, D. A. Braje, P. Kolchin, G. Y. Yin, and S. E. Harris, "Generation of paired photons with controllable waveforms", Physical Review Letters **94**, 183601 (2005).

[77] T. Chanelière, D. N. Matsukevich, S. D. Jenkins, T. A. B. Kennedy, M. S. Chapman, and A. Kuzmich, "Quantum telecommunication based on atomic cascade transitions", Physical Review Letters **96**, 93604 (2006).

[78] P. Kolchin, S. Du, C. Belthangady, G. Y. Yin, and S. E. Harris, "Generation of narrow-bandwidth paired photons: use of a single driving laser", Physical Review Letters **97**, 113602 (2006).

[79] P. Kolchin, "Electromagnetically-induced-transparency-based paired photon generation", Physical Review A **75**, 33814 (2007).

[80] S. Du, P. Kolchin, C. Belthangady, G. Y. Yin, and S. E. Harris, "Subnatural linewidth biphotons with controllable temporal length", Physical Review Letters **100**, 183603 (2008).

[81] S. Du, J. Wen, and M. H. Rubin, "Narrowband biphoton generation near atomic resonance", J. Opt. Soc. Am. B **25**, C98–C108 (2008).

[82] B. Srivathsan, G. K. Gulati, C. M. Y. Brenda, G. Maslennikov, D. Matsukevich, and C. Kurtsiefer, "Narrow band source of transform-limited photon pairs via four-wave mixing in a cold atomic ensemble", Physical Review Letters **111**, 123602 (2013).

[83] M.-X. Dong, W. Zhang, S. Shi, K. Wang, Z.-Y. Zhou, S.-L. Liu, D.-S. Ding, and B.-S. Shi, "Two-color hyper-entangled photon pairs generation in a cold ^85Rb atomic ensemble", Optics Express **25**, 10145 (2017).

[84] A. Cerè, B. Srivathsan, G. K. Gulati, B. Chng, and C. Kurtsiefer, "Characterization of a photon-pair source based on a cold atomic ensemble using a cascade-level scheme", Physical Review A **98**, 23835 (2018).

[85] Y. Mei, Y. Zhou, S. Zhang, J. Li, K. Liao, H. Yan, S.-L. Zhu, and S. Du, "Einstein-podolsky-rosen energy-time entanglement of narrow-band biphotons", Physical Review Letters **124**, 10509 (2020).

[86] J.-S. Shiu, Z.-Y. Liu, C.-Y. Cheng, Y.-C. Huang, I. A. Yu, Y.-C. Chen, C.-S. Chuu, C.-M. Li, S.-Y. Wang, and Y.-F. Chen, "Observation of highly correlated ultrabright biphotons through increased atomic ensemble density in spontaneous four-wave mixing", Physical Review Research **6**, L032001 (2024).

[87] J.-K. Lin, T.-H. Chien, C.-T. Wu, R. Chinnarasu, S. Du, I. A. Yu, and C.-S. Chuu, "Observation of subnatural-linewidth biphotons in a two-level atomic ensemble", Physical Review Letters **134**, 43602 (2025).

[88] J. Wen and M. H. Rubin, "Transverse effects in paired-photon generation via an electromagnetically induced transparency medium. I. Perturbation theory", Physical Review A **74**, 23808 (2006).

[89] J. Wen and M. H. Rubin, "Transverse effects in paired-photon generation via an electromagnetically induced transparency medium. II. Beyond perturbation theory", Physical Review A **74**, 23809 (2006).

[90] C. H. Raymond Ooi, Q. Sun, M. S. Zubairy, and M. O. Scully, "Correlation of photon pairs from the double raman amplifier: generalized analytical quantum langevin theory", Physical Review A **75**, 13820 (2007).

[91] Q. Glorieux, R. Dubessy, S. Guibal, L. Guidoni, J.-P. Likforman, T. Coudreau, and E. Arimondo, "Double-Λ microscopic model for entangled light generation by four-wave mixing", Physical Review A **82**, 033819 (2010).

[92] C.-S. Chuu and S. Du, "Narrowband biphotons: generation, manipulation, and applications", (Mar. 14, 2015) `http://arxiv.org/abs/1503.04339`, pre-published.

[93] Y. Jiang, Y. Mei, and S. Du, "Quantum langevin theory for two coupled phase-conjugated electromagnetic waves", Physical Review A **107**, 53703 (2023).

[94] L. Zhao, X. Guo, C. Liu, Y. Sun, M. M. T. Loy, and S. Du, "Photon pairs with coherence time exceeding 1 μs", Optica **1**, 84 (2014).

[95] L. Zhao, Y. Su, and S. Du, "Narrowband biphoton generation in the group delay regime", Physical Review A **93**, 33815 (2016).

[96] S. Du, J. Wen, and C. Belthangady, "Temporally shaping biphoton wave packets with periodically modulated driving fields", Physical Review A **79**, 43811 (2009).

[97] L. Zhao, X. Guo, Y. Sun, Y. Su, M. M. T. Loy, and S. Du, "Shaping the biphoton temporal waveform with spatial light modulation", Physical Review Letters **115**, 193601 (2015).

[98] R. W. Boyd, A. L. Gaeta, and E. Giese, "Nonlinear optics", in *Springer Handbook of Atomic, Molecular, and Optical Physics* (Springer, 2008).

[99] K.-J. Boller, A. Imamoğlu, and S. E. Harris, "Observation of electromagnetically induced transparency", Physical Review Letters **66**, 2593–2596 (1991).

[100] M. Fleischhauer, A. Imamoglu, and J. P. Marangos, "Electromagnetically induced transparency: optics in coherent media", Reviews of Modern Physics **77**, 633–673 (2005).

[101] J.-M. Chen, T. Peters, P.-H. Hsieh, and I. A. Yu, "Review of biphoton sources based on the double-λ spontaneous four-wave mixing process", Advanced Quantum Technologies **7**, 2400138 (2024).

[102] Q. Glorieux, "Quantum optics in dense atomic media: from optical memories to fluids of light", (2018) pre-published.

[103] W. Ketterle, K. B. Davis, M. A. Joffe, A. Martin, and D. E. Pritchard, "High densities of cold atoms in a *dark* spontaneous-force optical trap", Physical Review Letters **70**, 2253–2256 (1993).

[104] N. Radwell, G. Walker, and S. Franke-Arnold, "Cold-atom densities of more than 10 12 cm - 3 in a holographically shaped dark spontaneous-force optical trap", Physical Review A **88**, 43409 (2013).

[105] M. D. Reid, "Demonstration of the einstein-podolsky-rosen paradox using nondegenerate parametric amplification", Physical Review A **40**, 913–923 (1989).

[106] L.-M. Duan, G. Giedke, J. I. Cirac, and P. Zoller, "Inseparability criterion for continuous variable systems", Physical Review Letters **84**, 2722–2725 (2000).

[107] A. I. Lvovsky, "Squeezed light", (July 28, 2016) pre-published.

[108] M. S. Shahriar and P. R. Hemmer, "Generation of squeezed states and twin beams via non-degenerate four-wave mixing in a L system", Optics Communications **158**, 273–286 (1998).

[109] C. F. McCormick, V. Boyer, A. M. Marino, E. Arimondo, and P. D. Lett, "Strong relative intensity squeezing by 4-wave mixing in Rb vapor", in 2007 Quantum Electronics and Laser Science Conference (May 2007).

[110] G. Triginer, M. D. Vidrighin, N. Quesada, A. Eckstein, M. Moore, W. S. Kolthammer, J. E. Sipe, and I. A. Walmsley, "Understanding high-gain twin-beam sources using cascaded stimulated emission", Physical Review X **10**, 031063 (2020).

[111] S. Lemieux, "Applications of high-gain parametric down-conversion to metrology", (University of Ottawa, 2023).

[112] D. T. Smithey, M. Beck, M. Belsley, and M. G. Raymer, "Sub-shot-noise correlation of total photon number using macroscopic twin pulses of light", Physical Review Letters **69**, 2650–2653 (1992).

[113] A. Lamas-Linares, J. C. Howell, and D. Bouwmeester, "Stimulated emission of polarization-entangled photons", Nature **412**, 887–890 (2001).

[114] M. Eibl, S. Gaertner, M. Bourennane, C. Kurtsiefer, M. Żukowski, and H. Weinfurter, "Experimental observation of four-photon entanglement from parametric down-conversion", Physical Review Letters **90**, 200403 (2003).

[115] C. Simon and D. Bouwmeester, "Theory of an entanglement laser", Physical Review Letters **91**, 53601 (2003).

[116] Y. Mei, X. Guo, L. Zhao, and S. Du, "Mirrorless optical parametric oscillation with tunable threshold in cold atoms", Physical Review Letters **119**, 150406 (2017).

[117] Z.-Y. J. Ou, "Multi-photon quantum interference", (Springer, New York, 2007).

[118] V. Giovannetti, S. Lloyd, and L. Maccone, "Quantum-enhanced measurements: beating the standard quantum limit", Science **306**, 1330–1336 (2004).

[119] J. P. Dowling, "Quantum optical metrology – the lowdown on high-N00N states", Contemporary Physics **49**, 125–143 (2008).

[120] R. H. Brown and R. Q. Twiss, "Correlation between photons in two coherent beams of light", Nature **177**, 27–29 (1956).

[121] J. H. Shapiro and K.-X. Sun, "Semiclassical versus quantum behavior in fourth-order interference", Journal of the Optical Society of America B **11**, 1130 (1994).

[122] T. Evans and D. Steer, "Wick's theorem at finite temperature", Nuclear Physics B **474**, 481–496 (1996).

[123] M. Mücke, J. Bochmann, C. Hahn, A. Neuzner, C. Nölleke, A. Reiserer, G. Rempe, and S. Ritter, "Generation of single photons from an atom-cavity system", Physical Review A **87**, 063805 (2013).

[124] I. Aharonovich, D. Englund, and M. Toth, "Solid-state single-photon emitters", Nature Photonics **10**, 631–641 (2016).

[125] H. J. Kimble, M. Dagenais, and L. Mandel, "Photon antibunching in resonance fluorescence", Physical Review Letters **39**, 691–695 (1977).

[126] A. Lenhard, J. Brito, M. Bock, C. Becher, and J. Eschner, "Coherence and entanglement preservation of frequency-converted heralded single photons", Optics Express **25**, 11187 (2017).

[127] N. Maring, D. Lago-Rivera, A. Lenhard, G. Heinze, and H. De Riedmatten, "Quantum frequency conversion of memory-compatible single photons from 606 nm to the telecom C-band", Optica **5**, 507 (2018).

[128] Y. Wang, J. Li, S. Zhang, K. Su, Y. Zhou, K. Liao, S. Du, H. Yan, and S.-L. Zhu, "Efficient quantum memory for single-photon polarization qubits", Nature Photonics **13**, 346–351 (2019).

[129] W. Chang, C. Li, Y.-K. Wu, N. Jiang, S. Zhang, Y.-F. Pu, X.-Y. Chang, and L.-M. Duan, "Long-distance entanglement between a multiplexed quantum memory and a telecom photon", Physical Review X **9**, 41033 (2019).

[130] P.-J. Tsai, Y.-F. Hsiao, and Y.-C. Chen, "Quantum storage and manipulation of heralded single photons in atomic memories based on electromagnetically induced transparency", Physical Review Research **2**, 033155 (2020).

[131] M. Erhard, M. Krenn, and A. Zeilinger, "Advances in high-dimensional quantum entanglement", Nature Reviews Physics **2**, 365–381 (2020).

[132] D. M. Greenberger, M. A. Horne, and A. Zeilinger, "Going beyond bell's theorem", in *Bell's Theorem, Quantum Theory and Conceptions of the Universe*, edited by M. Kafatos (Springer Netherlands, Dordrecht, 1989), pp. 69–72.

[133] M. Eibl, N. Kiesel, M. Bourennane, C. Kurtsiefer, and H. Weinfurter, "Experimental realization of a three-qubit Entangled W State", Physical Review Letters **92**, 077901 (2004).

[134] D. Bouwmeester, J.-W. Pan, M. Daniell, H. Weinfurter, and A. Zeilinger, "Observation of three-photon greenberger-horne-zeilinger entanglement", Phys. Rev. Lett. **82**, 1345–1349 (1999).

[135] J.-W. Pan, M. Daniell, S. Gasparoni, G. Weihs, and A. Zeilinger, "Experimental demonstration of four-photon entanglement and high-fidelity teleportation", Physical Review Letters **86**, 4435–4438 (2001).

[136] C. F. Roos, M. Riebe, H. Häffner, W. Hänsel, J. Benhelm, G. P. T. Lancaster, C. Becher, F. Schmidt-Kaler, and R. Blatt, "Control and measurement of three-qubit entangled states", Science **304**, 1478–1480 (2004).

[137] Z. Zhao, Y.-A. Chen, A.-N. Zhang, T. Yang, H. J. Briegel, and J.-W. Pan, "Experimental demonstration of five-photon entanglement and open-destination teleportation", Nature **430**, 54–58 (2004).

[138] J. Park and H. S. Moon, "Generation of a bright four-photon entangled state from a warm atomic ensemble via inherent polarization entanglement", Applied Physics Letters **120**, 24001 (2022).

[139] H. Weinfurter and M. Żukowski, "Four-photon entanglement from down-conversion", Physical Review A **64**, 10102 (2001).

[140] N. Kiesel, C. Schmid, G. Tóth, E. Solano, and H. Weinfurter, "Experimental observation of four-photon entangled dicke state with high fidelity", Phys. Rev. Lett. **98**, 63604 (2007).

[141] D. R. Hamel, L. K. Shalm, H. Hübel, A. J. Miller, F. Marsili, V. B. Verma, R. P. Mirin, S. W. Nam, K. J. Resch, and T. Jennewein, "Direct generation of three-photon polarization entanglement", Nature Photonics **8**, 801–807 (2014).

[142] Z. M. E. Chaisson, P. F. Poitras, M. Richard, Y. Castonguay-Page, P.-H. Glinel, V. Landry, and D. R. Hamel, "Phase-stable source of high-quality three-photon polarization entanglement by cascaded down-conversion", Physical Review A **105**, 063705 (2022).

[143] T. E. Keller, M. H. Rubin, Y. Shih, and L.-A. Wu, "Theory of the three-photon entangled state", Physical Review A **57**, 2076–2079 (1998).

[144] J. Wen, P. Xu, M. H. Rubin, and Y. Shih, "Transverse correlations in triphoton entanglement: geometrical and physical optics", Physical Review A **76**, 023828 (2007).

[145] T. Guerreiro, A. Martin, B. Sanguinetti, J. S. Pelc, C. Langrock, M. M. Fejer, N. Gisin, H. Zbinden, N. Sangouard, and R. T. Thew, "Nonlinear interaction between single photons", Physical Review Letters **113**, 173601 (2014).

[146] W. Dür, G. Vidal, and J. I. Cirac, "Three qubits can be entangled in two inequivalent ways", Physical Review A **62**, 062314 (2000).

[147] A. Cabello, "Bell's theorem with and without inequalities for the three-qubit greenberger-horne-zeilinger and Wstates", Physical Review A **65**, 032108 (2002).

[148] P. W. Shor, "Scheme for reducing decoherence in quantum computer memory", Physical Review A **52**, R2493–R2496 (1995).

[149] K. Bencheikh, F. Gravier, J. Douady, A. Levenson, and B. Boulanger, "Triple photons: a challenge in nonlinear and quantum optics", Comptes Rendus Physique **8**, 206–220 (2007).

[150] M. Khoshnegar, T. Huber, A. Predojević, D. Dalacu, M. Prilmüller, J. Lapointe, X. Wu, P. Tamarat, B. Lounis, P. Poole, G. Weihs, and H. Majedi, "A solid state source of photon triplets based on quantum dot molecules", Nature Communications **8**, 15716 (2017).

[151] M. V. Chekhova, O. A. Ivanova, V. Berardi, and A. Garuccio, "Spectral properties of three-photon entangled states generated via three-photon parametric down-conversion in a$\chi(3)$medium", Physical Review A **72**, 023818 (2005).

[152] M. Corona, K. Garay-Palmett, and A. B. U'Ren, "Third-order spontaneous parametric down-conversion in thin optical fibers as a photon-triplet source", Physical Review A **84**, 033823 (2011).

[153] M. Corona, K. Garay-Palmett, and A. B. U'Ren, "Experimental proposal for the generation of entangled photon triplets by third-order spontaneous parametric downconversion in optical fibers", Optics Letters **36**, 190 (2011).

[154] C. Okoth, A. Cavanna, N. Y. Joly, and M. V. Chekhova, "Seeded and unseeded high-order parametric down-conversion", Physical Review A **99**, 043809 (2019).

[155] A. Agustí, C. W. S. Chang, F. Quijandría, G. Johansson, C. M. Wilson, and C. Sabín, "Tripartite genuine non-gaussian entanglement in three-mode spontaneous parametric down-conversion", Physical Review Letters **125**, 020502 (2020).

[156] D. Zhang, Y. Cai, Z. Zheng, D. Barral, Y. Zhang, and M. Xiao, "Non-gaussian nature and entanglement of spontaneous parametric nondegenerate triple-photon generation", Physical Review A **103**, 013704 (2021).

[157] H. Hübel, D. R. Hamel, A. Fedrizzi, S. Ramelow, K. J. Resch, and T. Jennewein, "Direct generation of photon triplets using cascaded photon-pair sources", Nature **466**, 601–603 (2010).

[158] L. K. Shalm, D. R. Hamel, Z. Yan, C. Simon, K. J. Resch, and T. Jennewein, "Three-photon energy–time entanglement", Nature Physics **9**, 19–22 (2013).

[159] S. Krapick, B. Brecht, H. Herrmann, V. Quiring, and C. Silberhorn, "On-chip generation of photon-triplet states", Optics Express **24**, 2836 (2016).

[160] X. Jia, Z. Yan, Z. Duan, X. Su, H. Wang, C. Xie, and K. Peng, "Experimental realization of three-color entanglement at optical fiber communication and atomic storage wavelengths", Physical Review Letters **109**, 253604 (2012).

[161] Z. Qin, L. Cao, H. Wang, A. M. Marino, W. Zhang, and J. Jing, "Experimental generation of multiple quantum correlated beams from hot rubidium vapor", Physical Review Letters **113**, 023602 (2014).

[162] D.-S. Ding, W. Zhang, S. Shi, Z.-Y. Zhou, Y. Li, B.-S. Shi, and G.-C. Guo, "Hybrid-cascaded generation of tripartite telecom photons using an atomic ensemble and a nonlinear waveguide", Optica **2**, 642 (2015).

[163] J. Wen, E. Oh, and S. Du, "Tripartite entanglement generation via four-wave mixings: narrowband triphoton W state", Journal of the Optical Society of America B **27**, A11 (2010).

[164] H. de Riedmatten, V. Scarani, I. Marcikic, A. Acin, W. Tittel, H. Zbinden, and N. Gisin, "Two independent photon pairs versus four-photon entangled states in parametric down conversion", Journal of Modern Optics **51**, 1637–1649 (2004).

[165] J. Wen and M. H. Rubin, "Distinction of tripartite Greenberger-Horne-Zeilinger and Wstates entangled in time (or energy) and space", Physical Review A **79**, 025802 (2009).

[166] H. Kang, G. Hernandez, and Y. Zhu, "Slow-light six-wave mixing at low light intensities", Physical Review Letters **93**, 73601 (2004).

[167] Y. Zhang, A. W. Brown, and M. Xiao, "Opening four-wave mixing and six-wave mixing channels via dual electromagnetically induced transparency windows", Physical Review Letters **99**, 123603 (2007).

[168] D. Felinto, D. Moretti, R. A. de Oliveira, and J. W. R. Tabosa, "Delayed four- and six-wave mixing in a coherently prepared atomic ensemble", Optics Letters **35**, 3937 (2010).

[169] Z. Wang, P. Li, H. Zheng, S. Sang, R. Zhang, Y. Zhang, and M. Xiao, "Interference of three multiwave mixings via electromagnetically induced transparency", Journal of the Optical Society of America B **28**, 1922 (2011).

[170] K. Li, J. Wen, Y. Cai, S. V. Ghamsari, C. Li, F. Li, Z. Zhang, Y. Zhang, and M. Xiao, "Direct generation of time-energy-entangled W triphotons in atomic vapor", Science Advances **10**, eado3199 (2024).

[171] T. Hänsch and A. Schawlow, "Cooling of gases by laser radiation", Optics Communications **13**, 68–69 (1975).

[172] C. N. Cohen-Tannoudji, "Nobel lecture: manipulating atoms with photons", Reviews of Modern Physics **70**, 707–719 (1998).

[173] S. Chu, L. Hollberg, J. E. Bjorkholm, A. Cable, and A. Ashkin, "Three-dimensional viscous confinement and cooling of atoms by resonance radiation pressure", Physical Review Letters **55**, 48–51 (1985).

[174] H. e. Perrin, "Les houches lectures on laser cooling and trapping", 2012.

[175] C. Cohen-Tannoudji and D. Guéry-Odelin, "Advances in atomic physics: an overview", (World Scientific, Singapore ; Hackensack, NJ, 2011).

[176] W. D. Phillips, "Laser cooling and trapping of neutral atoms", Rev. Mod. Phys. **70**, 721 (1998).

[177] P. D. Lett, R. N. Watts, C. I. Westbrook, W. D. Phillips, P. L. Gould, and H. J. Metcalf, "Observation of atoms laser cooled below the doppler limit", Physical Review Letters **61**, 169–172 (1988).

[178] J. Dalibard and C. Cohen-Tannoudji, "Laser cooling below the doppler limit by polarization gradients: simple theoretical models", Journal of the Optical Society of America B **6**, 2023 (1989).

[179] A. Aspect, E. Arimondo, R. Kaiser, N. Vansteenkiste, and C. Cohen-Tannoudji, "Laser cooling below the one-photon recoil energy by velocity-selective coherent population trapping", Physical Review Letters **61**, 826–829 (1988).

[180] M. Kasevich and S. Chu, "Laser cooling below a photon recoil with three-level atoms", Physical Review Letters **69**, 1741–1744 (1992).

[181] C. Monroe, D. M. Meekhof, B. E. King, S. R. Jefferts, W. M. Itano, D. J. Wineland, and P. Gould, "Resolved-sideband raman cooling of a bound atom to the 3D zero-point energy", Physical Review Letters **75**, 4011–4014 (1995).

[182] A. Griffin, D. W. Snoke, and S. Stringari, eds., "Bose-einstein condensation", 1st ed. (Cambridge University Press, Apr. 6, 1995).

[183] L. Pruvost, I. Serre, H. T. Duong, and J. Jortner, "Expansion and cooling of a bright rubidium three-dimensional optical molasses", Physical Review A **61**, 53408 (2000).

[184] G. Labeyrie, F. Michaud, and R. Kaiser, "Self-sustained oscillations in a large magneto-optical trap", Physical Review Letters **96**, 23003 (2006).

[185] S. R. Muniz, K. M. F. Magalhães, E. A. L. Henn, L. G. Marcassa, and V. S. Bagnato, "Creating a self-induced dark spontaneous-force optical trap for neutral atoms", Optics Communications **235**, 333–340 (2004).

[186] S. Zhang, J. F. Chen, C. Liu, S. Zhou, M. M. T. Loy, G. K. L. Wong, and S. Du, "A dark-line two-dimensional magneto-optical trap of ^{85} Rb atoms with high optical depth", Review of Scientific Instruments **83**, 73102 (2012).

[187] G. Reinaudi, T. Lahaye, Z. Wang, and D. Guéry-Odelin, "Strong saturation absorption imaging of dense clouds of ultracold atoms", Optics Letters **32**, 3143 (2007).

[188] A. Eloy, Z. Yao, R. Bachelard, W. Guerin, M. Fouché, and R. Kaiser, "Diffusing-wave spectroscopy of cold atoms in ballistic motion", Physical Review A **97**, 13810 (2018).

[189] K. Hueck, N. Luick, L. Sobirey, J. Siegl, T. Lompe, H. Moritz, L. W. Clark, and C. Chin, "Calibrating high intensity absorption imaging of ultracold atoms", Optics Express **25**, 8670 (2017).

[190] C. E. Wieman and L. Hollberg, "Using diode lasers for atomic physics", Review of Scientific Instruments **62**, 1–20 (1991).

[191] R. W. P. Drever, J. L. Hall, F. V. Kowalski, J. Hough, G. M. Ford, A. J. Munley, and H. Ward, "Laser phase and frequency stabilization using an optical resonator", Applied Physics B: Photophysics and Laser Chemistry **31**, 97–105 (1983).

[192] B. L. Ng, "Progress towards realizing atom-light interface with blue-detuned tweezers array", PhD thesis (National University of Singapore, 2023).

[193] G. C. Bjorklund, "Frequency-modulation spectroscopy: a new method for measuring weak absorptions and dispersions", Optics Letters **5**, 15 (1980).

[194] D. J. McCarron, S. A. King, and S. L. Cornish, "Modulation transfer spectroscopy in atomic rubidium", Measurement Science and Technology **19**, 105601 (2008).

[195] B. Wu, Y. Zhou, K. Weng, D. Zhu, Z. Fu, B. Cheng, X. Wang, and Q. Lin, "Modulation transfer spectroscopy for D1 transition line of rubidium", Journal of the Optical Society of America B **35**, 2705 (2018).

[196] J.-B. Long, S.-J. Yang, S. Chen, and J.-W. Pan, "Magnetic-enhanced modulation transfer spectroscopy and laser locking for 87Rb repump transition", Optics Express **26**, 27773 (2018).

[197] "Rubidium 87 D line data", ().

[198] V. Prakash, "Narrowband photon pairs for atoms: high resolution spectral engineering and characterisation", PhD thesis (Universitat Politècnica de Catalunya, 2021).

[199] A. Ahlrichs, C. Berkemeier, B. Sprenger, and O. Benson, "A monolithic polarization-independent frequency-filter system for filtering of photon pairs", Applied Physics Letters **103**, 241110 (2013).

[200] "Nonlinear optical parametric processes in liquids and gases", (Elsevier, 1984).

[201] P. R. Hemmer, D. P. Katz, J. Donoghue, M. S. Shahriar, P. Kumar, and M. Cronin-Golomb, "Efficient low-intensity optical phase conjugation based on coherent population trapping in sodium", Optics Letters **20**, 982 (1995).

[202] D. A. Braje, V. Balić, S. Goda, G. Y. Yin, and S. E. Harris, "Frequency mixing using electromagnetically induced transparency in cold atoms", Physical Review Letters **93**, 183601 (2004).

[203] R. J. Glauber, "The quantum theory of optical coherence", Physical Review **130**, 2529–2539f (1963).

[204] X. Guo, "Time-frequency entanglement of narrowband biphotons", PhD thesis (Hong Kong University of Science and Technology, 2018).

[205] S. H. Autler and C. H. Townes, "Stark effect in rapidly varying fields", Physical Review **100**, 703–722 (1955).

[206] R. Finkelstein, S. Bali, O. Firstenberg, and I. Novikova, "A practical guide to electromagnetically induced transparency in atomic vapor", New Journal of Physics **25**, 35001 (2023).

[207] A. V. Andreev and V. I. Emel'yanov, "Collective spontaneous emission (dicke superradiance)", Sov. Phys. Usp. **23**, 493 (1980).

[208] D. Budker, W. Gawlik, D. F. Kimball, S. M. Rochester, V. V. Yashchuk, and A. Weis, "Resonant nonlinear magneto-optical effects in atoms", Reviews of Modern Physics **74**, 1153–1201 (2002).

[209] A. Lezama, S. Barreiro, and A. M. Akulshin, "Electromagnetically induced absorption", Physical Review A **59**, 4732–4735 (1999).

[210] J. F. Clauser, "Experimental distinction between the quantum and classical field-theoretic predictions for the photoelectric effect", Phys. Rev. D **9**, 853–860 (1974).

[211] P. Sekatski, N. Sangouard, F. Bussieres, C. Clausen, N. Gisin, and H. Zbinden, "Detector imperfections in photon-pair source characterization", Journal of Physics B: Atomic, Molecular and Optical Physics **45**, 124016 (2012).

[212] P. Lassègues, M. A. F. Biscassi, M. Morisse, A. Cidrim, P. G. S. Dias, H. Eneriz, R. C. Teixeira, R. Kaiser, R. Bachelard, and M. Hugbart, "Transition from classical to quantum loss of light coherence", Physical Review A: Atomic, Molecular, and Optical Physics **108**, 42214 (2023).

[213] C. Gardiner and P. Zoller, "Quantum noise: a handbook of markovian and non-markovian quantum stochastic methods with applications to quantum optics", Springer Series in Synergetics (Springer, 2004).

[214] R. Loudon, "The quantum theory of light", Third Edition (Oxford University PressOxford, Sept. 7, 2000).

[215] F. L. Pedrotti, L. M. Pedrotti, and L. S. Pedrotti, "Introduction to optics", 3rd ed. (Cambridge University Press, Dec. 21, 2017).

[216] D. C. Champeney, "A handbook of fourier theorems", (Cambridge University Press, 1987).

[217] D. Ferreira, R. Bachelard, W. Guerin, R. Kaiser, and M. Fouché, "Connecting field and intensity correlations: the siegert relation and how to test it", American Journal of Physics **88**, 831–837 (2020).

[218] J. Keaveney, A. Sargsyan, U. Krohn, I. G. Hughes, D. Sarkisyan, and C. S. Adams, "Cooperative lamb shift in an atomic vapor layer of nanometer thickness", Physical Review Letters **108**, 173601 (2012).

[219] T. Peyrot, Y. R. P. Sortais, A. Browaeys, A. Sargsyan, D. Sarkisyan, J. Keaveney, I. G. Hughes, and C. S. Adams, "Collective lamb shift of a nanoscale atomic vapor layer within a sapphire cavity", Physical Review Letters **120**, 243401 (2018).

[220] S. J. Roof, K. J. Kemp, M. D. Havey, and I. M. Sokolov, "Observation of single-photon superradiance and the cooperative lamb shift in an extended sample of cold atoms", Physical Review Letters **117**, 73003 (2016).

[221] S. Jennewein, M. Besbes, N. J. Schilder, S. Jenkins d. D, C. Sauvan, J. Ruostekoski, J.-J. Greffet, Y. R. P. Sortais, and A. Browaeys, "Coherent scattering of near-resonant light by a dense microscopic cold atomic cloud", Physical Review Letters **116**, 233601 (2016).

[222] R. Friedberg and S. R. Hartmann, "Frequency shifts in emission and absorption by resonant systems of two-level atoms", Physics Reports **7**, 101–179 (1972).

[223] R. Friedberg and J. T. Manassah, "Effects of including the counterrotating term and virtual photons on the eigenfunctions and eigenvalues of a scalar photon collective emission theory", Physics Letters A **372**, 2514–2521 (2008).

[224] M. O. Scully, "Collective lamb shift in single photon dicke superradiance", Physical Review Letters **102**, 143601 (2009).

[225] H. Ma and S. F. Yelin, "Collective lamb shift and modified linewidth of an interacting atomic gas", (Feb. 22, 2024) `http://arxiv.org/abs/2305.01865`, pre-published.

[226] R. Chinnarasu, Y.-F. Ding, C.-Y. Lee, T.-H. Hsieh, I. A. Yu, and C.-S. Chuu, "Efficient generation of subnatural-linewidth biphotons by controlled quantum interference", Physical Review A **101**, 063837 (2020).

[227] R. H. Dicke, "Coherence in spontaneous radiation processes", Physical Review **93**, 99–110 (1954).

[228] M. Gross and S. Haroche, "Superradiance: an essay on the theory of collective spontaneous emission", Physics Reports **93**, 301–396 (1982).

[229] M. O. Scully and A. A. Svidzinsky, "The super of superradiance", Science **325**, 1510–1511 (2009).

[230] A. Goban, C.-L. Hung, J. D. Hood, S.-P. Yu, J. A. Muniz, O. Painter, and H. J. Kimble, "Superradiance for atoms trapped along a photonic crystal waveguide", Phys. Rev. Lett. **115**, 63601 (2015).

[231] S. J. Masson, I. Ferrier-Barbut, L. A. Orozco, A. Browaeys, and A. Asenjo-Garcia, "Many-body signatures of collective decay in atomic chains", Physical Review Letters **125**, 263601 (2020).

[232] O. Rubies-Bigorda and S. F. Yelin, "Superradiance and subradiance in inverted atomic arrays", Phys. Rev. A **106**, 53717 (2022).

[233] F. Robicheaux, "Theoretical study of early-time superradiance for atom clouds and arrays", Physical Review A **104**, 63706 (2021).

[234] E. Sierra, S. J. Masson, and A. Asenjo-Garcia, "Dicke superradiance in ordered lattices: dimensionality matters", Phys. Rev. Res. **4**, 23207 (2022).

[235] N. Skribanowitz, I. P. Herman, J. C. MacGillivray, and M. S. Feld, "Observation of dicke superradiance in optically pumped HF gas", Phys. Rev. Lett. **30**, 309–312 (1973).

[236] F. Gounand, M. Hugon, P. R. Fournier, and J. Berlande, "Superradiant cascading effects in rubidium rydberg levels", Journal of Physics B: Atomic and Molecular Physics **12**, 547 (1979).

[237] W. Guerin, M. O. Araújo, and R. Kaiser, "Subradiance in a large cloud of cold atoms", Physical Review Letters **116**, 83601 (2016).

[238] M. O. Araújo, I. Krešić, R. Kaiser, and W. Guerin, "Superradiance in a large and dilute cloud of cold atoms in the linear-optics regime", Physical Review Letters **117**, 73002 (2016).

[239] A. A. Svidzinsky, F. Li, H. Li, X. Zhang, C. H. R. Ooi, and M. O. Scully, "Single-photon superradiance and radiation trapping by atomic shells", Physical Review A **93**, 43830 (2016).

[240] T. Laske, H. Winter, and A. Hemmerich, "Pulse delay time statistics in a superradiant laser with calcium atoms", Physical Review Letters **123**, 103601 (2019).

[241] G. Ferioli, A. Glicenstein, F. Robicheaux, R. T. Sutherland, A. Browaeys, and I. Ferrier-Barbut, "Laser-driven superradiant ensembles of two-level atoms near dicke regime", Physical Review Letters **127**, 243602 (2021).

[242] R. Pennetta, M. Blaha, A. Johnson, D. Lechner, P. Schneeweiss, J. Volz, and A. Rauschenbeutel, "Collective radiative dynamics of an ensemble of cold atoms coupled to an optical waveguide", Physical Review Letters **128**, 73601 (2022).

[243] R. G. DeVoe and R. G. Brewer, "Observation of superradiant and subradiant spontaneous emission of two trapped ions", Phys. Rev. Lett. **76**, 2049–2052 (1996).

[244] A. F. Van Loo, A. Fedorov, K. Lalumière, B. C. Sanders, A. Blais, and A. Wallraff, "Photon-mediated interactions between distant artificial atoms", Science **342**, 1494–1496 (2013).

[245] M. Gross, P. Goy, C. Fabre, S. Haroche, and J. M. Raimond, "Maser oscillation and microwave superradiance in small systems of rydberg atoms", Phys. Rev. Lett. **43**, 343–346 (1979).

[246] D. D. Grimes, S. L. Coy, T. J. Barnum, Y. Zhou, S. F. Yelin, and R. W. Field, "Direct single-shot observation of millimeter-wave superradiance in rydberg-rydberg transitions", Phys. Rev. A **95**, 43818 (2017).

[247] A. Karnieli, N. Rivera, A. Arie, and I. Kaminer, "Superradiance and subradiance due to quantum interference of entangled free electrons", Physical Review Letters **127**, 60403 (2021).

[248] M. O. Scully, E. S. Fry, C. H. R. Ooi, and K. Wódkiewicz, "Directed spontaneous emission from an extended ensemble of N atoms: timing is everything", Physical Review Letters **96**, 10501 (2006).

[249] A. A. Svidzinsky, J.-T. Chang, and M. O. Scully, "Dynamical evolution of correlated spontaneous emission of a single photon from a uniformly excited cloud of N atoms", Physical Review Letters **100**, 160504 (2008).

[250] L. Ortiz-Gutiérrez, L. F. Muñoz-Martínez, D. F. Barros, J. E. O. Morales, R. S. N. Moreira, N. D. Alves, A. F. G. Tieco, P. L. Saldanha, and D. Felinto, "Experimental fock-state superradiance", Physical Review Letters **120**, 83603 (2018).

[251] N. Piovella and S. Olivares, "Single photon superradiance and subradiance as collective emission from symmetric and antisymmetric states", Symmetry **15**, 1817 (2023).

[252] R. A. De Oliveira, M. S. Mendes, W. S. Martins, P. L. Saldanha, J. W. R. Tabosa, and D. Felinto, "Single-photon superradiance in cold atoms", Physical Review A **90**, 23848 (2014).

[253] P. Weiss, A. Cipris, R. Kaiser, I. M. Sokolov, and W. Guerin, "Superradiance as single scattering embedded in an effective medium", Physical Review A **103**, 23702 (2021).

[254] M. Gross, C. Fabre, P. Pillet, and S. Haroche, "Observation of near-infrared dicke superradiance on cascading transitions in atomic sodium", Physical Review Letters **36**, 1035–1038 (1976).

[255] L. Sczaniecki and J. Buchert, "Subharmonic superradiance", Optics Communications **27**, 463–465 (1978).

[256] M. Gross, J. Raimond, and S. Haroche, "Doppler beats in superradiance", Physical Review Letters **40**, 1711 (1978).

[257] C. Liedl, F. Tebbenjohanns, C. Bach, S. Pucher, A. Rauschenbeutel, and P. Schneeweiss, "Observation of superradiant bursts in a cascaded quantum system", Physical Review X **14**, 11020 (2024).

[258] C. W. Chou, S. V. Polyakov, A. Kuzmich, and H. J. Kimble, "Single-photon generation from stored excitation in an atomic ensemble", Physical Review Letters **92**, 213601 (2004).

[259] D. Meiser, J. Ye, D. R. Carlson, and M. J. Holland, "Prospects for a millihertz-linewidth laser", Phys. Rev. Lett. **102**, 163601 (2009).

[260] J. G. Bohnet, Z. Chen, J. M. Weiner, D. Meiser, M. J. Holland, and J. K. Thompson, "A steady-state superradiant laser with less than one intracavity photon", Nature **484**, 78–81 (2012).

[261] J. G. Bohnet, Z. Chen, J. M. Weiner, K. C. Cox, and J. K. Thompson, "Active and passive sensing of collective atomic coherence in a superradiant laser", Physical Review A **88**, 13826 (2013).

[262] H. H. Jen, "Superradiant laser: effect of long-range dipole-dipole interaction", Physical Review A **94**, 53813 (2016).

[263] H. Liu, S. B. Jäger, X. Yu, S. Touzard, A. Shankar, M. J. Holland, and T. L. Nicholson, "Rugged mHz-linewidth superradiant laser driven by a hot atomic beam", Physical Review Letters **125**, 253602 (2020).

[264] G. Ferioli, A. Glicenstein, I. Ferrier-Barbut, and A. Browaeys, "A non-equilibrium superradiant phase transition in free space", Nature Physics **19**, 1345–1349 (2023).

[265] S. Agarwal, E. Chaparro, D. Barberena, A. P. Orioli, G. Ferioli, S. Pancaldi, I. Ferrier-Barbut, A. Browaeys, and A. Rey, "Directional superradiance in a driven ultracold atomic gas in free space", PRX Quantum **5**, 40335 (2024).

[266] D. Meiser and M. J. Holland, "Intensity fluctuations in steady-state superradiance", Physical Review A **81**, 63827 (2010).

[267] D. Goncalves, L. Bombieri, G. Ferioli, S. Pancaldi, I. Ferrier-Barbut, A. Browaeys, E. Shahmoon, and D. Chang, "Driven-dissipative phase separation in free-space atomic ensembles", PRX Quantum **6**, 20303 (2025).

[268] H. J. Briegel and R. Raussendorf, "Persistent entanglement in arrays of interacting particles", Physical Review Letters **86**, 910–913 (2001).

[269] A. N. Boto, P. Kok, D. S. Abrams, S. L. Braunstein, C. P. Williams, and J. P. Dowling, "Quantum interferometric optical lithography: exploiting entanglement to beat the diffraction limit", Physical Review Letters **85**, 2733–2736 (2000).

[270] P. Kok, A. N. Boto, D. S. Abrams, C. P. Williams, S. L. Braunstein, and J. P. Dowling, "Quantum-interferometric optical lithography: towards arbitrary two-dimensional patterns", Physical Review A **63**, 063407 (2001).

[271] K. Yu. Spasibko, T. Sh. Iskhakov, and M. V. Chekhova, "Spectral properties of high-gain parametric down-conversion", Optics Express **20**, 7507 (2012).

[272] T. S. Iskhakov, V. C. Usenko, R. Filip, M. V. Chekhova, and G. Leuchs, "Low-noise macroscopic twin beams", Physical Review A **9**, 043849 (2016).

[273] D. Achilles, C. Silberhorn, and I. A. Walmsley, "Direct, loss-tolerant characterization of nonclassical photon statistics", Physical Review Letters **97**, 43602 (2006).

[274] C. Weedbrook, S. Pirandola, R. García-Patrón, N. J. Cerf, T. C. Ralph, J. H. Shapiro, and S. Lloyd, "Gaussian quantum information", Reviews of Modern Physics **84**, 621–669 (2012).

[275] S. L. Braunstein and P. van Loock, "Quantum information with continuous variables", Rev. Mod. Phys. **77**, 513 (2005).

[276] Y. Zhou, J. Simon, J. Liu, and Y. Shih, "Third-order correlation function and ghost imaging of chaotic thermal light in the photon counting regime", Physical Review A **81**, 43831 (2010).

[277] R. J. Glauber, "Nobel lecture: one hundred years of light quanta", Reviews of Modern Physics **78**, 1267–1278 (2006).

[278] S. Bettelli, “Comment on "coherence measures for heralded single-photon sources"”, Physical Review A **81**, 37801 (2010).

[279] B. Srivathsan, “Heralded single photons for efficient interaction with single atoms”, PhD thesis (National University of Singapore, 2015).

[280] P. Grangier, G. Roger, and A. Aspect, “Experimental evidence for a photon anticorrelation effect on a beam splitter: a new light on single-photon interferences”, Europhysics Letters (EPL) **1**, 173–179 (1986).

[281] M. Razavi, I. Söllner, E. Bocquillon, C. Couteau, R. Laflamme, and G. Weihs, “Characterizing heralded single-photon sources with imperfect measurement devices”, Journal of Physics B: Atomic, Molecular and Optical Physics **42**, 114013 (2009).

[282] P. Senellart, G. Solomon, and A. White, “High-performance semiconductor quantum-dot single-photon sources”, Nature Nanotechnology **12**, 1026–1039 (2017).

[283] C. Couteau, S. Barz, T. Durt, T. Gerrits, J. Huwer, R. Prevedel, J. Rarity, A. Shields, and G. Weihs, “Applications of single photons to quantum communication and computing”, Nature Reviews Physics **5**, 326–338 (2023).

[284] G. Brassard, N. Lütkenhaus, T. Mor, and B. C. Sanders, “Limitations on practical quantum cryptography”, Physical Review Letters **85**, 1330–1333 (2000).

[285] M. A. Broome, A. Fedrizzi, S. Rahimi-Keshari, J. Dove, S. Aaronson, T. C. Ralph, and A. G. White, “Photonic boson sampling in a tunable circuit”, Science **339**, 794–798 (2013).

[286] C. Liu, “Generation and application of narrowband photon pairs”, PhD thesis (Hong Kong University of Scinece and Technology, 2014).

[287] L. Zhao, “Narrowband biphoton generation in the group delay regime”, PhD thesis (Hong Kong University of Scinece and Technology, 2016).

[288] C. Ma, X. Wang, V. Anant, A. D. Beyer, M. D. Shaw, and S. Mookherjea, “Silicon photonic entangled photon-pair and heralded single photon generation with CAR $>$ 12,000 and g$\hat{}$(2)(0) $<$ 0006”, Optics Express **25**, 32995 (2017).

[289] T. J. Steiner, J. E. Castro, L. Chang, Quynh Dang, W. Xie, J. Norman, J. E. Bowers, and G. Moody, "Ultrabright entangled-photon-pair generation from an AlGaAs-on-insulator microring resonator", PRX Quantum **2**, 10337 (2021).

[290] J. Du, G. F. R. Chen, H. Gao, J. A. Grieve, D. T. H. Tan, and A. Ling, "Demonstration of a low loss, highly stable and re-useable edge coupler for high heralding efficiency and low g(2)(0) SOI correlated photon pair sources", Optics Express **32**, 11406 (2024).

[291] M. Förtsch, J. U. Fürst, C. Wittmann, D. Strekalov, A. Aiello, M. V. Chekhova, C. Silberhorn, G. Leuchs, and C. Marquardt, "A versatile source of single photons for quantum information processing", Nature Communications **4**, 1818 (2013).

[292] B. L. Ng, "Towards correlated photon triplets from six-wave mixing", MA thesis (National University of Singapore, 2018).

[293] M. S. Safronova, C. J. Williams, and C. W. Clark, "Relativistic many-body calculations of electric-dipole matrix elements, lifetimes, and polarizabilities in rubidium", Physical Review A **69**, 22509 (2004).

[294] D. Sheng, A. Pérez Galván, and L. A. Orozco, "Lifetime measurements of the 5 d states of rubidium", Physical Review A **78**, 62506 (2008).

[295] R. Beard, K. W. Martin, J. D. Elgin, B. L. Kasch, and S. P. Krzyzewski, "Two-photon rubidium clock detecting 776 nm fluorescence", Optics Express **32**, 7417 (2024).

[296] L. V. Hau, S. E. Harris, Z. Dutton, and C. H. Behroozi, "Light speed reduction to 17 metres per second in an ultracold atomic gas", Nature **397**, 594–598 (1999).

[297] M. Fleischhauer and T. Richter, "Pulse matching and correlation of phase fluctuations in Λ systems", Physical Review A **51**, 2430–2442 (1995).

[298] M. Fleischhauer and M. D. Lukin, "Dark-state polaritons in electromagnetically induced transparency", Physical Review Letters **84**, 5094–5097 (2000).

[299] F. Campaioli, J. H. Cole, and H. Hapuarachchi, "Quantum master equations: tips and tricks for quantum optics, quantum computing, and beyond", PRX Quantum **5**, 20202 (2024).

[300] G. Ferioli, S. Pancaldi, A. Glicenstein, D. Clément, A. Browaeys, and I. Ferrier-Barbut, "Non-gaussian correlations in the steady state of driven-dissipative clouds of two-level atoms", Physical Review Letters **132**, 133601 (2024).

[301] G. Ferioli, I. Ferrier-Barbut, and A. Browaeys, "Emergence of second-order coherence in the superradiant emission from a free-space atomic ensemble", Physical Review Letters **134**, 153602 (2025).

[302] F. Andreoli, M. J. Gullans, A. A. High, A. Browaeys, and D. E. Chang, "Maximum refractive index of an atomic medium", Physical Review X **11**, 011026 (2021).

[303] M. Johnsson, E. Korsunsky, and M. Fleischhauer, "Eliminating nonlinear phase mismatch in resonantly enhanced 4-wave mixing", Optics Communications **212**, 335–341 (2002).

[304] M. T. Turnbull, P. G. Petrov, C. S. Embrey, A. M. Marino, and V. Boyer, "Role of the phase-matching condition in nondegenerate four-wave mixing in hot vapors for the generation of squeezed states of light", Physical Review A **88**, 33845 (2013).

Appendix A

Polarization calibration

In the lab frame, circular polarization can be altered by optical elements such as mirrors, which may flip its handedness. As the polarization of the generated photons is defined in the atomic frame, aligning the detection polarization with that at the atom is nontrivial in the circular basis. However, thanks to the near-axis configuration used in our setup, we can bypass this complexity introduced by polarization changes after reflections. Since the laser leakage photons can be collected along the same spatial modes as the generated photons (e.g., Stokes or anti-Stokes), they experience the same optical path. This allows us to use the polarization of the leaked laser light as a reliable reference for calibration. In this thesis, the notations σ^+/σ^- refer to circular polarizations at the side of the atomic cloud, with respect to a fixed quantization axis (x-axis). In contrast, the terms "left-" and "right-hand circular polarization" denote the polarization states defined along the beam propagation direction, which is used to align the optics.

In practice, we calibrate the polarization filter, consisting of a quarter-wave plate (QWP) and a half-wave plate (HWP), by monitoring the sinusoidal modulation of the leakage photon detection as the QWP angle of the pump field is varied. This approach enables accurate calibration of pump field and generated field polarizations at the atom side, without needing to account for polarization changes along the collection path.

The pump laser is initially prepared in horizontal (H) linear polarization using a polarizing beam splitter, and is then converted to the desired circular polarization using a quarter-wave plate (QWP). To ensure accurate control of the detected polarization, the QWP and half-wave plate (HWP) in the polarization analysis setup must first be calibrated. As shown in Figure A.1, when the polarization filter is

configured to represent σ^+ polarization, we observe that varying the QWP angle in the pump path does not yield the expected sinusoidal modulation in the collected leakage photon signal. However, introducing a slight compensation of approximately 10° to the HWP restores the expected sinusoidal dependence, indicating proper polarization alignment. In this modulation pattern, the dip corresponds to the case where the pump polarization is opposite to that of the generated photons in the laboratory frame, while the peak indicates matching polarizations between the pump and the generated photons. The required compensation implies that there exists an additional relative phase between the H and V bases introduced in the optical path. However, the underlying cause of this discrepancy remains unclear. The deviation persists even after replacing several optical components, including the QWP and HWP.

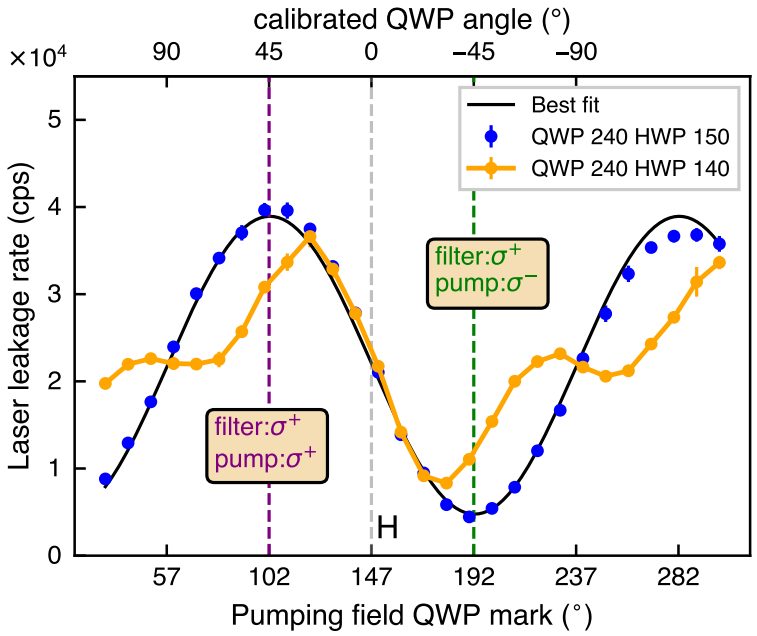

Figure A.1: Calibration between the QWP of the pumping field and the corresponding right-hand circular polarization filter for the Stokes field consisting of a QWP and a HWP. The label of "QWP 240 HWP 140" corresponds to nominal σ^+ polarization based on individual calibration of QWP and HWP. The configuration "QWP 240 HWP 150" represents the optimized setting for σ^+ polarization, determined by optimizing the expected sinusoidal modulation of the leakage laser (see blue data).

The coupling field is initially linearly polarized (H) by a PBS and then converted

to circular polarization using a QWP. In the calibration between the anti-Stokes polarization filter and the coupling field polarization in Figure A.2, the above problem does not exist. A clear sinusoidal modulation pattern is observed when the QWP of the coupling field varies and the polarization filter for the anti-Stokes field is fixed at σ^-. The observed dip corresponds to opposite circular polarizations: σ^+ for the coupling field and σ^- for the filtered anti-Stokes field (defined along the coupling field's propagation direction). Conversely, the peak indicates matching circular polarizations: both coupling and anti-Stokes fields being σ^-. Additionally, when the filtered polarization matches that of the coupling field, the leakage of coupling photons into the anti-Stokes detection channel increases to an unacceptable level.

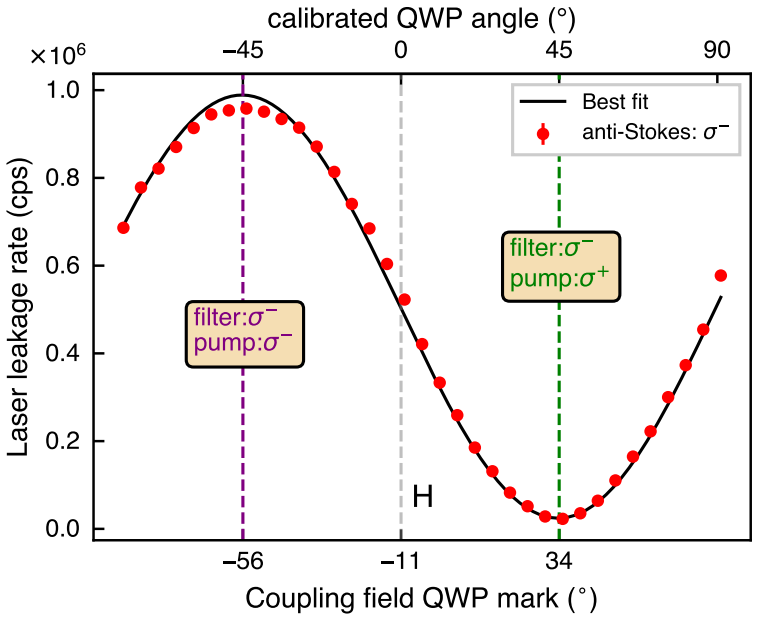

Figure A.2: Calibration between the QWP of the pumping field and the corresponding left-hand circular polarization filter for the anti-Stokes field.

In Figure A.3, when the etalon filters are fixed to transmit Stokes photons with σ^+ polarization and anti-Stokes photons with σ^- polarization, and the coupling field is set to the polarization that maximizes the pair rate (at 20° of the QWP mask, corresponding approximately to σ^+ polarization), the corrected correlated photon pair rate reaches its maximum around 182°, which is close to the σ^- polarization of the pump field.

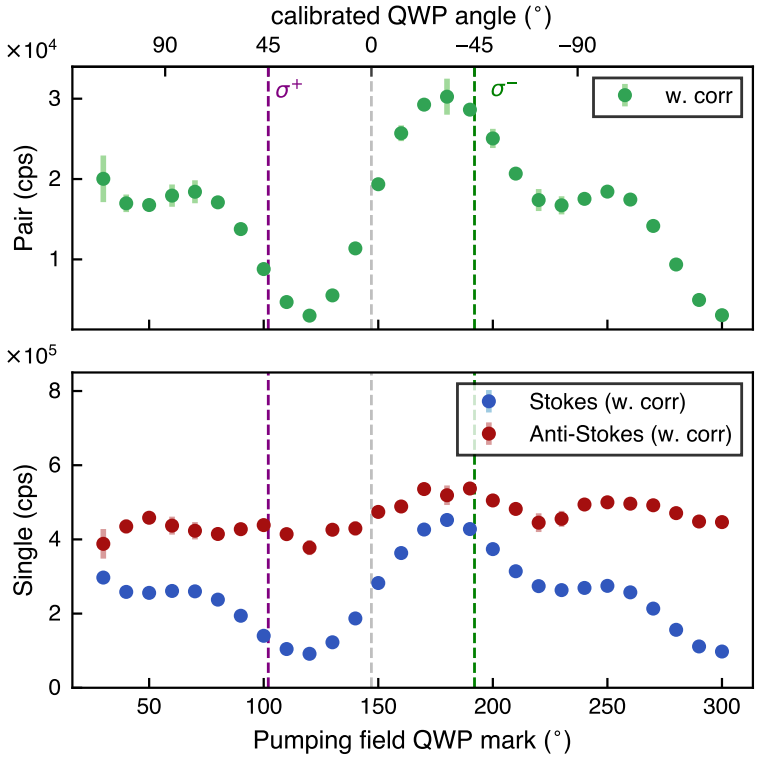

Figure A.3: Top: Correlated photon pair rate, calibrated by a factor of R/R_{as}, where R is a fixed reference value (the mean value of R_{as}) and R_{as} is the anti-Stokes single count for each configuration. This normalization compensates for fluctuations in the anti-Stokes count rate, primarily caused by variations in the transmission of the etalon filter. Bottom: Single counts in the Stokes and anti-Stokes channels, corrected for laser leakage and detector dark counts.

In Figure A.4, under the same configuration of etalon filters, the pumping field has the polarization maximizing the pair rate (at 182° of the QWP mark, close to the σ^- polarization for pumping field), the corrected correlated photon pair rate reaches its maximum around 20° of the coupling fields.

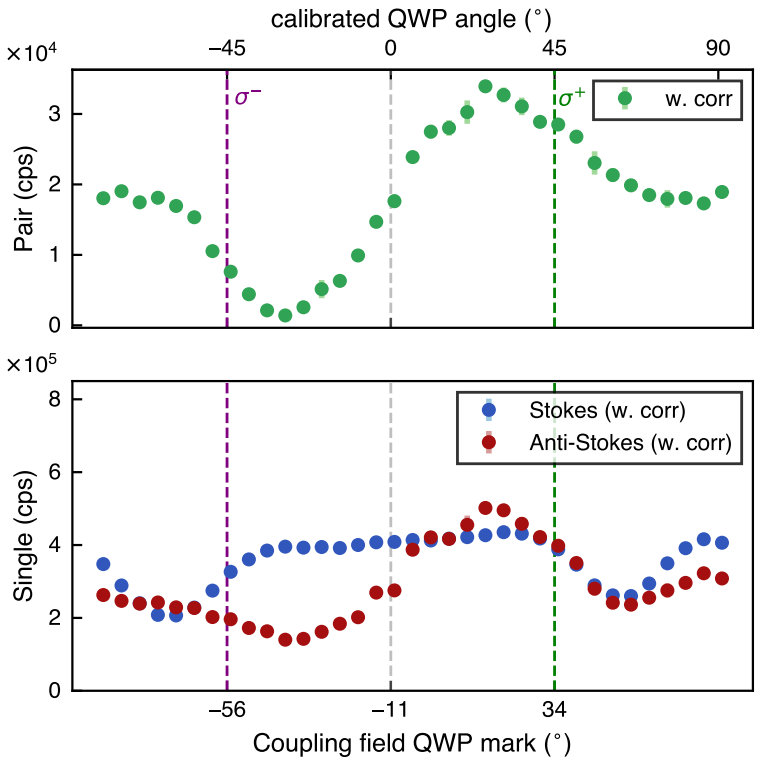

Figure A.4: Top: Correlated photon pair rate, calibrated by a factor of R/R_s, where R is a fixed reference value and R_s is the Stokes single count for each configuration. Bottom: Single counts in the Stokes and anti-Stokes channels, corrected for laser leakage and detector dark counts.

Appendix B

Atomic spectroscopy

B.1 D2 transitions from F = 2 (780 nm)

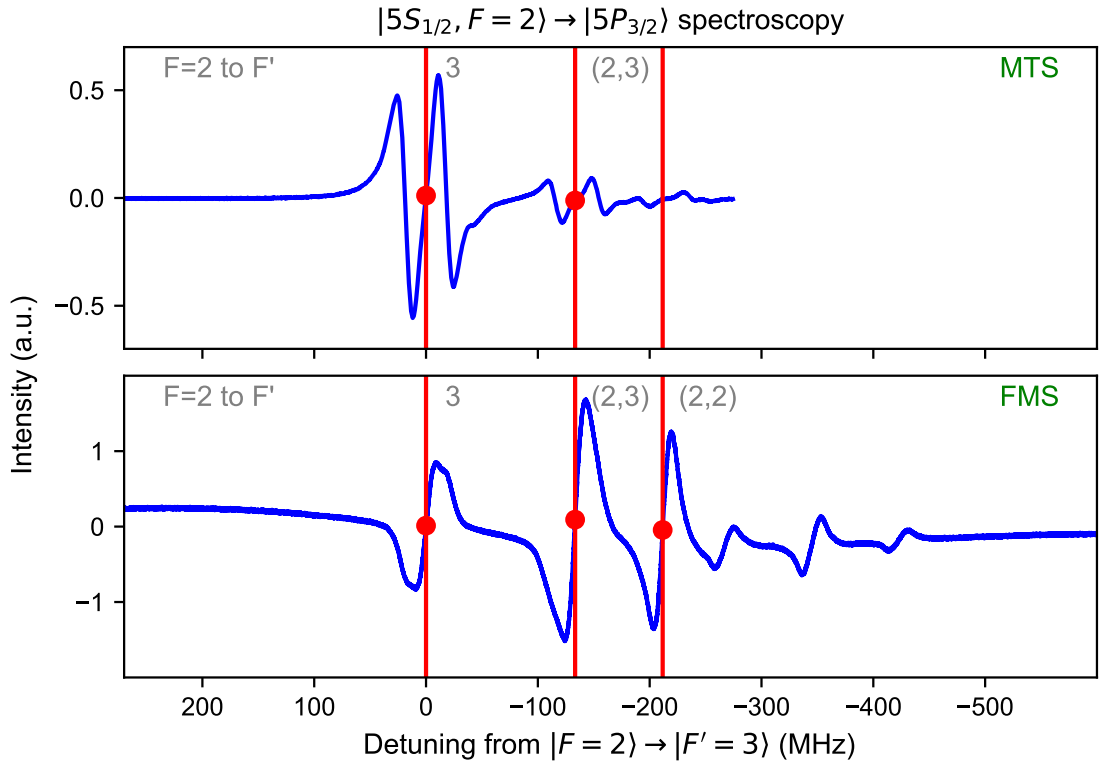

Figure B.1: The error signal in the modulation transfer spectroscopy and frequency modulation spectroscopy of $|5S_{1/2}, F = 2\rangle \rightarrow |5P_{3/2}, F'\rangle$ transition.

B.2 D2 transitions from F = 1(780 nm)

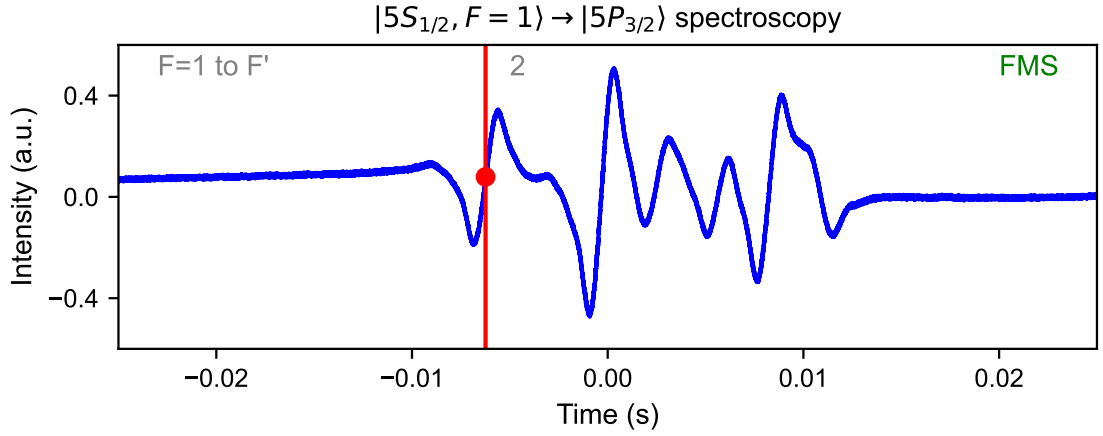

Figure B.2: The error signal in the frequency modulation spectroscopy of the $|5S_{1/2}, F = 1\rangle \rightarrow |5P_{3/2}, F'\rangle$ transition.

B.3 D1 transitions from F = 1,2 (795 nm)

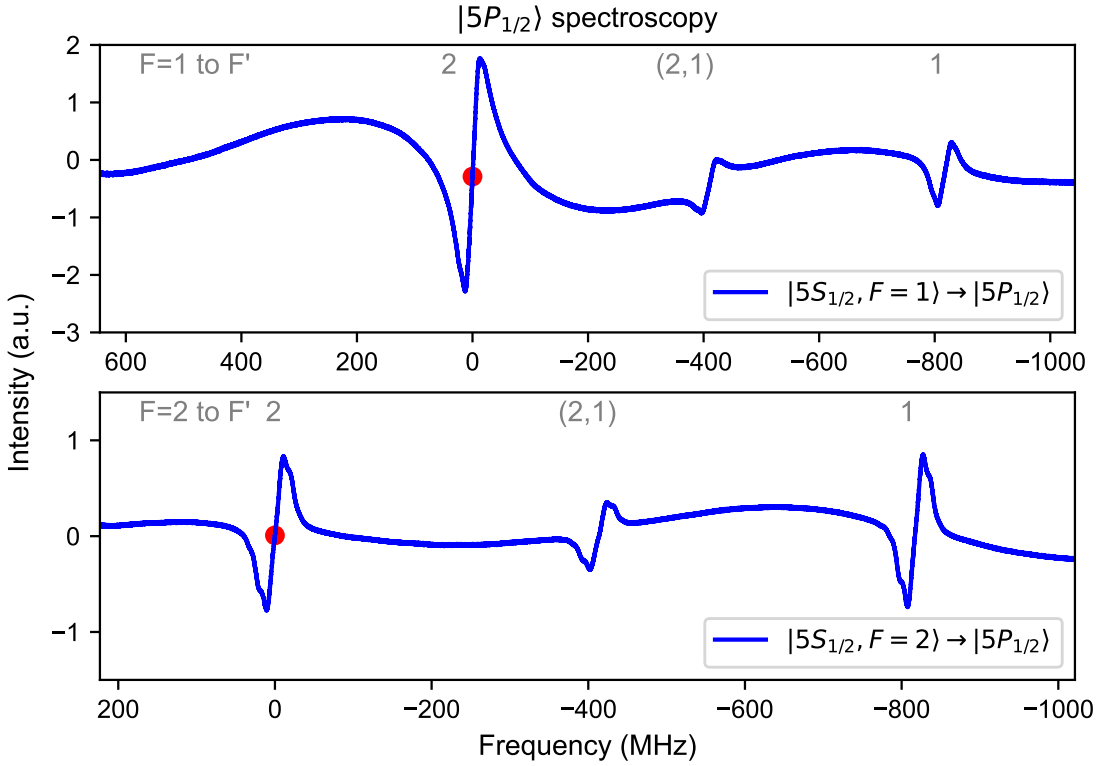

Figure B.3: The error-signal in the frequency modulation spectroscopy of the $5S_{1/2}, F = 1\rangle \rightarrow |5P_{1/2}, F'\rangle$ and $5S_{1/2}, F = 2\rangle \rightarrow |5P_{1/2}, F'\rangle$ transitions.

B.4 Two-photon transitions to $|5D_{3/2}\rangle$ (776 nm)

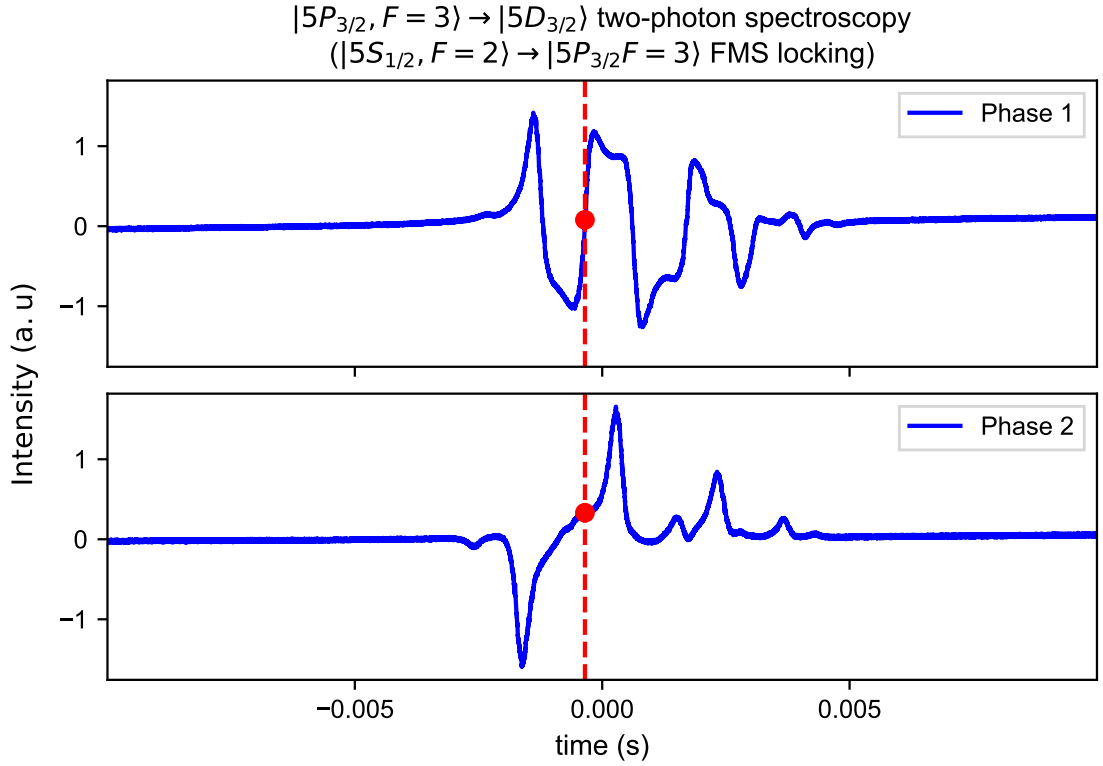

Figure B.4: The error signal in two-photon spectroscopy of the $|5P_{3/2}, F = 3\rangle \rightarrow |5D_{3/2}\rangle$ transition, with the first laser near-resonant with the $|5S_{1/2}, F = 2\rangle \rightarrow |5P_{3/2}, F = 3\rangle$ transition. The signals are shown under two different demodulation phase settings (neither purely in-phase nor quadrature).

B.5 Two-photon transitions to $|5D_{5/2}\rangle$ (776 nm)

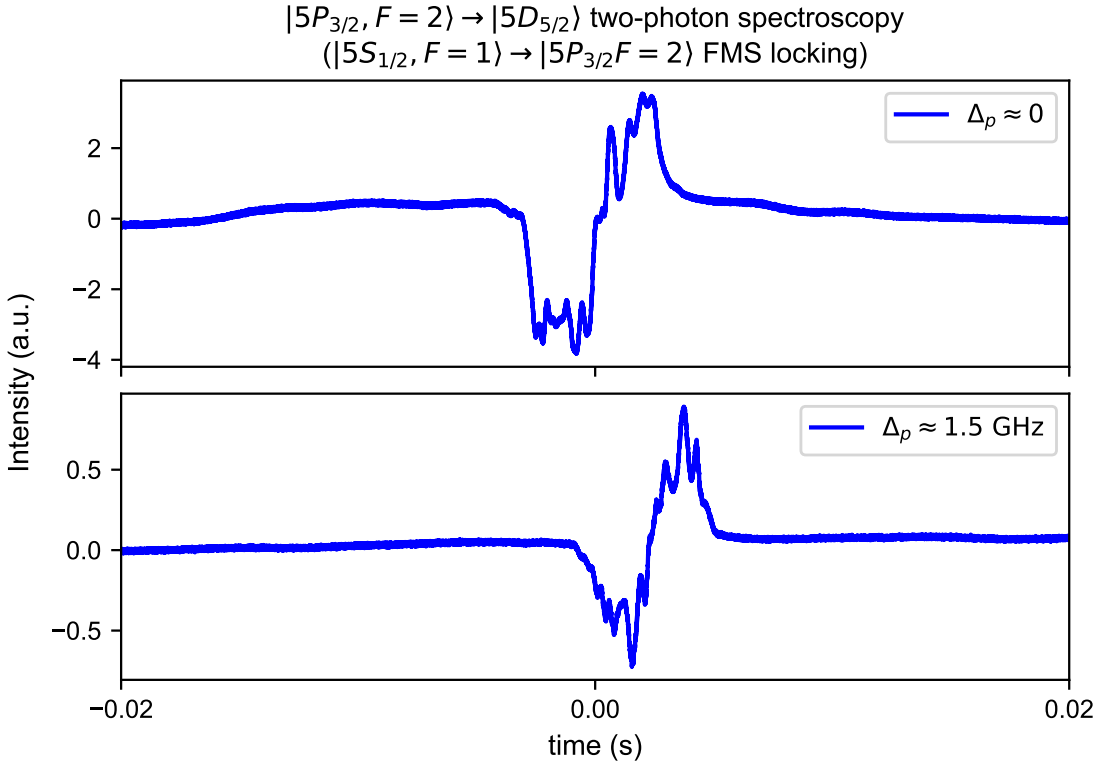

Figure B.5: The error signal in two-photon spectroscopy of the $|5P_{3/2}, F = 3\rangle \rightarrow |5D_{5/2}\rangle$ transition, recorded under two conditions for the first laser: (top) near-resonant with the $|5S_{1/2}, F = 1\rangle \rightarrow |5P_{3/2}, F = 2\rangle$ transition, and (bottom) significantly detuned from it.

Appendix C

Four-wave mixing

C.1 Propagation equations

We consider a near-resonant quantized electromagnetic field propagating along the z-axis through an atomic medium. This field can be expressed in terms of a slowly varying envelope modulating a rapidly oscillating carrier as

$$\hat{E}^{(+)}(z,t) = \mathcal{E}_0 \hat{a}(z,t) e^{-i(\omega t - kz)}\,, \tag{C.1}$$

where $k = \omega/c$, and $\hat{a}(z)$ is the annihilation operator representing the slowly varying component. This field corresponds to a polarization $\hat{P}(z,t)$ in the atomic medium, which is determined by the relevant atomic transition. The propagation of the field obeys Maxwell's propagation equation as

$$\left(\frac{\partial^2}{\partial z^2} \pm \frac{1}{c^2}\frac{\partial^2}{\partial t^2}\right)\hat{E}(z,t) = \mu_0 \frac{\partial^2 \hat{P}(z,t)}{\partial t^2}\,, \tag{C.2}$$

where μ_0 is the vacuum permeability and the $+$ sign corresponds to a forward-propagating field along z-axis, and $-$ sign for a backward-propagating field. Under the slowly varying envelope approximation (SVEA), we neglect second derivatives of the envelope

$$\begin{aligned} \frac{\partial^2}{\partial z^2}\left[\hat{a}(z,t)e^{ikz}\right] &\approx 2ik\frac{\partial \hat{a}}{\partial z}e^{ikz}\,, \\ \frac{\partial^2}{\partial t^2}\left[\hat{a}(z,t)e^{-i\omega t}\right] &\approx -2i\omega\frac{\partial \hat{a}}{\partial t}e^{-i\omega t}\,. \end{aligned} \tag{C.3}$$

Consequently, the propagation of this field is approximated as

$$\left(\frac{\partial}{\partial z} \pm \frac{1}{c}\frac{\partial}{\partial t}\right)\hat{a}(z,t) = i\frac{\mu_0\omega^2}{2k\mathcal{E}_0}\hat{P}(z,t)\,. \tag{C.4}$$

The macroscopic polarization $\hat{P}(z,t)$ is composed of contributions from individual atomic transitions. Therefore, the propagation equation connects the evolution of the field envelope to the corresponding atomic coherence as

$$\left(\frac{\partial}{\partial z} \pm \frac{1}{c}\frac{\partial}{\partial t}\right)\hat{a}(z,t) = ig_{jk}N\hat{\sigma}_{jk}(z,t)\,, \tag{C.5}$$

where the g_{jk} denotes the coupling strength between the quantized field and the atomic transition $|k\rangle \leftrightarrow |j\rangle$, and N is the atomic number density contributing to the interaction. In the frequency domain, the propagation can be expressed as

$$\pm c\frac{\partial \hat{a}(z,\omega)}{\partial z} = ig_{jk}N\hat{\sigma}_{jk}(z,\omega)\,. \tag{C.6}$$

In the case of spontaneous four-wave mixing, the two coupled generated fields follow [79, 91, 297]

$$\begin{aligned}\left(\frac{\partial}{\partial t} + c\frac{\partial}{\partial z}\right)\hat{a}_{as}(z,t) &= ig_{13}N\hat{\sigma}_{13}(z,t)\ ,\\ \left(\frac{\partial}{\partial t} - c\frac{\partial}{\partial z}\right)\hat{a}_{s}^{\dagger}(z,t) &= -ig_{24}^{*}N\hat{\sigma}_{42}(z,t)\,,\end{aligned} \tag{C.7}$$

where Stokes field ($\hat{a}_s$) propagates in the forward direction and anti-Stokes field ($\hat{a}_{as}^{\dagger}$) propagates in the backward direction under the counter-propagating configuration. Each field adopts a solution in the form of an input-output relation as

$$\hat{a}(L,t) = \hat{a}_{\text{in}}\,(0,0) + ig_{jk}N\int_0^L dz, \hat{\sigma}_{jk}\left(z, t - \frac{z}{c}\right)\ , \tag{C.8}$$

where the first term represents the input field, which is a vacuum state in the absence of a seed laser, and the second term accounts for the accumulated atomic coherence acting as a source along the propagation path.

C.2 Heisenberg Langevin equations

C.2.1 Electromagnetic fields

In quantum optics, the electromagnetic field is described as a superposition of its positive and negative components as

$$\hat{\mathbf{E}}(t,z) = \frac{1}{2}\left[\hat{E}^{(+)}(t,z) + \hat{E}^{(-)}(t,z)\right]\ , \tag{C.9}$$

which can be expressed in the frequency domain by the Fourier transform as

$$\hat{E}(\omega,t)=\frac{1}{\sqrt{2\pi}}\int d\omega\hat{E}^{(+)}(t,z)e^{i(\pm kz+\omega t)}\,. \tag{C.10}$$

The pump fields used are treated by the classical fields, denoted by their positive frequency component as

$$\begin{aligned}\hat{E}_p^{(+)}(t,z)&=E_p e^{i(k_p z-\omega_c t)}\,,\\ \hat{E}_c^{(+)}(t,z)&=E_c e^{i(-k_c z-\omega_c t)}\,,\end{aligned} \tag{C.11}$$

where the pumping field with the wavevector k_p, propagates forward along z-axis, while the coupling field with wavevector $-k_c$ counter-propagates in the opposite direction. In the spontaneous process without a seed laser, the generated Stokes and anti-Stokes fields emerge at the photon-countable level; hence, they are modeled as quantized fields.

$$\begin{aligned}\hat{E}_s(\omega_s,z)&=\sqrt{\frac{2\hbar\omega_s}{c\varepsilon_0 A}}\hat{a}_s(\omega_s,z)e^{ik_s z}\\ \hat{E}_s(\omega_{as},z)&=\sqrt{\frac{2\hbar\omega_{as}}{c\varepsilon_0 A}}\hat{a}_s(\omega_{as},z)e^{-ik_{as}z},\end{aligned} \tag{C.12}$$

where A is the single-mode cross-section area. The creation and annihilation operators defined in the Stokes and anti-Stokes modes satisfy the bosonic commutation relations

$$[\hat{a}_s(\omega),\hat{a}_s^{\dagger}(\omega')]=\delta(\omega-\omega')\,;\;\;[\hat{a}_{as}(\omega),\hat{a}_{as}^{\dagger}(\omega')]=\delta(\omega-\omega')\,. \tag{C.13}$$

C.2.2 Collective atomic operators

For a single atom, the atomic operator $\hat{\sigma}_{jk}=|j\rangle\langle k|$ describes the transition from states $|k\rangle$ to $|j\rangle$. In an atomic ensemble, the excitation and emission processes are indistinguishable between atoms; thus, the ensemble collectively interacts with the optical fields. In this formalism, the atomic operators in Equation 4.1 are replaced by slowly varying collective atomic operators [79, 88, 90, 93, 298] as

$$\tilde{\sigma}_{jk}(z,t)=\frac{\sum_i^N\hat{\sigma}_{jk}^{(i)}(z,t)}{N}=\frac{1}{N}\sum_{i=1}^{N}|j^{(i)}\rangle\langle k^{(i)}|e^{-i\omega_{jk}t}\,, \tag{C.14}$$

where N denotes the atom number along the z-axis participating in the nonlinear interaction. For simplicity, we continue to use the notation $\hat{\sigma}_{jk}(z,t)$ to represent these

slowly varying collective operators in the following. The interaction Hamiltonian $\hat{H}$, describing the coupling between the atomic ensemble and the classical pump fields as well as the generated quantized fields, is given by

$$\begin{aligned}\hat{H} = &-\frac{N}{L}\int_0^L dz\hbar(\Delta_p\hat{\sigma}_{44} + \delta_{as}\hat{\sigma}_{33} + (\delta_{as}-\Delta_c)\hat{\sigma}_{22} + \Omega_p\hat{\sigma}_{41} + \Omega_c\hat{\sigma}_{32} \\ &+ g_{42}\hat{a}_s\hat{\sigma}_{42} + g_{31}\hat{a}_{as}\hat{\sigma}_{31}) + \text{H.c}\,.\end{aligned} \tag{C.15}$$

C.2.3 Heisenberg-Langevin equations

A set of Heisenberg–Langevin equations (HLEs) describes the dynamics of the slowly varying collective atomic operators, providing a microscopic description of the evolution of atomic populations and coherences. Following [79, 88, 90, 91, 93], the Heisenberg–Langevin equations for spontaneous four-wave mixing are given by

$$\frac{\partial}{\partial t}\hat{\sigma}_{jk} = \frac{i}{\hbar}[\hat{H}, \hat{\sigma}_{jk}] - \gamma_{jk}\hat{\sigma}_{jk} + \hat{R}_{jk} + \hat{F}_{jk}\,, \tag{C.16}$$

where γ_{jk} denotes the dephasing rate between states $|j\rangle$ and $|k\rangle$, where $|j\rangle$ is the lower-energy state. For simplicity, we take $\gamma_{jk} = \Gamma_k/2$, with Γ_k being the total spontaneous decay rate from state $|k\rangle$. The term $\hat{R}_{jk}$ represents the relaxation processes associated with spontaneous emission, and $\hat{F}_{jk}$ denotes the corresponding collective atomic Langevin noise operators, which have zero time-averaged expectation value and exhibit δ-correlations as

$$\langle\hat{F}^\dagger_{jk}(z,t)\hat{F}_{j'k'}(z',t')\rangle = \frac{L}{N}\mathcal{D}_{jk,j'k'}(z,t)\delta(t-t')\delta(z-z')\,, \tag{C.17}$$

where $\mathcal{D}_{jk,j'k'}(z,t)$ is the diffusion coefficient determined via the Einstein relation [79, 91, 93, 299]. These expectation values characterize the correlations between the quantum noises.

The Heisenberg equations can also be expressed in matrix form [93] as

$$\frac{\partial}{\partial t}\hat{\mathcal{S}} = i[\hat{\mathcal{V}}, \hat{\mathcal{S}}] + \hat{\mathcal{R}} + \hat{\mathcal{F}}\,, \tag{C.18}$$

where $\hat{\mathcal{S}}$, $\hat{\mathcal{V}}$, $\hat{\mathcal{R}}$, and $\hat{\mathcal{F}}$ represent, the matrices of atomic operators, the interaction Hamiltonian, the total relaxation terms (including spontaneous emission and

dephasing), and the Langevin noise operators, respectively. They are given by

$$\hat{\mathcal{S}} = \begin{bmatrix} \hat{\sigma}_{11} & \hat{\sigma}_{12} & \hat{\sigma}_{13} & \hat{\sigma}_{14} \\ \hat{\sigma}_{21} & \hat{\sigma}_{22} & \hat{\sigma}_{23} & \hat{\sigma}_{24} \\ \hat{\sigma}_{31} & \hat{\sigma}_{32} & \hat{\sigma}_{33} & \hat{\sigma}_{34} \\ \hat{\sigma}_{41} & \hat{\sigma}_{42} & \hat{\sigma}_{43} & \hat{\sigma}_{44} \end{bmatrix}, \tag{C.19}$$

$$\hat{\mathcal{V}} = -\begin{bmatrix} 0 & 0 & g_{31}\hat{a}_{as} & \Omega_p \\ 0 & \delta_{as} & \Omega_c & g_{42}\hat{a}_s \\ g_{31}^*\hat{a}_{as}^\dagger & \Omega_c^* & \delta_{as} & 0 \\ \Omega_p^* & g_{42}^*\hat{a}_s^\dagger & 0 & \Delta_p \end{bmatrix}, \tag{C.20}$$

$$\hat{\mathcal{R}} = \begin{bmatrix} \Gamma_{13}\hat{\sigma}_{33} + \Gamma_{14}\hat{\sigma}_{44} & -\gamma_{12}\hat{\sigma}_{12} & -\gamma_{13}\hat{\sigma}_{13} & -\gamma_{14}\hat{\sigma}_{14} \\ -\gamma_{12}\hat{\sigma}_{21} & \Gamma_{23}\hat{\sigma}_{33} + \Gamma_{24}\hat{\sigma}_{44} & -\gamma_{23}\hat{\sigma}_{23} & -\gamma_{24}\hat{\sigma}_{24} \\ -\gamma_{13}\hat{\sigma}_{31} & -\gamma_{23}\hat{\sigma}_{32} & -(\Gamma_{13}+\Gamma_{23})\hat{\sigma}_{33} & -\gamma_{34}\hat{\sigma}_{34} \\ -\gamma_{14}\hat{\sigma}_{41} & -\gamma_{24}\hat{\sigma}_{42} & -\gamma_{34}\hat{\sigma}_{43} & -(\Gamma_{14}+\Gamma_{24})\hat{\sigma}_{44} \end{bmatrix}, \tag{C.21}$$

where Γ_{jk} denotes the spontaneous decay rate from state $|k\rangle$ to $|j\rangle$, and the dephasing rate γ_{jk} represents the decoherence associated with the coherence between $|k\rangle$ and $|j\rangle$. The relaxation matrix encompasses all possible decay channels, including population decay and coherence dephasing. In general, the dephasing rate is approximated by its corresponding spontaneous emission rate as

$$\begin{aligned} \Gamma_{13} &\simeq \Gamma_{23} \simeq \Gamma_3/2\,, \\ \Gamma_{14} &\simeq \Gamma_{24} \simeq \Gamma_4/2\,, \\ \gamma_{13} &\simeq \gamma_{23} \simeq \Gamma_3/2\,, \\ \gamma_{14} &\simeq \gamma_{24} \simeq \Gamma_4/2\,, \\ \gamma_{34} &\simeq (\Gamma_3+\Gamma_4)/2\,. \end{aligned} \tag{C.22}$$

C.2.4 Atomic dynamics

The differential equations of population terms and coherence terms under the condition of $\Delta_c = 0$ are given by

$$\begin{aligned}
\frac{\partial}{\partial t}\hat{\sigma}_{11} &= \Gamma_{31}\hat{\sigma}_{33} + \Gamma_{41}\hat{\sigma}_{44} - i\Omega_p\hat{\sigma}_{41} + i\Omega_p^*\hat{\sigma}_{14} + ig_{31}^*\hat{\sigma}_{13}\hat{a}_{as}^\dagger - ig_{31}\hat{a}_{as}\hat{\sigma}_{31} + \hat{f}_{11}^{(\sigma)}\,,\\
\frac{\partial}{\partial t}\hat{\sigma}_{22} &= \Gamma_{32}\hat{\sigma}_{33} + \Gamma_{42}\hat{\sigma}_{44} - i\Omega_c\hat{\sigma}_{32} + i\Omega_c^*\hat{\sigma}_{23} - ig_{42}\hat{a}_s\hat{\sigma}_{42} + ig_{42}^*\hat{\sigma}_{24}\hat{a}_s^\dagger + \hat{f}_{22}^{(\sigma)}\,,\\
\frac{\partial}{\partial t}\hat{\sigma}_{33} &= -\Gamma_3\hat{\sigma}_{33} + i\Omega_c\hat{\sigma}_{32} - i\Omega_c^*\hat{\sigma}_{23} + ig_{31}\hat{a}_{as}\hat{\sigma}_{31} - ig_{31}^*\hat{a}_{as}^\dagger\hat{\sigma}_{13} + \hat{f}_{33}^{(\sigma)}\,,\\
\frac{\partial}{\partial t}\hat{\sigma}_{44} &= -\Gamma_4\hat{\sigma}_{44} + i\Omega_p\hat{\sigma}_{41} - i\Omega_p^*\hat{\sigma}_{14} + ig_{42}\hat{\sigma}_{42}\hat{a}_s - ig_{42}^*\hat{a}_s^\dagger\hat{\sigma}_{24} + \hat{f}_{44}^{(\sigma)}\,,\\
\frac{\partial}{\partial t}\hat{\sigma}_{21} &= -(\gamma_{12} + i\delta_{as})\hat{\sigma}_{21} - i\Omega_c\hat{\sigma}_{31} + i\Omega_p^*\hat{\sigma}_{24} - ig_{42}\hat{a}_s\hat{\sigma}_{41} + ig_{31}^*\hat{\sigma}_{23}\hat{a}_{as}^\dagger + \hat{f}_{21}^{(\sigma)}\,,\\
\frac{\partial}{\partial t}\hat{\sigma}_{31} &= -(\gamma_{13} + i\delta_{as})\hat{\sigma}_{31} + i\Omega_p^*\hat{\sigma}_{34} - i\Omega_c^*\sigma_{21} + ig_{31}^*\hat{\sigma}_{33}\hat{a}_{as}^\dagger - ig_{31}^*\hat{a}_{as}^\dagger\hat{\sigma}_{11} + \hat{f}_{31}^{(\sigma)}\,,\\
\frac{\partial}{\partial t}\hat{\sigma}_{41} &= -(\gamma_{14} + i\Delta_p)\hat{\sigma}_{41} + i\Omega_p^*(\hat{\sigma}_{44} - \hat{\sigma}_{11}) - ig_{42}^*\hat{a}_s^\dagger\hat{\sigma}_{21} + ig_{31}^*\hat{\sigma}_{43}\hat{a}_{as}^\dagger + \hat{f}_{41}^{(\sigma)}\,,\\
\frac{\partial}{\partial t}\hat{\sigma}_{32} &= -\gamma_{23}\hat{\sigma}_{32} + i\Omega_c^*(\hat{\sigma}_{33} - \hat{\sigma}_{22}) + ig_{42}^*\hat{\sigma}_{34}\hat{a}_s^\dagger - ig_{31}^*\hat{a}_{as}^\dagger\hat{\sigma}_{12} + \hat{f}_{32}^{(\sigma)}\,,\\
\frac{\partial}{\partial t}\hat{\sigma}_{42} &= -(\gamma_{24} + i(\Delta_p - \delta_{as}))\hat{\sigma}_{42} - i\Omega_p^*\hat{\sigma}_{12} + i\Omega_c^*\hat{\sigma}_{43} + ig_{42}^*\hat{\sigma}_{44}\hat{a}_s^\dagger - ig_{42}^*\hat{a}_s^\dagger\hat{\sigma}_{22} + \hat{f}_{42}^{(\sigma)}\,,\\
\frac{\partial}{\partial t}\hat{\sigma}_{43} &= -(\gamma_{34} + i(\Delta_p - \delta_{as}))\hat{\sigma}_{43} - i\Omega_p^*\hat{\sigma}_{13} + i\Omega_c\hat{\sigma}_{42} - ig_{42}^*\hat{a}_s^\dagger\hat{\sigma}_{23} + ig_{42}^*\hat{\sigma}_{41}\hat{a}_{as} + \hat{f}_{43}^{(\sigma)}\,.
\end{aligned} \tag{C.23}$$

Since the coupling strengths are real, we denote $g_{31} = g_{31}^* \equiv g_{\mathrm{as}}$ and $g_{42} = g_{42}^* \equiv g_{\mathrm{s}}$. For clarity and conciseness, we introduce the following notations to simplify the subsequent expressions:

$$\begin{aligned}
\Gamma_{21} &= -(-\gamma_{12} - i(\delta_{as} - \Delta_c)) = (\gamma_{12} + i\delta_{as})\,,\\
\Gamma_{43} &= -(-\gamma_{34} - i(\Delta_p - \Delta_c - \delta_{as})) = (\gamma_{34} + i(\Delta_p - \delta_{as}))\,,\\
\Gamma_p &= (\gamma_{14} + i\Delta_p)\,,\\
\Gamma_c &= (\gamma_{23} - i\Delta_c) = \gamma_{23}\,,\\
\Gamma_s &= (\gamma_{24} + i(\Delta_p - \delta_{as}))\,,\\
\Gamma_{as} &= (\gamma_{13} + i\delta_{as})\,.
\end{aligned} \tag{C.24}$$

In the zeroth-order perturbation expansion [91], the quantized fields $\hat{a}s$ and $\hat{a}as$, along with the quantum Langevin noise terms, are considered weak compared to the classical driving fields. Under this assumption, the system reaches a steady state described by a series of atomic expectation values $\langle\hat{\sigma}_{jk}^{(0)}\rangle$, where the Langevin

noise terms and all interactions with quantized fields are neglected in Eq. C.23. The response of the atomic operators to the weak quantized fields can then be linearized as

$$\langle \hat{\sigma}_{jk} \rangle \approx \langle \hat{\sigma}_{jk}^{(0)} \rangle + \langle \hat{\sigma}_{jk}^{(1)} \rangle \,, \tag{C.25}$$

where $\langle \hat{\sigma}_{jk}^{(1)} \rangle$ represents the first-order component induced by the perturbation of the quantized fields. To highlight the dominant contributions, we apply the ground-state approximation $\langle \hat{\sigma}_{11}^{(0)} \rangle \approx 1$, along with the weak-pumping condition $\Delta_p \gg \Omega_p \gg \Gamma_4$, in certain steps. In the following, $\langle : \rangle$ expectation value notation is omitted for simplicity. According to steady-state condition $\frac{\partial}{\partial t}\hat{\sigma}_{41}^{(0)} = 0$ (see Equation C.23), and neglecting the interaction terms involving quantized fields, the zeroth-order atomic coherence $\hat{\sigma}_{41}^{(0)}$ reaches a steady-state as

$$\begin{aligned} \hat{\sigma}_{41}^{(0)} &\approx \frac{i\Omega_p^*}{\Gamma_p} \,, \\ \hat{\sigma}_{44}^{(0)} &\approx \left(\frac{2\gamma_{14}}{\Gamma_4}\right) \frac{|\Omega_p|^2}{\Gamma_p \Gamma_p^*} \,, \\ \hat{\sigma}_{33}^{(0)} &\approx \frac{\Gamma_{42}}{\Gamma_{31}} \hat{\sigma}_{44}^{(0)} \,. \end{aligned} \tag{C.26}$$

Importantly, this steady-state coherence $\hat{\sigma}_{41}^{(0)}$ represents the atomic coherence induced by the pumping field in the first Λ subsystem of the four-wave mixing process, which subsequently propagates and drives the second Λ-type interaction. In contrast, due to small population represented in $\hat{\sigma}_{22}^{(0)}$ and $\hat{\sigma}_{33}^{(0)}$, the steady-state coherence term $\hat{\sigma}_{32}^{(0)} \approx 0$ under the ground-state approximation. An analytical solution [79] for $\hat{\sigma}_{32}^{(0)}$ can, in principle, be obtained based on $\hat{\sigma}_{41}^{(0)}$; however, it represents a higher-order contribution in terms of Ω_p and should therefore be neglected under the linearization approximation. In contrast, $\hat{\sigma}_{41}^{(0)}$ presents the first-order contribution in term of Ω_p of the four-wave mixing and therefore remains. With the assistance of the pump-field-induced coherence $\hat{\sigma}_{41}^{(0)}$, four mutually coupled first-order coherence terms $\hat{\sigma}_{21}^{(1)}, \hat{\sigma}_{31}^{(1)}, \hat{\sigma}_{24}^{(1)}, \hat{\sigma}_{34}^{(1)}$, arising from the perturbation by quantized fields, can be solved as a set of mutually coupled equations as

$$\begin{pmatrix} \Gamma_{12} & i\Omega_c & -i\Omega_p^* & 0 \\ i\Omega_c^* & \Gamma_{as} & 0 & -i\Omega_p^* \\ -i\Omega_p & 0 & \Gamma_s^* & i\Omega_c \\ 0 & -i\Omega_p & i\Omega_c^* & \Gamma_{43}^* \end{pmatrix} \begin{pmatrix} \hat{\sigma}_{21}^{(1)} \\ \hat{\sigma}_{31}^{(1)} \\ \hat{\sigma}_{24}^{(1)} \\ \hat{\sigma}_{34}^{(1)} \end{pmatrix} = \begin{pmatrix} -ig_s \sigma_{41}^{(0)} \hat{a}_s \\ -ig_{as} \hat{a}_{as}^\dagger \\ 0 \\ -ig_s \sigma_{14}^{(0)} \hat{a}_{as}^\dagger \end{pmatrix} , \tag{C.27}$$

which has a format of

$$M\vec{x} = \vec{b}\,. \tag{C.28}$$

In fact, the full expression for the vector $\vec{b}$ is given as

$$\vec{b} = \begin{pmatrix} -ig_s\sigma_{41}^{(0)}\hat{a}_s + ig_{as}\sigma_{23}^{(0)}\hat{a}_{as}^\dagger \\ ig_{as}(\hat{\sigma}_{33}^{(0)} - \hat{\sigma}_{11}^{(0)})\hat{a}_{as}^\dagger \\ ig_s(\hat{\sigma}_{22}^{(0)} - \hat{\sigma}_{44}^{(0)})\hat{a}_s \\ -ig_s\sigma_{14}^{(0)}\hat{a}_{as}^\dagger + ig_s\hat{\sigma}_{32}^{(0)}\hat{a}_s \end{pmatrix}, \tag{C.29}$$

in which only the terms involving $\hat{\sigma}_{41}^{(0)}$, $\hat{\sigma}_{41}^{(0)}$, and the ground-state population $\hat{\sigma}_{11}^{(0)} \approx 1$ are maintained, such that only the lowest-order contributions are preserved. The full solutions for $\hat{\sigma}_{31}^{(1)}$ and $\hat{\sigma}_{23}^{(1)}$ are given by

$$\hat{\sigma}_{31}^{(1)} = \frac{ig_s\Omega_c^*\Omega_p^*\left(\Gamma_{34}^*\Gamma_s^* + |\Omega_c|^2 - |\Omega_p|^2\right)\hat{a}_s}{\Gamma_p\left[(\Gamma_{12}\Gamma_{as} + |\Omega_c|^2)(\Gamma_{34}^*\Gamma_s^* + |\Omega_c|^2) + |\Omega_p|^2(\Gamma_{12}\Gamma_s^* + \Gamma_{as}\Gamma_{34}^* - 2|\Omega_c|^2 + |\Omega_p|^2)\right]} + \frac{i\left[g_s\Gamma_p|\Omega_p|^4 - \Gamma_p\left(g_{as}\Gamma_{12}\Gamma_p^*(\Gamma_{34}^*\Gamma_s^* + |\Omega_c|^2) + |\Omega_p|^2\left(-g_s\Gamma_{12}\Gamma_s^* + g_{as}\Gamma_{34}^*\Gamma_p^* + g_s|\Omega_c|^2\right)\right)\right]\hat{a}_{as}^\dagger}{\Gamma_p\Gamma_p^*\left[(\Gamma_{12}\Gamma_{as} + |\Omega_c|^2)(\Gamma_{34}^*\Gamma_s^* + |\Omega_c|^2) + |\Omega_p|^2(\Gamma_{12}\Gamma_s^* + \Gamma_{as}\Gamma_{34}^* - 2|\Omega_c|^2 + |\Omega_p|^2)\right]}, \tag{C.30}$$

$$\hat{\sigma}_{24}^{(1)} = \frac{-ig_s|\Omega_p|^2(\Gamma_{as}\Gamma_{34}^* - |\Omega_c|^2 + |\Omega_p|^2)\hat{a}_s}{\Gamma_p\left[(\Gamma_{12}\Gamma_{as} + |\Omega_c|^2)(\Gamma_{34}^*\Gamma_s^* + |\Omega_c|^2) + |\Omega_p|^2(\Gamma_{12}\Gamma_s^* + \Gamma_{as}\Gamma_{34}^* - 2|\Omega_c|^2 + |\Omega_p|^2)\right]} + \frac{-i\Omega_c\Omega_p\left[g_{as}\Gamma_p^*(\Gamma_{12} + \Gamma_{34}^*) + g_s(\Gamma_{12}\Gamma_{as} + |\Omega_c|^2 - |\Omega_p|^2)\right]\hat{a}_{as}^\dagger}{\Gamma_p^*\left[(\Gamma_{12}\Gamma_{as} + |\Omega_c|^2)(\Gamma_{34}^*\Gamma_s^* + |\Omega_c|^2) + |\Omega_p|^2(\Gamma_{12}\Gamma_s^* + \Gamma_{as}\Gamma_{34}^* - 2|\Omega_c|^2 + |\Omega_p|^2)\right]}. \tag{C.31}$$

Under the weak-pumping and large pumping detuning limit, the first-order coherence terms $\hat{\sigma}_{31}^{(1)}$ can be approximated in terms of the field operators $\hat{a}_s$ and $\hat{a}_{as}^\dagger$ as follows:

$$\hat{\sigma}_{31}^{(1)} \approx \frac{ig_s\Omega_c^*\Omega_p^*}{\Gamma_p(\Gamma_{12}\Gamma_{as} + |\Omega_c|^2)}\hat{a}_s + \frac{-ig_{as}\Gamma_{12}}{(\Gamma_{12}\Gamma_{as} + |\Omega_c|^2)}\hat{a}_{as}^\dagger\,, \tag{C.32}$$

which is consistent with earlier studies [81, 88, 93, 202, 204]. $\hat{\sigma}_{24}^{(1)}$ has two type of approximations, one is given by

$$\hat{\sigma}_{24}^{(1)} \approx \frac{ig_s|\Omega_p|^2}{\Gamma_p(\Gamma_{12}\Gamma_{as} + |\Omega_c|^2)}\hat{a}_s + \frac{-ig_{as}\Omega_c\Omega_p}{\Gamma_p^*(\Gamma_{12}\Gamma_{as} + |\Omega_c|^2)}\hat{a}_{as}^\dagger\,, \tag{C.33}$$

which aligns with the result in [88]. Another form of approximation, which neglects $|\Omega_c|^2$ in both the numerator and denominator, is consistent with the results reported

in [81, 93, 202, 204]. This approximation gives

$$\hat{\sigma}_{24}^{(1)} \approx \frac{-ig_s|\Omega_p|^2\Gamma_{as}}{\Gamma_p\Gamma_s^*\left(\Gamma_{12}\Gamma_{as}+|\Omega_c|^2\right)}\hat{a}_s + \frac{-ig_{as}\Omega_c\Omega_p}{\Gamma_p^*\left(\Gamma_{12}\Gamma_{as}+|\Omega_c|^2\right)}\hat{a}_{as}^\dagger\,. \tag{C.34}$$

Under the linearization approximation, the atomic coherence induced by the perturbation of the generated fields is expressed in terms of the Stokes and anti-Stokes field operators. The corresponding coefficients relate to the linear and third-order nonlinear susceptibilities, respectively. These two coupled atomic coherences give rise to the macroscopic polarizations [68] on the respective transitions of the generated fields as

$$\begin{aligned}\mathcal{P}_s &= \varepsilon_0\chi_s^{(1)}\mathcal{E}_s + \varepsilon_0\chi_s^{(3)}\mathcal{E}_{as}^*\mathcal{E}_p\mathcal{E}_c\exp(i\delta\vec{k}\vec{r})\,,\\ \mathcal{P}_{as} &= \varepsilon_0\chi_{as}^{(1)}\mathcal{E}_{as} + \varepsilon_0\chi_{as}^{(3)}\mathcal{E}_s^*\mathcal{E}_p\mathcal{E}_c\exp(i\delta\vec{k}\vec{r})\,.\end{aligned} \tag{C.35}$$

According to Equation C.33, the linear susceptibilities for Stokes and anti-Stokes modes are

$$\begin{aligned}\chi_s &= \frac{iN|\mu_{24}|^2}{\hbar\varepsilon_0}\frac{|\Omega_p|^2}{\Gamma_p(\Gamma_{12}\Gamma_{as}+|\Omega_c|^2)}\frac{\Gamma_{as}}{\Gamma_p\Gamma_s^*}\,,\\ \chi_{as} &= \frac{iN|\mu_{13}|^2}{\hbar\varepsilon_0}\frac{\Gamma_{12}^*}{(\Gamma_{12}^*\Gamma_{as}^*+|\Omega_c|^2)}\,.\end{aligned} \tag{C.36}$$

The third-order susceptibility is given by

$$\begin{aligned}\chi_{as}^{(3)} &= \frac{iN\mu_{13}\mu_{32}\mu_{24}\mu_{41}}{\varepsilon_0\hbar^3}\frac{1}{\Gamma_p^*(\Gamma_{12}^*\Gamma_{as}^*+|\Omega_c|^2)}\,,\\ \chi_s^{(3)} &= \frac{iN\mu_{13}\mu_{32}\mu_{24}\mu_{41}}{\varepsilon_0\hbar^3}\frac{1}{\Gamma_p^*(\Gamma_{12}\Gamma_{as}+|\Omega_c|^2)}\,.\end{aligned} \tag{C.37}$$

Having derived both the linear and third-order nonlinear susceptibilities from the microscopic model of atomic dynamics, we can now construct a macroscopic, phenomenological description of two coupled phase-conjugated electromagnetic fields. The resulting coupled propagation equations, which account for gain, loss, and a complex nonlinear coupling coefficient, arise directly from the atomic coherence dynamics captured in Equation C.7. Consequently, the coupled propagation equations [68, 91, 93] for coupled Stokes and anti-Stokes fields in the double-Λ spontaneous four-wave mixing are expressed as

$$\frac{\partial}{\partial z}\begin{bmatrix}\hat{a}_{as}\\ \hat{a}_s^\dagger\end{bmatrix} = \begin{bmatrix}-\alpha_{as}+i\frac{\Delta k}{2} & i\kappa_{as}\\ i\kappa_s & \alpha_s^*-i\frac{\Delta k}{2}\end{bmatrix}\begin{bmatrix}\hat{a}_{as}\\ \hat{a}_s^\dagger\end{bmatrix} + \begin{bmatrix}\hat{F}_{as}\\ -\hat{F}_s^\dagger\end{bmatrix}\,, \tag{C.38}$$

which include the gain α_s and absorption α_{as} in the atomic medium, phase mismatching $i\Delta k/2$, Langevin noises $\hat{F}_{as}$, $\hat{F}_s$ and nonlinear parametric coupling coefficients κ_{as}, κ_s, which are defined as

$$\begin{aligned}
\alpha_{as} &= -i\frac{\omega_{as}}{2c}\chi_{as}\,, \\
\alpha_s &= -i\frac{\omega_s}{2c}\chi_s\,, \\
\kappa_{as} &= \frac{\sqrt{\omega_{as}\omega_s}}{2c}\chi_{as}^{(3)}\mathcal{E}_p\mathcal{E}_c\,, \\
\kappa_s &= \frac{\sqrt{\omega_{as}\omega_s}}{2c}(\chi_s^{(3)})^*\mathcal{E}_p^*\mathcal{E}_c^*\,.
\end{aligned} \tag{C.39}$$

Appendix D

Collective emission

D.1 Dynamics of photon emission

In the scenario of a near-resonant field with a detuning of $\Delta = \omega_k - \omega_a$ interacting with an ensemble of two-level atoms, the intensity of photon emission into a specific electromagnetic field mode $\mathbf{k}$ denoted $I_{\mathbf{k}}(t)$, is defined as the time rate of change of the expectation value of the photon number operator as

$$I_{\mathbf{k}}(t) = \frac{d}{dt}\langle \hat{n}_{\mathbf{k}} \rangle \,, \tag{D.1}$$

which follows the Heisenberg equation as

$$\frac{d}{dt}\langle \hat{n}_{\mathbf{k}} \rangle = \frac{d}{dt}\langle \hat{a}^{\dagger}_{\mathbf{k}} \hat{a}_{\mathbf{k}} \rangle = \frac{i}{\hbar}\left\langle [\hat{H}_{\text{int}}, \hat{a}^{\dagger}_{\mathbf{k}} \hat{a}_{\mathbf{k}}] \right\rangle \,, \tag{D.2}$$

where the interaction Hamiltonian $\hat{H}_{\text{int}}$ in the interaction picture is given as

$$\hat{H}_{\text{int}}(t) = \sum_{\mathbf{k}} \hbar \left[g \hat{a}_{\mathbf{k}} \hat{S}^{+} e^{-i\Delta t} + g^{*} \hat{a}^{\dagger}_{\mathbf{k}} \hat{S}^{-} e^{i\Delta t} \right] \quad \Delta = \omega_k - \omega_a \,. \tag{D.3}$$

where g is the coupling strength. Considering the single electromagnetic field mode $\mathbf{k}$, we obtain

$$\frac{d}{dt}\langle \hat{a}^{\dagger}_{\mathbf{k}} \hat{a}_{\mathbf{k}} \rangle = ig \langle \hat{S}^{+} \hat{a}_{\mathbf{k}} \rangle e^{-i\Delta t} - ig^{*} \langle \hat{a}^{\dagger}_{\mathbf{k}} \hat{S}^{-} \rangle e^{i\Delta t} \,. \tag{D.4}$$

The field annihilation operator is solved via the Heisenberg equation with the initial vacuum state as

$$\hat{a}_{\mathbf{k}}(t) = -ig \int_0^t dt' \hat{S}^{-}(t') e^{-i\Delta t'} \,. \tag{D.5}$$

Correspondingly, we obtain the expectation values

$$\begin{aligned} \langle \hat{S}^{+}(t) \hat{a}_{\mathbf{k}}(t) \rangle &= -ig \int_0^t dt' \langle \hat{S}^{+}(t) \hat{S}^{-}(t') \rangle e^{-i\Delta t'} \\ \langle \hat{a}^{\dagger}_{\mathbf{k}}(t) \hat{S}^{-}(t) \rangle &= ig^{*} \int_0^t dt' \langle \hat{S}^{+}(t') \hat{S}^{-}(t) \rangle e^{i\Delta t'} \,. \end{aligned} \tag{D.6}$$

Under Born-Markov approximation, the dynamics of the photon number operator is linked to the $\langle \hat{S}^+(t)\hat{S}^-(t-\tau)\rangle$ as

$$\frac{d}{dt}\langle \hat{n}_{\mathbf{k}}\rangle = 2\mathrm{Re}\left[|g|^2 \int_0^\infty d\tau\, e^{i\Delta\tau}\langle \hat{S}^+(t)\hat{S}^-(t-\tau)\rangle\right]. \tag{D.7}$$

The Fourier transformation allows the following approximation as

$$\int_0^\infty d\tau\, e^{i\Delta\tau}\langle \hat{S}^+(t)\hat{S}^-(t-\tau)\rangle \approx \pi\delta(\Delta)\langle \hat{S}^+(t)\hat{S}^-(t)\rangle\,, \tag{D.8}$$

$$\frac{d}{dt}\langle \hat{a}^\dagger_{\mathbf{k}}\hat{a}_{\mathbf{k}}\rangle \approx 2\pi|g|^2\delta(\Delta)\langle \hat{S}^+(t)\hat{S}^-(t)\rangle\,. \tag{D.9}$$

Thus, the photon emission intensity is given as

$$I_{\mathbf{k}}(t) = \frac{d}{dt}\langle \hat{a}^\dagger_{\mathbf{k}}\hat{a}_{\mathbf{k}}\rangle \approx I_{\mathrm{sp}}\langle \hat{S}^+(t)\hat{S}^-(t)\rangle\,, \tag{D.10}$$

where $I_{\mathrm{sp}} = 2\pi|g|^2\delta(\Delta)$. This expression indicates that the photon emission rate in mode $\mathbf{k}$ is directly proportional to the collective atomic excitation, represented by $\langle \hat{S}^+(t)\hat{S}^-(t)\rangle$. This result, derived using collective atomic operators, is analogous to the form obtained for a single atom, where the emission rate is proportional to the single-atom excitation $\langle \hat{\sigma}^+\hat{\sigma}^-\rangle$.

D.2 Intensity correlation

The intensity correlation is also considered a hallmark of superradiance. Specifically, it corresponds to the second-order correlation function of the collective excitation operators associated with the superradiant field as

$$g^{(2)}_N(0) = \frac{\langle \hat{a}^\dagger_{\mathbf{k}}\hat{a}^\dagger_{\mathbf{k}}\hat{a}_{\mathbf{k}}\hat{a}_{\mathbf{k}}\rangle}{|\langle \hat{a}^\dagger_{\mathbf{k}}\hat{a}_{\mathbf{k}}\rangle|^2} \approx \frac{\langle (\hat{S}^+)^2(\hat{S}^-)^2\rangle}{|\langle \hat{S}^+\hat{S}^-\rangle|^2}\,, \tag{D.11}$$

$$g^{(2)}_N(0) \approx \frac{\sum_i^N\sum_j^N\sum_l^N\sum_m^N e^{i\mathbf{k}(\mathbf{r}_i+\mathbf{r}_j-\mathbf{r}_l-\mathbf{r}_m)}\langle \hat{\sigma}^i_+\hat{\sigma}^j_+\hat{\sigma}^l_-\hat{\sigma}^m_-\rangle}{\left(\sum_i^N\sum_j^N e^{i\mathbf{k}(\mathbf{r}_i-\mathbf{r}_j)}\langle \hat{\sigma}^i_+\hat{\sigma}^j_-\rangle\right)^2}\,. \tag{D.12}$$

The intensity correlation of a superradiant burst can be evaluated for the maximal population inversion state $|s = N/2, m = N/2\rangle$. As shown by Masson et al. [231], the theoretical prediction in the large atom number limit is given by

$$g^{(2)}_N(0) \approx 2 - \frac{2}{N}\,. \tag{D.13}$$

This result is also discussed by Meiser et al. [266], Agarwal et al. [265], and Goncalves et al. [267], who predict that the intensity will behave differently according to the pump field intensity. In the weak pumping regime, although the intensity scales with N^2, the intensity correlation is $g_N^{(2)}(0) = 1 - \frac{2}{N} + \frac{1}{N^2}$, which is consistent with the value for a coherent state. Conversely, in the strong driving regime, the intensity correlation is $g_N^{(2)}(0) \approx 2 - \frac{2}{N}$, similar to a thermal state [265]. Meanwhile, a theoretical model for spontaneous emission also yields the same result in the large saturation regime [212]. All these predictions use the mean-field approximation for non-interacting particles (e.g., $\langle \hat{\sigma}_\alpha^i \hat{\sigma}_\beta^j \rangle = \langle \hat{\sigma}_\alpha^i \rangle \langle \hat{\sigma}_\beta^j \rangle$). These similarities between superradiance and spontaneous emission, as predicted by theoretical frameworks based on atomic coherence moments, make it difficult to distinguish between the underlying mechanisms and phenomena.

A series of recent experimental studies has investigated the intensity correlations of superradiant light. For large ensembles (with small effective atom numbers), an increase in the drive-to-collective dissipation ratio leads to a gradual rise of $g^{(2)}(0)$ from 1 to approximately 1.5 [264]. Another experiment with a slightly larger atomic cloud revealed that non-Gaussian correlations in the steady-state atomic medium can suppress the intensity correlation below the Gaussian limit $g^{(2)} = 2$ [300]. Additionally, within a superradiant burst, the second-order correlation function has been observed to develop dynamically over time [301]. These experimental results reveal the complexity involved in using intensity autocorrelation to characterize collective emission.

Appendix E

Phase matching

E.1 Four-wave mixing

For comparison, we examine the optimal phase-matching condition for a double-Λ SFWM process. Assuming a refractive index of unity for all fields within the atomic ensemble, the phase mismatch is given by:

$$|\Delta\vec{k}| = |\vec{k}_p + \vec{k}_c - (\vec{k}_s + \vec{k}_{as})|\,, \tag{E.1}$$

where $\vec{k}_p$ and $\vec{k}_c$ denote the wavevectors of the pump and coupling fields, respectively, and $\vec{k}_s$ and $\vec{k}_{as}$ correspond to the wavevectors of the generated Stokes and anti-Stokes photons. The phase mismatch $|\Delta\vec{k}|$ is minimized, reaching approximately 0.6 rad $\cdot$ m^{-1}, well below 1 rad $\cdot$ m^{-1}, when the collection angles are $\theta_s \approx 3.5°$ and $\theta_{as} \approx 183.6°$. These optimal estimations are obtained based on a numerical evaluation of the phase mismatch minimum via Mathematica. This result may correspond only to a local rather than a global minimum, and is susceptible to numerical errors. As shown in Figure E.1, the phase mismatch can remain below a practical threshold (e.g., 10^3 rad $\cdot$ m^{-1}) over a broad region of the parameter space, particularly near the counter-propagation configuration. In practice, however, the phase-matching angles may deviate slightly due to variations in the linear susceptibility near atomic resonance, which depends on the specific pump configuration. Notably, the dispersion of the refractive index near the EIT resonance can be explored to compensate for residual phase mismatch arising from propagation geometry, collection angle, and uncompensated light shifts [66]. Experimentally, the optimal collection angles are determined empirically and are constrained by the optical access of the setup. In our configuration, Stokes photons are collected at an angle of approximately 1°

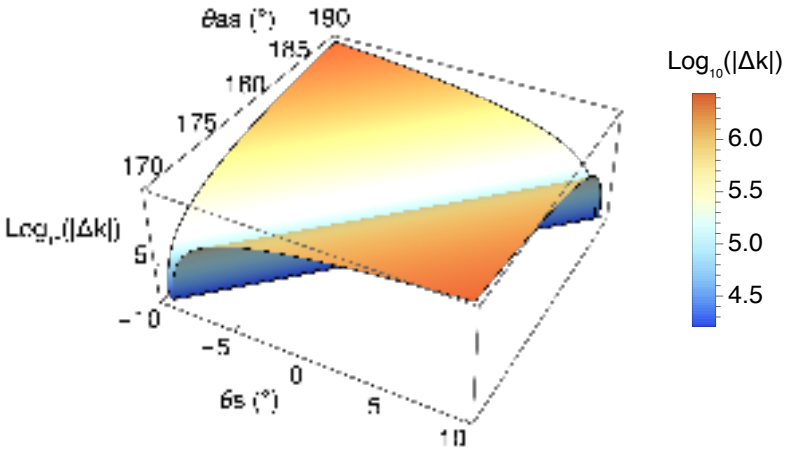

Figure E.1: Logarithmic-scale of phase mismatching term $\log_{10}|\Delta\vec{k}|$ as a function of the Stokes collection angle θ_s and the anti-Stokes collection angle θ_{as} for a double-Λ SFWM process.

relative to the pump axis, while anti-Stokes photons are collected in a direction nearly opposite to that of the Stokes photons.

E.2 Six-wave mixing

Similarly, we neglect the refractive index change for the idler, signal, and anti-Stokes fields within the atomic ensemble. This assumption is justified for the first two generated photons (idler and signal) because the majority of atoms remain in the $|F = 1\rangle$ ground state once the system reaches a steady state. For the anti-Stokes field, which is nearly resonant with the atomic transition in the presence of the coupling field, the refractive index depends on the real part of the linear susceptibility for the anti-Stokes field, approximately given by $n(\omega_{as}) \approx 1 + \frac{1}{2}\mathrm{Re}[\chi(\omega_{as})]$. Under the condition of EIT, the contribution of $\mathrm{Re}[\chi(\omega_{as})]$ could be small but varies rapidly, resulting in a steep dispersion relation. Consequently, the phase mismatch term is

expressed as

$$\begin{aligned}
|\Delta\vec{k}| &= |\vec{k}_p + \vec{k}_c + \vec{k}_d - (\vec{k}_i + \vec{k}_s + \vec{k}_{as})| \\
&= \sqrt{(A)^2 + (B)^2}\,, \\
A &= \frac{\omega_p}{c}\sin\theta_p + \frac{\omega_d}{c}\sin\theta_d + \frac{\omega_c}{c}\sin\theta_c - \frac{\omega_i}{c}\sin\theta_i - \frac{\omega_s}{c}\sin\theta_s - \frac{n_{as}\omega_{as}}{as}\sin\theta_{as}\,, \\
B &= \frac{\omega_p}{c}\cos\theta_p + \frac{\omega_d}{c}\cos\theta_d + \frac{\omega_c}{c}\cos\theta_c - \frac{\omega_i}{c}\cos\theta_i - \frac{\omega_s}{c}\cos\theta_s - \frac{n_{as}\omega_{as}}{as}\cos\theta_{as}\,,
\end{aligned} \tag{E.2}$$

where $\theta_p, \theta_d, \theta_c, \theta_i, \theta_s, \theta_{as}$ denote the propagation angles of the pump, drive, coupling, idler, signal, and anti-Stokes fields, respectively, with respect to the x-axis. The refractive index variation in atomic media is fundamentally bounded within a certain value range [302]. In the presence of the EIT, a positive dispersion slope arises near the two-photon resonance, implying that anti-Stokes photons satisfying energy conservation experience only a small change in refractive index, as opposed to the large variations encountered far from resonance [100]. However, in practice, residual geometric phase mismatch can arise due to imperfect propagation and collection geometry or uncompensated light shifts. The steep dispersion near the EIT resonance enables both negative and positive refractive index variations within a narrow frequency range, which can be important to compensate for residual geometric phase mismatch and enhance the efficiency of the nonlinear parametric process [66]. Although this slow-light-induced change in refractive index Δn is small compared to the vacuum case, the consequent wave-vector shift

$$\Delta k = \Delta n \frac{\omega}{c}\,, \tag{E.3}$$

can still be comparable to the phase-matching tolerance. Considering a cold atomic ensemble with a length of 5 mm, the upper bound of phase-matching tolerance under ideal conditions is given as

$$\frac{\pi}{L} \sim 10^3 \text{ rad} \cdot \text{m}^{-1}\,. \tag{E.4}$$

where is related to the gain profile $\exp(i\Delta\vec{k}L)$. As long as $|\Delta k| \lesssim \pi/L$, the nonlinear process is not completely suppressed, because the generated waves can still constructively interfere before significant dephasing occurs. In practice, imperfections in the optical beams, inhomogeneous atomic cloud distribution, and wavefront distortions reduce the tolerance for phase matching. This limitation is more pronounced in

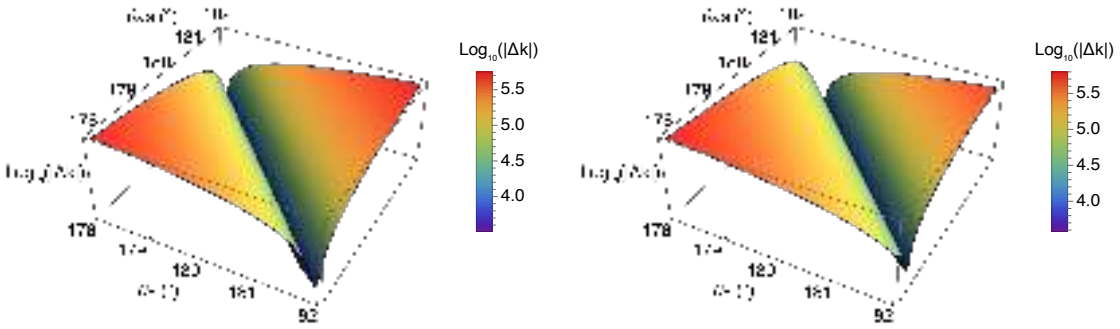

Figure E.2: Logarithmic-scale of phase mismatching term $\log_{10}|\Delta\vec{k}|$ as a function of the Stokes collection angle θ_s and the anti-Stokes collection angle θ_{as} with the pump and coupling field angles fixed at 0° and 180°, respectively. The signal collection angle is fixed at 1°.

the co-propagating configuration, where the nonlinear process is highly sensitive to phase mismatch. In contrast, the counter-propagating pump geometry is less affected by intensity phase coupling [303]. In a certain sense, this still offers a coarse but useful indicator of whether a given pump geometry is feasible [304].

As shown in Figure E.2, we consider the near-axis configuration for spontaneous four-wave mixing (SFWM) with counter-propagating pump and coupling fields ($\theta_p = 0°$ and $\theta_c = 180°$). The driving field differs between the two configurations: (a) $\theta_d = 179°$ and (b) $\theta_d = 179.5°$. The signal photon collection angle is fixed at $\theta_s = 1°$. In both cases, a range of Stokes and anti-Stokes collection angle combinations yield a phase mismatch below the tolerance threshold ($|\Delta\vec{k}| < 10^3$ rad $\cdot$ m^{-1}), indicating viable geometries for efficient six-wave mixing. In particular, the numerical minimization yields two collection angle configurations that correspond to minimal phase mismatch and are experimentally feasible:

- When $\theta_d = 179°$, $\theta_i \approx 178.95°, \theta_{as} \approx 181.07°$
- When $\theta_d = 179.5°$, $\theta_i \approx 181.07°, \theta_{as} \approx 179.41°$